Numerical Simulation of Gas-Liquid Bubbly Flows

Kenneth Sele Asiagbe

Student Number: 200824447

Submitted in accordance with the requirements for the degree
of
Doctor of Philosophy

The University of Leeds

School Chemical and Process Engineering

Faculty of Engineering

October, 2018

Intellectual Property and Publication Statements

The candidate confirms that the work submitted is his own, except where work which has formed part of jointly authored publications has been included. The contribution of the candidate and the other authors to this work has been explicitly indicated below. The candidate confirms that appropriate credit has been given within the thesis where reference has been made to the work of others.

In this thesis; work from jointly authored publications have been used in chapters 4, 5 and 6. The work contained within this publication is directly attributable to the candidate where the co-authors have provided overall guidance and expertise. The citations for these publications are as follows.

List of Article Publications and Presentations:

(From February 2014 to date)

Published papers / Renounced Journal articles:

Asiagbe, K.S., Fairweather, M., Njobuenwu, D.O. and Colombo, M. 2017. Large eddy simulation of microbubble transport in a turbulent horizontal channel flow. *International Journal of Multiphase Flow.* **94**, pp.80-93.

Asiagbe, K.S., Fairweather, M., Njobuenwu, D.O. and Colombo, M. 2018. Large eddy simulation of microbubble dispersion and flow field modulation in vertical channel flows. *AIChE Journal*. https://doi.org/10.1002/aic.16509.

Published Conference papers:

Asiagbe, K.S., Fairweather, M., Njobuenwu, D.O. and Colombo, M. 2016. Multiscale Simulation of Bubbly Flows. In: Zdravko, K. and Miloš, B. eds. *Computer Aided Chemical Engineering.* Elsevier, pp.625-630.

Asiagbe, K.S., Fairweather, M., Njobuenwu, D.O. and Colombo, M. 2017. Large eddy simulation of microbubble transport in vertical channel flows. In: Espuña, A., et al. eds. *Computer Aided Chemical Engineering.* Elsevier, pp.73-78

Asiagbe, K.S., Fairweather, M., Njobuenwu, D.O. and Colombo, M. 2018. Microbubbles coalescence during transport in vertical channel flows. In: Friedl, A., et al. eds. *Computer Aided Chemical Engineering.* Elsevier, pp.79-84

Asiagbe, K.S., Fairweather, M., Njobuenwu, D.O. and Colombo, M. 2018. Microbubble coalescence and breakup in turbulent vertical channel flows. In: Hanjalic, K, A., et al. eds. *Turbulence, Heat and Mass Transfer 9.* Begell House Inc., pp.587-590

Acknowledgements

While trying to write this section, the memories of these four years with all its ups and downs were reminisced in my mind, reminding me that without the support of many people, it was impossible to go this distance alone. Yet it is not possible to mention all the names here and I hope that I will be excused by those whose names are not here.

First, I would like to express the utmost appreciation to my most revered project supervisor Professor Michael Fairweather, who has been a tremendous mentor to me. His attitude, encouragement and constant availability conveyed a spirit of adventure regarding research and scholarship. Without his supervision and constant guidance this thesis would not have been possible. I also want to thank Dr. Derrick O Njobuenwu for his enthusiastic encouragement and useful critiques of this research. He accommodated me, accepted me, and showed me the right approach in learning and morale. Thanks also to Dr Marco Colombo for his 'ever willing to help' spirit. I greatly benefited from his valuable comments, and suggestions.

I also appreciate the financial support of the Niger Delta Development Commission (NDDC) Nigeria for the scholarship provided me for my PhD study.

My sincere gratitude is extended Dr LEJ Konboye, Professor MFN Abowei and Apostle David Zilly Aggrey. Their kindness and prayers will never be forgotten.

A special thanks to my mother, brother and sisters for their payers. At the end I would like to express my deepest appreciation to my beloved wife (Ebitimi) for her continuous support and encouragement, and to my children (Deborah, Daniel and Davies). Their presence motivated me each day.

Abstract

Gas-liquid bubbly flows exist in many engineering processes. However, limitations in understanding prevent the optimal design and operation of multiphase equipment. The bubble size distribution is a key parameter in such flows as it governs the interfacial area and the rate of exchange of mass, momentum and energy between the phases. Evolution of the bubble population is to a large extent driven by the coalescence and breakup of bubbles. Due to the lack of experimental studies of these phenomena, accurate predictions from numerical models are of value in improving understanding, and for use in developing engineering models. The work described furthers our insight of and ability to predict bubbly flows by combining large eddy simulation and Lagrangian bubble tracking. Horizontal and vertical channel flows of water over a range of shear Reynolds numbers and air bubble diameters are considered. Coalescence and breakup are favoured in upflows, with high turbulence levels impacting bubble interaction. Coalescence is dominant at low turbulence levels, and increases with decreasing bubble size, whereas breakup is favoured at high turbulence levels. The breakup of air bubbles, under the flow conditions studied, is almost negligible. The simulations are therefore extended to bubbles of refrigerant R134a, with a considerably lower surface tension than air bubbles, with significant levels of breakup detected at high Reynolds numbers. The investigation is a novel contribution to the literature and provides a comprehensive study of next generation predictive techniques. The model developed can predict microbubble behaviour in turbulent flows up to the level of four-way coupling, where inter-bubble collisions, coalescence and breakup are accounted for. Its application extends existing knowledge of these flows, including the effect of bubbles on the carrier fluid. Overall, the tool developed and the understanding generated are of value to industry in allowing the design of more efficient flow processes.

Table of Contents

List of Tables

List of Figures

Nomenclatures

Symbol	Meaning	Unit
A	Area of cross section	m^2
C	Concentration of bubble particle	$kg\ m^{-3}$
C_{AM}	Added mass coefficient	
C_D	Drag coefficient	
$\mathbf{F}_{\mathrm{AM}}$	Added mass	
$\mathbf{F}_{BG}$	Gravity-buoyancy term	
$\mathbf{F}_D$	Drag force	
$\mathbf{F}_{\mathrm{PG}}$	Pressure gradient	
$\mathbf{F}_{\mathrm{SL}}$	Shear lift force	
h	Channel half-height	m
l	Length	m
m	Mass	kg
n_b	Number of bubbles	
$N_x\ N_y\ N_z$	Number of computational nodes	
P	Pressure	$kg\ m\ s^{-2}$
Re_τ	Shear Reynolds number	
Re_B	Bulk Reynolds number	
St	Stokes number	
t	Time	s
σ	Surface tension	$kg\ s^{-2}$
$\mathrm{u}_x\ \mathrm{u}_y\ \mathrm{u}_z$	Fluid velocity in three coordinates	$m\ s^{-1}$
$\mathrm{v}_x\ \mathrm{v}_y\ \mathrm{v}_z$	Bubble velocity in three coordinates	$m\ s^{-1}$
μ	Fluid dynamic viscosity	$kg\ m^{-1}\ s^{-1}$
v	Kinematic viscosity	$m^2\ s^{-1}$
ϕ	Void fraction	
V	Volume	m^3
x	Wall normal direction	m
y	Spanwise direction	m
z	Streamwise direction	m

Δ	Filter width; grid spacing	
$\in$	Turbulent kinetic energy dissipation rate	$m^2\ s^{-3}$
ρ	Liquid density	$kg\ m^{-3}$
ρ_b	Bubble density	$kg\ m^{-3}$
d_b	Bubble diameter	μm
τ_b	Relaxation/response time	s
s_{ij}	Strain rate tensor	s^{-1}
u_τ	Friction/wall shear velocity	$m\ s^{-1}$
δ_{ij}	Kronecker delta function	
τ_{ij}	Stress tensor	$kg\ m^{-1}\ s^{-2}$
τ_w	Wall shear stress	$kg\ m^{-1}\ s^{-2}$

Sub/super-scripts

$'$	Instantaneous value
$+$	Non-dimensionalized value
τ	Shear stress

Abbreviations

CFD	Computational Fluid Dynamics
CFR	Constant Flow Rate
CPG	Constant Pressure Gradient
CV	Control Volume
DNS	Direct Numerical Simulation
FVM	Finite Volume Method
HPC	High Performance Computing
IDDES	Improved Delayed Detached-Eddy simulation
LES	Large Eddy Simulation
ODE	Ordinary Differential Equations
PDE	Partial Differential Equations
RANS	Reynolds Averaged Navier-Stokes equations
RP	Rayleigh-Plesset
SGS	Sub Grid Scale
TKE	Turbulence Kinetic Energy
VOF	Volume of Fluid

CHAPTER 1

INTRODUCTION

1.1 Background

Dispersed multiphase flows, where discrete elements in the form of bubbles, droplets or particles are transported within a continuous phase fluid, occur in many natural and industrial processes. Depending on the nature of the continuous and dispersed phases, several classes can be distinguished (Balachandar and Eaton, 2010; Zhou, 2018). Most commonly considered are two-phase flows such as gas-solid flows (dust storms in nature, gas-fluidised beds, pneumatic conveying of solids in industry), see, for example, Mudde (2005). Others are liquid-solid (sediment transport in rivers, liquid-fluidised beds, stirred vessels, slurry flows), see Christopher (2005), and gas-liquid flows (gas bubbles in boiling flows, fluidised bed and stirred reactors, evaporators, heat exchangers, in cavitation, or liquid drops in rainfall, atomization and sprays, inkjet printing, oil/gas transport in pipelines, uptake of greenhouse gases by the ocean), as considered by Thorpe (1982), Molin et al. (2012) and Mudde (2005). However, many flows also involve three or more phases, such as gas-liquid-solid flows (transport and treatment of sewage) and flows with several types of fluids (transport of oil, gas and water in pipelines) or particles (multimodal particle size distribution), see Lee et al. (2014). The wide range of natural phenomena and industrial processes that can benefit from an increased understanding of multiphase flows is evident from these examples.

In this thesis, only gas-liquid flows are considered. Gas-liquid flow is the most complex of the classes of multiphase flows because it combines the characteristics of a deformable interface with those of a compressible phase (Hewitt, 2011). In addition, the interfacial configurations in gas-liquid two-phase flows are very complicated, since there exists heat and mass transfer between the phases, and the interface itself can vary over a wide range of length scales. For a chosen flow configuration (horizontal, vertical or inclined orientation), and for given fluids fed into the system at know flow rates, different flow regimes or flow pattern exist in gas-liquid flows (Taitel et al., 1980; Ren et al., 2017). The typical flow regimes in a horizontal pipe or duct flow are shown in Figure 1.1. Here,

gravity acts normal to the flow direction, and therefore separation of the phases occurs due to gravitational settling. The heavier phase is more likely to be found in the bottom region of the flow domain, resulting in the axial symmetry of the flow being destroyed. The respective flow regimes are:

i. Dispersed bubble flow: the bubbles are dispersed in the liquid continuum (though there is some separation due to gravity as illustrated);

ii. Annular dispersed flow: the liquid flows on the wall of the tube as a film (with some liquid entrained in the core) and the gas flows in the centre;

iii. Elongated bubble flow: there are large bubbles flowing near the top of the tube;

iv. Slug flow: very large waves are present in the stratified layer which touch the top of the tube and form a liquid slug which passes rapidly along the channel;

v. Stratified flow: where gravitational separation is complete; and

vi. Stratified-wavy flow: which occurs with an increase in the gas velocity.

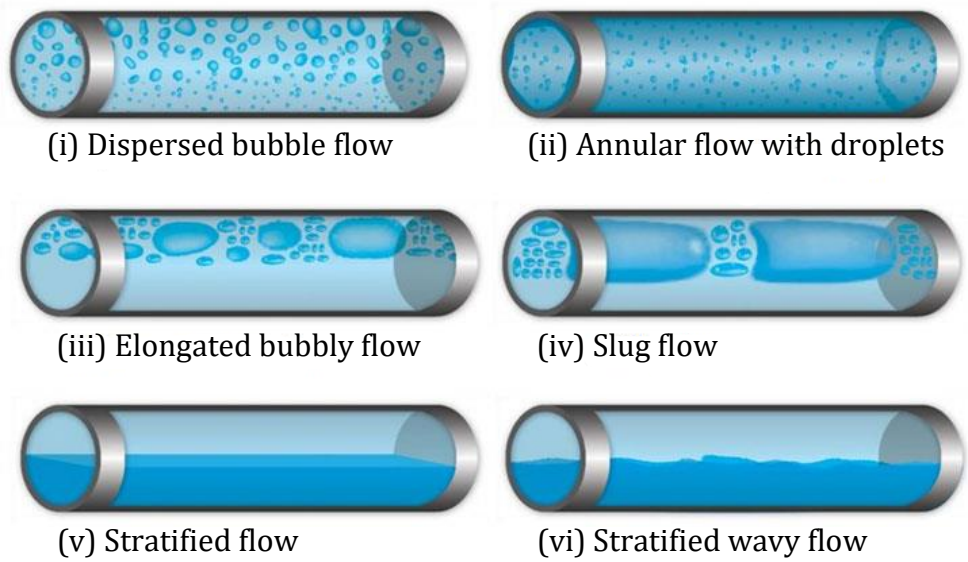

Figure 1.1 Gas-liquid flow regimes in horizontal pipes. Adapted from Bratland (2010).

Vertical flow can be either a downflow, where the flow is moving in the same direction as the gravity, or an upflow, where the flow moves against gravity. The flow regimes occurring in vertical flows are shown in Figure 1.2 and are similar to those in horizontal flows, except for the absence of stratification driven by gravity. The difference between

these two kinds of vertical flows is mainly due to the buoyancy force, which acts either with or against the flow of fluid depending on its direction of flow. The gas, which is the lighter phase, moves faster than the liquid in the case of upflow. In the case of downflow, the buoyancy force acts in the opposite direction and the liquid flows faster than the gas.

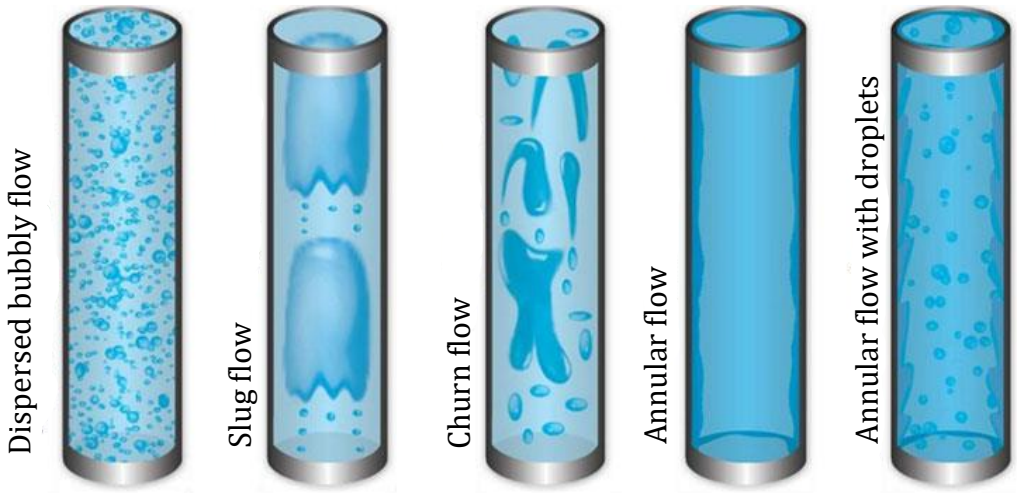

Figure 1.2 Gas-liquid flow regimes in vertical pipes. Adapted from Bratland (2010).

Following the numerous flow regimes that exist, many fluid mechanics practitioners have concluded that, although theoretically possible, it is simply too difficult to solve all the two-phase flow problems that using classical methods (Delnoij, 2001). To circumvent these challenges, the flow distribution classifications in Figure 1.1 and Figure 1.2 are adopted and the main characteristics of each distinct flow pattern are then studied separately. In this thesis, therefore, the focus is on dispersed bubbly flow, also commonly referred to simply as gas-liquid bubbly flow. Gas-liquid bubbly flow, therefore, is a two-phase flow where gas bubbles are dispersed or suspended in a liquid continuum.

Due to the widespread nature and importance of gas-liquid bubbly flows in industrial processes, improvement in the efficiency of unit operations (e.g. bubble columns, atomization and sprays, stirred reactors, etc.) which employ bubbly flows has always been a goal for engineers. Over time, many studies have been published in the literature concerning the design, scale-up and performance enhancement of these unit operations, e.g. see McCabe et al. (1993), Perry and Green (2008), and Coulson et al. (1978).

With the aim of enhancing our understanding of the physics of bubbly flows, extensive experimental investigations have been performed over the years (Liu and Bankoff, 1993;

Serizawa et al., 1975; Descamps et al., 2008; Xu et al., 2012; Lance et al., 1996; Colin et al., 2012; Pitsch, 2006). However, experiments are expensive and the level of detail achievable is limited by the scale of the unit operation and the availability of high-resolution measurement techniques. For example, non-intrusive imaging techniques are limited by the sheer number of bubbles present at a high void fractions. Additionally, the measurement of flow initial and boundary conditions, and of phenomena such as bubble coalescence and breakup, is challenging. In view of the limitations in available experimental measurements, industrial applications of gas-liquid dispersed flows have generally been based on empirical and semi-empirical correlations derived with dimensional analysis from measurements of bulk flow quantities. These correlations are usually not sufficiently robust, however, since they are based on global process parameters and are usually only valid for a specific unit operation and for a limited range of operating conditions. One way to overcome some experimental limitations is the use of numerical simulation using computational fluid dynamics (CFD). Once properly validated, CFD can provide valuable insight into the physics of bubbly flows and support, together with experimental data, improvements in the design and operation of multiphase flow equipment.

Over the last few decades, along with advancements in high-performance computing and modelling software for multiphase flows, CFD has become a powerful tool for use by engineers and scientists (Delnoij et al., 1997; Bini and Jones, 2008; Cinosi et al., 2014; Afkhami et al., 2015; Schwarzkopf et al., 2011; Prosperetti and Tryggvason, 2009). Interestingly, CFD offers several advantages in terms of time, cost and complexity when compared to empirical and semi-empirical approaches. CFD allows the acquisition of a priori information concerning the unit operations of interest, e.g. determining the limiting factors for the performance of a reactor, or calculating the optimum height-to-diameter ratio of a full-scale bubble column (Grube, 2015). In addition, CFD simulations of high accuracy and fine spatial and temporal resolution are increasingly utilised for fundamental studies that aims at gaining a better understanding of the underlying physics of multiphase flows. In doing so, it is possible to explore the influence of a specific phenomenon (i.e. sensitivity studies) on the total performance of the system (e.g. the influence of gas volume fraction, or bubble breakup and coalescence, on process parameters). However, although time-dependent, three-dimensional simulations with a

sophisticated level of detail are feasible at the present time (Sungkorn, 2011), gas-liquid bubbly flows are intrinsically complex and have many modelling issues due to their multiscale nature (Mudde, 2005).

For dispersed multiphase flows, three kinds of modelling approach can generally be identified based on the spatial and temporal resolution of the model (Deen et al., 2004; Delnoij, 2001). These include: (i) the averaged Eulerian-Eulerian approach (also called the two-fluid model), (ii) the Eulerian-Lagrangian intermediate level of modelling and (iii) interface tracking, where all the interface scales are fully resolved (Dhotre et al., 2013; Fraga et al., 2016; Sungkorn et al., 2012). For the engineering modelling of large-scale industrial units (e.g. reactors), which may contain hundreds of millions of bubbles, the averaged Eulerian-Eulerian approach is typically used due to its relatively low computational cost (Gruber et al., 2013). This modelling approach treats both phases as interacting continua, which are coupled with closure models for interphase exchanges of mass, momentum and energy. However, the Eulerian-Eulerian approach suffers from a lack of detail at the bubble level (Colombo and Fairweather, 2016), making direct modelling of the details of processes occurring at this scale impossible (Dhotre et al., 2013).

The Eulerian-Lagrangian approach tracks each bubble individually as a point, i.e. only the centre of the bubble is tracked, but its volume is considered with respect to the displacement of the surrounding fluid phase (Sungkorn et al., 2012). Here, the trajectory of each individual bubble is tracked by solving Newton's second law of motion, accounting for the forces acting on the bubbles. In contrast, the continuous phase is modelled using an Eulerian approach. At this intermediate level of modelling, the Eulerian-Lagrangian approach offers a more detailed description of multiphase flow processes, and is, therefore, widely used (Fraga et al., 2016; Gruber et al., 2013; Lain et al., 2002; Lau et al., 2014; Mallouppas and van Wachem, 2013; Pang et al., 2010; Shams et al., 2011; Sommerfeld et al., 2003; Sungkorn et al., 2012; Vreman et al., 2009; Xue et al., 2017; Subramaniam, 2013). Although the computational cost of tracking a large number of bubbles is high, several studies have shown that Eulerian-Lagrangian models are physically more realistic than those based on the Eulerian-Eulerian approach (Breuer and Alletto, 2012). Hence, the Eulerian-Lagrangian method is preferable for detailed studies of the hydrodynamics of bubbly flows, including bubble coalescence and breakup (Dhotre

et al., 2012; Gruber et al., 2013; Sommerfeld et al., 2003; Sungkorn et al., 2012; Xue et al., 2017).

Interfacial exchange and interactions between the phases can be entirely resolved if the position and shape of each interface structure in the flow is known with accuracy. This is achieved by interface tracking models that explicitly track the interface of each individual bubble. Examples are the volume-of-fluid approach of Hirt and Nichols (1981) and the front tracking approach of Unverdi and Tryggvason (1992) and Tryggvason et al. (2001). In these models, the continuous fluid phase is computed in an Eulerian framework. However, these approaches are still restricted to single bubbles or a few interacting bubbles due to their excessive computational requirements (Deen et al., 2004). Additional details on the modelling methods for multiphase flows are provided in Chapter 2 of this thesis.

Once the method to treat the dispersed phase is defined, the flow and turbulence fields in the continuous phase can be predicted with different approaches, namely direct numerical simulation (DNS), large-eddy simulation (LES) and Reynolds-averaged Navier-Stokes (RANS) models. In DNS, all the turbulent scales are numerically solved (Dabiri and Tryggvason, 2015). In LES, instead, only the largest and most energetic eddies are resolved, while the impact of the small-scale turbulence structures on the flow field is modelled by means of a sub-grid scale model. In RANS, the entire turbulence spectrum is modelled and only the time-averaged flow field is resolved (Fraga et al., 2016).

In view of their relatively low computational cost, RANS models are the most commonly employed in industry (Lain et al., 2002), often with turbulence models based on the isotropic, linear eddy-viscosity assumption. Therefore, these models have clear limitations in most flow conditions and are generally not fully equipped to account for unsteadiness in the flow. Even at a low Reynolds number of the continuous phase, the dispersed phase induces significant turbulence of an anisotropic nature, hence violating the isotropic assumption on which many RANS turbulence closure models are based (Dhotre et al., 2013). On the other hand, DNS is the most accurate approach to predict gas-liquid bubbly flow dynamics. However, the high computational cost makes it impracticable for practical engineering problems involving high Reynolds number flows. At the present time, DNS is most useful for fundamental research on the physics of

multiphase interactions (Molin et al., 2012), or for producing highly accurate solutions for benchmark and validation of less accurate approaches in the absence of appropriate experimental data. In view of this, LES has received great attention in recent years as a compromise between accuracy and applicability. LES with proper modelling of the sub-grid scale (SGS), and its impact on bubble dispersion, can reproduce the results of DNS of turbulent two-phase flows with reasonable accuracy and improved computational efficiency (Delnoij et al., 1997; Deen et al., 2001; van den Hengel et al., 2005; Lau et al., 2014; Bini and Jones, 2008; Shams et al., 2011; Yamamoto et al., 2001).

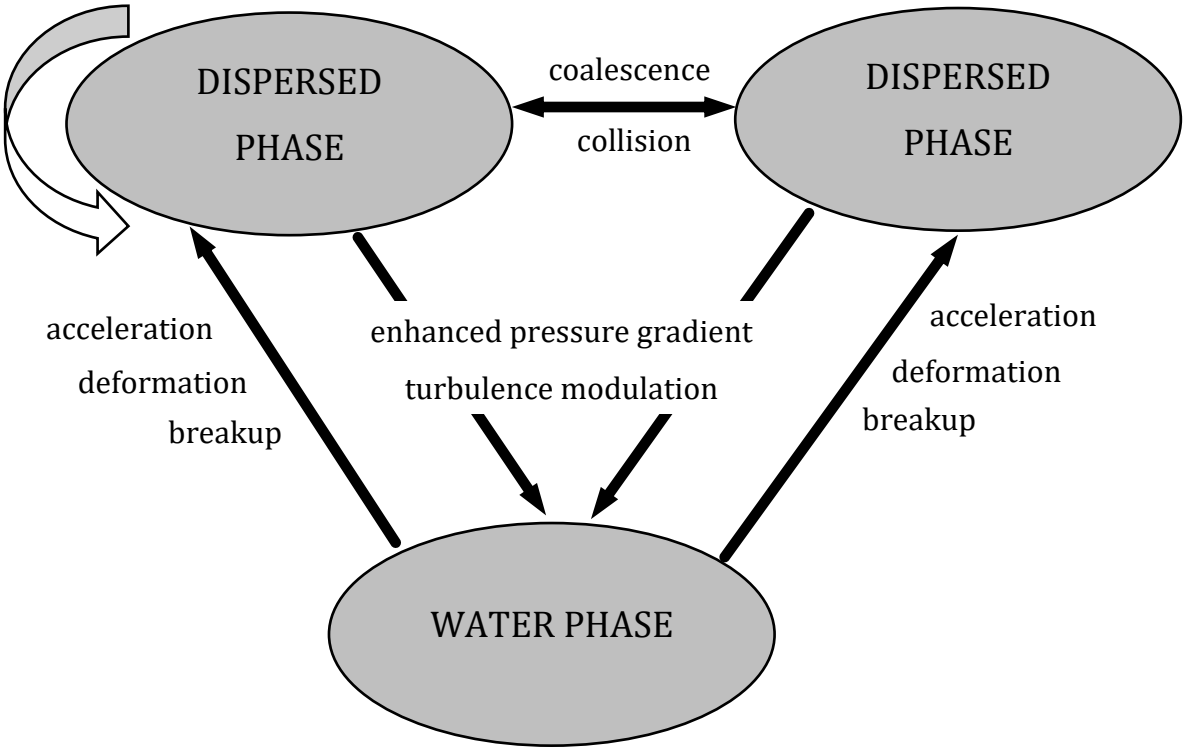

Figure 1.3 Some of the most important and generally accepted interactions between the different phases.

The Eulerian-Lagrangian method is adopted in this thesis. The method is the most appropriate considering the range of bubble sizes investigated in this work (hundreds of microns in diameter and comparable to the computational cell size) and the level of detail in the description of physical phenomena that the work aims to achieve, i.e. at the level of bubble coalescence and breakup. In the Eulerian-Lagrangian approach, the dynamics of

the liquid phase is predicted using LES while the motion of each bubble is tracked with a Lagrangian bubble tracker. At low bubble volume fractions (e.g. $\phi \leq 10^{-6}$) the effect of a bubble on the flow of the continuous field are negligible and one-way coupling between the gas and the liquid phase can be assumed. At higher void fractions ($10^{-6} < \phi < 10^{-3}$), however, two-way coupling which accounts for the impact and feedback of the bubbles on the liquid velocity and turbulence fields is required. With further increases in the bubble volume fraction ($\phi \leq 10^{-3}$), bubble-bubble interactions, bubble coalescence and bubble breakup are also included in a truly four-way coupling fashion (Elghobashi, 1994). Figure 1.3 illustrates some of the complex interactions, and their outcomes, between the two flow phases.

1.2 Motivation, Objectives and Scope of Research

The numerical simulation techniques available for predicting turbulent gas-liquid bubbly flows are still in need of substantial improvement. Although an extensive amount of research has been performed in the past, the simultaneous existence of physical phenomena (bubble dynamics, bubble coalescence and breakup, bubble size distribution) spanning a wide range of length scales makes the modelling of gas-liquid bubbly flows extremely complex. In addressing this multiscale complexity, until recently one of the key challenges has been the limitation in available computational resources. This has led to engineers having to make significant assumptions and simplifications, neglecting certain physical effects or limiting the size of the computational domain. These difficulties, coupled with limitations in the experimental measurement techniques available, have resulted in many physical aspects of bubbly flows still being poorly understood. This lack of understanding, and modelling limitations, negatively affects the design and the performance of multiphase equipment such as chemical reactors.

Therefore, this thesis is motivated by the necessity to advance numerical modelling of such flows, and to improve understanding of the underlying physics of turbulent gas-liquid bubbly flows. To this end, numerical simulations are performed to study dispersed and dense bubbly flows by varying the bubble volume fraction. In the flow, the size of the bubbles can undergo continuous change due to breakup and coalescence. The size of the bubbles determines the interfacial area density that drives exchanges of mass,

momentum and energy between the phases. Therefore, accurate description of the bubble size and its distribution is of paramount importance for the accurate simulation of bubbly flow behaviour. In view of this, a significant portion of the work is focused on extending Lagrangian modelling capabilities to account for bubble breakup and coalescence in a truly four-way coupled fashion.

Specifically, the objective of this thesis is to develop a comprehensive and robust numerical approach for turbulent gas-liquid bubbly flows based on the Eulerian-Lagrangian method and LES. The overall model is used to obtain detailed information and insight into the hydrodynamics of bubbly flows at the small scale, and to quantify their impact on large scale processes with only moderate computational requirements. The modelling techniques used in this study include the following elements:

- The continuous liquid phase is modelled using the LES method, where only the largest and most energetic turbulence scales are resolved, and the small scales are modelled with a SGS model. Specifically, the dynamic Smagorinsky SGS model (Germano et al., 1991; Piomelli and Liu, 1995) has been used to model the effects of the sub-filter scales on the resolved field. It has been shown that LES, when the SGS influence on bubble dispersion is correctly accounted for, can reproduce the results of DNS-based predictions with reasonable accuracy and computational efficiency for turbulent two-phase flows (Delnoij et al., 1997; Deen et al., 2001; van den Hengel et al., 2005; Lau et al., 2014). Recently, Schutte et al. (2015) have demonstrated that the properties of particle agglomerates formed in such flows change when a two-way coupling model is considered rather than one-way coupling. In contrast, no difference was noticed when LES was employed rather than DNS. The work of Schutte et al. (2015), therefore, demonstrates that eddy-resolving simulations (LES and DNS) can successfully capture particle-particle and particle-turbulence interactions.

- The trajectories of individual microbubbles are computed in a Lagrangian framework under the action of gravity, buoyancy and hydrodynamic forces (drag, pressure gradient, shear-lift and added-mass forces), see Maxey and Riley (1983). A set of closure relations for these inter-phase hydrodynamic forces was carefully chosen. The Schiller Naumann drag correlation (Cliff et al., 1978) is used for the drag coefficient, the Legendre and Magnaudet (1998) correlation for the lift coefficient, and the Fukagata et

al. (2001) correction coefficient for drag modification due to a wall. Impact of SGS velocity fluctuations on microbubble acceleration is considered with a stochastic Markov method (Bini and Jones, 2007; Bini and Jones, 2008). It should be noted that the Eulerian-Lagrangian approach adopted in this work considers bubbles as pointwise objects with a size smaller than the grid spacing and does not resolve the gas-liquid interface.

- Two-way coupling between the continuous fluid phase and the microbubbles is implemented by including, in the Navier-Stokes equations, momentum source terms due to the dispersed phase (Schwarzkopf et al., 2011; Lain et al., 2002; Bini and Jones, 2008). The source terms are calculated by time and ensemble averaging of the bubble trajectories for each control volume.

- A CFD code based on the Eulerian-Lagrangian framework previously applied to particle simulations (Bini and Jones, 2007; Njobuenwu, 2010; Njobuenwu and Fairweather, 2014) is modified to handle bubbly flows and extended to account for bubble coalescence and breakup. In doing so, a deterministic bubble-bubble collision model based on Hoomans et al. (1996) hard-sphere collision model is employed. An efficient collision search algorithm based on virtual cells is also implemented. After a collision is detected, the Prince and Blanch (1990) film drainage model is adopted for the description of bubble coalescence. This method is selected due to its accuracy in predicting experimental results (Darmana et al., 2006; Chesters, 1991) and its compatibility with bubbly flows considered using the Lagrangian framework. For bubble breakup, the model of Martinez-Bazan et al. (1999) is adopted, again in the Lagrangian framework. This choice was motivated by the fact that it has an extensive theoretical basis and its results are comparable with experimental data (Lasheras et al., 2002; Liao and Lucas, 2009).

- First, the CFD model developed is validated using DNS solutions for gas-solid turbulent channel flows at shear Reynolds numbers $Re_\tau = 150$ (Marchioli et al., 2008), $Re_\tau = 300$ (Marchioli and Soldati, 2007) and $Re_\tau = 590$ (Moser et al., 1999). In order to study both the effect of bubble-bubble interactions (collision and coalescence) and the effects of bubble-fluid interactions (turbulence modulation and breakup), four kinds of simulations are addressed: (1) a turbulent channel flow with bubbles (bubble size, $d_b =$ 110, 220 and 330 μm) at three shear Reynolds numbers ($Re_\tau = 150$, 300 and 590) under

a one-way coupled assumption; (2) a turbulent channel flow with bubbles, but without collisions using two-way coupling; (3) a turbulent channel flow with bubble-bubble interaction (four-way coupled case), and (4) a turbulent channel flow with bubble breakup. For the latter case, four shear Reynolds numbers ($Re_\tau = 150$, 300, 590 and 2000) are considered, and an additional fluid system with a refrigerant at $Re_\tau = 1154$. The differences between cases (1) and (2) quantify the effects of bubble-fluid interactions, whilst the differences between cases (2) and (3) quantify the effects of the bubble-bubble interactions. Differences between cases (3) and (4), if any, quantify the effects of bubble breakup.

- The CFD model is used to carry out comprehensive and detailed sensitivity studies of microbubble dynamics, turbulence modulation and microbubble coalescence and breakup with respect to channel flow orientation and bubble size. Specifically, different channel orientations are considered, with no gravity, horizontal and vertical downward and upward flow conditions considered.

1.3 Contributions and Originality

The main contribution of this work is the development of a comprehensive modelling technique for gas-liquid bubbly flows capable of high accuracy and applicable to industrial-scale process (i.e. high Reynolds number flows). The following points cover the significant contributions provided by the work described in this thesis:

- The efficient, deterministic Eulerian-Lagrangian technique developed is able to predict time-dependent, three-dimensional phenomena down to the bubble-scale. The technique is based on LES and the Lagrangian tracking approach and allows for one-way, two-way and four-way coupled investigations depending on the flow conditions.

- Implementation of new numerical techniques in the LES code that provide a systematic and efficient method for investigating the effects of bubble-bubble interaction (i.e. collision and coalescence) as well as bubble-liquid interaction (i.e. turbulence modulation and bubble breakup) on the dynamics of the gas-liquid flow. The modelling techniques are based on elementary physical principles that are valid for a wide range of

scales. Therefore, the overall applicability of the modelling approach is not limited only to laboratory-scale systems but is also valid for large-scale systems.

- A model capable of providing better understanding and insight into the hydrodynamics of gas-liquid flows. At the same time, by using LES, a model that remains computationally acceptable and applicable to flow conditions of industrial interest in the design of multiphase equipment. This is particularly relevant in view of the still restricted applicability of DNS to large-scale flows and the limited availability of experimental measurements at the smallest scales in bubbly flows. The amount of local detailed information obtainable from the LES Eulerian-Lagrangian model developed can be used to underpin the development and validation of more macroscopic approaches such as RANS-based models, population balance models and Eulerian-Eulerian two-fluid model closures.

1.4 Thesis Outline

The outline of this thesis is as follows:

- Chapter 2 is dedicated to the fundamental theory of turbulent gas-liquid flows, the respective modelling and simulation techniques and relevant previous works. Chapter 2 outlines the fundamental concepts and theories regarding turbulent gas-liquid flows and the numerical and experimental techniques for bubbly flows. Specific subjects covered in this chapter include previous works on one-way, two-way and four-way coupled simulations. Other subjects include modelling techniques such as direct numerical simulation, large eddy simulation, Reynolds-averaged Navier-Stokes models, Eulerian-Eulerian and Eulerian-Lagrangian techniques. Previous works on the study of bubble dynamics, the effect of geometry shape and orientation, bubble-bubble collision, bubble coalescence and bubble breakup are reviewed. A summary reflecting the state of the art and gaps in the literature that provide justification for carrying out the work covered in this thesis is also presented.

- Chapter 3 introduces the mathematical modelling of turbulent gas-liquid bubbly flows. The focus is on the LES descriptive equations, SGS modelling, modelling of the pressure gradient required to drive the flow and bubble feedback effects in two-way

coupled simulations. Thereafter, the bubble tracking technique is presented. The fundamental concepts of Lagrangian bubble tracking and the closure models for drag, lift and SGS forces are given. This is followed by a description of the models used for investigating bubble-bubble collision, bubble coalescence and bubble breakup.

- In Chapter 4, the first set of results is discussed. The velocity statistics for single-phase and dispersed phase flow injected with solid particles for Reynolds numbers Re_τ = 150, 300 and 590 are discussed to ascertain the viability of the Lagrangian tracking technique. Additional simulations are carried out in a vertical (upflow and downflow) channel at Re_τ = 150 and 590 with a bubble size of d_b = 220 μm under a one-way coupled flow regime using the modified Langragian tracker with and without the inclusion of the lift force term to predict the effects of lift in turbulent flows. The chapter also provides two-way coupled simulation results for horizontal channel and vertical channels (upflow and downflow) laden with bubbles of d_b = 110, 220 and 330 μm at Re_τ = 150 and 590. The results demonstrate the effect of bubbles on the fluid flow, and its turbulence field, and the effect of Reynolds number on turbulence modulation and bubble preferential concentration pertaining to the flow direction. The Re_τ = 150 results are compared with available DNS data.

- Chapters 5 and 6 further discuss the extension of the modelling technique presented in Chapter 4. Bubble coalescence, bubble breakup and the interaction between bubbles and turbulence are discussed in detail. Simulations of gas-liquid bubbly flow in vertical channels are performed. In the absence of experimental data or DNS solutions, the LES results are compared with earlier LES predictions to demonstrate the effect of the added physical phenomena to the overall bubbly flow dynamics. The chapters demonstrate the feasibility of using an LES-based Eulerian-Lagrangian technique as a tool to gain insights and accurate prediction of gas-liquid bubbly flows.

- General conclusions and the outlook for future research are discussed in Chapter 6. The main findings of the research are briefly summarised. Achievements are presented and challenges for future research discussed.

CHAPTER 2

LITERATURE REVIEW

In this chapter, a brief review of the modelling of turbulent two-phase flows is provided, together with a review of numerical and physical modelling of such flows in various geometries. Recent developments and trends in the numerical computation of single-phase flows on the basis of DNS (direct numerical simulation), LES (large eddy simulation) and RANS (Reynolds-averaged Navier-Stokes) approaches are summarised. Various techniques and concepts used in modelling bubbly flows are reviewed, including Eulerian-Eulerian, Eulerian-Lagrangian and fully resolved modelling approaches. Physical phenomena such as bubble dispersion, bubble-bubble collision, coalescence and breakup are discussed, and the main modelling advances reviewed. Significant experimental studies of gas-liquid bubbly flows, the data from which are crucial for the validation of any numerical technique, are summarised. Finally, gaps in the literature are identified, and the intended contribution of the work discussed in this thesis is outlined.

2.1 Modelling of Turbulent Two-Phase Flows

Turbulent dispersed multiphase flows are often encountered in many applications from small-scale laboratory equipment to large industrial plant. Multiphase flow equipment includes bubble columns, fluidized beds, chemical reactors and sprays, and applications are not limited to chemical engineering but extend over the entire engineering field. For a more detailed discussion of turbulent dispersed flow applications, the reader is referred to the numerous published books and reviews (Zhou, 2018; Yang et al., 2017; Zhou, 2010; Balachandar and Eaton, 2010).

The design, scale-up and optimization of turbulent multiphase equipment involves significant complexities and requires substantial understanding. Most of the time, different local phase arrangements and flow regimes, often over a large range of length scales, can be found in different regions of the same equipment. In view of this, simulation of the entire range of flow regimes is extremely challenging, and frequently practically impossible because of the number of physical phenomena present and the range of length

and time scales involved. Due to this complexity, the most promising approach is the so-called multi-scale method, where mathematical models at the different scales are explicitly coupled in the same computational framework, or interfaced and allowed to exchange information between each other. Various attempts have been made in this regard in an attempt to advance understanding of the physics involved at an achievable computational cost (Pitsch, 2006; Van den Akker and Harry, 2010).

In the next section, before moving to dispersed flows in Section 2.3, the modelling of single-phase flows, which is the starting point for modelling of the continuous-phase in an Eulerian-Lagrangian model, is considered.

2.2 Modelling Single-Phase Flows

Computationally, to simulate turbulent single-phase flows, three options are at our disposal: direct numerical simulation (DNS), where all the scales in the flow are resolved, Reynolds averaged Navier-Stokes (RANS), where the turbulence field is entirely modelled, and large eddy simulation (LES). In LES, only the large, energy-containing turbulent eddies are resolved, while the smallest scale motions are modelled with a sub-grid scale (SGS) model.

2.2.1 Direct Numerical Simulation

DNS is the most accurate modelling technique. The time dependent Navier-Stokes equations are fully-resolved numerically without any turbulence model requirement. DNS predicts the instantaneous flow field at any point within the flow and the mean flow and the turbulent velocity fluctuations can be determined by averaging of the instanteneous field. In order for DNS to solve all the time and length scales in the flow, it requires sufficiently fine space and time discretizations, which results in a large computational workload. For this reason, DNS is limited to flows with a relatively low Reynolds number, and for simple geometries. The use of DNS as a method to simulate industrially relevamt flows is still mostly impracticable. The main use of DNS at present is as an engineering tool to improve less computationally expensive methods, for single-phase and two-phase flows (i.e. RANS and LES). Several DNS studies of bubbly flows have

been published in vertical (Giusti et al., 2005; Pang et al., 2010; Santarelli and Fröhlich, 2016) and in horizontal (Mazzitelli et al., 2003; Xu et al., 2002; Pang et al., 2014) channels.

2.2.2 Large Eddy Simulation

In LES, the spatially filtered Navier-Stokes equations are solved. LES also requires fine computational grids. However, since only the large energy-containing scales are resolved while the sub-grid turbulent scales are modelled (Porté-Agel et al., 2000; Piomelli and Liu, 1995), computational requirements are reduced with respect to DNS. LES calculates the large scales in space directly, as illustrated in Figure 2.1. Separation between large and small scales is based on a cut-off length that has to be determined. Those scales that have a characteristic size greater than the cut-off length are resolved scales, while those below are modelled with an appropriate SGS model.

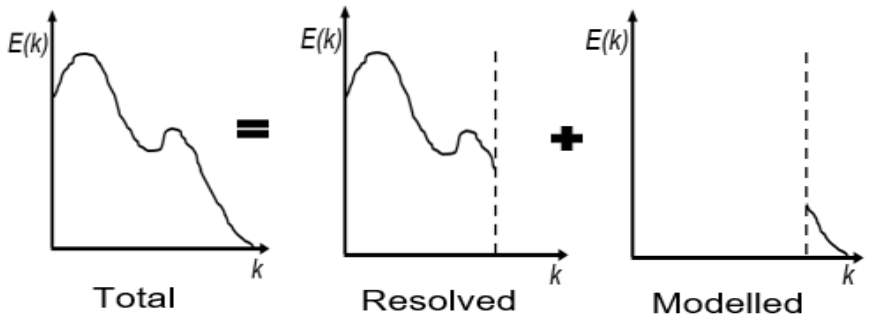

Figure 2.1 LES decomposition of turbulence energy spectrum (Hinze, 1975).

This approach to modelling turbulent flows allows a significant decrease in the computational cost over DNS, as noted, but additonally allows more of their dynamics to be captured than simple RANS models. It has therefore emerged as the next generation of numerical simulation techniques for use in and on behalf of industry in recent years. With time, more accurate models for the residual turbulent stress tensor, necessary for closure of the filtered Navier-Stokes equations, have been developed. The first SGS model was developed in 1963 by Smagorinsky (1963), for simulation of the dynamics of the atmosphere's air currents, followed by the models of Smagorinsky et al. (1965) and Fischer (1965). Deardorff (1970) was the first to use the Smagorinsky model for prediction of the turbulent shear flow in a channel at large Reynolds numbers. Based on

its many applications, LES has been recently adopted to investigate the complexities of turbulent bubbly flows.

2.2.3 Reynolds-Averaged Navier-Stokes Modelling

The RANS approach is, generally, based on Reynolds-averaging, i.e. time-averaging, of the instantaneous Navier-Stokes equations, which are separated into mean and fluctuating components. RANS methods are less computationally expensive compared to DNS and LES. However, time averaging of the momentum equation leads to the loss of details contained in the instantaneous fluctuations and the appearance of unknown correlations known as the Reynolds stress terms. To model these terms and capture the action of the turbulence on the mean flow field, an additional turbulence model is required to close the equation set. Common RANS turbulence models are generally classified according to the number of additional transport equations that need to be solved in conjunction with the time-averaged Navier-Stokes equations.

Over the years, many turbulence models have been developed: mixing length, Spalart-Allmaras, $k-\varepsilon$, $k-\omega$, algebraic stress and Reynolds stress models (Davidson, 2017). $k-\varepsilon$ and RSM are the most frequently used (Wilcox, 2006). RANS approaches are commonly used in practical engineering applications, mainly for predicting steady-state flows. Unsteady versions, commonly known as URANS (unsteady Reynolds-Averaged Navier-Stokes) methods, have been developed to predict time-dependent and transient flow conditions (Speziale, 1991; Pope, 2000; Durbin and Reif, 2010; Hedlund, 2014).

2.2.4 Comparative Analysis of DNS, LES and RANS

Of the three modelling methodologies, RANS is the least computationally demanding. Therefore, it has been extensively applied to model single- and two-phase flows of industrial relevance with relative speed and robustness compared to LES and DNS. However, RANS models have limitations and they are not equipped to accurately predict the small scale and unsteady fluid-bubble and bubble-bubble interactions in a turbulent bubbly flow. LES can predict the instantaneous flow field and the increase in computational capacity over recent years has made LES studies of high Reynolds number two-phase flows achievable. Although DNS may provide more accurate predictions, the

exceptional computational demand still limits its applicability to more fundamental studies and benchmarking of LES and RANS models. LES is now capable of delivering more quantitative solutions for bubble dispersion, coalescence and breakup in two-phase bubbly flows of industrial relevance. For modelling the small turbulence scales, a dynamic Smagorinsky SGS closure is chosen. In the recent comparisons of Afkhami et al. (2015), this type of model provided the best results when compared with predictions of the Smagorinsky model, the Vreman model and the wall-adapting local eddy-viscosity model, and DNS results.

2.2.5 Other Techniques

Other numerical approaches to the prediction of continuous phase flows are the fluid-in-cell method of Müller (1994) and Gentry et al. (1966), the vorticity stream function approach of Fromm and Harlow (1963), the marker and cell method of Harlow and Welch (1965), the lattice Boltzmann method of Sankaranarayanan et al. (2003), and the boundary element method. The finite element method is also used by engineers, scientists and mathematicians to obtain solutions of the partial differential equations that describe, or approximately describe, a wide variety of physical (and non-physical) problems, as opposed to the finite-volume method used herein.

The immersed boundary method is an accurate, highly efficient approach for use in the simulation of unsteady three-dimensional incompressible flows with complex particle/bubble trajectories. This is achieved by using boundary body forces which allow the imposition of boundary conditions on a given surface not coinciding with the computational meshing network. The governing equations, therefore, can be discretized and solved on a regular mesh thus retaining the advantages and efficiency of standard solution procedures. The predominant issue is then interpolation of the forcing over the mesh used to represent a particle or a bubble which determines the accuracy of the scheme; this ranges from zeroth-order for the most commonly used interpolations up to second-order for an ad-hoc velocity interpolation (Laccarino and Verzicco, 2003; Badreddine et al., 2017)

2.3 Modelling Particle-Laden Flows

The two modelling approaches most frequently employed to simulate multiphase flows are the Eulerian-Eulerian approach (Pfleger and Becker, 2001; Becker et al., 1994), and the Eulerian-Lagrangian approach (Lau et al., 2014). While the Eulerian-Lagrangian approach is more fundamental and tracks each single bubbles as a point source, the Eulerian-Eulerian method is preferred in higher gas volume fraction and churn turbulent flows.

2.3.1 Eulerian-Eulerian Technique

In the Eulerian-Eulerian description of two-phase flow, the dispersed phase and the continuous phase are treated as two interpenetrating continua. Therefore this approach is often referred to as the two-fluid formulation. To derive the equations of motion, the infinitesimal volume dV shown in Figure 2.2, over which the field quantities of both phases experience an infinitesimal change, is split into two separate volumes (Mashayek and Pandya, 2003; Zhou, 2015).

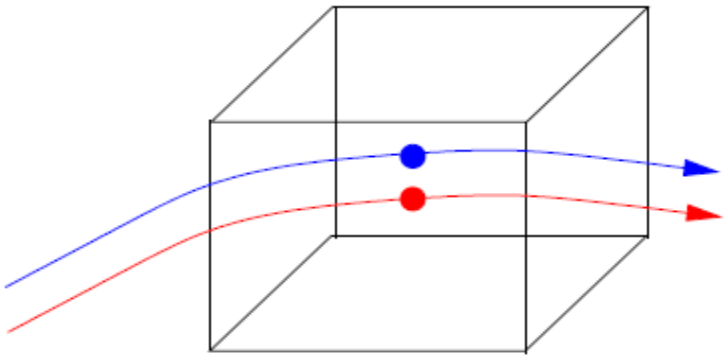

Figure 2.2 Eulerian–Eulerian approach: Concept of two interpenetrating continua – red (dispersed) and blue (carrier) phases.

The equations of motion for both phases are derived separately. The continuous and dispersed phase are therefore each described by a set of Navier-Stokes equations, closed within LES or RANS formulations. In Eulerian-Eulerian models, interphase transfer of mass, momentum and energy are entirely modelled (rather than simulated). These processes are driven by the interfacial area density and the evolution of the bubble size distribution. Accurate prediction of changes in the bubble size distribution as a

consequence of bubble coalescence and breakup is therefore of paramaount importance in Eulerian-Eulerian models (Calderbank et al., 1964; Bhaga and Weber, 1980; Crabtree and Bridgwater, 1971; Wilkinson et al., 1993; Otake et al., 1977; Chahed et al., 2003; Colombo and Fairweather, 2015).

2.3.2 Eulerian-Lagrangian Technique

The Eulerian-Lagrangian approach is commonly used for dilute two-phase flows where one phase is finely dispersed in a continuous carrier phase. The flow of the continuous phase is calculated in an Eulerian framework according to one of the three aforementioned options (RANS, LES or DNS). Then, the behaviour of the dispersed phase is predicted by tracking the path of individual point bubbles in a Lagrangian framework (Apte et al., 2003) using a Lagrangian particle tracking (LPT) technique. The coupling between the phases can be one-way (Marchioli et al., 2008), when the presence of the dispersed phase has no impact on the flow of the carrier phase. When the dispersed phase impacts the flow field of the continuous phase, the coupling is two-way (Molin et al., 2012) or four-way (Yamamoto et al., 2001), with the latter also accounting for bubble-bubble interaction. The consequence of treating bubbles as pointwise, however, is that the flow induced by the presence and the motion of the bubbles remains unresolved (Sommerfeld, 1996; Sommerfeld et al., 2003).

2.3.3 Inter-phase Tracking

This approach is based on solving a single set of transport equations for the whole computational domain and treating the different phases as a single fluid with variable material properties. Changes in these properties are accounted for by advecting a phase indicator function. Interfacial exchange terms are incorporated by adding the appropriate sources as delta functions or smoothed gradients of the composition field at or across the interface (Lakehal et al., 2002). Alternatively, phenomena taking place at the interface are either modelled (Bishop, 1975) or fully-resolved if the topology and shape of the interface is explicitly simulated through use of a *interface tracking method* (Fulgosi et al., 2001).

2.4 Literature Review on Bubbly Flows

In this section previous works on bubbly flows are reviewed, from modelling and simulation approaches (divided between DNS, LES and RANS) to experimental studies and the modelling of bubble coalescence and breakup.

2.4.1 Modelling and Simulation Approaches

2.4.1.1 Direct numerical simulation

DNS has been employed by several authors to predict the behaviour of bubbles in turbulent flows. Among others, the front-tracking method has been proposed to handle the smallest time and length scales of the bubble and the surrounding fluid (Unverdi and Tryggvason, 1992; Tryggvason et al., 2001; Kanai and Miyata, 2001; Göz et al., 2002; Irfan and Muradoglu, 2017). This approach can generate insight into the behaviour of a single rising gas bubble, or the behaviour of a few rising gas bubbles, and supports the development of closures for bubble-liquid interaction. Lu et al. (2005) worked on the effect of bubbles on wall drag in a turbulent channel flow. The authors performed DNS simulations of 16 bubbles at Reynolds number $Re_\tau = 135$, with bubbles that were 54 wall units in diameter. All the flow scales of the bubbles and the surrounding flow were resolved.

Esmaelli and Tryggvason (1999) and Delnoij et al. (1997) used an approach which provides the most detailed insight into single-bubble dynamics, as well as bubble-bubble and bubble-fluid interactions. The authors evaluated the influence of basic physical and geometrical parameters such as inertia, viscosity, surface tension, bubble size and gas volume fraction on the evolution of bubble swarms.

Bunner (2000) investigated gas-liquid bubbly flows by DNS using a parallelized version of a finite-difference method and three-dimensional simulations of up to 216 bubbles at a bubble Reynolds number of approximately 20. The effects of inertia, viscosity, surface tension and interface deformation are all accounted for. Homogeneous flows were analyzed first to examine the interaction of the bubbles in the absence of walls. Simulations were performed for both spherical and ellipsoidal bubbles. Results showed

that as the void fraction increases, the average rise velocity decreases, but the fluctuation velocities continue to increase.

Lee and Balachandar (2017) carried out DNS of a system of a few two- and three-dimensional bubbles at a low but finite Reynolds number, in the range of $2 \leq Re \leq 100$, in an initially quiescent homogeneous flow modelled as a periodic domain. The simulations included a fully deformable interface, surface tension, inertia and viscosity. While the bubbles were deformable, the actual deformations were small due to the low flow Reynolds number. The aim of this work was to compare the evolution of freely evolving bubbles with respect to fixed arrays of bubbles, and to examine the utility of two-dimensional simulations for the understanding of a fully three-dimensional system. The results showed that regular arrays of both two- and three-dimensional bubbles are unstable and split relatively quickly, with the regular arrays replaced by the formation of vertically orientated bubble pairs through 'drafting', followed by 'kissing and tumbling' (Esmaelli and Tryggvason, 1999).

Biswas (2007) carried out a DNS study of multiphase bubbly flows in vertical and horizontal channels. Results were compared with predictions from the steady-state two-fluid model of Antal et al. (1991). The simulations were performed assuming a two-dimensional system and the model coefficients were adjusted slightly to match the data for upflow. The model was tested with different values of flow rate and gravity, as well as in downflow conditions. Results reasonably correlate in the middle of the channel. However, in upflow, the model performed poorly near the no-slip wall. Deformability of the bubbles was found to play a significant role in the flow structure and the averaged flow rate obtained. The aim was to examine how a simple one-dimensional model for the averaged void fraction captures the unsteady bubble motion by using void fraction dependent velocities. Results suggested that bubble dispersion by the fluctuating liquid velocities must be included, and an improved agreement was found by using a simple model for the bubble dispersion.

Bogdevich et al. (1977), Madavan et al. (1984), Merkle and Deutsch (1989), Gutiérrez-Torres et al. (2008) and Ceccio (2010) studied drag reduction by microbubbles. Drag reduction rates as high as 80% were obtained by injecting air through a porous plate to produce bubbles. In these works, drag reduction by microbubbles was found to be related

to numerous factors such as gas type, gas injection rate, surface roughness and configuration, the presence of surfactant, bubble size and shape, flow velocity, Froude number, Reynolds number, and global void fraction. Kanai and Miyata (2001) and Shen et al. (2006) pointed out that bubble size is a critical factor. Drag reduction was achieved only when the bubble diameter was less than approximately 1 mm, and the drag reduction rate was generally higher with even smaller bubble diameters. Sanders et al. (2006), Xu et al. (2007) and Zhou and Bai (2011) also studied drag reduction techniques by micorbubbles. Results from these authors confirm that drag reduction by microbubbles can be as high as 80%.

Shams et al. (2011) developed a two-way coupled Eulerian-Lagrangian approach to simulate cavitating flows using DNS/LES and an unstructured grid approach. The Rayleigh-Plesset equation was applied to determine the behaviour of the bubble radius, but bubble coalescence or breakup were not accounted for. Numerical simulation of a growing bubble inside a micro-channel was simulated by Mukherjee et al. (2011). The bubble was placed at the centre of the channel surrounded by superheated liquid. The length of the bubble was initially found to increase linearly with time but as the bubble approached the channel wall, the bubble downstream interface was found to be accelerated. The bubble growth rate was also found to increase with the liquid superheat.

Bolotnov et al. (2010) carried out detached direct numerical simulations of a two-phase turbulent bubbly channel flow at $Re_\tau = 180$ (based on friction velocity and channel half-width) using a stabilized 'finite element method (FEM)', a level set algorithm to track the interface, and sub-grid wall models. Fully developed turbulent single-phase DNS results obtained previously by Trofimova et al. (2009) with the same stabilized FEM code were used as the initial flow field, and the level-set distance field was introduced to resolve and track the gas bubbles. Surface tension and gravity forces were used in the simulations to physically represent the behaviour of a bubbly air-water flow.

Molin et al. (2012) studied liquid turbuelnce and bubble dispersion patterns in pressure-driven bubbly flows. The physical understanding of bubble-turbulence interaction for small, non-deformable microbubbles in dilute systems was expanded and a benchmark for further comparison established. The effect of the bubble size on the overall behaviour of the two-phase system was obtained. This work is used as a test-case to compare the

the results of the LES-LPT developed in this thesis in view of the detailed results available for the vertical channel domain.

Pang et al. (2014) investigated drag reduction by microbubbles in detail with the Eulerian-Lagrangian two-way coupling method. The liquid velocity field was solved with DNS, and the bubble trajectory was calculated using Newton's law of motion. The interfacial momentum transfer between the gas and liquid phases was accounted for by introducing interphase forces. Results showed a low drag-reduction rate. The liquid-phase velocity was slightly increased in the region away from the channel wall while the Reynolds shear stress of the liquid phase was changed across the whole channel height. The results suggested that drag reduction depends on mutual interactions between the microbubbles and the liquid turbulence, and on interphase forces. The DNS results from Pang et al. (2014) have also been used in this thesis to evaluate the accuracy of the proposed LES-LPT model in a horizontal channel.

The DNS approach was also used in bubble coalescence and breakup studies. Levich (1962) developed a criterion for bubble breakup that is similar to that of Kolmogorov (1949) and Hinze (1955), except that the density of the bubble as well as that of the liquid appears in the criterion. The criterion suggested by Shinnar (1961) for bubble breakup is based on the size of the bubble and its surrounding turbulent eddies. Baldyga and Bourne (1995) generalized the above results to account for turbulent intermittency using a multifractal approach. The multifractal method accounts for the (often large) deviations of the local energy dissipation rate from the mean value. Senhaji (1993) suggested a critical Weber number (a measure of the relative importance of the fluid's inertia compared to its surface tension) of approximately 0.25, based on experimental studies on air bubbles in a uniform turbulent downflow under normal gravity conditions. The results of simulations of the deformation and breakup of bubbles in homogeneous turbulence under zero gravity conditions were also discussed.

Overall, DNS studies are important for discovering the detailed physics of bubbly flows at the bubble scale. However, large-scale simulations of engineering problems with bubbly flows at high flow Reynolds numbers, and with thousands or millions of bubbles are, impractical with DNS due to the large computational requirements. Numerical

simulations of such systems require approaches that are less computationally demanding, as described below.

2.4.1.2 Large eddy simulation

The main difference between conventional RANS modelling approaches and LES is the 'averaging' procedure used to derive the equations of motion. In LES, the instantaneous Navier-Stokes equations are spatially filtered and the filtered, "sub-grid" part of the turbulence spectrum is modelled by means of a SGS model. A number of models for the SGS motion have been proposed, the first and simplest being that of Smagorinsky (1963). Germano et al. (1991) subsequently developed a more promising model, which was later modified by Ghosal et al. (1995) in order to meet certain modelling constraints. Sangani and Didwania (1993) and Smereka (1993) carried out simulations of the potential flow motion of spherical bubbles in a periodic box (both with and without viscous drag) and observed that bubbles tend to form horizontal clusters when the variance of the bubble velocity is small. When the drag force was included, the variance was found to diminish with time. The inclusion of drag force alone (Sangani and Didwania, 1993; Smereka, 1993) in the dispersed phase equation will not result in absolute true behaviour bubbles in turbulence. Added mass alters the drag effect hence plays a major role bubbly flow. Also lift force accounts for mean velocity gradients within the boundary layer and should have been considered.

Mattson (2011) developed a one-way coupled Eulerian-Lagrangian approach that included bubble-bubble collision and coalescence and variable bubble radius. The model was employed to simulate a large number of cavitating bubbles in complex geometries using DNS and LES. Simulations were performed for bubble migration in a turbulent boundary layer, bubble coalescence in a turbulent pipe flow and cavitation inception in a turbulent flow over a cavity. Mattson's work serves as a good take off ground for further research work by considering two-way and four-way coupling techniques.

Ghosal and Moin (1995) evaluated the performance of LES for flows in complex geometries and proposed a varying filter width technique to reflect the changing length scale of the characteristic structures in complex flows. An assessment of the state of LES simulations was carried out by Rodi et al. (1997) and several test cases were considered

for the evaluation of its predictive capabilities. The results revealed that control over parameters such as grid resolution, boundary conditions and numerical method was essential to obtain good results. van den Hengel et al. (2005) used LES with a Langrangian approach to study gas-liquid flows in a square cross-section bubble column domain. The liquid phase was computed using LES and a Lagrangian approach was used for the dispersed phase. The study of Ghosal and Moin (1995) presented LES in complex flow geometries nevertheless starting from a simple computation domain like channel with well-defined initial conditions before proceed to complex flow domains was as well an option to thoroughly predict bubbles behaviour in turbulence.

2.4.1.3 Reynolds-averaged Navier-Stokes modelling

The RANS modelling approach is widely used in the industrial sector despite its shortcomings and limitations. The main criticism of these techniques is their structural inability to represent fundamental turbulence processes, such as energy transfer within the inertial sub-range, and therefore they lack universality in their formulation. In RANS, averaging is performed over time (or realizations) and the averaged variables do not depend on time. Except in cases of simple flow situations, RANS models often struggle to accurately reproduce complex flow fields. They may be accurate in some locations of the flow while being very inaccurate in others.

Laborde-Boutet et al. (2009) carried out computational fluid dynamic (CFD) simulations of gas-liquid flows in a full three-dimensional, unsteady, Eulerian-Eulerian framework and discussed their relevance to laboratory scale bubble columns, with a particular interest in churn-turbulent flows. The available choices for turbulence modelling in the RANS approach were tested using nine different options, i.e. three possible formulations of the k– ε model (standard, re-normalisation group (RNG), realizable) combined with three different modalities to account for gas-phase effects (dispersed, dispersed with bubble-induced turbulence, per-phase). The standard and realizable versions of the k– ε model were unable to reproduce the expected gulf-stream patterns of bubble columns. However, the RNG k– ε model exhibited much better descriptions of the flow features. The inclusion of bubble-induced terms in the turbulence equations led to a minor impact on the performance of the RNG k– ε model. The superior performance of the latter model

was essentially due to it better representation of the turbulence energy dissipation rate and turbulent viscosity. Thus, the application of RNG k– ε models was also recommended for further implementation with bubble population balance models.

Colombo and Fairweather (2015) investigated the ability of a two-fluid Eulerian–Eulerian computational multiphase fluid dynamic model to predict bubbly air–water flows. Upward and downward pipe flows were considered and a database of 19 experiments from 6 different literature sources were used to assess the accuracy of the model, with the aim of evaluating and predicting these kinds of flows and to contribute to ongoing efforts to develop more advanced simulation tools. Emphasis was focused on the prediction of multiphase turbulence due to its relevance in the modelling of bubbly flows in general, including bubble coalescence and breakup, and boiling at a wall. Overall, a satisfactory accuracy was obtained in the prediction of liquid velocities and void fraction distributions in all the flow conditions. Following experimental evidence, the drag model of Tomiyama et al. (2002) was used which assumes that the bubble shape is closer to spherical near a wall and employs a correlation to calculate the bubble aspect ratio. An increase in the drag coefficient due to the higher bubble aspect ratio increased the accuracy of calculated velocity profiles in the near-wall region, even if additional validation is still required due to the possible loss of predictive accuracy in the pipe centre.

In Samir et al. (2017), a computational analysis of a dynamic vortex-cavitation flow was performed. The flow calculations were carried out using a RANS technique as well as improved delayed detached-eddy simulation models. The flow-field was realized as a continuous mixture of liquid and vapour bubbles, in the context of the Eulerian volume of fluid (VOF) method. For predicting the growth and collapse of cavitation bubbles, the multiphase VOF solver was coupled with different cavitation models based on the Rayleigh-Plesset equation, which also accounts for the inertia of bubbles as well as surface tension and viscous effects (Brennen, 1995). The results obtained were validated against reported experimental measurements of the lift force and the vortex shedding frequency. In addition, model predictions were also compared against equivalent CFD simulations reported in the literature (Bensow, 2011). The evaluation of the predicted results suggests that inertial effects of cavitating bubbles have a major impact on the transient characteristics of multiscale vortex cavitation flows.

2.4.1.4. Other techniques

There are several other modelling techniques that have been used to analyse turbulent two-phase flows, as noted ealrier, including detailed studies based on the lattice Boltzmann method (LBM) (Rothman and Zaleski, 1997; Succi, 2001; Chen and Doolen, 1998). Ryskin and Leal (1984) used an adaptive grid finite difference method to simulate the deformation of steadily rising axisymmetric bubbles. Kang and Leal (1987) used the Ryskin and Leal (1984) approach to study the deformation and breakup of bubbles in an axisymmetric flow, although they did not include buoyancy in their study. The front tracking finite difference method of Unverdi and Tryggvason (1992) was used to perform the simulation together with a discrete bubble model, originally developed by Delnoij et al. (1999), which was extended to incorporate models describing bubble breakup and coalescence. The mean and fluctuating velocities predicted in the simulations showed good agreement with the experimental data of Deen (2001).

The LBM guarantees solutions of the Navier-Stokes equations by solving a kinetic equation for the probability distribution functions of an artificial lattice gas. The Chapman-Enskog procedure (Chapman and Cowling, 1961) is used to show that the velocity and pressure fields obtained from the LBM are approximate solutions of the Navier-Stokes equation, as long as they vary slowly in space and time. LBM has the advantage that it is relatively easy to develop for multiphase flows and flows in complex geometries. It can also be used readily in parallel computations since information transfer is local in time and space, as well as, for a given computational domain, being independent of the number of bubbles.

The immersed boundary method was first developed by Peskin (1972) to simulate cardiac mechanics and associated blood flow. The entire simulation was carried out on a Cartesian grid, which did not conform to the geometry of the heart, and a novel procedure was formulated for imposing the effect of the immersed boundary on the flow. Since the inception of this method, several modifications and refinements have been proposed and a number of variants of this approach now exist such as “Cartesian grid methods,” which were originally developed for simulating non-viscous flows with complex embedded solid boundaries on Cartesian grids (Rajat and Gianluca, 2005; Clarke et al., 1986; Zeeuw and Powell, 1991). These methods have been extended to simulate unsteady viscous

flows (Udaykumar et al., 1996; Ye et al., 1999) and thus have capabilities similar to those of immersed boundary methods.

2.4.2 Experimental Studies

In parallel to the development of numerical modelling, many authors have investigated bubbly flows experimentally to better understand their physics (Serizawa et al., 1975; Lance et al., 1996; Pitsch, 2006; Descamps et al., 2008; Colin et al., 2012; Xu et al., 2012). In their experiments, these authors measured the void fraction distribution of the bubbles, the liquid velocity profile and turbulence structure, pressure drops and the effects of bubble size on flow parameters in both upflow and downflow conditions.

Several experimental techniques such as hot film anemometry (HFA) (Kataoka et al., 1986), particle image velocimetry (PIV) (Balachandar and Eaton, 2010), magnetic resonance velocimetry (Baldwin and Barth, 1991; Berger and Aftosmis, 1998), laser Doppler velocimetry (LDV) (Bishop, 1975) and phase Doppler anemometry (Hammami and Ratulowski, 2007) have been used in different flow geometries to understand the bubble behaviour in gas-liquid flows. With these techniques, forces that act on bubbles moving in a continuous turbulent fluid field, the radial and axial void fraction distribution and the liquid and gas phase velocity profiles and turbulent shear stresses (Lucas et al., 2005). Tomiyama et al. (2002); Hosokawa et al. (2010) showed that the dispersion of bubbles occurs in a non-uniform fashion and gives rise to complex interactions with the turbulent flow structures. Other relevant experimental investigations include those of Serizawa and Kataoka (1990), Liu (1997), Mudde et al. (1997), Tran-Cong et al. (1998) and De Matos et al. (2004). Their experiments all showed that nearly spherical bubbles result in a wall-peaking of the void fraction profile in upflow, but in a bubble free wall-layer in downflow. The velocity in the core of the channel flows studied was also found to become nearly uniform in both cases.

The effect of bubbles on the turbulence spectrum was experimentally investigated by Bataille and Lance (1991). They found that relatively large bubbles modify the inertial range scaling. The Kolmogorov energy spectrum power law (-5/3 slope) was replaced by a -8/3 slope with increasing bubble concentration. It was argued by Wang and Maxey (1993) that the steeper spectrum originates from immediate dissipation of energy

production within the bubbles' wakes. In contrast, Mudde et al. (1997) found the classical $-5/3$ power law in a bubble column even for a gas volume fraction of 0.25. Yang and Thomas (1994), and Wang and Maxey (1993) in a previous investigation, showed that solid particles moving in a turbulent flow fall faster than in stagnant fluid, whereas bubbles rise slower than in a non-turbulent flow. This effect is attributed to the phenomenon of "preferential sweeping" of particles and bubbles in downward fluid velocity regions.

Mukherjee et al. (2011) experimentally explored different flow regimes during boiling of water in channels. Experiments were carried out with six channels each with a 1 mm hydraulic diameter. The different flow regimes observed were bubbly flow, slug flow, annular/slug flow and dry out. Large pressure fluctuations were measured in the channels due to boiling. In some situations, slug growth was found to occur in the direction counter to the bulk flow, forcing liquid and vapour back into the inlet manifold.

Kataoka and Serizawa (1989) carried out measurements of turbulence intensity in gas–liquid two-phase flows in vertical pipes and detected turbulence modification via LDV. Gore and Crowe (1989) investigated turbulence modification caused by the addition of droplets in a gas flow, and pointed out that the modification is well correlated with the so-called critical parameter d/l_t, the ratio of the bubble diameter d to a turbulence length scale l_t. They applied this parameter to turbulence modification caused by bubbles and droplets and confirmed that the d/l_t parameter is also applicable to gas-liquid dispersed flows. The critical parameter can also be regarded as the ratio of a characteristic length scale of the turbulence induced by the dispersed phase to that of the shear-induced turbulence. Reese et al. (1995), Enwald et al. (1996), Seol et al. (2007) and Ziegenhein et al. (2016) all used particle tracking velocimetry (PTV) to measure both the dispersed and continuous phases. An important aspect in the processing of the PIV images is the identification of the dispersed phase. Hassan et al. (1992) also performed simultaneous measurements of both the gas and the liquid phase in a system of single bubbles rising in a heavy mineral oil. In order to detect the bubble images, the bubbles needed to be over exposed, with a threshold function used to determine the position of the edges of the bubble. Both tracers and bubbles were tracked within the flow, and in order to obtain the velocity field on a regular grid, the PIV data were interpolated. Results indicated that the

PIV method used was an effective method for studying the specific interactions which occur between the phases in multiphase systems.

Liu (1997) considered the effects of bubble size by using a special gas injector that allowed bubble size variations independently of liquid and gas mass fluxes. All three parameters, bubble size, liquid mass flux and gas mass flux, were changed in the investigation. A vertical upflow of water and air in a round pipe with inner diameter 57.2 mm was studied. Radial profiles of void fraction, bubble size, liquid velocity and axial liquid turbulence intensity were measured at an axial position of $L/D = 60$. In addition, the wall shear stress was measured. A change in the void fraction profile from wall to core peaked with increasing bubble size was observed, as well as turbulence suppression in the pipe centre at high liquid and low gas mass flux, which corresponded to the smallest bubble sizes. This work was also used in previous modelling studies on bubble induced turbulence by Troshko and Hassan (2001) and Politano et al. (2003).

Hosokawa et al. (2007) conducted a study at different liquid and gas mass fluxes in a vertical upflow of water and air in a round cross section small pipe of 25 mm inside diameter. Radial profiles of void fraction, liquid and gas velocity and liquid turbulence kinetic energy were measured at an axial position of $L/D = 68$. The bubble diameter distribution was also recorded. The data show both wall and core peaking void fraction profiles. Turbulence suppression was observed for cases with high liquid velocity, but no clear relation with bubble size was discerned**.** Shawkat et al. (2008) carried out a study, varying the liquid and gas mass fluxes in a vertical upflow of water and air in a round pipe with an inner diameter of 200 mm. Radial profiles of void fraction, bubble diameter, liquid and gas velocities and turbulence intensity were measured at an axial position of $L/D = 42$. A varying void fraction profile from wall to core peaked with increasing bubble size was observed as well as turbulence suppression at the pipe wall for combinations of high liquid and low gas mass fluxes.

Jones and Zuber (1979) and Trabold and Kumar (2001) made phase distribution and velocity measurements in a high aspect ratio rectangular duct, and measured phase distribution in triangular ducts. Neither investigation determined turbulence quantities due to the intrusive nature of the probes used in the HFA technique, which generally alter the flow velocity and other properties. Lopez de Bertodano et al. (1994) obtained multi-

dimensional bubbly two-phase flow data in an isosceles triangular duct having $D_h = 40$ mm at $L/D = 73$. The measurements were performed with a single sensor and X-sensor cylindrical hot film probes of 0.025 mm diameter. These small probes had good bubble penetration characteristics and were capable of simultaneous measurement of the liquid phase instantaneous velocity and the phase indicator function. The data collected were also used in the validation of multidimensional two-fluid CFD models.

2.4.3 Bubble Collision and Coalescence

When the bubble volume fraction is greater than approximately 10^{-3}, the two-phase regime is no longer dilute and bubble-bubble interactions come in to play. Bubble collisions play an important role in affecting the continuous phase flow, and in leading to bubble coalescence, and have to be taken into account by four-way coupled simulations. A bubble, while moving through the liquid phase, may therefore undergo turbulence-driven random collisions with neighbouring bubbles that can result in two bubbles coalescing. The rate of these collisions depends on the bubble approach velocity and the bubble spacing, and the frequency of collision is expected to be higher in regions with higher bubble concentrations.

Several numerical techniques have been developed to model collisions over the past few decades (Ashgriz and Poo, 1990; Tanaka and Tsuji, 1991; Sommerfeld and Zivkovic, 1992; Sommerfeld et al., 2003; Sharma et al., 2016). Numerous experimental studies of coalescence have also been performed (Estrade et al., 1999; Qian and Law, 1997; Kuschel and Sommerfeld, 2010; Brabcová et al., 2015). Elghobashi (1994) presented a diagram (Figure 2.3), as a function of the Stokes number $St = \tau_p/\tau_\eta$, defined using the Kolmogorov time scale τ_η, and the volume fraction ϕ, to characterize the different flow regimes appearing in gas–solid flows. The author ascertained that inter-particle collisions have an effect on the flow if the particle volume fraction is larger than 10^{-3} for homogeneous, isotropic turbulence.

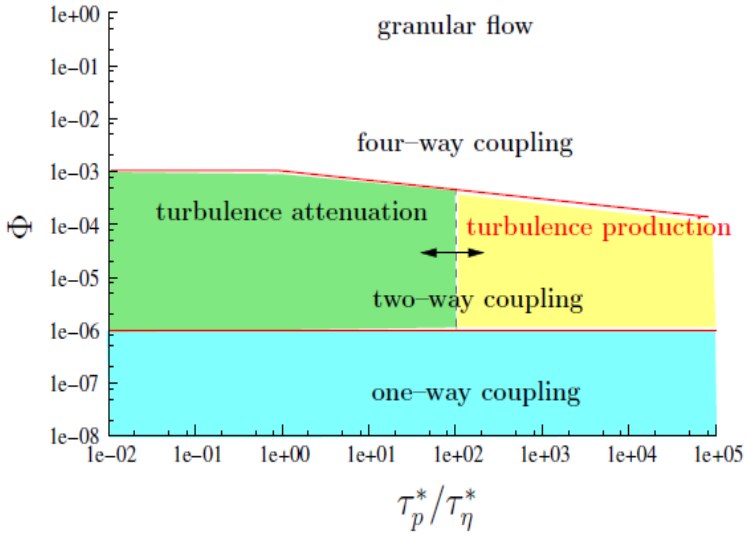

Figure 2.3 Map of different regimes in particle-laden flows (Elghobashi, 1994).

Particle or bubble collisions require two additional elements in any simulation; an algorithm that searches for collisions and a method that determines the result of a collision. The impact between two bubbles can be obtained from their position and relative motion. However, although this approach is numerically very accurate it is computationally very expensive for flows involving a large number of dispersed bubbles. Another technique is to model the collisions by means of a stochastic approach, where the interactions between bubbles are modelled by means of collision probabilities. Such techniques are of course microscopically invalid, but for high number densities they become reliable in the macroscopic sense. Stochastic collision models were originally developed for bubbles by Sommerfeld and Zivkovic (1992).

Yamamoto et al. (2001) investigated a turbulent gas flow with particles in a turbulent vertical channel downward flow. In particular, the effect of inter-particle collision on the two-phase flow field was investigated. The gas flow field was obtained using LES. Particles were treated by a Lagrangian method, with inter-particle collisions calculated with a deterministic method. The spatial resolution of the LES was examined and relations between grid resolution and Stokes number were presented. Results show that the particle mean velocity, the particle wall-normal fluctuating velocity and the number density were flattened as a result of inter-particle collisions, and these results were found to be in good agreement with experimental measurements.

Collision between bubbles can be modelled with the hard sphere (Hoomans et al., 1996) or soft sphere (Tanaka and Tsuji, 1991) collision models, or the statistics-based stochastic inter-particle collision model (Sommerfeld, 2001). In the latter stochastic model, no direct collisions take place. Instead, a probable collision partner is assumed and a collision probability is established from kinetic theory for each parcel at each time step. The bubble size and velocity of the probable collision partner are randomly generated based on statistical information regarding the bubble size distribution and the bubble velocity at Eulerian grid nodes. The probable collision partner normally has similar properties and can be considered representative of surrounding bubbles. The collision probability P_{coll} is calculated based on the properties of the bubble (and its collision partner), and the local fluid properties, as $P_{coll} = \frac{\pi}{4}(d_1 - d_2)^2 \lfloor v_{b1} - v_{b2} \rfloor n_b \Delta t$, where d_1 is the primary bubble and d_2 is the fictitious collision partner.

Breuer and Alletto (2012) also simulated particle-laden two-phase flows based on the Eulerian–Lagrangian approach. The methodology developed was driven by two major requirements: (i) the necessity to tackle complex turbulent flows by eddy-resolving schemes such as LES; and (ii) the requirement to predict dispersed multiphase flows at high mass loadings. A highly efficient particle tracking algorithm was developed working with a curvilinear, block-structured grid and particle–particle collisions (four-way coupling) were predicted using a deterministic collision model. The computational cost was reduced by using the concept of virtual cells, where only adjacent particles were accounted for in the search for potential collision partners. The methodology was applied to different test cases (plane channel flow, combustion chamber flow). The computational results were compared with experimental measurements and good agreement was found, with the technique developed providing a high level of accuracy.

In bubbly flows, coalescence and break up governs the bubble size distribution and the interfacial area density, which drives exchanges of mass, momentum and energy between the phases. Three distinctive theories have been proposed to describe the coalescence process: the kinetic collision model (Howarth, 1964; Sovová and Procházka, 1981); the film drainage model (Prince and Blanch, 1990; Chesters, 1991; Tsouris and Tavlarides, 1994); and the critical velocity model (Lehr et al., 2002).

In the kinetic collision or energetic model, the coalescence process is strictly based on the intensity of the impact between the colliding bubbles. If the approach velocity of the two colliding bubbles exceeds a critical value (leading to deformation of the bubbles' surface), the two bubbles will coalesce. The critical velocity model states that bubble-bubble collision only results in coalescence if the approach velocities of both bubbles are lower than the critical velocity (maximum velocity resulting in coalescence). For a distilled water and air system, the critical velocity is 0.08 ms^{-1} and does not depend on the bubble size. Lehr et al. (2002) used this approach in a population balance equation to predict bubble size distributions in bubble columns. At high superficial gas velocities, bubbles became divided in two groups, one with small and the other with large bubble diameters. In the film drainage model, it is assumed that a certain amount of liquid remains trapped between two bubbles when they collide. For these bubbles to coalesce, the time of their interaction must be enough to allow draining of the film down to a critical thickness. If this is the case, film rupture occurs, and the bubbles coalesce. Otherwise, the bubbles bounce without coalescing (Prince and Blanch, 1990).

For bubbles, coalescence has been studied mainly using an Eulerian-Eulerian (two-fluid) or an Eulerian-Lagrangian approach. With the Eulerian-Lagrangian model, Darmana et al. (2006) developed a coalescence model using the film-drainage timescale previous proposed by Prince and Blanch (1990) and the bubble-bubble interaction timescale proposed by Sommerfeld et al. (2003). Bokkers et al. (2006), in contrast, performed Eulerian-Lagrangian simulations with a hard-sphere collision model, assuming all collisions lead to coalescence (until a maximum bubble size was reached).

In the Eulerian–Eulerian model, the dispersed gas phase is treated as a separate continuum with averaged properties (i.e. a mean bubble diameter). To model the interfacial momentum transfer, most interfacial force models require knowledge of the bubble size distribution or the interfacial area concentration. Some earlier studies have simplified the problem with a single bubble size (or so-called "mean" bubble diameter) (Krishna et al., 2000; Ramkrishna, 2000). Such an assumption is obviously invalid, except for mono dispersed bubbly size distributions, and in most industrial applications. Therefore, a population balance equation (PBE), with coalescence and breakup models, is often embedded in the Eulerian-Eulerian model to handle the evolution of the size distribution statistically. This method has emerged as a promising tool to simulate the

local hydrodynamics in bubble columns (Simonin et al., 1993; Sokolichin and Eigenberger, 1994; Boisson and Malin, 1996; Pfleger et al., 1999; Sokolichin and Eigenberger, 1999). Olmos et al. (2001) coupled an Eulerian-Eulerian model with the population balance equations to simulate the evolution of the bubble size. The coalescence model of Prince and Blanch (1990) was used, with a $k-\varepsilon$ turbulence model for the liquid phase, and assuming isotropic turbulence in the determination of the bubble-bubble collisions. Chen et al. (2005) performed Eulerian-Eulerian simulations using a the population balance equation and compared a variety of bubble breakup and coalescence models. The liquid-phase flow was also simulated with a $k-\varepsilon$ turbulence model.

In the CFD framework, many population balance modelling approaches have been proposed over the years. The multiple sized-group (MUSIG) model has been extensively applied by different researches (Liu et al., 2015; Yuan et al., 2016; Sha et al., 2006). In this model, the bubble diameter distribution is discretised in a number of bubble size classes and a discrete population balance equation with sources for bubble coalescence and breakup is solved for each class.

A relatively simpler approach was proposed with the average bubble number density (ABND) model (Cheung et al., 2007; Cheung et al., 2010; Deju et al., 2013) and the interfacial area transport equation (IATE) (Brooks and Hibiki, 2016; Hibiki et al., 2003; Ishii and Kim, 2004). In these, however, an average diameter over the entire bubble diameter spectrum is employed and the behaviour of the bubble diameter distribution is not predicted. In contrast, the direct quadrature method of moments (DQMOM) model is based on the solution of a number of transport equations for the moments of the dispersed phase size distribution. Therefore, the evolution of the bubble diameter distribution is predicted with this method and as a consequence it has received considerable attention (Santos et al., 2013; Fox et al., 2008; Fan et al., 2004). The Monte Carlo approach is another method that is based on statistical ensembles of a finite large number of realizations of the bubble evolution (Liffman, 1992; Maisels et al., 2004). This method has the advantage of flexibility and accuracy, but it needs substantial computational resources because its accuracy is directly proportional to the number of system realizations.

Overall, numerous numerical approaches have been developed to solve the population balance equation within the two-fluid Eulerian-Eulerian model. However, the limitation of Eulerian-Eulerian models is their inability to account for properties of single bubbles at the bubble scale. Instead, only averaged values are available (mean bubble diameter). Therefore, as mentioned before, the Eulerian-Lagrangian technique has been selected for this work. In this framework, the film drainage model of Prince and Blanch (1990) has been selected to predict bubble coalescence due to its acceptable performance in predicting this phenomenon.

2.4.4 Bubble Breakup

Together with bubble coalescence, bubble breakup plays a critical role in the evolution of the bubble size distribution and the interfacial area available for mass and heat transfer exchanges between the phases. The breakup of gas bubbles in a liquid involves interface-related phenomena. Amongst these, the surface tension is arguably one of the most important parameters. Surface tension occurs when there is a difference between the intermolecular forces across an interface between two immiscible fluids. The resultant product is a force per unit length or an energy per unit area which resists the creation of a new interface (Israelachvili, 2011). Surface tension depends on the strength of the intermolecular attraction forces, the size of the molecules, and the chemistry along the interface. For instance, low surface tensions ($\sim 20\ \mathrm{mNm^{-1}}$) are observed at air/oil interfaces while for the air/water interface the surface tension is higher ($\sim 72.8\ \mathrm{mNm^{-1}}$). Bubble breakup can be due to different mechanisms: (1) turbulent fluctuations and bubble collisions; (2) viscous shear stress; (3) the shearing-off process; and (4) interfacial instabilities. In the following, available models of bubble breakup are reviewed and the application of these in Eulerian-Eulerian and Eulerian-Lagrangian models for the prediction of bubbly flows is considered.

Researchers have been interested in determining the conditions that lead to bubble deformation and breakup for many years. The theory of bubble or droplet breakup in turbulent flow was first developed by Kolmogorov (1949), see Hinze (1955). It was suggested that a bubble breaks as a result of interactions with turbulent eddies that are of approximately of the same size of the bubble. It was assumed that the bubble size was

in the inertial sub-range of turbulence scales and Kolmogorov's universal energy spectrum was used to estimate the strength of eddies having sizes comparable to the bubble. Specifically, Hinze (1955) formulated a criterion for breakup based on a force balance. This criterion states that, in a strong turbulence field, a bubble deforms and breaks if the restoring force due to the surface tension is unable to balance the random pressure fluctuations that cause the deformation.

Following Kolmogorov (1949) and Hinze (1955), many subsequent studies have examined bubble breakup in turbulent flows. Levich (1962) updated the Kolmogorov (1949) and Hinze (1955) criteria by including the density of the air. Zeitling and Tavlarides (1972) approached the breakup problem by modelling the breakage efficiency of bubbles in a stirred tank. Coulaloglou and Tavlarides (1977) developed a phenomenological model that assumed breakup would only occur if the turbulence kinetic energy overcomes the surface energy of a bubble. Prince and Blanch (1990) examined the effect of eddy size on bubble breakup and concluded that breakup was due to interactions with turbulent eddies of a length scale between 0.2 and 1.0 times the bubble diameter. The authors also concluded that eddies larger than this size are only responsible for transporting the bubbles, and those that are smaller deform but are not capable of breaking the bubble. In addition to the length scale, the impact of eddies of different energy has been considered. For instance, Luo and Svendsen (1996) postulated that the minimum energy to initiate breakup should be comparable to the increase in the surface energy associated with the increase in surface area caused by the deformation.

Risso and Fabre (1998) obtained critical values of the Weber number for breakup between 2.7 and 7.8 from experiments under microgravity conditions. The experiments were performed with two sets of bubbles: type A bubbles, which ranged from 2 mm to 6 mm in size, and type B bubbles, ranging from 12.4 mm to 21.4 mm in size. Breakup was observed only for type B bubbles and in around 50% of the cases considered. The authors identified two bubble breakup mechanisms: force imbalance and resonance oscillation. In weak turbulence, it was postulated that a bubble breaks through a resonance phenomenon in which the $n = 2$ bubble oscillation mode is dominant. The $n = 2$ mode of oscillation is a degenerate mode that consists of an axisymmetric mode and two non-axisymmetric modes (Risso, 2000; Ravelet et al., 2011) and in which the bubble volume

is conserved. When the turbulence is sufficiently strong, the resonance mode is bypassed, and the bubble breaks up abruptly.

Qian et al. (2006) studied the feasibility of using the lattice Boltzmann method to simulate bubble breakup in turbulence by simulating the deformation and breakup of bubbles in homogeneous turbulence under zero gravity conditions. The other goal of the simulations was to understand the breakup mechanism. The Reynolds numbers of the simulations, based on the spatial period and the turbulence intensity, were too small for the existence of an inertial sub-range. However, the Reynolds number based on the equivalent spherical bubble diameter and the turbulence intensity was typically around 10^2. The results obtained for bubble breakup agreed well with the low gravity bubble breakup experiments of Risso and Fabre (1998). However, due to the computational demands of the simulations, Qian et al. (2006) were unable to obtain statistical results for the characteristics of the flow field. The number of daughter bubbles from bubble break up during the simulations was never more than 3. In the Risso and Fabre (1998) experiments, however, bubbles were observed to breakup into as many as 10 daughter bubbles. It seems plausible that the difference between these two studies is due to the fact that, in the simulations, the energy spectrum of the turbulence decreased more quickly with wavenumber than in the experiments, in which the bubbles were in the inertial sub-range of length scales. The finite size of the computational domain and the associated interaction of a bubble with the periodic boundaries are also likely sources of discrepancies between the simulations and the experiments. Finally, it was observed that small bubbles may simply dissolve due to Ostwald ripening.

Lehr et al. (2002) studied bubble size distributions and the flow field in bubble columns with cylindrical cross-section using the Eulerian-Eulerian method. The authors used a population balance equation for the average bubble volume. The model developed predicted the rate of bubble breakup and coalescence based on physical principles. The calculated volume fractions, velocities and bubble-size distributions agreed well with existing and previously published experimental results for bubble columns up to 0.3 m in diameter. The breakup constraint was determined by the balance between the interfacial force of the smallest daughter bubbles and the critical value of the inertial force of the interacting turbulent eddies.

Few authors have used the Eulerian-Lagrangian approach to predict the bubble size distribution. In view of its ability to provide more detailed and physically more realistic predictions with respect to the Eulerian-Eulerian model (Göz et al., 2006; Lain et al., 1999) however, the Eulerian-Lagrangian approach has been adopted for studies of coalescence and breakup processes in bubble columns and ducts (Sungkorn et al., 2012; Lau et al., 2014; Xue et al., 2016). According to Lau et al. (2014), the incorporation of breakup models originally developed for the PBE in an Eulerian-Lagrangian approach is not straightforward due to the differences in the mathematical representation. However, the underlying physics that represents these phenomena still hold and the associated constraints can still be used to formulate criteria for breakup in the Eulerian-Lagrangian technique.

In Lau et al.'s (2014) work, the simulations were performed for a square air-water bubble column. The column had a square cross-section of 0.15×0.15 m^2 and a height of 0.45 m. Air was introduced into the system through the bottom of the column via gas injection points. The gas inlet consists of 7×7 points, which were positioned in the centre of the bottom plane of the column with a square pitch of 6.25 mm. The diameter of the bubbles entering the column was set to 4 mm as experimentally observed by (Deen, 2001). The computational domain had an equidistant numerical grid of $30 \times 30 \times 90$ and a fixed time step for the flow solver of 1.0×10^{-3} s. The total simulation time was set to 120 s, the first 20 s of which were discarded to exclude initial condition effects. Results showed that the bubble breakup rate was predominant at the inlet and at the top of the bubble column where incoming bubbles were prone to large turbulent stresses. Breakup probability was very high at the bubble inlet. At the top of the bubble column, the change of liquid flow direction also caused the bubbles to experience large shear stresses. Breakup was assumed to be binary, as generally used in the literature, and the size of two daughter bubbles was determined from a prescribed probability function and the initial bubble volume.

Different probability distributions have been proposed to determine the size of the daughter bubbles. The 'U-shape', which implies that the probability that a small daughter bubble breaks off from the parent bubble, is the highest, and equal sized daughter bubbles has the lowest probability, as used by Tsouris and Tavlarides (1994), Luo and Svendsen (1996) and Tsouris and Tavlarides (1994). The 'M-shape' implies that neither equal sized

breakup nor a small daughter bubble break up have a high probability, but rather that breakup values in between these two extremes have the highest probability (Lehr et al., 2002). The uniform distribution, in contrast, infers that parent bubbles break up into daughter bubbles of any size with equal probability (Narsimhan et al., 1979; Prince and Blanch, 1990). Finally, the 'bell-shape', also known as the normal distribution, was proposed by Lee et al. (1987) and Martinez-Bazan et al. (1999). With this distribution, daughter bubbles with equal size have the highest probability of occurring, while one large and one small daughter bubble have a lower probability.

2.5 Summary of State-of-the-Art and Present Contribution

As stated earlier in this Section, air bubbles suspended in a turbulent liquid flow can interact with each other and with the surrounding fluid. Bubbles deform, vary in size, breakup and coalesce, and bubble behaviour crucially impacts the operation of industrial multiphase equipment, the performance of which is still negatively affected by the lack of detailed understanding of many physical aspects of bubbly flows. In recent decades, CFD has become a widely used and powerful tool for predicting the bubble size distribution (void fraction) and other parameters of two-phase bubbly flows. These parameters are crucial in analysing, optimising and supporting the design and operation of industrial units and engineering equipment that involve two-phase turbulent flows.

In numerical modelling of two-phase turbulent flows, the local grid resolution may be such that the bubbles are fully resolved or under-resolved in relation to the resolution of the underlying mesh (Shams et al., 2011). In addition, the range of length scales in bubbly flows is often very large. Thus, the gas volume fraction impacts the component-scale average flow field. At the same time, the gas distribution is driven by microscale phenomena such as bubble coalescence and the drainage of a liquid film only a few micrometres in thickness. Different approaches have been applied to model this range of scales accurately, leading to multi-scale modelling strategies. The gas-liquid multi-scale modelling hierarchy includes fully resolved direct numerical simulations or lattice Boltzmann modelling approaches with interface tracking, the Eulerian-Lagrangian approach and Eulerian-Eulerian modelling (Lau, 2013). From the fully-resolved to the

under-resolved models, the amount of detail (and the computational cost) decreases while the geometric scale of the simulation increases.

The Eulerian-Eulerian approach, also called the two-fluid model, treats both the carrier liquid phase and the dispersed gas phase as interpenetrating continua (Mashayek and Pandya, 2003; Zhou, 2015; Colombo and Fairweather, 2015). After averaging of the instantaneous phase field, closure relations are required to incorporate the (temporally and/or spatially averaged) interfacial mass, momentum and energy exchanges (Lau, 2013). As information on individual bubbles is lost in this approach, the PBE is often embedded in Eulerian-Eulerian models to predict the bubble size distribution in industrial bubbly flows. The PBE handles the evolution of the size distribution of the dispersed phase statistically through coalescence and breakup models (Lau et al., 2014; Colombo and Fairweather, 2016).

The Eulerian-Lagrangian method involves the use of DNS, LES or RANS for the carrier phase, whereas the motion of each dispersed phase bubble is tracked in a Lagrangian framework using Newton's second law of motion, with the equation closed using model coefficients. The bubbles are usually modelled as spherical pointwise subjected to hydrodynamic and body forces. An additional dispersion model can be included to account for the contribution of the SGS velocity fluctuations in LES, or of the entire turbulence field if the carrier phase is obtained using RANS models, on the bubble acceleration.

At an intermediate bubble volume fraction, the effect of the presence of the dispersed phase on the carrier phase has to be considered. This is represented by a force applied on the continuous phase by the dispersed phase, and such models are commonly referred to as two-way coupled (Shams et al., 2011; Molin et al., 2012). With further increases in the bubble volume fraction, bubble-bubble interactions become significant and, when they are accounted for through collision, coalescence and breakup models, the approach is known as four-way coupled (Shams et al., 2011). The Eulerian-Lagrangian approach is generally accurate in predicting bubble dynamics and transport when all bubble trajectories relevant to a problem are tracked (Shams et al., 2011). In addition, interaction mechanisms and the impact of small (in the range of the bubble length scale) fluid structures on bubble motion can be accurately predicted. In view of this capability of

being able to achieve predictive accuracy and insights into the physics of bubbly flows, without using the computational complexity of a full interface-tracking method, the Eulerian-Lagrangian approach is adopted in this thesis.

For any advanced bubbly flow model, the ability to accurately predict the bubble size distribution is a requirement. The bubble size distribution depends mainly on the competition between bubble breakup and coalescence. Several breakup and coalescence models have been developed assuming different mechanisms, such as turbulence fluctuations in the surrounding liquid and the shear rate of the liquid phase. An overview of these models is given by Liao and Lucas (2009, 2010). The bubble-bubble interaction process consists of two sub-processes, i.e. collision and coalescence. The collision between bubbles is caused by their relative motion, which may be caused by a variety of mechanisms associated with the flow conditions in the carrier phase. The collision between bubbles can be modelled with direct collision models such as the hard sphere (Hoomans et al., 1996) and soft sphere (Tanaka and Tsuji, 1991) collision models, or statistics-based approaches (Sommerfeld, 2001). After colliding, the bubbles can either coalesce or separate without coalescing (Lau, 2013). For the determination of the probability of coalescence during a collision event, there are several descriptions of the coalescence process ranging from the kinetic collision model (Howarth, 1964; Sovová, 1981), the film drainage model (Tsouris and Tavlarides, 1994) and the critical velocity model (Lehr et al., 2002). Between these models, the film drainage approach has been the most popular. Attractive forces between the interfaces drive the liquid film trapped between two colliding bubbles to drain out until the bubbles collapse, and coalescence follows. According to the model, coalescence will occur only if the interaction time exceeds the time needed for the film to drain out down to the critical rupture thickness. In this work, the deterministic event driven approach for bubble-bubble collision, and the film-drainage approach for the collision efficiency, are adopted due to their previous successes in handling these phenomena, as noted earlier in this review.

Turbulent velocity fluctuations are not only a key contributor to the local relative velocity of the bubbles during coalescence but are also a major driver of bubble breakup. Often, a poor knowledge of the local turbulence behaviour in bubbly flows is a major limitation to breakup and coalescence model accuracy. In Eulerian carrier phase models based on RANS approaches, information on the turbulence field is only available through averaged

values, often of limited accuracy, of the turbulence fluctuations and the turbulence energy dissipation rate. In this work, use of the LES technique will enable the prediction of details of the turbulence behaviour at the bubble scale that are required for accurate prediction of breakup and coalescence events. LES is therefore chosen as a compromise between the inaccuracies associated with RANS approaches, and the computational demands of DNS-based predictions.

Despite their relevance, there have been relatively few attempts to model bubbly flows with four-way coupled, high-fidelity turbulent flow solvers that use eddy-resolving techniques coupled to coalescence and breakup models. Therefore, the abilities of such techniques to tackle the complex nature of bubbly flow processes have not been fully explored. At best, most numerical investigations of bubbly flows based on LES and DNS are limited to one-way coupled (Mattson and Mahesh, 2012; Giusti et al., 2005) or two-way coupled (Fraga et al., 2016; Pang et al., 2016) simulations. Previous works on four-way coupled simulation, where all the scales of the bubbles and the surrounding flow are resolved, have been limited to simulations of a few bubbles in turbulence at low shear Reynolds numbers (Lu et al., 2005; Bunner, 2000; Lee and Balachandar, 2017). More specifically, very few authors have employed LES coupled with a Lagrangian bubble tracker to study the hydrodynamics, coalescence and breakup of bubbles in two-phase flows, and those that have considered flows in square cross-section bubble columns (Delnoij et al., 1997; van den Hengel et al., 2005; Lau et al., 2014). In these systems, the smallest bubble size considered is of the order of a few millimetres. Additionally, there have been simulation studies of turbulent bubbly flows in horizontal and vertical channels. The one-way and two-way coupled DNS studies of bubbly flows in vertical (Giusti et al., 2005; Santarelli and Fröhlich, 2016; Pang et al., 2010) and in horizontal (Mazzitelli et al., 2003; Xu et al., 2002; Pang et al., 2014) channels are good examples. However, because of the multiplicity of physical effects, vertical and horizontal channel flows still remain a challenging application for computational tools, and very few studies have treated this problem with four-way coupled eddy-resolving techniques. It is therefore important to extend, and where possible to validate, the modelling capabilities of such techniques to incorporate bubble-bubble collisions, bubble coalescence and bubble breakup, and their effects on the bubble diameter distribution and the

instantaneous and mean flow field, for such simple flows ahead of their application to more realistic geometries of practical importance.

In summary, the main contribution of the work described in this thesis is the development of a comprehensive four-way coupled numerical technique based on an eddy-resolving method. Additionally, the work demonstrates the ability of this technique to predict realistic bubbly flows using deterministic methods and to give new insights into the characteristics of bubbly flows in wall-bounded turbulence. A major limitation associated with such approaches is the rather high computational cost required by eddy-resolving techniques. In view of this, the use of LES will limit computational requirements with respect to those required by DNS, whilst allowing resolution of the majority of the turbulence scales responsible for fluid-bubble and bubble-bubble interactions (i.e. the bubble scale). The computational cost of tracking a large number of dispersed bubbles in a four-way coupled fashion is another constraint to the development of high-fidelity CFD approaches for bubbly flows. Specifically, the detection of collision and coalesce events is particularly onerous, and scales linearly with the number of bubbles in the computational domain. From this point of view, the development of an efficient numerical technique to simulate turbulent bubbly flows at high mass loadings within the four-way coupled regime has significant potential. The algorithm described later efficiently detects bubble-bubble collisions and, once a collision is detected, tests for bubble coalescence based on the film-drainage model requirements and subsequently tests for possible bubble breakup. The performance of the technique developed is tested by performing parametric studies on the influence the bubble size, flow Reynolds number, orientation of the channel and surface tension of the fluid. Although the thesis focuses on channel flows, the impact and outcomes are far reaching, and applicable to any flow geometry. The model can therefore, subsequently, be extended to different geometries and other fields of application and industries where accurate information is required on bubbly flow dynamics and bubble size distribution. This is particularly of value in view of the current lack of detailed experimental measurements of relevance to the many applications of bubbly flows. The developed methodology can also provide details, at the bubble scale, that are difficult, if not impossible, to obtain currently, even with the most advanced experimental techniques.

CHAPTER 3

METHODOLOGY

3.1 Introduction

This chapter presents the mathematical formulation of the Eulerian-Lagrangian framework used in the present work, with a Lagrangian particle/bubble tracker (LPT) implemented in the large eddy simulation (LES) CFD code BOFFIN (Jones et al., 2002). Additionally, the numerical solution methods used to solve the descriptive equations are also described. The models and the numerical techniques were implemented to systematically study the complex behaviour of microbubbles in turbulent flow, beginning from a one-way coupled approach and ultimately with a four-way coupled model accounting for bubble collisions, coalescence and breakup. The BOFFIN LES flow solver and the bubble tracker, originally developed for solid particulate flows, were modified and extended to cover bubbly flows. In addition to the main models for the LES and the LPT, the sub-grid scale (SGS) model used within the LES, and the momentum feedback terms from the bubbles to the fluid, are also described. The bubble force models, collision model and models for coalescence and breakup implemented in the bubble tracker are presented.

The specific contributions of the present work to the development of the overall numerical model were:

- *In the Lagrangian particle tracking algorithm, drag, lift and added mass force terms for bubbles were implemented. These greatly differ from similar models for solid particles. An additional force term, the wall correction coefficient, C_W, was also implemented. This is specific to bubbles and accounts for further modification of the drag force in the vicinity of a solid wall boundary.*

- *The bubble feedback effect (two-way coupling) on the continuous phase liquid flow, and the bubble-bubble collision model (four-way coupling), were developed and implemented.*

- *Models for the coalescence and breakup of bubbles were adapted from the literature, to comply with the Lagrangian tracking framework, and implemented in the bubble tracker.*

3.2 Mathematical Model for Continuous Phase

The evolution of a continuous fluid flow in space and time is described by a set of non-linear, partial differential equations, commonly referred to as the Navier-Stokes equations. The non-linearity of the conservation equations arises from the convective transport of momentum and, if heat transfer or mass transfer are present, energy and scalar variables.

In two-phase flows, the presence of a dispersed gas phase has to be considered while treating the continuous liquid flow. In this work, it is assumed that the characteristic dimension of the dispersed phase is smaller than the smallest turbulence length scales, enabling the gas bubbles to be viewed, in respect of their influence on the fluid phase, as point sources. This means that source terms appear in the differential forms of the conservation equations for the liquid phase to represent the effects of all bubbles contained within each fluid element (Bini and Jones, 2008). For an isothermal non-reacting flow, as considered herein, only the continuity and momentum equations are required, as presented below.

The Eulerian approach is based on solving the partial differential equations which describe the conservation of mass and momentum for three-dimensional, turbulent, incompressible and isothermal flows. The mass and momentum conservation equations expressed in Cartesian tensor form, are obtained respectively as:

$$\frac{\partial u_i}{\partial x_i} = 0 \tag{3.1}$$

where x_i is the i-th spatial co-ordinate and u_i is the corresponding velocity component, and

$$\frac{\partial u_i}{\partial t} + u_j \frac{\partial u_i}{\partial x_j} = -\frac{1}{\rho}\frac{\partial p}{\partial x_i} + \frac{\partial}{\partial x_j}\left[\mu\left(\frac{\partial u_i}{\partial x_j} + \frac{\partial u_j}{\partial x_i}\right)\right] + S_{mom,i} \tag{3.2}$$

where p represents the pressure of the fluid, ρ is the fluid density and μ is the dynamic viscosity of the fluid. The source term S represents momentum source terms due to the presence of the dispersed phase and the external body force field. Solution of the continuity and momentum equations gives a full description of the Newtonian-fluid flow.

3.2.1 Large Eddy Simulation

In LES, the fluid flow field is decomposed into large-scale motions that are resolved by the computation and small-scale, sub-grid fluctuations, using a filtering operation. The resolved flow field is obtained by considering the effects of the SGS fluctuations on the filtered continuity and momentum equations. The governing equations are filtered by applying a filter operator to the equations. The filter operator is defined as:

$$f(x) = \bar{f}(x) + f_{SGS}(x) \tag{3.3}$$

where $\bar{f}(x)$ represents the resolved large scales and $f_{SGS}(x)$ is the sub-grid contribution. The spatial filter of a function $f = f(\mathbf{x})$ is defined as its convolution with a filter function, G, according to (Leonard, 1974):

$$\bar{f}(\mathbf{x}) = \int_{\Omega} G[\mathbf{x} - \mathbf{x}'; \Delta(\mathbf{x})] f(\mathbf{x}') \mathrm{d}\mathbf{x}' \tag{3.4}$$

where $G[\mathbf{x} - \mathbf{x}'; \Delta(\mathbf{x})]$ denotes the filter function. The integration is carried out over the entire flow domain, Ω, and Δ denotes the filter width. The filter width serves to define the minimum length scales that are preserved, and various filter kernels are commonly used such as the "sharp cut off", the Gaussian and the box or "top-hat" filter (Sagaut et al., 2002; Kleissl et al., 2002). In the present work, top-hat filter is applied as this fits naturally into the formalism of the finite volume method used to discretize the governing equations. This filter is defined by the following equation (Kuerten et al., 1999; Bini and Jones, 2008):

$$G(x - x'; \Delta(x)) = \begin{cases} \Pi_{j=1}^{3} \frac{1}{\Delta_j}, & for \left|x - x_j'\right| \leq \frac{\Delta_j}{2} \\ 0, & for \left|x - x_j'\right| > \frac{\Delta_j}{2} \end{cases} \tag{3.5}$$

where $\Pi_{j=1}^{3}\frac{1}{\Delta_j}$ corresponds to the inverse volume of a finite volume cell used in the numerical solution, and the filter corresponds to volume averaging over the cell. The filter function has a characteristic with, Δ (the filter width), which may in general vary with position ($\Delta = \Delta(x)$) and is commonly taken as $\Delta = \left(\Delta_x \times \Delta_y \times \Delta_z\right)^{1/3}$, with Δ_x, Δ_y and Δ_z being the mesh spacings in the three coordinate directions.

3.2.2 Filtered Navier-Stokes Equations

The governing equations, Eqs. (3.1) and (3.2), must be filtered to obtain the LES equations. The filtered Navier-Stokes equations are presented below.

Filtering the continuity equation, Eq. (3.1), using the filtering operation of Eq. (3.4) gives:

$$\frac{\partial \bar{u}_i}{\partial x_i} = 0 \tag{3.6}$$

Comparison between Eqs. (3.6) and (3.1) shows that the filtering does not introduce any extra terms to the original continuity equation, but it only replaces unfiltered quantities with their filtered equivalents

Similarly, the filtered momentum equation is written as:

$$\frac{\partial(\bar{u}_i)}{\partial t} + \bar{u}_j \frac{\partial \bar{u}_i}{\partial x_j} = -\frac{\partial \bar{p}}{\partial x_i} + \frac{\partial}{\partial x_j}\left[\mu\left(\frac{\partial \bar{u}_j}{\partial x_i} + \frac{\partial \bar{u}_i}{\partial x_j}\right)\right] + \bar{S}_{mom,i} \tag{3.7}$$

Comparison between Eqs.(3.2) and (3.2) shows that all the terms can be rewritten as a function of filtered quantities, except for the non-linear convection term. Similar to temporal averaging in RANS modelling, LES filtering results in an unknown contribution, the so-called sub-grid stress tensor τ_{ij}^{sgs}:

$$\overline{u_i u_j} = \bar{u}_i \bar{u}_j + \tau_{ij}^{sgs} \tag{3.8}$$

Substitution of the sub-grid stress tensor, Eq. (3.8), into the filtered momentum equation, Eq. (3.7) gives:

$$\frac{\partial \bar{u}_i}{\partial t} + \bar{u}_j \frac{\partial \bar{u}_i}{\partial x_j} = -\frac{1}{\rho}\frac{\partial \bar{p}}{\partial x_i} + \frac{\partial}{\partial x_j}\left[\nu\left(\frac{\partial u_j}{\partial x_i} + \frac{\partial u_i}{\partial x_j}\right) - \tau_{ij}^{sgs}\right] + \bar{S}_{mom,i} \tag{3.9}$$

3.2.3 Sub-Grid Scale Modelling

The filtered LES equations are unclosed, and modelling is required for the unknown sub-grid stress tensor τ_{ij}^{sgs}. Compared to RANS turbulence models, the sub-grid stresses in LES are expected to be small, if the filter width is chosen in such a manner that most of the energy containing turbulence scales are resolved. Hence, as the filter width tends to zero, the LES solution approaches the DNS limit (Fox and Lilly, 1972).

The dynamic SGS stress model of Germano et al. (1991) was applied, using the approximate localization procedure of Piomelli and Liu (1995) and the modification proposed by Di Mare and Jones (2003). This represents the SGS stresses as the product of a SGS viscosity, ν_{SGS}, and the resolved part of the strain tensor, $\bar{S}$. The SGS viscosity is evaluated as the product of the filter length Δ times an appropriate velocity scale, taken to be $\Delta\|\bar{S}\|$. Hence, the anisotropic part of the SGS stresses is given as:

$$\tau_{ij}^{sgs} = 2C_s\Delta^2\left\|\bar{S}_{ij}\right\|\bar{S}_{ij} \tag{3.10}$$

where C_s is the Smagorinsky constant that needs to be modelled. Additionally:

- $\nu_{sgs} = (C_s\Delta^2)\left\|\bar{S}_{ij}\right\|$ is the SGS eddy kinematic viscosity
- $\left\|\bar{S}_{ij}\right\| = \sqrt{2\bar{S}_{ij}\bar{S}_{ij}}$ is the Frobenius norm of the filtered strain tensor
- $\bar{S}_{ij} = 0.5\left(\frac{\partial \bar{u}_i}{\partial x_j} + \frac{\partial \bar{u}_j}{\partial x_i}\right)$ is the filtered strain tensor

In the dynamic model, estimation of the model coefficient C_s is achieved by applying a second filtering operation, T_{ij}. The test-filtered SGS stresses are:

$$T_{ij} = \overline{\overline{u_i u_j}} - \bar{\bar{u}}_i \bar{\bar{u}}_j \tag{3.11}$$

In this equation, the topmost overbar represents the test filter operation. The parameters T_{ij} and $\bar{\tau}_{ij}$ are unknown but are related by Germano's identity (Kuerten et al., 1999) through the resolved stress tensor:

$$L_{ij} = T_{ij} - \bar{\tau}_{ij} = \overline{\overline{u_i u_j}} - \bar{\bar{u}}_i \bar{\bar{u}}_j \tag{3.12}$$

which can be calculated from the resolved quantities. To give the required expression for C_s, some form of relationship between the model constant values C_s and $C_s^2(\bar{\bullet})$ at the grid- and test-filter levels must be specified and, based on the hypothesis that the cut-off length falls inside the inertial sub-range, $C^2 = C^2(\bar{\bullet})$. However, such a sub-range is not guaranteed to occur in wall bounded or low Reynolds number flows, with the largest deviation from the universality of the SGS motions expected to occur in the regions of weakest resolved strain. Based on this, the two values of the model parameter at two different filter levels are liable to differ. To account for this, Di Mare and Jones (2003) proposed the following:

$$C_s^2(\bar{\bullet}) = C_s^2 \left(1 + \frac{\epsilon}{2\sqrt{2}\bar{\Delta}^2 \left\| \bar{\bar{S}} \right\| \left\| \bar{\bar{S}}^a \right\|^2} \right) \tag{3.13}$$

where ϵ represents the assumed turbulence energy dissipation rate, such that $\epsilon \sim v^3/l$, with v and l being the velocity and length scales, respectively, and $v = u_b$ and $l = h$, where u_b and h are the bulk velocity and channel half-height for the flows considered herein.

Equation (3.13) is related to the assumption that the scale invariance of C_s can only be invoked if the cut-off falls inside an inertial sub-range, and when this occurs, the modelled dissipation should represent the entire dissipation in the flow. Conversely, in the high Reynolds number limit, the dissipation is only determined by v and l so that the ratio of ϵ to $\bar{\Delta}^2 \left\| \bar{\bar{S}} \right\|^3$ is a measure of how far the flow is from scale preserving conditions. This equation represents a first-order expansion of other scale dependent expressions for C_s, for example that of Porté-Agel et al. (2000), which also use a single length and velocity

scale. Equations (3.12) and (3.13), with contraction of both sides with the tensor $\bar{\bar{S}}$, then give:

$$C_s^2 = \frac{\left[2\sqrt{2(C_*^2\Delta)^2}\parallel \bar{S} \parallel \parallel \bar{\bar{S}}_{ij}^a \parallel \bar{\bar{S}}_{ij}^a - L_{ij}^a \bar{\bar{S}}_{ij}^a\right]}{\epsilon + 2\sqrt{2\bar{\Delta}^2}\parallel \bar{\bar{S}} \parallel \parallel \bar{\bar{S}}^{\mathrm{a}} \parallel^2} \tag{3.14}$$

where C_*^2 is a provisional value for the field C_s^2, for example, its value at the previous time step (Piomelli and Liu, 1995). The dependence embodied in Eq. (3.14) gives a simple correlation for C_s^2. The main advantage of this method is that it is well conditioned and avoids the spiky and irregular behaviour exhibited by some implementations of the dynamic model and, as the resolved strain tends to zero, C_s^2 also tends to zero, while $C_s^2(\bar{\bullet})^2$ remains bounded. The dissipation term also yields smooth C_s^2 fields without a need for averaging, and the maxima of C_s^2 are of the same order of magnitude as Lilly's (1967) estimates for the Smagorinsky model constant. Negative values of the model parameters are possible, with such values set to zero to prevent instability. Negative values of the SGS viscosity are similarly set to zero. In this work, test filtering was performed in all space directions, with no averaging of the calculated model parameter field. The ratio $\bar{\Delta}/\Delta$ was set to 2.

3.2.4 Periodic Boundary Conditions and Driving Pressure Drop

The momentum source terms S_{mom} for a turbulent two-phase flow depend on the computational domain, the flow direction and the dispersed phase concentration. For a turbulent channel flow driven by a pressure gradient, the momentum source term includes the pressure gradient that drives the flow, the gravity-buoyancy source term and the dispersed phase feedback effect (as in two-way coupling). This sub-section describes the model for the pressure gradient that drives the flow in a turbulent channel. The other momentum source term due to two-way coupling will be discussed in a later section.

As the computational domain used in this work is a channel flow with a periodic boundary condition in the direction of the flow, an additional source term is required to drive it. This additional source term is added to the filtered momentum equation, Eq. (3.9), analogously to the pressure drop. Furthermore, there are two ways to implement this: (i) by a constant flow rate, $\dot{m}$, which is corrected by adjusting the forcing term in the

momentum equation at every timestep; and (ii) by specifying a constant pressure gradient, $\mathrm{d}p/\mathrm{d}z$, which can be applied when the required wall shear stress is known (Mallouppas and van Wachem, 2013). The source term is then equal to the integrated wall shear stress.

The pressure gradient ($S_{pg,i} = \mathrm{d}p/\mathrm{d}z$) based on a constant flow rate is given by:

$$S_{pg,i} = -\frac{\dot{m}_0 - \dot{m}_n}{A_{cross}\Delta t_n}\delta_{i3} \tag{3.15}$$

where $\dot{m}$ is the specified mass flow rate at a given cross-section with an area, A_{cross}, $\dot{m}_n$ is the computed mass flow rate at the current time step Δt_n, δ_{i3} is the Kronecker function ($\delta_{ij} = 1$ for $i = j$, $\delta_{ij} = 0$ for $i \neq j$) and S_{pg} has the unit of a pressure gradient, $\mathrm{kgm^{-2}s^{-2}}$. The flow rate per channel cross sectional area is the bulk velocity, u_B, and the corresponding Reynolds number for a constant flow rate is thus the bulk Reynolds number Re_B:

$$Re_B = u_B h/\nu \tag{3.16}$$

The pressure gradient ($S_{pg,i} = \mathrm{d}p/\mathrm{d}z$) based on a constant pressure gradient is given as:

$$S_{pg,i} = -(\tau_w/h)\delta_{i3} \tag{3.17}$$

where τ_w is the mean value of the wall shear stress and h the channel half-height. By using the shear velocity, $u_\tau = (\tau_w/\rho)^{0.5}$, the forcing term based on a constant pressure gradient becomes:

$$S_{pg,i} = -\left(\frac{u_\tau^2 \rho}{h}\right)\delta_{i3} \tag{3.18}$$

The resultant Reynolds number based on u_τ is referred to as the shear Reynolds number Re_τ and is given by:

$$Re_\tau = u_\tau h/\nu \tag{3.19}$$

where ν is the kinematic viscosity of the fluid.

For vertical flows, an additional source term is required. The pressure gradient, $S_{pg,i}$, taking into account gravity and buoyancy forces, is given as (Molin et al., 2012; Yamamoto et al., 2001):

$$S_{pg,3} = -\frac{\rho u_\tau^2}{h} \pm \Phi(\rho - \rho_b)g \tag{3.20}$$

where Φ is the bubble volume fraction. The sign $\pm$ depends on the flow direction and ρ_b is the density of the bubble.

3.3 Mathematical Model for Dispersed Phase

It is noteworthy that bubbles flowing in a liquid are not spherical by default, but their shape varies due to the action of different physical parameters. Specifically, freely moving bubbles under the influence of gravity can be classified as:

- Spherical: The bubbles are considered spherical if interfacial and viscous forces dominate over inertial forces
- Ellipsoidal: The bubbles are considered ellipsoidal if they are oblate with a convex surface
- Spherical cap or ellipsoidal cap: Larger bubbles that tend to be flat, dimpled or skirted at the rear fall under the category of spherical or ellipsoidal cap.

Cliff et al. (1978) state that the different shapes of bubbles can be categorised by three dimensionless numbers: the Eotvos number, E_o, Morton number, M, and bubble Reynolds number Re_b:

$$E_o = \frac{g\Delta_\rho d_{eq}^2}{\sigma} \tag{3.21}$$

$$M_{or} = \frac{g\mu^4\Delta_\rho}{\rho^2\sigma^3} \tag{3.22}$$

$$Re_b = \frac{|\mathbf{u} - \mathbf{v}|d_{eq}}{\nu} \tag{3.23}$$

where g is gravitational acceleration, Δ_ρ is the density difference between the continuous phase and the dispersed phase, σ is the surface tension, d_{eq} is the diameter of the volume-

equivalent sphere and $|\mathbf{u} - \mathbf{v}|$ is the magnitude of the slip velocity. These dimensionless numbers are used to classify the shape of bubbles moving through a liquid under the effects of gravity. For instance, a bubble is termed spherical if its Eotvos number has a high value and the Reynolds number is low, or the Reynolds number is high and the Eotvos number low, or both numbers are low.

3.3.1 Forces Affecting Bubble Motion

The motion of a small rigid spherical bubble in a turbulent flow field is described by Newton's second law of motion (Maxey and Riley, 1983). With the bubble-fluid density ratio $\rho_b/\rho \ll 1$, the microbubbles are subjected to drag, lift, gravity, buoyancy, pressure gradient and added mass forces, and a stochastic contribution arising from the SGS velocity fluctuations (Elghobashi and Truesdell, 1992). Therefore, the motion of microbubbles obeys the following Lagrangian equation:

$$m_b \frac{\mathrm{d}\mathbf{v}}{\mathrm{d}t} = \sum \mathbf{F} = \mathbf{F}_\mathrm{D} + \mathbf{F}_\mathrm{BG} + \mathbf{F}_\mathrm{SL} + \mathbf{F}_\mathrm{PG} + \mathbf{F}_\mathrm{AM} + \boldsymbol{\chi}_\mathrm{sgs} \tag{3.24}$$

where:

- $\mathbf{F}_\mathrm{D}$ is the drag force
- $\mathbf{F}_\mathrm{BG}$ is the buoyancy-gravity force
- $\mathbf{F}_\mathrm{SL}$ is the shear lift force
- $\mathbf{F}_\mathrm{PG}$ is the pressure gradient force
- $\mathbf{F}_\mathrm{AM}$ is the added mass force
- $\boldsymbol{\chi}_\mathrm{sgs}$ is the SGS contribution
- m_b is the mass of the bubble

The bubble position vector $\mathbf{x}_b = (\mathrm{x}_b, \mathrm{y}_b, \mathrm{z}_b)$ is obtained from the bubble equation motion:

$$\frac{\mathrm{d}\mathbf{x}_b}{\mathrm{d}t} = \mathbf{v} \tag{3.25}$$

Drag Force

The drag force, $\mathbf{F}_\mathrm{D}$, is due to the viscous friction between the bubble and the carrier fluid, and is given by:

$$\mathbf{F}_\mathrm{D} = \frac{1}{2}\rho A_b C_D C_w |\mathbf{u} - \mathbf{v}|(\mathbf{u} - \mathbf{v}) \tag{3.26}$$

where $\mathbf{u} = (u_x, u_y, u_z)$ is the resolved fluid velocity vector at the bubble position, $\mathbf{v} = (v_x, v_y, v_z)$ is the bubble velocity vector and $A_b = \pi d_b^2/4$ is the cross-sectional area of the bubble. The drag coefficient C_D is a function of the bubble Reynolds number, Re_b, and various expressions are available in literature. The Schiller and Naumann (1935) expression for the drag coefficient is used in the present work as it includes a non-linear correction coefficient to modify the Stokesian drag force for bubbles with finite Reynolds number:

$$C_D = \begin{cases} 24/Re_b, & Re_b \leq 1, \quad \text{Stokes region} \\ 24/Re_b(1 + 0.15Re_b^{0.687}), & 1 < Re_b < 1000, \quad \text{Schiller and Neumann} \\ 0.44, & Re_b \geq 1000, \quad \text{Newton region} \end{cases} \tag{3.27}$$

The wall correction coefficient, C_W, accounts for further modifications to the drag force due to the presence of a solid boundary in the vicinity of the bubble. C_W is modelled following Fukagata et al. (2001) and has different expressions in the directions parallel, $C_{W\parallel}$, and perpendicular, $C_{W\perp}$, to the wall:

$$\begin{aligned} C_{W\parallel} &= \left[1 - \frac{9}{16}\left(\frac{d_b}{2x}\right) + \frac{1}{8}\left(\frac{d_b}{2x}\right)^3 - \frac{45}{256}\left(\frac{d_b}{2x}\right)^4 - \frac{1}{16}\left(\frac{d_b}{2x}\right)^5\right]^{-1} \\ C_{W\perp} &= \left\{\left[1 - \frac{9}{8}\left(\frac{d_b}{2x}\right) + \frac{1}{2}\left(\frac{d_b}{2x}\right)^2\right]\left[1 - \exp\left(-2.686\left(\frac{2x}{d_b} - 0.999\right)\right)\right]\right\}^{-1} \end{aligned} \tag{3.28}$$

where the term $d_b/2x$ indicates the ratio between the bubble radius and the distance between the wall and the bubble centre of mass.

Buoyancy-Gravity Force

The buoyancy and gravity forces are often computed together due to the simplicity of their expressions. These are due to the force acting on a bubble due to the gravity field and the difference in density between the bubble and the surrounding fluid:

$$\mathbf{F}_{\mathrm{BG}} = \left(m_b - m_f\right)\mathbf{g} \tag{3.29}$$

m_b and m_f are the mass of the bubble and the fluid element the bubble displaces, and they are given as:

$$\begin{aligned} m_b &= \rho_b V_b \\ m_f &= \rho V_D \\ V_b &= \tfrac{1}{6}\pi d_b^3 = \tfrac{4}{3}\pi r_b^3 \end{aligned} \tag{3.30}$$

were V_b is the volume of a spherical bubble, V_D is the volume of the computational domain and r_b is the radius of the spherical bubble.

Shear Lift Force

The shear lift force is due to the velocity gradient in the flow and the force is given as (Mazzitelli et al., 2003):

$$\mathbf{F}_{\mathrm{SL}} = m_f C_L(\mathbf{u} - \mathbf{v}) \times \boldsymbol{\omega} \tag{3.31}$$

where $\boldsymbol{\omega} = 0.5(\nabla \times \mathbf{u})$ is the fluid rotation. The lift force coefficient, C_L, accounts for the correction due to small and large bubble Reynolds number. C_L is a function of the bubble Reynolds number, Re_b, and the dimensionless shear rate, $Sr_b = [(\mathbf{u} - \mathbf{v}) \times \boldsymbol{\omega}]d_b/(\mathbf{u} - \mathbf{v})^2$. Based on McLaughlin (1991) and Kurose and Komori (1999), $\mathrm{C_L}$ is given as:

$$C_L = \begin{cases} C_{\mathrm{L-MCL}} = \left[5.816\left(\dfrac{Sr_b}{2Re_b}\right)^{0.5} - 0.875\dfrac{Sr_b}{2}\right]\dfrac{3}{4Sr_b}\dfrac{J(\in)}{2.255}, & \text{for } \mathrm{Re_b} < 1 \\ \mathrm{C_{L-MCL}} = \dfrac{5 - Re_b}{4} + \mathrm{C_{L-KK}}\dfrac{Re_b - 1}{4}, & \text{for } 1 < Re_b < 5 \\ \mathrm{C_{L-KK}} = \left[\left(K_0\left(\dfrac{Sr_b}{2}\right)^{0.9} + K_1\left(\dfrac{Sr_b}{2}\right)^{1.1}\right)\right]\dfrac{3}{4Sr_b}, & \text{for } Re_b > 5 \end{cases} \tag{3.32}$$

where $C_{\mathrm{L-MCL}}$ represents the coefficient calculated following McLaughlin (1991). The function, $J(\in) = 2.225/(1 + 0.2\ \in^{-2})^{3/2}$ is also used in McLaughlin (1991), with $\in=$

$(Sr_b/Re_b)^{1/2}$. The coefficient $C_{\mathrm{L-KK}}$ is calculated as noted in Kurose and Komori (1999), where K_0 and K_1 are coefficients which are functions of Re_b.

Pressure Gradient Force

The pressure gradient force is the acceleration of the bubble due to the pressure field in the surrounding fluid (Auton et al., 1988) and it is given as:

$$\mathbf{F}_{\mathrm{PG}} = m_f \frac{\mathrm{D}\mathbf{u}}{\mathrm{D}t} \tag{3.33}$$

Added-Mass Force

The added-mass force accounts for the fact that a bubble accelerating relative to the fluid surrounding it transfers momentum at a certain rate to the carrier flow. The increase in the apparent mass of the bubble compared to the mass of the displaced fluid is commonly referred to as the added mass (Lahey Jr et al., 1980). In order to accelerate the bubble, both the bubble and the surrounding fluid must be set in motion. For a constant volume and added mass coefficient, the added mass force is expressed as:

$$\mathbf{F}_{\mathrm{AM}} = \rho V_b C_{AM} \left(\frac{\mathrm{d}\mathbf{u}}{\mathrm{d}t} - \frac{\mathrm{d}\mathbf{v}}{\mathrm{d}t} \right) \tag{3.34}$$

where C_{AM} is the added mass coefficient. For a single non-deformable spherical bubble, $C_{AM} = 0.5$. An important notation convention is that the derivatives $(\mathrm{d}/\mathrm{d}t)$ and $(\mathrm{D}/\mathrm{D}t)$ represent the time derivatives following the moving bubble and the surrounding fluid element, respectively. Therefore, the following relations hold when the derivatives are calculated along the bubble trajectory (bold face symbols denote vector quantities):

$$\frac{\mathrm{d}}{\mathrm{d}t} = \frac{\partial}{\partial t} + \mathbf{v}.\nabla \tag{3.35}$$

and

$$\frac{\mathrm{D}}{\mathrm{D}t} = \frac{\partial}{\partial t} + \mathbf{u}.\nabla \tag{3.36}$$

3.3.2 Bubble Equation of Motion

Inserting the expression of the forces into the force balance equation, Eq. (3.24), and dividing the resulting equation by the mass of the bubble, m_b, gives:

$$\begin{aligned}\frac{\mathrm{d}\mathbf{v}}{\mathrm{d}t} = \left(1 - \frac{\rho}{\rho_b}\right)\mathbf{g} + \frac{(\mathbf{u}-\mathbf{v})}{\tau_b} C_D C_w + C_L \frac{\rho}{\rho_b}[(\mathbf{u}-\mathbf{v}) \times \boldsymbol{\omega}] \\ + \frac{\rho}{\rho_b}\frac{\mathrm{D}\mathbf{u}}{\mathrm{D}t} + \frac{1}{2}\frac{\rho}{\rho_b}\left(\frac{\mathrm{d}\mathbf{u}}{\mathrm{d}t} - \frac{\mathrm{d}\mathbf{v}}{\mathrm{d}t}\right) + \boldsymbol{\chi}_{\mathrm{sgs}}\end{aligned} \tag{3.37}$$

The terms on the right-hand side of Eq. (3.37) represent the forces per unit mass acting on a bubble and describe the effect of gravity, drag, shear lift, pressure gradient and added mass forces, while the last term $\boldsymbol{\chi}_{\mathrm{sgs}}$ represents the effect of SGS velocity fluctuations on the bubble motion. Subscript b refers to the bubble and τ_b is the bubble relaxation time, corrected to account for added mass effects to give $\check{\tau}_b = \tau_b(1 + 0.5\,\rho/\rho_b)$. Therefore, Eq. (3.37) is the force equation that is applied for the calculation of the bubble trajectories in turbulent flows. It is important to point out that calculation of the Basset history force is usually time consuming, and Maxey (1990) and Rivero et al. (1991) found that its contribution for a bubble is always negligible in comparison with the other forces. Similar findings were obtained by Sridhar and Katz (1995). Therefore, the Basset history force was neglected, as was also assumed in the works of Thomas et al. (1983), Onslow et al. (1993), Yang and Thomas (1994) and Sene et al. (1994).

3.3.3 Modelling Sub-grid Scale Velocity Fluctuation Effects on Bubble Dispersion

The last term in Eq. (3.37), representing the effect of the SGS velocity fluctuations on bubble motion, is determined using a stochastic Markov model (Bini and Jones, 2008) that represents the influence of the unresolved fluctuations on bubble acceleration:

$$\boldsymbol{\chi}_{sgs} = C_0 \left(\frac{k_{sgs}}{\tau_t}\right) \frac{\mathrm{d}\mathbf{W}_t}{\mathrm{d}t} \tag{3.38}$$

where k_{sgs} is the unresolved turbulence kinetic energy of the liquid phase, C_0 is a model constant taken as unity, and $\mathrm{d}\mathbf{W}_t$ represents the increment of the Wiener process. During the simulation, $\mathrm{d}\mathbf{W}_t$ is represented by $\xi_i \times \sqrt{\Delta t}$, where ξ_i is a random variable sampled from a normal distribution with zero mean and a variance of unity, and which is independent for each time step and for each velocity component. τ_t is a sub-grid time scale which affects the rate of interaction between the bubble and the turbulence, defined as:

$$\tau_t = \frac{\tau_b^{1.6}}{\left(\Delta / k_{sgs}^{0.5}\right)^{0.6}} \tag{3.39}$$

The SGS kinetic energy is obtained from $k_{sgs} = \left(2\Delta v_{sgs}\bar{S}_{ij}\bar{S}_{ij}\right)^{2/3}$, an expression derived using equilibrium arguments (Bini and Jones, 2008). Interaction and collision of the bubbles with a wall are handled using the hard sphere collision model (Njobuenwu and Fairweather, 2017).

3.4 Two-way Coupling Model

Two-way coupling applies to a dispersed multiphase flow when the volume fraction of the dispersed phase is larger than 10^{-6} and at moderately high bubble mass loading. The momentum transfer from the bubble suspension is large enough to modify the structure of the turbulence. This interaction is referred to as two-way coupling. The coupling effect is enforced by the addition in the momentum balance equation, Eq.(3.9), of the source term $S_{2w,i}$ that has the units of pressure gradient and represents the force per unit volume exerted by the bubbles on the fluid:

$$S_{2w,i} = -\frac{1}{\Delta^3}\sum_{j=1}^{n_b} f_{H,i}^{j} \tag{3.40}$$

Here, the summation is defined over the number of bubbles n_b in the finite-volume cell under consideration. $f_{H,i}^{j}$ is the source term arising from the j^{th} bubble in the i^{th} direction and the subscript H represents the hydrodynamic force terms. In the present case, the

relevant source term used in the momentum equation is the summation of all the hydrodynamic forces (drag, shear-lift, pressure gradient and added mass), with the body forces (gravity and buoyancy) already included via the pressure gradient term of Eq. (3.20):

$$f_{H,i}^{j} = \mathbf{F}_{\mathrm{D}}^{j} + \mathbf{F}_{\mathrm{SL}}^{j} + \mathbf{F}_{\mathrm{PG}}^{j} + \mathbf{F}_{\mathrm{AM}}^{j} \tag{3.41}$$

3.5 Four-way Coupling Model

3.5.1 Modelling Bubble-bubble Collision

In the four-way coupled mechanistic approach, the technique employed to handle bubble-bubble collisions is important. As noted in the review of previous studies, the hard sphere collision model is used to predict bubble interactions within the fluid. This deterministic approach is preferred to the stochastic collision technique which is often used due to its lower computational cost (Sommerfeld, 2001; Breuer and Alletto, 2012). Only binary collisions are accounted for. To calculate bubble trajectories, two distinct stages are involved, namely: (i) bubbles are moved based on the equation of motion without bubble-bubble interaction; (ii) the occurrence of collisions in (i) is examined for all bubbles. If a collision is found, the velocities and positions of the collision pair are replaced by the post-collision values.

The collision handling technique is carried out in two stages:

- In the first step, likely collision partners are recorded by taking into account the smallest possible time step within the flow. Since for small time steps only collisions between neighbouring bubbles are likely, substantial computational time savings are achieved by further splitting the computational domain into virtual cells. This method stores for each bubble a list of neighbouring bubbles. For instance, for a specific bubble A, all neighbouring bubbles within a certain distance are stored. The collision occurrence is only checked between bubble A and its neighbours. The details of the algorithm used are given in Hoomans et al. (1996) and Vreman et al. (2009).

- In the second step, the collision-detection algorithm based on search cells is applied. In this, the computational domain is split into three-dimensional cells and only bubbles located inside these search cells are checked for collisions (Breuer and Alletto, 2012; Mallouppas and van Wachem, 2013; Breuer and Almohammed, 2015).

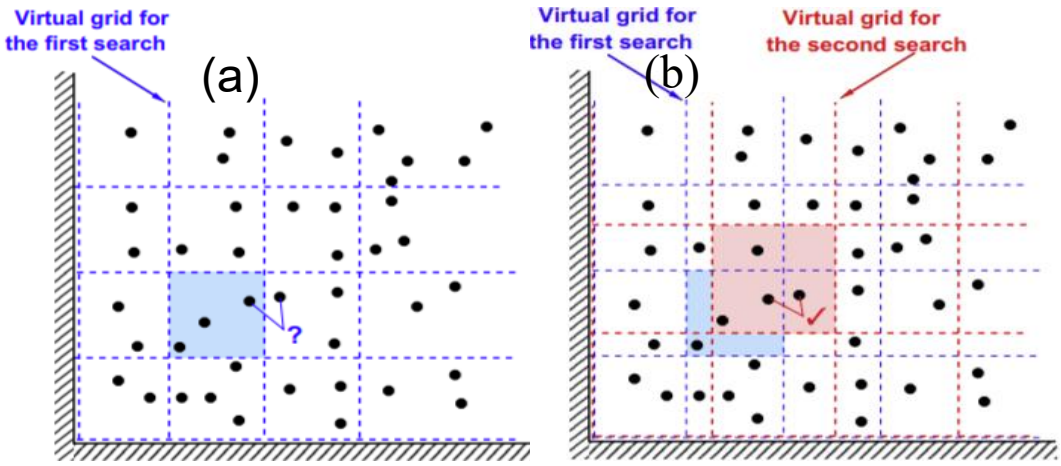

Figure 3.1 Collision detection technique by virtual cell: (a) first search and (b) second search (Breuer and Alletto, 2012).

A schematic of the two step approach is presented in Figure 3.1. The computational domain of size (n_i, n_j, n_k) is split into (i_c, j_c, k_c) cells.

$$\begin{aligned} i_c &= \mathbf{int}\, {}^{n_i}/_{d_i} + 1 \\ j_c &= \mathbf{int}\, {}^{n_j}/_{d_i} + 1 \\ k_c &= \mathbf{int}\, {}^{n_k}/_{d_i} + 1 \end{aligned} \tag{3.42}$$

where d_i is a factor adjusted dynamically during the simulation to limit the maximum number of bubbles in a virtual cell to an amount specified by the user. Based on the bubble coordinates in the computational domain, (ξ_b, η_b, ζ_b), the corresponding index details of the virtual cells can be obtained:

$$\begin{aligned} i_b &= \mathbf{int}\, {}^{\xi_b}/_{d_i} + 1 \\ j_b &= \mathbf{int}\, {}^{\eta_b}/_{d_i} + 1 \\ k_b &= \mathbf{int}\, {}^{\zeta_b}/_{d_i} + 1 \end{aligned} \tag{3.43}$$

The bubble tracking in Cartesian space has an advantage for the collision algorithm, since the bubble coordinates are naturally available. Finally, a bubble property is defined by assigning the index of the virtual cell, denoted i_{vc}, in which the bubble is located:

$$i_{vc} = i_b + (j_b - 1) \times i_c + (k_b - 1) \times i_c \times j_c \tag{3.44}$$

Here, all bubbles within the same virtual cell are characterized by the same index, i_{vc}. In this way, the collision detection procedure can be limited to the bubbles in each virtual cell. Furthermore, to avoid overlapping cells or the necessity to take all 26 surrounding cells into account during the first step, the collision detection procedure is carried out a second time with slightly larger virtual cell sizes, i.e. the ratio of edge lengths is equal to the quotient of the two prime numbers 17 and 13, and hence about 1.3, as presented in Figure 3.1(b) and recommended by Breuer and Alletto (2012). This ensures that potentially colliding bubbles on the border of two cells are detected.

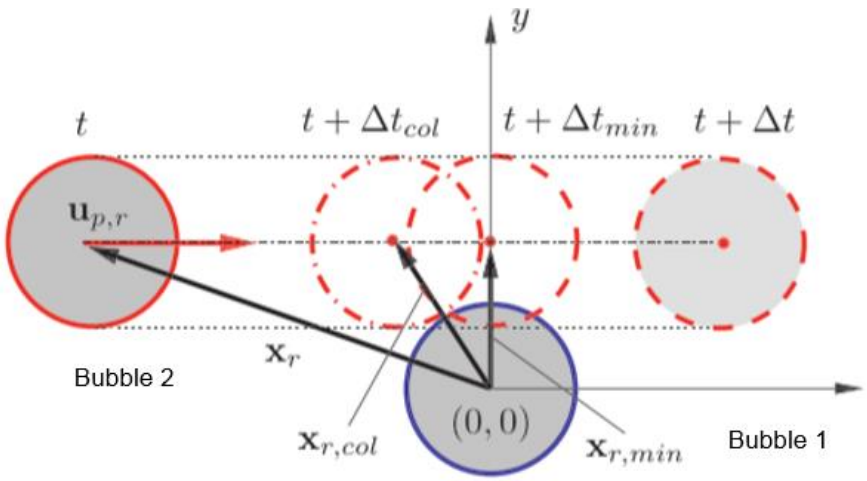

Figure 3.2 Relative motion of two colliding bubbles (Tanaka and Tsuji, 1991).

The second step takes each bubble in one virtual cell into account. The algorithm relies on the assumption of constant velocity within a time step, which is reasonable for the small-time step sizes applied in LES. Figure 3.2 represents the relative motion of two colliding bubbles on the assumption of linear displacements during a time step. It is possible to detect the collision of two bubbles by the purely kinematic condition that the two bubbles must approach one another, expressed by:

$$\mathbf{x}_r . \mathbf{v}_{b,r} < 0 \tag{3.45}$$

Otherwise, a collision is impossible. Here, $\mathbf{x}_r$ and $\mathbf{v}_{b,r}$ are the relative distance and the relative velocity between the two bubbles, respectively. For those bubble pairs within a virtual cell for which this condition is met a second more detailed condition is checked. Thus, the computational effort required is further reduced. The second condition must ensure that the minimum separation between the bubbles within a time step is less than the sum of their radii. For this purpose, the time $\Delta t_{\min}$ at which the bubble separation distance is a minimum $x_{r,min}$ are expressed as:

$$\Delta t_{\min} = -\frac{\mathbf{x}_r \mathbf{v}_{b,r}}{\left|\mathbf{v}_{b,r}\right|^2} \tag{3.46}$$

and:

$$\mathbf{x}_{r,\min} = \mathbf{x}_r + \mathbf{v}_{b,r}\, \Delta t_{\min} \tag{3.47}$$

The condition that two bubbles interact is thus:

$$\left(\Delta t_{\min} \leq \Delta t \text{ and } \left|\mathbf{x}_{r,\min}\right| \leq d_{b12}\right) \mathrm{v} \left(|\mathbf{x}_r| \leq d_{b12}\right) \tag{3.48}$$

where d_{b12} is the sum of the radii of the two interacting bubbles. If the condition is fulfilled, the time required for the two bubbles to collide Δt_{coll} is calculated from the condition that the relative distance at that time must be equal to d_{b12}:

$$\left|\mathbf{x}_r + \Delta t_{\text{coll}}\, \mathbf{v}_{b,r}\right|^2 = d_{b12}^2 \tag{3.49}$$

The solution of this expression is given by:

$$\Delta t_{\text{coll}} = \Delta t_{\min}\left(1 - \sqrt{1 - K_1 K_2}\right) \tag{3.50}$$

where $K_1 = [\mathbf{x}_r]^2\left[\mathbf{v}_{b,r}\right]^2/\left(\mathbf{x}_r\mathbf{v}_{b,r}\right)^2$ and $K_2 = 1 - (d_{b12}^2/[\mathbf{x}_r]^2)$. The collision-normal vector required for the execution of the collision itself can be expressed as:

$$\mathbf{x}_{r,\mathrm{coll}} = \mathbf{x}_r + \mathbf{v}_{b,r}\,\Delta t_{\mathrm{coll}} \tag{3.51}$$

In handling the collision, it is vital to determine the bubble velocities before the collision (denoted by superscript -) in the direction normal to the collision:

$$\mathrm{v}_{1n}^{-} = \frac{x_{r,\mathrm{coll}}}{\left|\mathbf{x}_{\mathrm{r,coll}}\right|}\mathrm{v}_{1x} + \frac{\mathrm{y}_{r,\mathrm{coll}}}{\left|\mathbf{y}_{\mathrm{r,coll}}\right|}\mathrm{v}_{1y} + \frac{z_{r,\mathrm{coll}}}{\left|\mathbf{z}_{\mathrm{r,coll}}\right|}\mathrm{v}_{1z} \tag{3.52}$$

where $x_{r,\mathrm{coll}}$, $y_{r,\mathrm{coll}}$ and $z_{r,\mathrm{coll}}$ represent the Cartesian components of the collision-normal vector and v_{1x}, v_{1y} and v_{1z} the Cartesian velocity components of bubble 1 before the collision took place. An equivalent expression is used for bubble 2. After the detection of a collision, the velocities of the colliding bubbles are changed according to hard sphere inelastic collision principles, thus:

$$\begin{aligned}
\mathrm{v}_{1n}^{+} &= \frac{m_{b1}\mathrm{v}_{1n}^{-} + m_{b2}\mathrm{v}_{2n}^{-} - e\,m_{b2}(\mathrm{v}_{1n}^{-} - \mathrm{v}_{2n}^{-})}{m_{b1} + m_{b2}} \\
\mathrm{v}_{2n}^{+} &= \frac{m_{b1}\mathrm{v}_{1n}^{-} + m_{b2}\mathrm{v}_{2n}^{-} + e\,m_{b1}(\mathrm{v}_{1n}^{-} - \mathrm{v}_{2n}^{-})}{m_{b1} + m_{b2}}
\end{aligned} \tag{3.53}$$

In the equations above, v_{1n}^{+} and v_{2n}^{+} represent the bubble velocities in the direction normal to the collision after the collision (denoted by superscript +). Collisions are assumed to be frictionless. Only the velocity components in the collision-normal direction are changed by the collision. The Cartesian components of the bubble post-collision velocities are calculated as follows:

$$\begin{aligned}
\mathbf{v}_1^{+} &= \mathbf{v}_{1\mathrm{n}}^{+}\frac{\mathbf{x}_{\mathrm{r,coll}}}{\left|\mathbf{x}_{\mathrm{r,coll}}\right|} \\
\mathbf{v}_2^{+} &= \mathbf{v}_{2\mathrm{n}}^{+}\frac{\mathbf{x}_{\mathrm{r,coll}}}{\left|\mathbf{x}_{\mathrm{r,coll}}\right|}
\end{aligned} \tag{3.54}$$

3.5.2 Bubble Coalescence

Turbulent bubbly flows generally result in bubble coalescence and/or breakup, which are of major significance in the determination of bubble size distribution and the corresponding interfacial area between phases. There are several models of the coalescence process which were summarised in the literature review chapter. The film drainage approach was adopted in the present work in view of its higher accuracy with respect to experimental results (Chesters, 1991; Darmana et al., 2006).

In the film drainage model, the coalescence process is divided into three steps: (i) two bubbles collide and trap a small amount of liquid between them; (ii) while both bubbles stay in contact, the liquid film drains out to a critical thickness; and (iii) rupture of the liquid film occurs, leading to the coalescence of the bubbles. Otherwise, the bubbles bounce back without coalescing. The constraint for coalescence to occur is that the duration of the contact time of the bubbles must be sufficiently long for the liquid film to drain. Hence, using the Lagrangian approach, the contact time at the instance of collision can be expressed as:

$$\tau_{ij} = \frac{C_c R_{ij}}{u_n} \tag{3.55}$$

Here, R_{ij} is the equivalent bubble radius and is given as $R_{ij} = 2.0(2/d_{b1} + 2/d_{b2})^{-1}$. u_n is the relative approach velocity in the normal direction and C_c is the deformation distance as a fraction of the effective bubble radius. A value of 0.25 gave the best agreement with the experimental data of Sommerfeld et al. (2003) and is used throughout this work. Neglecting the effects due to surfactants and Hamaker forces (Sungkorn et al., 2012), the film drainage time can be expressed as:

$$t_{ij} = \sqrt{\frac{R_{ij}^3 \rho}{16\sigma}} \ln\left(\frac{h_0}{h_f}\right) \tag{3.56}$$

with the initial film thickness h_0 for air-water set to 1.0×10^{-4} m and the final film thickness before rupture h_f set to 1.0×10^{-8} m (Prince and Blanch, 1990). The properties

of the new bubble after coalescence were calculated from a mass and momentum balance. The new bubble diameter after coalescence is calculated as:

$$d_{b,\mathrm{new}} = \left(d_{d1}^3 + d_{\mathrm{d2}}^3\right)^{1/3} \tag{3.57}$$

The normal velocity of the bubbles after coalescence $\mathbf{v}_{b,new}$ can be expressed as:

$$\mathbf{v}_{b,n,new} = \frac{m_1\mathbf{v}_1 \times m_2\mathbf{v}_2}{m_1 + m_2} \tag{3.58}$$

The volume of the new bubble after coalescence is thus:

$$\mathrm{V}_{new} = \mathrm{V}_1 + \mathrm{V}_2 \tag{3.59}$$

The position of the new bubble after coalescence is given by:

$$\mathbf{x}_{b,n,new} = \frac{m_1\mathbf{x}_1 \times m_2\mathbf{x}_2}{m_1 + m_2} \tag{3.60}$$

where m_1 and m_2 represent the masses of the two colliding bubbles, and V_1 and V_2 are the volume of the two colliding bubbles.

3.6 Bubble Breakup

Breakup mechanisms have been classified into four different categories: (i) turbulent fluctuations and collision; (ii) viscous shear stress; (iii) the shearing off process; and (iv) interfacial instability (Lau et al., 2014). Out of these mechanisms, bubble breakup due to turbulent pressure fluctuations on the bubble surface is assumed to be the dominant breakup mechanism for the turbulent bubbly flows studied in this thesis.

The breakup model of Martinez-Bazan et al. (1999) was adopted under the Eulerian-Lagrangian framework due to the fact that it has an extensive theoretical basis and its results are highly compatible with experimental data. This has also been demonstrated by Lasheras et al. (2002) and Liao and Lucas (2009). The basic principle of this model is

that for a bubble to break, its surface has to be deformed and sufficient deformation energy must be provided by the surrounding fluid turbulent stresses.

The minimum energy required to deform a spherical bubble of diameter d_b is its surface energy:

$$E_s(D) = \pi\sigma d_b^2 \tag{3.61}$$

Where a bubble is non-spherical in shape, the surface area of the non-spherical bubble must be incorporated, although such bubbles are not considered herein. Using the aspect ratio, $E_b = \mathrm{d}x/\mathrm{d}z$, and the Eötvos number, $E_{ö}$, the surface energy of a bubble with an equivalent bubble diameter *d* is expressed as:

$$E_s(D) = \pi\sigma d_b^2.\gamma^{-1} \tag{3.62}$$

where $\gamma = \left[\left(1 + 2E_b^p\right)/\left(3E_b^{2/3p}\right)\right]^{-1/p}$ is a surface correction factor that is valid for $E_{ö} < 40$ and Morton number $< 10^{-6}$, $p = 1.6075$, and $E_s = f(E_{ö})$. For spherical bubbles $\gamma = 1$ (Lau et al., 2014). Martinez-Bazan et al. (1999) state that when the turbulent stresses due to the velocity fluctuations exceed the surface restoring pressure of the bubble, the bubble will eventually deform and breakup. The surface restoring pressure of a bubble with a diameter d_b is expressed as:

$$\tau_s(D) = 6\frac{\sigma}{d_b} \tag{3.63}$$

When air bubbles are introduced into the turbulent fluid phase, the velocity fluctuations of the turbulence cause pressure deformation forces that act on the bubbles' surface. When these forces exceed the cohesive forces due to surface tension, the bubble breaks up. When the size of the bubble is within that of the inertial sub-range, the average deformation stress, which results from velocity fluctuations existing in the liquid between two points separated by a distance equal to the bubble diameter d_b, is given by:

$$\tau_t(d_b) = \frac{1}{2}\rho\overline{\delta u^2(d_b)} \tag{3.64}$$

where $\overline{\delta u^2(d_b)}$ is the average value of the square of the velocity differences over a characteristic distance d_b, also expressed as $\beta\epsilon^{2/3}d_b^{2/3}$:

$$\tau_t(d_b) = \frac{1}{2}\rho\beta\epsilon^{2/3}d_b^{2/3} \tag{3.65}$$

β = 8.2 is a constant obtained by integrating the difference between the velocity fluctuations (Batchelor, 1951). The equality $\tau_s(d_b) = \tau_t(d_b)$ can also be rearranged in terms of the Weber number, which represents the ratio of the inertial to surface tension forces. Therefore, the criteria for bubble breakup can be expressed as a function of a critical Weber number We_{crit} that represents the maximum Weber number for which the bubble remains stable and does not break up, and is expressed as $\left(\overline{\delta u^2(D)}d_b\right)/\sigma = 12$. As:

$$We = \frac{\rho\overline{\delta u^2(d_b)}d_b}{\sigma} > We_{\text{crit}} \Longrightarrow \text{breakup} \tag{3.66}$$

then the criteria for bubble breakup becomes:

$$We > 12 \tag{3.67}$$

Because of the Lagrangian framework adopted, the location of each individual bubble is known and information on the placement of the daughter bubbles formed on breakup is essential. If a bubble meets the break-up criterion, therefore, the parent bubble breaks up into two separate daughter bubbles according to the volumetric breakup fraction which is determined from the daughter size distribution. Some typical examples of the latter include uniform, Bell-shaped, U-shaped and M-shaped (Liao and Lucas, 2009). In this work, the two daughter bubbles formed after the breakup event are assumed to be

of equal size for simplicity. Their location is also initially taken to be that of the parent bubble.

3.7 Numerical Solution Methods

3.7.1 Large Eddy Simulation Numerical Solver

The filtered governing equations and the SGS closure model were solved using the LES-BOFFIN (**Bo**undary **F**itted **F**low **In**tegrator) code (Jones et al., 2002). The flow solver implements a boundary conforming general curvilinear coordinate system with a co-located variable storage arrangement that is based on a fully implicit low Mach number formulation and is second order accurate in space and time. For the momentum equation convection expressions, an energy-conserving discretisation scheme is applied. Every other spatial derivative is approximated by a standard second-order central difference. Time derivatives are approximated by a three-point backward difference scheme with a variable time step to ensure that the maximum Courant number, based on the filtered velocity, always lies between 0.1 and 0.3 (Di Mare and Jones, 2003) as this is required for the maintenance of high accuracy (Choi and Moin, 1994). A two-step, second-order, time-accurate approximate factorisation method is used to determine the pressure and ensure mass conservation in conjunction with a Rhie and Chow (1983) pressure smoothing technique to prevent even-odd node uncoupling of the pressure and velocity fields. The system of algebraic equations resulting from the discretisation is solved using the matrix preconditioned conjugate gradient method BI-CGSTAB (Delnoij et al., 1999) for the matrix of velocity vectors, and ICCG (Descamps et al., 2008) for the pressure.

More information on the numerical algorithm and how it is implemented can be found in Jones et al. (2002) and references cited therein. In order to generate the flow conditions described in this study, it became necessary to modify the existing LES-BOFFIN code. The main modification was ensuring that the mean flow pressure gradient was constant throughout the simulations and adjusted dynamically to maintain a stable mass flux through the flow geometry in each case, as discussed earlier in section 3.2.4.

The solution of fluid dynamic problems in any CFD code involves three steps: pre-processing, solution and post-processing. These are briefly introduced below:

- Pre-processing – The user specifies the problem by assigning all the necessary information. This includes the geometry of the computational domain, from which a suitable volumetric computational mesh is generated, and the properties of the computational grid, number of phases, properties of materials, physical and chemical phenomena involved, transport and constitutive equations, time step, numerical schemes and the initial and boundary conditions. The stretching functions that can be used to produce the boundary-fitted non-orthogonal block-structured grid, with matching interfaces and collocated variable arrangement, include linear, power, hyperbolic, trigonometric (sine, cosine) and exponential functions. The computational mesh, boundary conditions for the flow geometry and the fluid material properties together create input files to the solver.

- Solution phase – At this stage, the code integrates the differential transport equations over each computational cell, applying the Gauss and Leibnitz theorems to yield a set of integral equations that express conservation laws on a control-volume basis. The code then converts these equations into algebraic equations by using discretization techniques that approximate some terms of the equations (for instance, the accumulation terms) or the values of some variables (for instance, cell-face values of variables used in convective fluxes) with finite differences. Finally, the code solves iteratively the set of algebraic equations and finds the cell-centre values of the flow variables.

- Post-processing phase – The user analyses and interprets the simulated results, generates plots, diagrams and creates snapshots as well as animations by using data management and graphics tools.

In this work, new terms for the bubble-fluid and bubble-bubble interactions were implemented in the code. The programming language required in the BOFFIN code is FORTRAN (Jones et al., 2002). The code was significantly modified since it was previously used for solid particle flows of low mass loadings. Therefore, additional force models, coefficients and closures that are needed for bubbly multiphase flow problems of both low and high mass loadings were implemented, as were algorithms to determine bubble-bubble collisions, coalescence and breakup.

This flow solver has been applied extensively in the LES of reacting (Jones et al., 2014) and non-reacting (Bini and Jones, 2008; Njobuenwu and Fairweather, 2015) turbulent flows. Further details of the numerical methods used in BOFFIN are also given in these references.

3.7.2 Lagrangian Bubble Tracker

The bubble tracking algorithm tracks the path of a bubble through the channel by updating its three-dimensional trajectory with time and by computing the bubble velocity from the instantaneous solution of the fluid's velocity field. The expression obtained through the implementation of the fourth-order Runge-Kutta scheme on Eq. (3.37) is used to determine the bubble position in the flow. In this procedure, Eq. (3.37) is integrated twice in time to determine the bubble position at every time step. The first integration is performed in order to calculate the bubble velocity in the computational space (Faires and Burden, 1994). In order to determine the new position of the bubble, this equation is integrated once more, and performing this efficienlty is crucially important for the overall performance of the code. It functions by determining the bubble position, followed by the interpolation of the fluid flow data at this location, and then integrating the equation of motion. From these steps, the effect of the bubble-wall collisions can also be calculated.

The bubbles were introduced into the flow at the start of a simulation, prior to which the carrier phase had reached a statistically steady state. The bubbles were injected in parcels across the inlet plane of the channel with initial locations uniformly distributed across this plane and with initial velocities set equal to those of the local fluid velocity at each bubble location. Once the fluid velocity at the bubble location had been established, the equation of motion for each bubble was solved using a fourth-order Runge-Kutta scheme for the integration. At the bubble's position, a trilinear interpolation scheme was utilised to obtain the fluid velocity, u, the unresolved turbulence kinetic energy, k_{sgs}, and the fluid rotation, ω. Both the fluid and bubbles were re-introduced back into the flow on exit from the channel, with periodic boundary conditions set in both the streamwise and spanwise directions. The flow was driven using a fixed pressure gradient imposed in the streamwise direction.

3.8 Summary of Methodology and Justification

In this work, the Eulerian-Lagrangian approach is adopted since this method is the most viable and appropriate in regards to the motivation for the present research which necessitates the accurate tracking of individual bubbles in the flow, and their subsequent coalescence due to bubble-bubble collisions and breakup due to interaction with turbulent eddies. The Eulerian-Lagrangian approach adopted is an extension of an existing LES-Lagrangian particle tracking code, with modifications to the code implemented to represent additional bubble force models, bubble-fluid flow feedback (two-way) terms, and four-way coupling including bubble-bubble collision, and bubble coalescence and breakup. The complete model developed is more sophisticated than those previously applied in studies of bubbly flows of the type described in subsequent chapters.

Many authors have employed large eddy simulation coupled with a Lagrangian bubble tracker to study the hydrodynamics of bubby flows, including bubble coalescence and breakup, but mostly in square cross-section bubble columns (Delnoij et al., 1997; van den Hengel et al., 2005; Lau et al., 2014). The smallest bubble size considered in all these studies are in the millimeter range. Microbubbles have a myriad of applications in the fields of medicine, pharmacology, materials science and the food industry (Rodríguez-Rodríguez et al., 2015). Therefore, this work is novel in considering the detailed prediction of the behaviour of microbubbles in turbulent flows.

Channel flows, though simple, are commonly used within the fluid mechanics community to study the physics of multiphase flows. Channel flow domains of varying configurations are adopted in this work due to the ease of implementation of boundary and initial conditions, and the reduced computer run times associated with such flows. The presence of walls ensures the existence of velocity gradients and turbulent shear stresses, making research findings in such flows relevant to more complex geometries. The use of a periodic boundary condition imposed along the streamwise and spanwise directions of the channel is also frequently employed, and reduces computer run times, as well as

reducing the difficulty in setting the initial conditions at the start of the simulation and the size of the domain required to obtain a fully developed flow.

CHAPTER 4

ONE- AND TWO-WAY COUPLED FLOWS

In this chapter, the LES and the LPT models are first tested and then developed to predict multiphase gas-liquid bubbly flows. Initial validation of the LES-LPT code capabilities includes the prediction of single-phase flows and the transport of solid particles in fully-developed turbulent liquid channel flows. Computations are performed at shear Reynolds numbers $Re_\tau = 150, 300$ *and* 590*, based on the shear velocity and channel half-height. The influence of the sub-grid scale stresses on the resolved LES and on the dispersed-phase acceleration are parametrised using the Germano's dynamic model and a stochastic Markov model, respectively. To allow validation, material and flow properties of the fluid and the particles are identical to those used in the DNS solutions of Marchioli et al. (2008) for* $Re_\tau = 150$*, of Marchioli and Soldati (2007) for* $Re_\tau = 300$*, and of Moser et al. (1999) for* $Re_\tau = 590$*. With regards to model development, the LES-LPT capabilities are extended to bubbly flows and to one-way and two-way coupled simulations, depending on the volume fraction of the bubbles. The sizes of bubbles considered are* $d_b = 110, 220$ *and* 330 μm*, with horizontal and vertical channel flows simulated. The model is successfully validated against DNS-based predictions from the literature and, through additional simulations, the range of parameters previously investigated is extended to allow greater insight into the hydrodynamics of bubbly flows. Analysis of the results includes the statistical properties of the fluid flow and the dispersed phase, and a comparison of one-way and two-way coupled simulations and the impact of the level of coupling on the predictions. Additionally, bubble preferential concentration, a force analysis in the wall-normal direction, and the effect of Reynolds number on the extent of turbulence modulation by the bubbles and on bubble concentration are all considered.*

4.1 Single Phase Flow Velocity Statistics

Before the two-phase simulations are presented and discussed, single-phase turbulent flows (i.e. with no bubbles or particles) were predicted for friction Reynolds numbers $Re_\tau = 150, 300$ and 590, based on the wall friction velocity u_τ and the channel half height h. The single-phase flow was assumed to be incompressible, isothermal and with constant

properties. Thermo-physical property data were chosen as those of water at room temperature. The size of the channel domain was $L_x \times L_y \times L_z = 2h \times 2\pi h \times 4\pi h$, which was resolved using 129 ×128 ×128 grid points in the x, y and z directions, respectively. These dimensions and grid resolution correspond to those employed by the authors below whose predictions are used to validate the present results, apart from the highest Re_τ case (discussed further below).

The instantaneous streamwise velocity field u_z (m s^{-1}) in the turbulent channel flow is presented in Figure 4.1 for the three shear Reynolds numbers. Results show increasing turbulence levels with respect to the increase in the shear Reynolds number. Red and blue colours identify maximum and minimum values, respectively, with higher velocity values at the core of the channel and lowest velocity values near the channel walls.

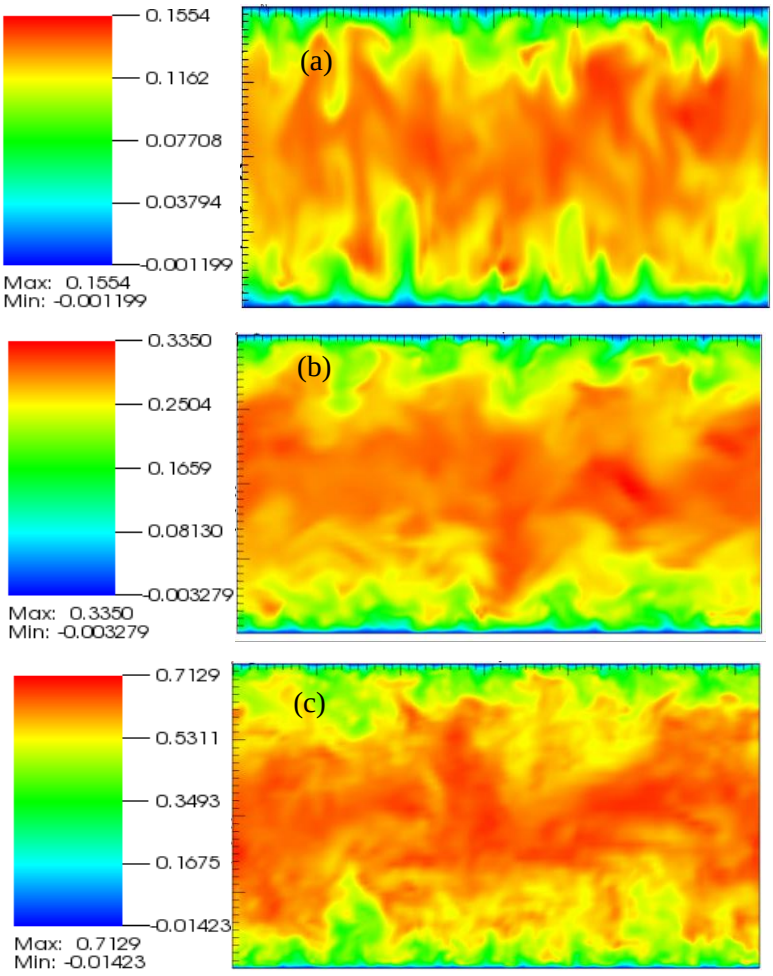

Figure 4.1 Two-dimensional representation of the single phase turbulent flow structures in the channel flow domain for shear Reynolds numbers, Re_τ = (a) 150, (b) 300, and (c) 590.

Presented in Figure 4.2, 4.3 and Figure 4.4 are the single-phase velocity statistics for the same three turbulent flows. In Figure 4.2**,** LES results at $Re_\tau = 150$ are compared against the DNS data of Marchioli et al. (2008) at the same shear Reynolds number. In Figure 4.3, the LES predictions are validated at $Re_\tau = 300$ against the DNS data of Marchioli and Soldati (2007), whilst in Figure 4.4, they are compared with the DNS results of Moser et al. (1999) for the $Re_\tau = 590$ flow. Results are shown using variables in wall units (identified with the superscript +), made dimensionless using u_τ, v and ρ. Also, for the LES, results are shown both with (LES + SGS) and without (LES) the inclusion of sub-grid scale velocity fluctuations.

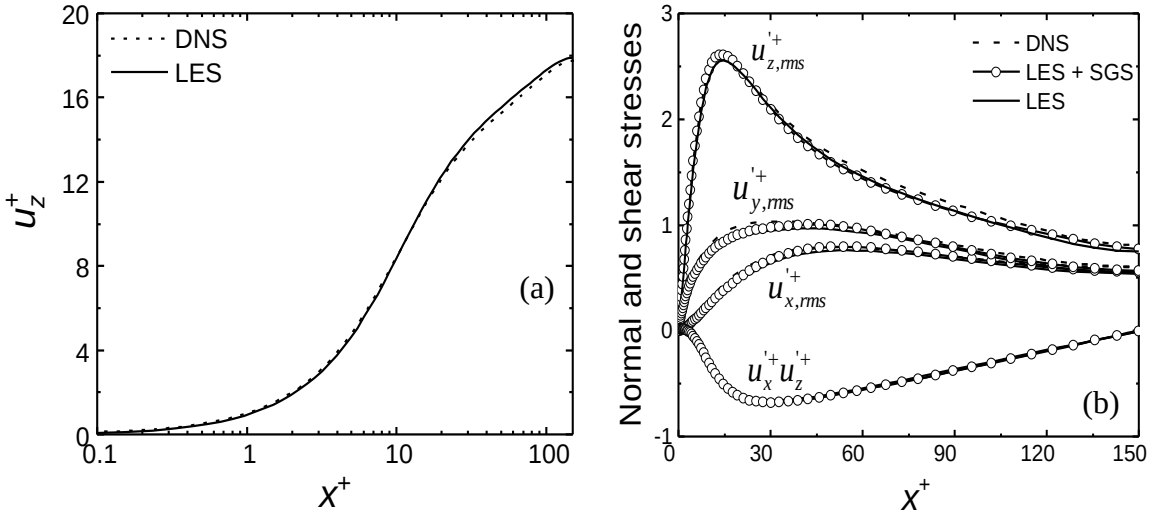

Figure 4.2 Plots of DNS versus LES single-phase velocity statistics for $Re_\tau = 150$: (a) mean streamwise fluid velocity u_z^+; (b) rms of fluid velocity fluctuations in the streamwise $u'^+_{z,rms}$, spanwise $u'^+_{y,rms}$, and wall normal $u'^+_{x,rms}$, directions, and fluid shear stress $u'^+_x u'^+_z$.

Figure 4.2(a) shows the time and space-averaged, single-phase streamwise mean velocity profile in the wall-normal direction for $Re_\tau = 150$ on a linear-logarithmic scale. As the simulation is for the least turbulent case, it shows good agreement with the higher resolution DNS study in the boundary layer close to the wall. For the streamwise velocity fluctuation $u'^+_{z,rms}$ in Figure 4.2(b), the agreement with the DNS predictions is again good in the bulk of the flow, although there is a small over-estimation of the peak in these fluctuations which is located at the interface of the bulk flow and the boundary layer. The spanwise and wall-normal velocity fluctuations ($u'^+_{y,rms}$ and $u'^+_{x,rms}$) also show good agreement with the DNS results, with slight deviations from the DNS limited to a few

percent, with peaks in the range of 10%–15% very close to the wall. The shear stress $u_x'^+ u_z'^+$ is similarly in good agreement with the DNS, except for a minor offset of about 0.05 across the majority of the channel. Nevertheless, overall, there is close agreement of the flow features predicted using LES when compared with the DNS results.

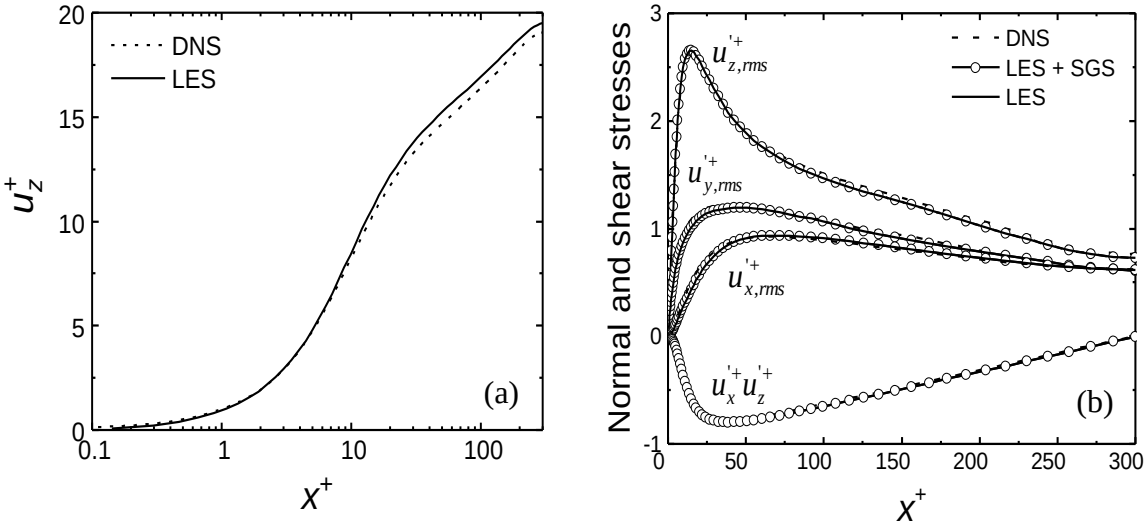

Figure 4.3 Plots of DNS versus LES single-phase velocity statistics at $Re_\tau = 300$: (a) mean streamwise fluid velocity u_z^+; (b) rms of fluid velocity fluctuations in the streamwise $u_{z,rms}'^+$, spanwise $u_{y,rms}'^+$ and wall-normal $u_{x,rms}'^+$ directions, and fluid shear stress $u_x'^+ u_z'^+$.

The results in Figure 4.3 also show the single-phase velocity statistics, but in this case for the $Re_\tau = 300$ flow. Figure 4.3(a) presents the mean streamwise velocity from the LES compared with the DNS on a linear-logarithmic plot. There is a slight over-estimation of by the LES in the region $20 \leq x^+ \leq 150$. However, the comparison still demonstrates quite good agreement. Figure 4.3(b) shows the rms of the velocity fluctuations in the three coordinate directions, and the shear stress. The results perfectly match the DNS predictions from Marchioli and Soldati (2007).

In Figure 4.4, the LES results for the $Re_\tau = 590$ flow are compared with the predictions of Moser et al. (1999), who carried out DNS of a channel flow at shear Reynolds numbers $Re_\tau = 180, 395$ and 590 using a spectral element numerical solution method. The LES results are in good agreement with those of Moser et al. (1999) for the latter flow, and in terms of both the mean streamwise velocity and the turbulent stresses, although the normal stresses are slightly under-predicted near the wall in the spanwise and wall

normal directions, and near the centre of the channel in the streamwise direction. Given the relatively high Reynolds number of this flow, Moser et al. (1999) used a grid resolution of $384 \times 257 \times 384$ in contrast to the resolution of $129 \times 128 \times 128$ used in this work. Despite the differences noted above, however, the LES predictions at all Reynolds numbers are in acceptable agreement with the DNS results, and the ability of the LES to resolve the main characteristics of the turbulent flows is evident. This, in the context of multiphase flows, translates into the ability of the LES to resolve the scales that are mainly responsible of fluid-bubble and fluid-particle interactions.

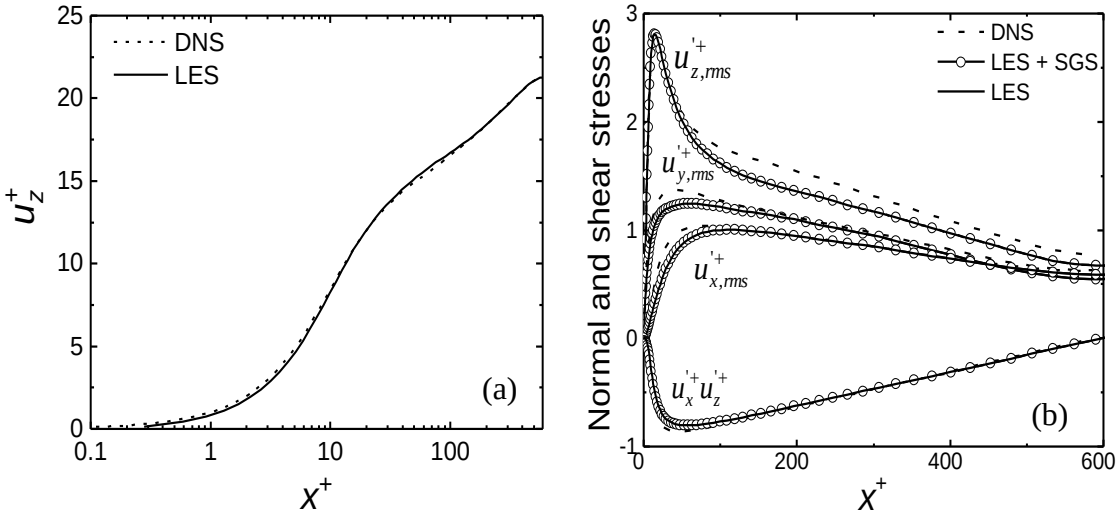

Figure 4.4 Plots of DNS versus LES single-phase velocity statistics at $Re_\tau = 590$: (a) mean streamwise fluid velocity u_z^+; (b) rms of the fluid velocity fluctuations in the streamwise $u'^+_{z,rms}$, spanwise $u'^+_{y,rms}$ and wall normal $u'^+_{x,rms}$ directions, and fluid shear stress $u'^+_x u'^+_z$.

Lastly, is should be noted that the inclusion of sub-grid scale velocity fluctuations in the LES-based predictions of the normal and shear stresses has little impact on the results. This is mainly due to the relatively high resolution of the LES grids employed, and implies that the turbulence energy spectrum is well resolved by the simulations.

4.2 One-way Coupled Flow Simulations

4.2.1 Horizontal Channel Flow

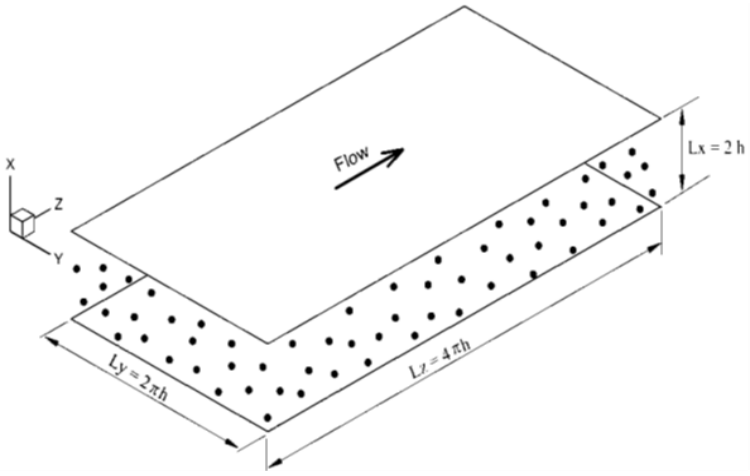

Figure 4.5 Schematic of horizontal channel computational domain.

Using the fully converged single-phase LES flow solutions presented in the previous section, solid particles were uniformly injected into the computational domain with their initial velocity set equal to that of the fluid at their initial position. The size of the channel domain was $L_x \times L_y \times L_z = 2h \times 2\pi h \times 4\pi h$, which was resolved using 129 ×128 ×128 grid points in the *x*, *y* and *z* directions, respectively, which corresponds to $300 \times 942 \times 1885$ wall units, with the reference geometry containing two infinite flat parallel walls as shown in Figure 4.5. The x, y and z axes point in the wall-normal, spanwise and streamwise directions, respectively. Particles, which are assumed pointwise, rigid and spherical, were injected into the flow at a concentration low enough to neglect particle collisions. The effect of particles onto the turbulence field was also neglected (one-way coupling assumption) due to the low particle concentration employed. The flow field was periodic in both the streamwise and spanwise directions, with no-slip conditions applied at the walls. All simulations were run at $Re_\tau = 150$, 300 and 590. These values correspond to shear velocities u_τ equal to 7.5×10^{-3} ms^{-1}, 1.50×10^{-2} ms^{-1} and 2.95×10^{-2} ms^{-1}, respectively, in a channel with a half width $h = 0.02\ m$. Results were again non-dimensionalized and variables expressed in wall units (identified with the superscript +), made dimensionless using u_τ, v and ρ.

As for the grids used in predicting the single-phase flows considered in the previous section, in the wall-normal direction grid points are clustered in the near-wall region. This was achieved by applying the hyperbolic function of Gamet et al. (1999). To calculate the mean particle velocities, detailed procedural steps were put in place. The channel height was therefore divided into N_b wall-parallel bins, with the b^{th} bin having a width $\Delta x_b^+ = Re_\tau/2[1-\cos(\pi(b-1)/(n_b-1))]$, which is equal to the wall-normal distance between two neighbouring grid points, and reduces toward the channel walls to provide a larger number of small bins in the near-wall region. The computation was carried out at each time step to determine the bin containing a particle, and the local instantaneous particle velocity within each bin was determined. Finally, the instantaneous mean particle velocities were averaged over time and space to give mean and fluctuating quantities.

The dispersed phase concentration was computed using the following steps: (i) the flow domain was split into control volumes; (ii) at each time step the number of particles within each control volume (C_V) was determined and was divided by the control volume to obtain the local concentration $C = n_b/C_V$; finally (iii) C was normalized by its initial value, C_0. With this approach, the ratio C/C_0 refers to a number density distribution and hence is larger than unity in the flow regions were particles tend to preferentially concentrate, and smaller than unity in the regions depleted of particles. All the results obtained below were time- and space-averaged along the homogeneous, i.e. the spanwise (y axis) and streamwise (z axis), directions. The quantities x^+ and t^+ represent the distance from the channel wall (0 being the lower channel wall) and the simulation time, respectively.

Table 4.1 presents the reference flow and particle parameters used in the simulations indicated. To initialize the position and velocity of the dispersed phase, the flow domain was split into 128 slices along the wall-normal direction and the thickness of each slice was made equal to the wall-normal grid spacing. The number of particles injected uniformly across the flow domain was 100,000. The computational time-step size in wall units was $\Delta t^+ = 0.045$ for the fluid and $\Delta t^+ = 0.45$ for the particles with $St = 1$ and 5, with three reference Reynolds numbers considered. The computations including particles were allowed to run for $t^+ = 1106$, where $t^+ = tv/u_\tau^2$ and t is the actual time

in seconds, before averaging. This ensured that all initial condition effects had disappeared from the flow field before averaging took place.

Table 4.1 Reference flow and particle parameters.

$St = \tau_p/\tau_f$	ν (m^2s^{-1})	u_τ (ms^{-1})	d_p^+	ρ_p/ρ	d_p(μm)
$Re_\tau = 150$					
1	1.0×10^{-6}	7.5×10^{-3}	0.153	769.23	20.4
5	1.0×10^{-6}	7.5×10^{-3}	0.342	769.23	45.6
$Re_\tau = 300$					
1	1.0×10^{-6}	1.5×10^{-2}	0.153	768.93	10.2
5	1.0×10^{-6}	1.5×10^{-2}	0.342	769.46	22.8
$Re_\tau = 590$					
1	1.0×10^{-6}	2.95×10^{-2}	0.153	768.93	5.18
5	1.0×10^{-6}	2.95×10^{-2}	0.342	769.46	11.59

The results in Figure 4.6 to Figure 4.9 compare predictions of particle velocity statistics and concentration profiles, for $St = 1$ and $St = 5$ particles, using the reference shear Reynolds number flows of $Re_\tau = 150$, $Re_\tau = 300$ and $Re_\tau = 590$. The particle velocity profiles presented in Figure 4.6 and Figure 4.7, for $Re_\tau = 150$ and $Re_\tau = 300$ and $St = 1$ and $St = 5$, compare LES-based predictions with the corresponding DNS-based results of Marchioli et al. (2008) and Marchioli and Soldati (2007), respectively. The results show very good agreement with the DNS, especially for the mean streamwise velocity (v_z^+) at $Re_\tau = 300$. The results for $Re_\tau = 150$ do, however, shown an over-prediction by the LES for both Stokes numbers. The rms of the velocity fluctuations, and the shear stress, are in close agreement with their DNS counterparts across the entire height of the channel for both flows. The only exception is a slight over-prediction of $v_{z,rms}^{\prime +}$ in the region $60 \leq x^+ \leq 100$ for $St = 1$ and 5 and $Re_\tau = 150$, and at $75 \leq x^+ \leq 225$ at $Re_\tau = 300$.

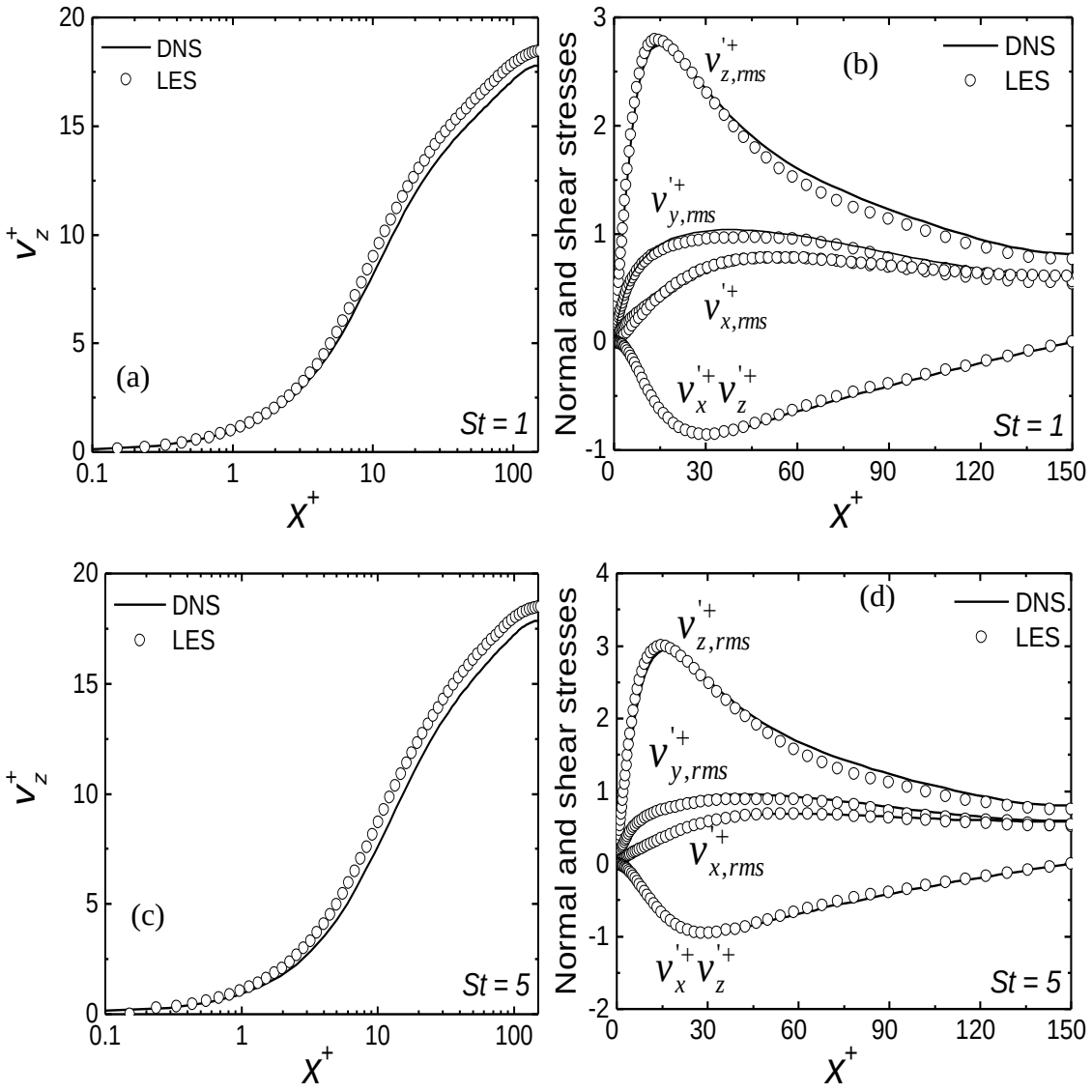

Figure 4.6 Plots of DNS versus LES particle velocity statistics at $Re_\tau = 150$: (a, c) mean streamwise particle velocity v_z^+; (b, d) rms of particle velocity fluctuations in the streamwise $v_{z,rms}^{\prime+}$, spanwise $v_{y,rms}^{\prime+}$ and wall normal $v_{x,rms}^{\prime+}$ directions, and particle shear stress $v_x^{\prime+}v_z^{\prime+}$. (a, b) $St = 1$; (c, d) $St = 5$.

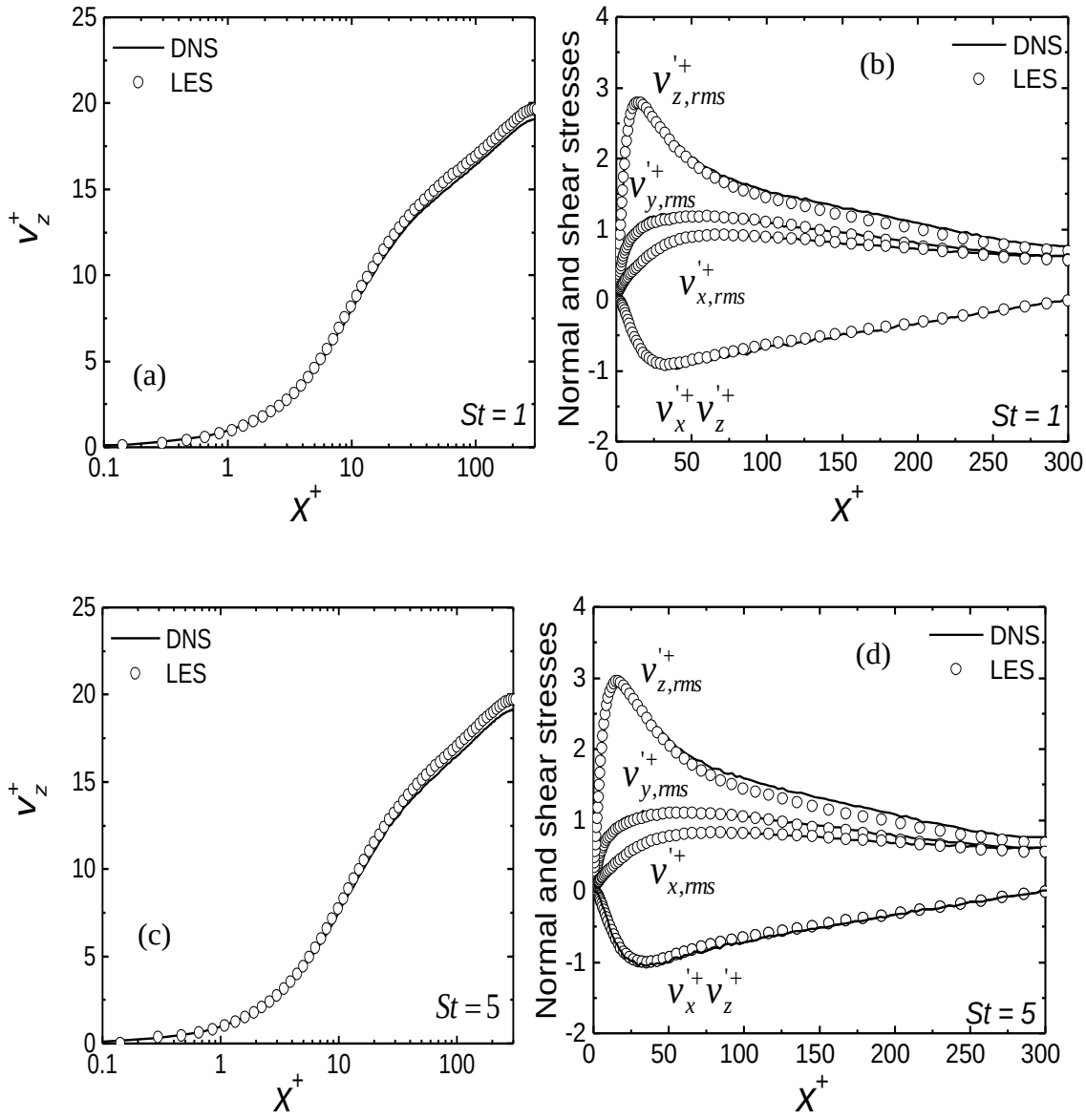

Figure 4.7 Plots of DNS versus LES particle velocity statistics at $Re_\tau = 300$: (a, c) mean streamwise particle velocity v_z^+; (b, d) rms of the particle velocity fluctuations in the streamwise $v_{z,rms}^{\prime+}$, spanwise $v_{y,rms}^{\prime+}$ and wall normal $v_{x,rms}^{\prime+}$ directions, and particles shear stress $v_x^{\prime+}v_z^{\prime+}$. (a, b) $St = 1$; (c, d) $St = 5$.

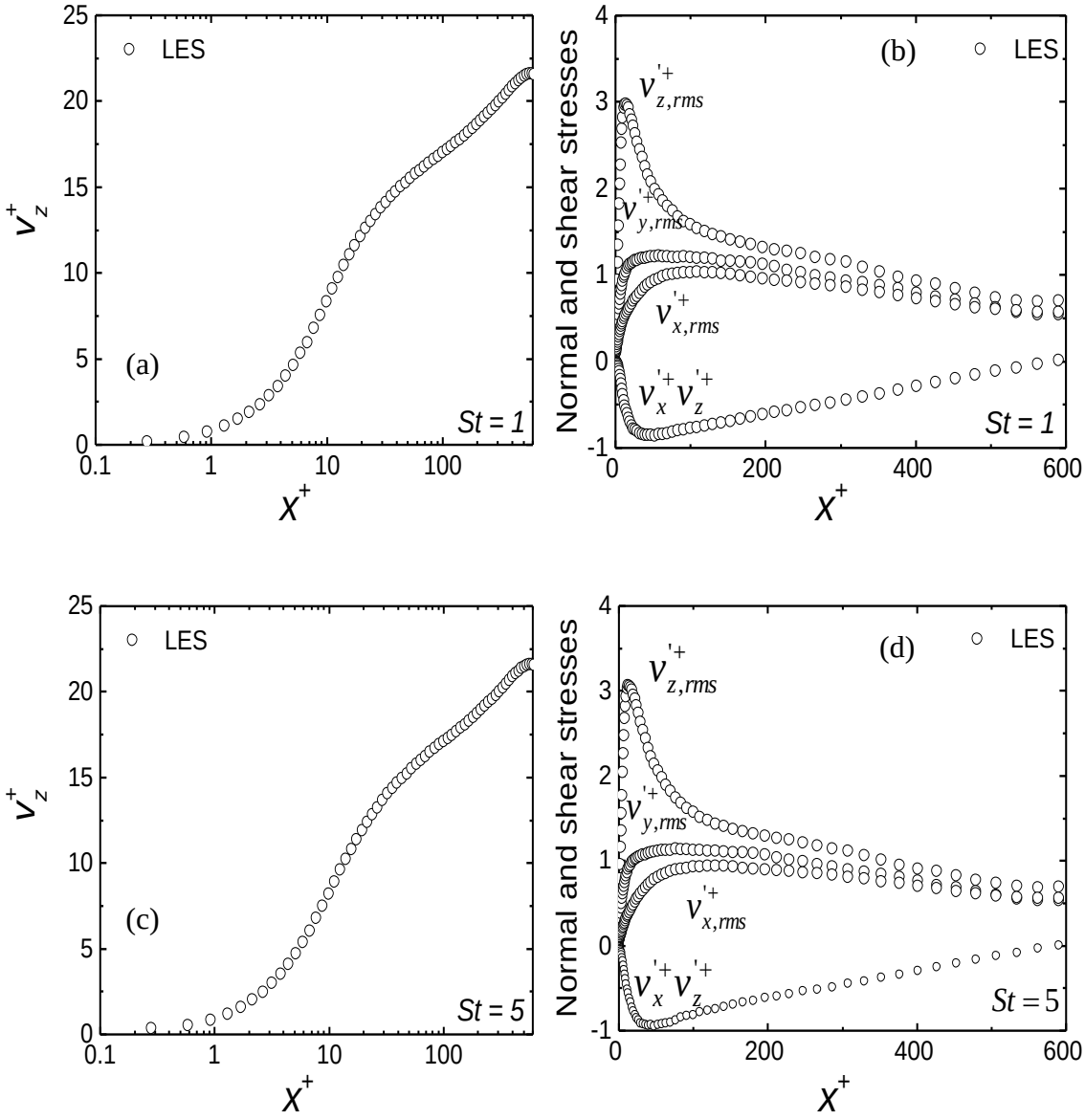

Figure 4.8 Plots of LES particle velocity statistics at $Re_\tau = 590$; (a, c) mean streamwise particles velocity v_z^+; (b, d) rms of the particle velocity fluctuations in the streamwise $v_{z,rms}^{\prime+}$, spanwise $v_{y,rms}^{\prime+}$ and wall normal $v_{x,rms}^{\prime+}$ directions, and particles shear stress $v_x^{\prime+}v_z^{\prime+}$. (a, b) $St = 1$; (c, d) $St = 5$.

Presented in Figure 4.8 are the results obtained from the LES-LPT code using a considerably higher Reynolds number of $Re_\tau = 590$, and particles with Stokes numbers $St = 1$ and $St = 5$. Unfortunately, there are no DNS results to compare with. Generally, however, Stokes numbers much greater than 1 describe particles that remain unaffected by fluid velocity changes, continuing on their original trajectory. Such interital particles therefore largely remain unaffected by the flow. If $St \ll 1$, in contrast, the particles follow

the fluid's velocity without influencing the flow structure. The Stokes number increases with particle size, and in doing so causes the inertial response of the particles to the motion of the fluid to reduce, leading to larger particles sizes being transported to, and remaining, near the wall, as is evident in the results of Figure 4.9.

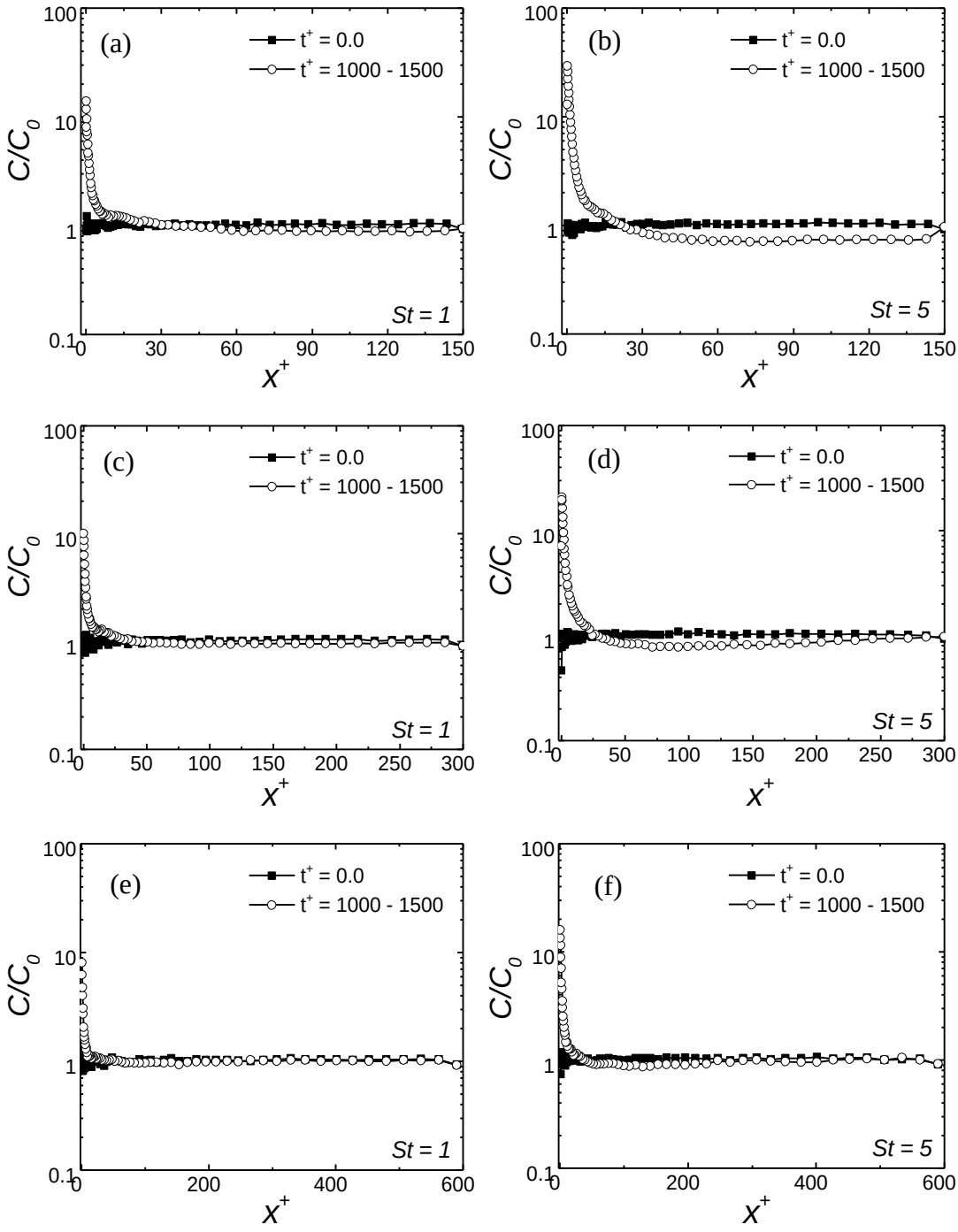

Figure 4.9 Plots of particle concentration profiles: (a, b) $Re_\tau = 150$; (c, d) $Re_\tau = 300$; (e), (f) $Re_\tau = 590$. (a, c, e) $St = 1$; (b, d, f) $St = 5$.

The concentration results of Figure 4.9 show that, starting from a flat profile ($C/C_0 \simeq 1$) at $t^+ = 0$, the expected near-wall concentration increases with increasing simulation time. The particle concentration reduces in the centre of the channel with time, and the particles migrate towards the wall for the three flows considered. This effect increases with increasing Stokes number, and decreases with the flow Reynolds number, and is due to the effects of turbophoresis which describes the tendency for particles to migrate in the direction of decreasing levels of turbulence level.

The above case studies, which considered single-phase and particle-laden flows, served as a preliminary test and validation of the capabilities of the BOFFIN LES code, with and without coupling with a Lagrangian particle tracking routine, before proceeding with modification of the tracker to accommodate and predict bubbly flows. The particlular single-phase and particle-laden flows predicted were considered since, in the majoirty of cases, DNS-based results were available for comparison purposes.

4.2.2 Vertical Channel Flow

The prediction of microbubbles in turbulence was carried out for upward and downward flows in a vertical channel. A sketch of the channel geometry is shown in Figure 4.10. The computational domain was 1885 × 942 × 300 wall units in z, y and x directions, respectively. A computational grid with 128 × 128 × 129 nodes was used, and the spacing between grid points in the streamwise and spanwise directions was $\Delta z^+ \approx 15$ and $\Delta y^+ \approx 7.5$ wall units. In the wall-normal direction, x^+, the distance between two grid points ranged from 0.045 near the walls to 3.682 in the centre of the channel. These grid resolutions were sufficient to describe the significant length scales in the channel flow.

A total number of 100,000 microbubbles with density $\rho_b = 1.3\ \mathrm{kgm}^{-3}$ and bubble diameter $d_b = 220 \times 10^{-6}$ m were injected in the flow field uniformly with initial velocities set equal to that of the fluid at the bubble position. The volume fraction in each flow configuration was fixed at 10^{-5}. To keep the average volume fraction of bubbles in the computational domain constant in time, when a bubble exited one of the domain boundaries in the streamwise or spanwise direction, it was reinjected into the domain according to the periodic condition of the flow field. Bubble-wall interaction was computed by enforcing rigid elastic rebound.

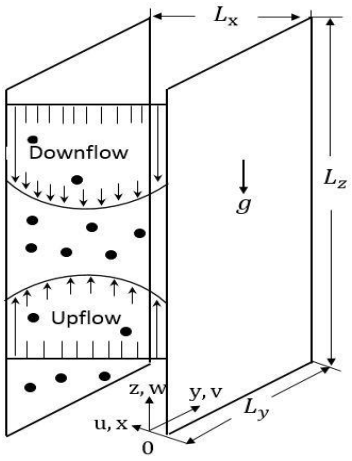

Figure 4.10 Vertical channel upflow and downflow computational domain.

The importance of the lift force on bubble behaviour is emphasized in the case of turbulent vertical channel flows. The objective of this test case was therefore to focus on the effect of the lift force on bubble behaviour in the near-wall region of the channel. Bubbles were tracked (under a one-way coupled assumption) with and without the lift force term in the force balance equation. The overall volume and mass fractions of the dispersed bubbles were equal, respectively, to $V = 4.889 \text{ x } 10^{-4}$ m^3 and $M = 3.76 \text{ x } 10^{-7}$ kg. The bubble response time, expressed as $\tau_b = \rho_b d_b^2/18\mu$ and corrected to account for added mass effects, was $\check{\tau}_b = \tau_b(1 + \rho_l/2\rho_b) = 385.6\,\tau_b$. The total simulation time for both upflow and downflow cases was $t^+ = 1093$. Averaging was started at $t^+ = 600$ and carried out for a sufficient time for a bubble moving at a speed equal to the average fluid velocity to move through the entire streamwise length of the channel more than eight times.

4.2.2.1 Validation test case

Presented in Figure 4.11 are the fluid velocity statistics for the vertical channel one-way coupled turbulent flows, compared with the DNS results of Giusti et al. (2005). The fluid mean velocity profiles for upflow and downflow, in Figure 4.11(a), are equivalent, since the one-way coupling approach was applied, with resonable agreement between LES and DNS predictions. Figure 4.11(c) and (e) show the time- and spacially-averaged mean streamwise velocity of the microbubbles. In Figure 4.11(c) the profiles for upward and downward flows with the lift force are presented, while Figure 4.11(e) shows the no lift

force case, in comparison with the DNS predictions. As is clearly shown, in the upward flow case the bubbles move faster than the fluid in the upward direction due to the effects of buoyancy. In the downward flow case, in contrast, the bubbles move slower than the fluid. The LES-based microbubble statistics obtained with and without lift both give mean velocities that, relative to the DNS-based results, over-predict for the upflow case, and under-predict for the downflow. In the centre of the channel, the non-dimensional velocity is 21.41 for upflow and 13.91 for downflow, with a positive difference of approximately 1.5 for upflow, and a negative difference of about 0.9 for downflow, with respect to the DNS.

Results for the normal and shear stresses in the fluid flow and for the microbubbles are also given in Figure 4.11(b), (d) and (f), although equivalent DNS based results are not available. In terms of the microbubbles, significant differences between the upflow and downflow cases are apparent, with values in upflow being larger than those encountered in the downflow case, particularly in the streamwise normal stresses.

Overall, the LES results with lift force effects are in qualitative agreement with the referenced DNS test case, as well as being in similar agreement with previous experimental studies (Wang et al., 1987) of spherical bubbles in turbulent flows. The results also confirm that bubble migration towards the wall in the upflow case, and away from the wall in the downflow case, is a combined result of the influence of gravity and the lift force, as considered in Figure 4.12.

In the absence of the lift force, therefore, the lateral drift of the bubbles is uniformly zero, which results in zero wall accumulation, as observed in the results of Figure 4.12(c) for both flow configurations. The trend of the LES results with lift (Figure 4.12(a) and 4.12(b)) from a qualitative point of view also shows similarities with respect to experimental works (Tomiyama et al., 2002; Shu et al., 2009), where bubbles were found to migrate in the wall normal direction, and in the directions shown. Figure 4.12(c) presents a combined plot of microbubble lateral evolution with and without lift, with the no lift test case in both flow configurations confirming that bubble migration towards or away from the channel walls is due to the lift force.

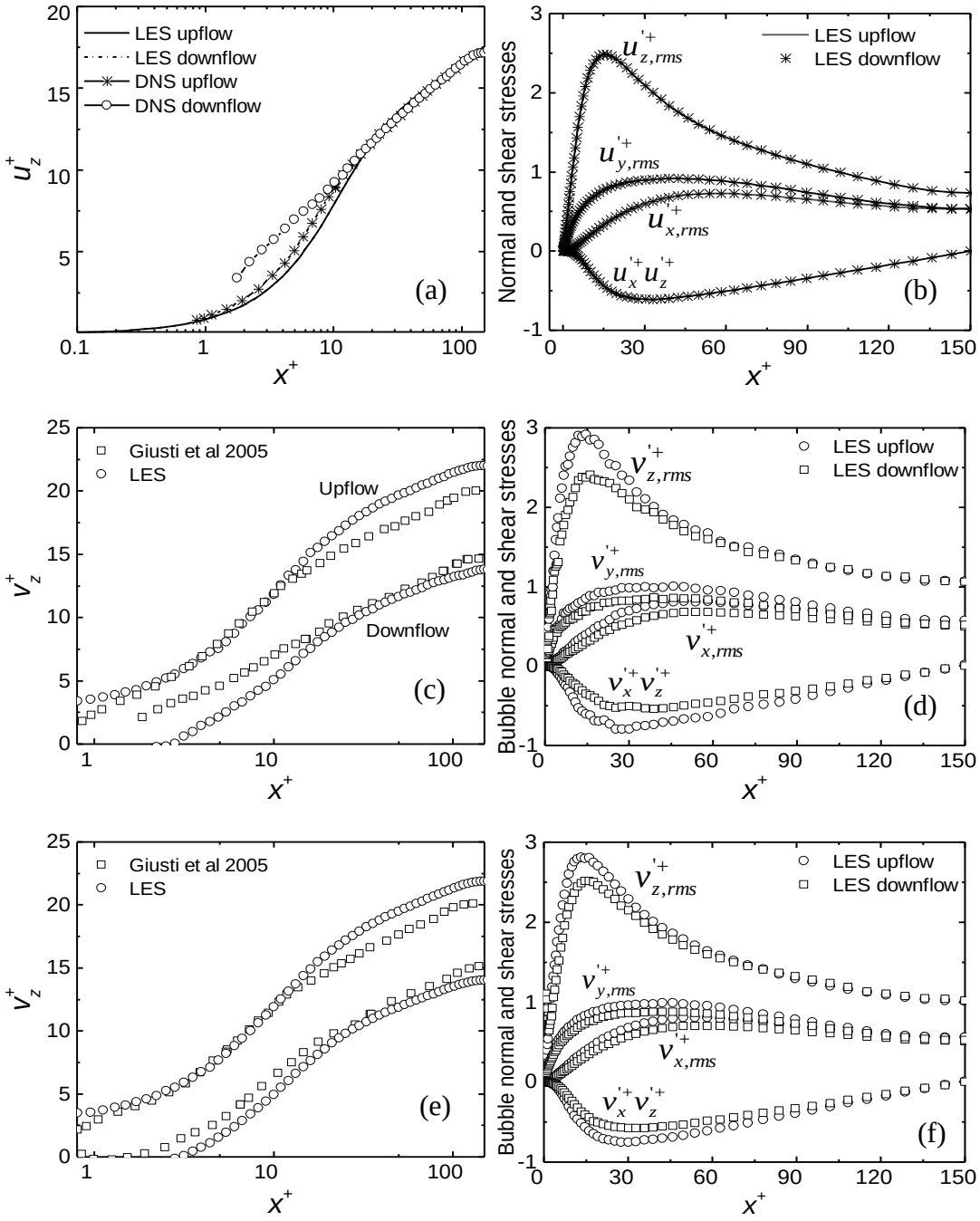

Figure 4.11 Fluid and microbubble velocity statistics for the vertical channel one-way coupled turbulent upflow and downflow compared with DNS results: (a) Fluid mean streamwise velocity; (b) rms of fluid velocity fluctuations and shear stress; (c) bubble mean streamwise velocity (with lift); (d) rms of bubble velocity fluctuations and shear stress (with lift); (e) bubble mean streamwise velocity (no lift); and (f) rms of bubble velocity fluctuations and shear stress (no lift).

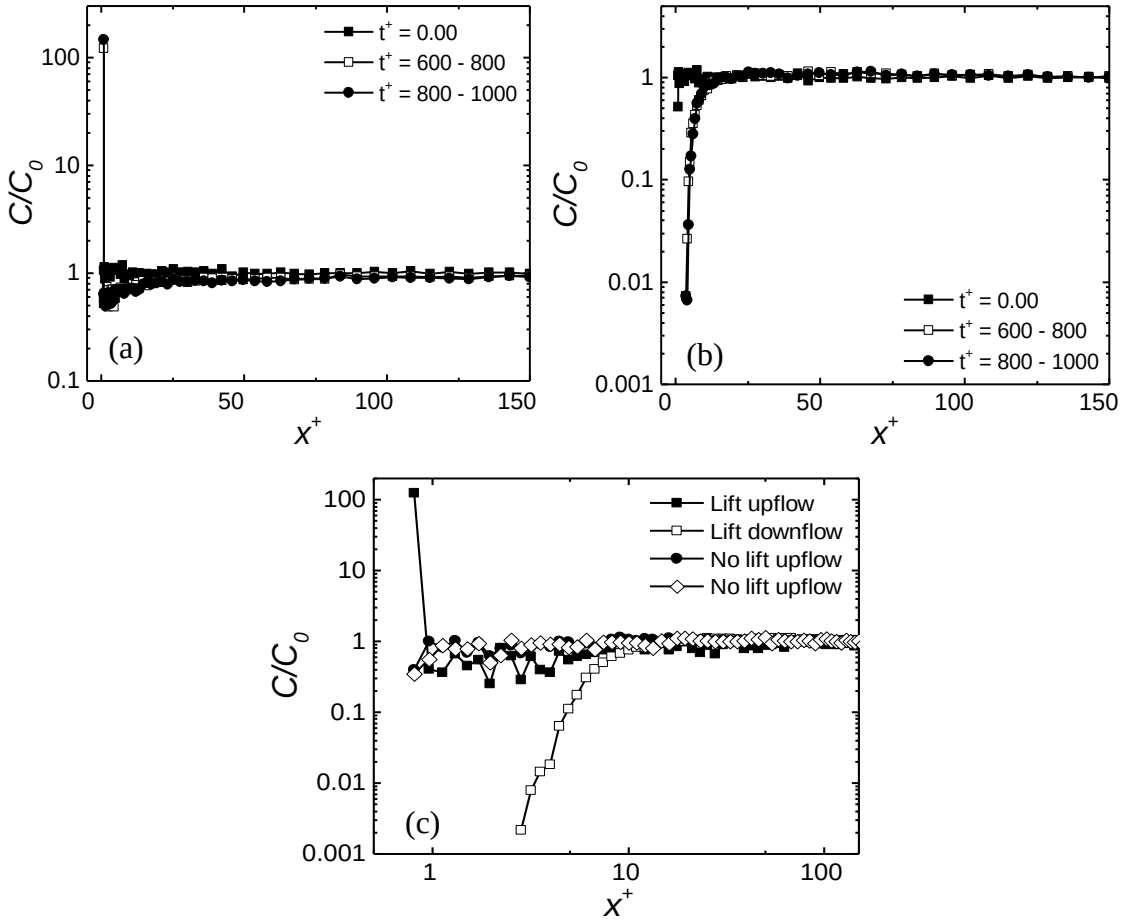

Figure 4.12 Profiles of microbubble concentration with increasing t^+ for upflow and downflow cases, with and without lift force: (a) upflow; (b) downflow; (c) combined profiles $t^+ = 900$.

4.2.2.2 Effect of flow Reynolds number

A higher Reynolds number flow of $Re_\tau = 590$ was also simulated with the LES under the one-way coupling framework, and in upflow and downflow configurations. Comparison with simulations at $Re_\tau = 150$, given in the previous section, allowed an analysis of the behaviour of microbubbles in different levels of turbulence, and the impact of turbulence on the lift force effect observed above, especially in the channel wall region.

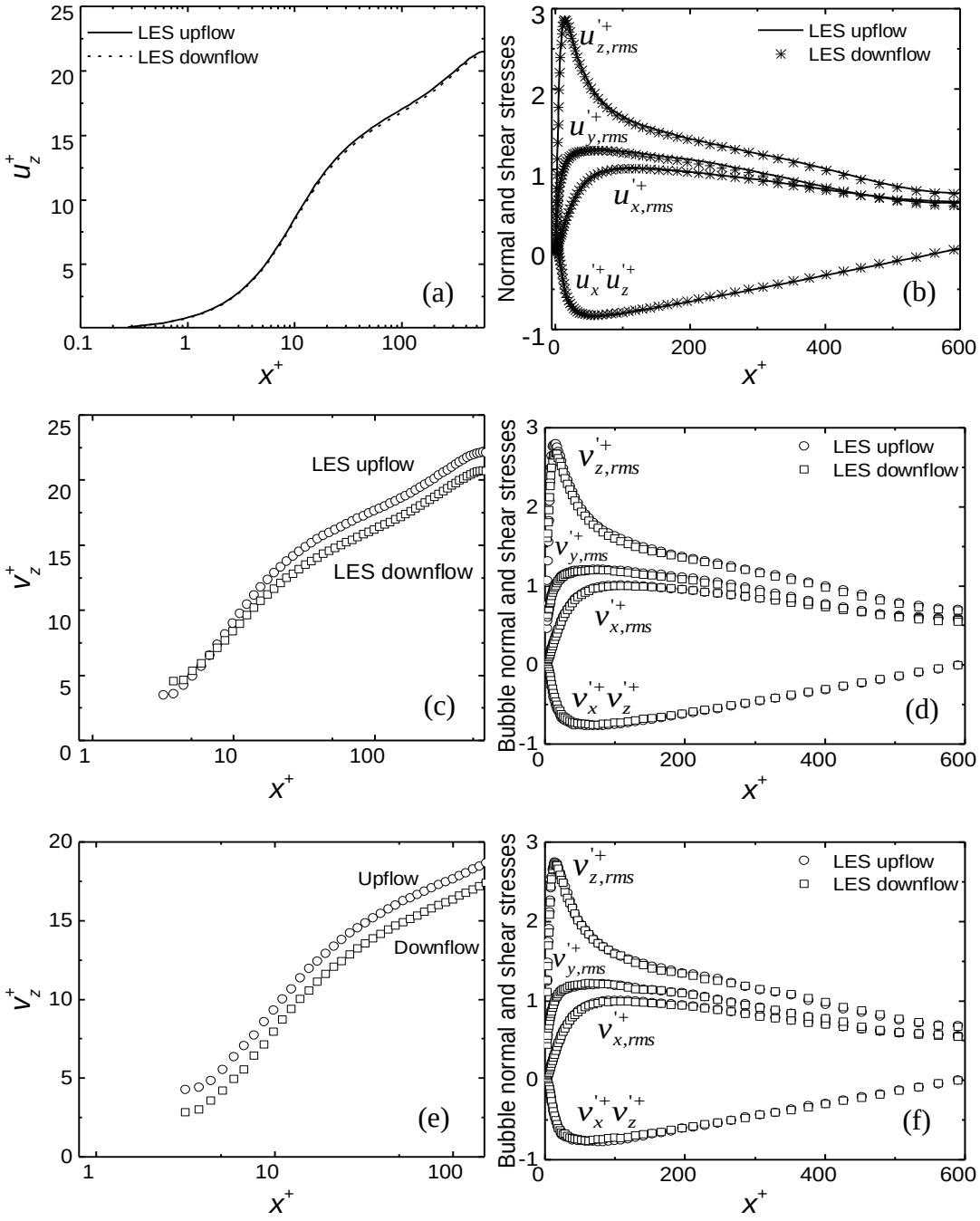

Figure 4.13 Fluid and microbubble velocity statistics for $Re_\tau = 590$ in upflow and downflow conditions and under the one-way coupled assumption: (a) Fluid mean streamwise velocity; (b) rms of fluid velocity fluctuations and shear stress; (c) bubble mean streamwise velocity (with lift); (d) rms of bubble velocity fluctuations and shear stress (with lift); (e) bubble mean streamwise velocity (no lift); and (f) rms of bubble velocity fluctuations and shear stress (no lift).

Presented in Figure 4.13(a) and (b) are the fluid velocity statistics for the vertical channel with upflow and downflow. The results show no real distinction between the two flows in terms of all the statistics, as would be expected under the one-way coupling assumption.

Figure 4.13(c) and (d) give the microbubble velocity statistics for the $Re_\tau = 590$ flow, with the lift force included. The mean streamwise velocity profiles for both flows closely match each other close to the channel wall. At around x^+=25, however, a gradual separation of the two velocities occurs, with the upflow case peaking on the centre line at 22.22, whereas the downflow peaks at 20.7. The normal and shear stresses in both flow configurations show no significant variations between the upflow and downflow cases.

In order to emphasise the relevance of the lift force component in bubbly flows, specifically in the near-wall region, Figure 4.13(e) and (f) gives the bubble mean streamwise velocity and normal and shear stresses without the effects of the lift force included. Again, apart from the mean velocity, all other statistics are similar for each of the flows, and comparable to the results obtained with the lift force included in Figure 4.13(c) and (d). Mean velocities are also comparable to those given in the latter figures, apart from very close to the channel walls.

The time-evolution of the microbubble concentration profiles for both upflow and downflow are shown in Figure 4.14, with the lateral bubble concentration profiles in upflow and downflow, and with and without the lift force, combined in Figure 4.14(c). In the upward flow configuration, the bubbles travel faster than the fluid due to buoyancy effects, whereas in the downward flow configuration the bubbles move slower than the fluid, as can be seen from the results of Figure 4.13. In the absence of the lift force, the bubble concentration profiles in Figure 4.14 remain similar to the initially uniform distribution with time, and show no tendency to migrate either towards or away from the wall. In contrast, inclusion of the lift force, as for the lower Reynolds number flow, causes bubbles to migrate towards the wall in upflow, and away from the wall in downflow.

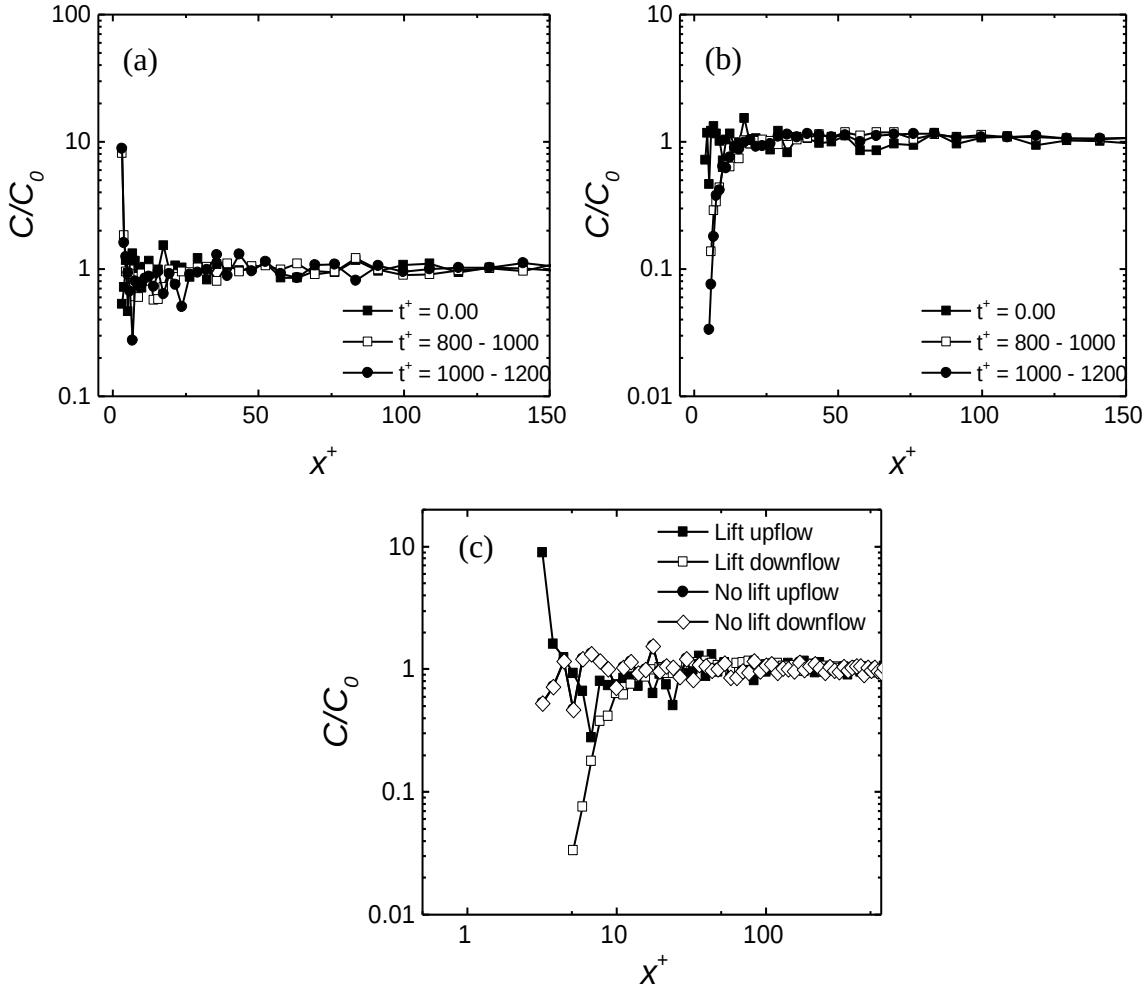

Figure 4.14 Profiles of microbubble concentration with increasing t^+ for upflow and downflow cases, with and without lift force, at $Re_\tau = 590$: (a) upflow; (b) downflow; (c) combined profiles $t^+ = 1200$.

Comparing the velocity profiles between the $Re_\tau = 150$ and $Re_\tau = 590$ flows under the same one-way coupling assumption, it is clear that the presence of the microbubbles has no effects on the surrounding fluid, as expected. In addition, the bubble mean streamwise velocity peaks for the $Re_\tau = 150$ flow were 21.41 and 13.91 for upflow and downflow, respectively. At $Re_\tau = 590$, the results obtained were 22.22 and 20.70, respectively. The higher flow velocity, with respect to a relative velocity between the bubble and the fluid that depends mainly on the bubble diameter and remains almost the same between the two cases, explains the lower relative difference between the upflow and downflow peaks. The bubble preferential concentration at the wall at $Re_\tau = 150$ is close to 100 for upflow and 0.001 for downflow, as shown in Figure 4.12. At $Re_\tau = 590$, the same values become 10 for upflow and 0.15 for downflow (Figure 4.14). This result quantifies the

much higher dispersion of the microbubbles promoted by the higher levels of turbulence at $Re_\tau = 590$. This addditional dispersion opposes and reduces the preferential accumulation induced by the lift force.

4.3 Two-way Coupled Simulations

The presence of bubbles in the fluid phase can lead to both turbulence enhancement or attenuation with respect to the single-phase turbulent flow (Serizawa et al., 1975; Hosokawa and Tomiyama, 2004). However, the physical process of turbulence modulation is not yet fully understood, and the reliable prediction of turbulence enhancement or attenuation by bubbles is still difficult (Lance and Bataille, 1991). This has stimulated much research on bubbly flows and promoted the requirement for a deeper understanding of bubble hydrodynamics and the role bubble-induced turbulence plays in modifying the characteristics of the continuous phase flow. The present study aims to add to the understanding of turbulence modulation by microbubbles in horizontal and vertical channel flows, and to provide a reliable predictive technique. The effect of pressure gradient on the bubbly flow and the impact of the liquid phase turbulence on bubble behaviour are also investigated.

The role of bubble-induced turbulence was analysed experimentally in a vertical duct by Zhang et al. (2015). The study indicated that higher levels of turbulence could be induced by bubbles in a large duct when compared to a smaller duct with a similar void fraction. Interaction between the shear-induced and the bubble-induced turbulence was also discussed. Results showed that the existence of a wall could suppress bubble-induced turbulence, and the presence of bubbles could also suppress the solely wall-induced turbulence as compared to a single-phase turbulent flow, even if the total turbulence was enhanced. Pang et al. (2013) investigated turbulence modulation by small bubbles in a liquid flow in detail using DNS, in an Eulerian-Lagrangian approach, of a vertical upward channel flow with a finite number of small bubbles. The investigation showed that the liquid turbulence is intensified near the wall and is slightly weakened in the channel central region due to the addition of bubbles.

From the literature it can be concluded that although many investigations into turbulence modulation by bubbles have been performed using DNS (e.g. Mazzitelli et al., 2003), the

turbulence modulation mechanism is still not fully understood and there are varying and slightly conflicting findings between experimental and modelling results (Pang et al., 2010). Ferante and Elghobashi (2004) argued that microbubbles in a spatially developing turbulent boundary layer push the developing streamwise vortices away from the wall, leading to less dissipation in the boundary layer. van den Berg et al. (2007) also concluded that microbubble modulation of turbulence is a boundary layer effect. Lu and Tryggvason (2008) in their study additonally showed that bubble deformation has a great influence on the liquid turbulence.

According to Yeo et al. (2010), turbulence modulation depends only slightly on the dispersion characteristics of a flow. Recently, Pang and Wei (2016) in their DNS work investigated the effect of the flow direction on the distribution of bubbles and the liquid turbulence in a vertical channel. The computational domain size was $10h \times 2h \times 5h$ in the streamwise, wall-normal and spanwise directions, respectively. The shear Reynolds number of the liquid phase was $Re_\tau = 150$ with bubbles of diameter 220 μm. Turbulence modulation mechanisms by bubbles were analyzed in the paper, but the analysis was limited to one bubble size and one flow Reynolds number.

4.3.1 Horizontal Channel Flow

The LES coupled with the modified Lagrangian bubble tracker was first used with the two-way coupling assumption for a flow of air microbubbles in a horizontal water channel flow. Results are first validated against the DNS results of Pang et al. (2014) at a shear Reynolds number $Re_\tau = 150$ and for spherical microbubbles of diameter $d_b =$ 220 μm. Additional simulations are then made at the higher shear Reynolds number of $Re_\tau = 590$ to study the effect of higher turbulence levels on bubble accumulation at the upper wall that is promoted by buoyancy effects, and the modifications induced by the presence of these bubbles in the continuous phase field. Also, two additional bubble sizes, $d_b = 110$ μm and $d_b = 330$ μm, are considered at both shear Reynolds numbers to investigate the complex mutual interactions between turbulence, bubble diameter and preferential bubble concentration near the upper wall.

Before introducing bubbles, a fully developed single-phase turbulent channel flow was obtained at shear Reynolds numbers $Re_\tau = u_\tau h/\nu$ of 150 and 590, with water as the

carrier phase fluid with a kinematic viscosity $\nu = 1 \times 10^{-7}\ \mathrm{m^2 s^{-1}}$ and density $\rho = 1000\ \mathrm{kgm^{-3}}$. The computational domain was a channel bounded by two infinite flat parallel walls, as illustrated in Figure 4.5, with the x, y and z axes pointing in the wall normal, spanwise and streamwise directions, respectively. Air bubbles with a density $\rho_b = 1.3\ \mathrm{kgm^{-3}}$ were introduced uniformly into fully-converged single-phase flow solutions, with the initial velocity of a bubble equal to the fluid velocity at the bubble location, obtained by interpolation. Three bubble sizes, $d_b = 110, 220$ and 330 μm, were considered, and the bubble volume fraction was chosen as $\phi = 1.12 \times 10^{-4}$, which is high enough to allow analysis of the effect of microbubbles on the continuous flow field but, at the same time, low enough to ensure negligible bubble-bubble interaction. This corresponds to a total number of 181,272 microbubbles for $d_b = 110$ μm, 25,400 for $d_b = 220$ μm and 6,714 for $d_b = 330$ μm.

Perfectly elastic collisions were assumed at the walls when the microbubble centre was at a distance from the wall lower than the bubble radius. The time-step for the bubble tracker was chosen equal to that of the fluid solver time-step, and corresponding to roughly one-fifth of the bubble relaxation time (see Table 4.2 below). The total simulation time was $t^+ = 200$ for $Re_\tau = 150$ and 2000 for $Re_\tau = 590$, with averaging carried out after 100 and 1000 t^+, respectively. Here, and below, the superscript ($^+$) refers to a non-dimensional quantity scaled by the wall (viscous) variables, where u_τ/ν, $\mathrm{u_\tau}$ and ν/u_τ^2 are the characteristic length, velocity and time scales. Also, t^+ values quoted relate to times after the bubbles were first introduced to the fully developed single-phase solutions.

4.3.1.1 Validation test case

This section gives the two-way coupled LES results compared with the DNS of Pang et al. (2014) at $Re_\tau = 150$ and for $d_b = 220$ μm. Figure 4.15 shows the bubble enhanced fluid velocity statistics and the bubble velocity statistics in this flow. Figure 4.15(a) and (b) give the bubble enhanced fluid mean streamwise velocity and the turbulent normal and shear stresses. The mean streamwise velocity of Pang et al. (2014) is slightly over-predicted by the LES, although this is probably as a consequence of the low grid resolution used by the latter authors who employed a 64 × 64 × 64 mesh, which is significantly less resolved than the present 128 129 ×128 ×128 mesh. In contrast, the

normal and shear stress results of both approaches are in good agreement. These results are in line with those obtained for the $Re_\tau = 150$ single phase flow considered in the previous section.

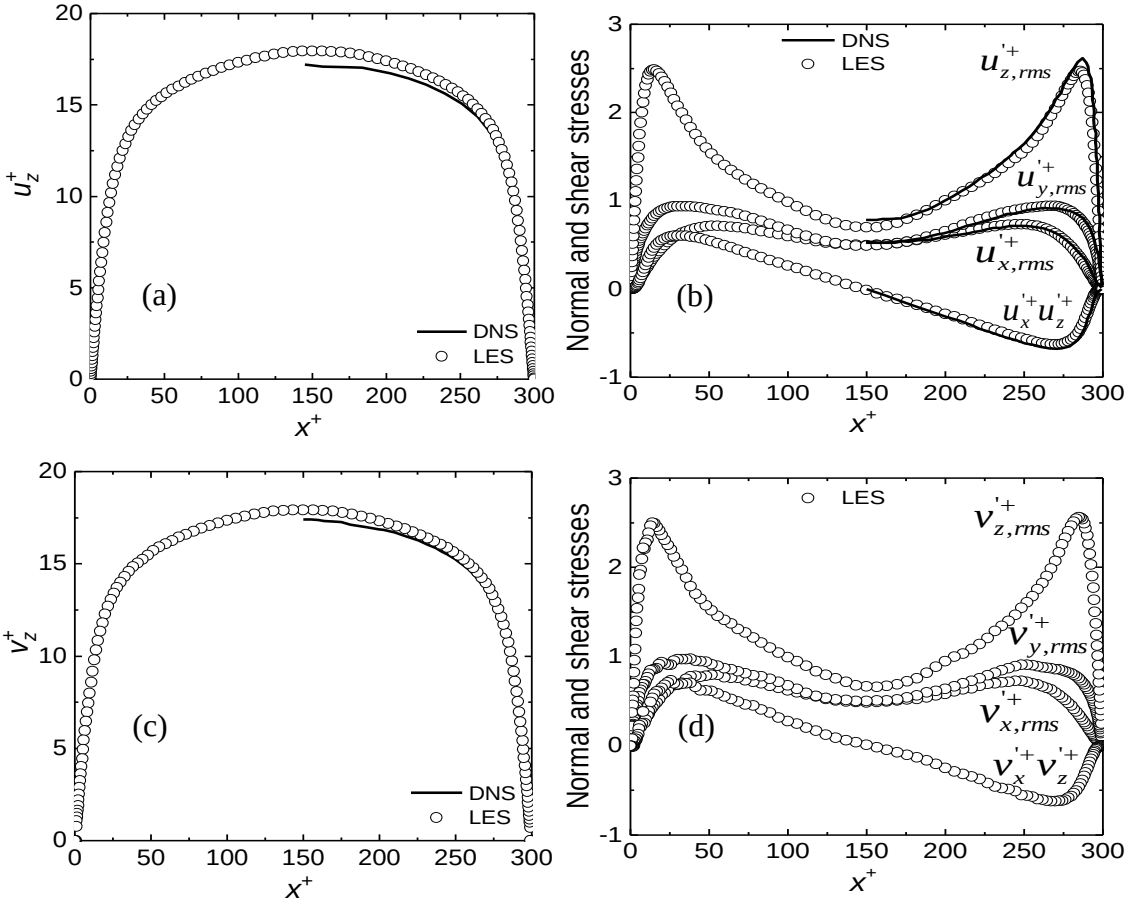

Figure 4.15 Fluid and bubble velocity statistics at $t^+ = 102$ in two-way coupled simulations compared with DNS at $Re_\tau = 150$: (a) mean streamwise fluid velocity; (b) fluid turbulent normal and shear stresses; (c) mean streamwise bubble velocity; and (d) bubble turbulent normal and shear stresses. DNS source Pang et al. (2014).

In Figure 4.15 (c, d), the microbubble mean velocity and turbulent stress profiles are also compared with the DNS predictions of Pang et al. (2014). For the mean bubble velocity, the DNS is found to be lower than the LES results, this again being a likely consequence of the low resolution used by the latter authors. Unfortunately, no DNS results for the turbulent stresses were provided by Pang et al. (2014), although the LES results are given in Figure 4.15(d). For both the LES and the DNS, the velocity profiles of the gas and liquid phases are very similar, with the microbubble mean velocity being slightly higher than that of the fluid phase. An explanation to this is provided by Pang et al. (2014). The

interphase forces acting on the microbubbles are the drag, lift, added mass, gravity-buoyancy and the pressure gradient forces. In the streamwise direction, the added mass, pressure gradient and gravity-buoyancy forces are negligible, and the drag force is expected to be weak due to the low mean slip velocity between the gas and liquid phases. The velocity difference is therefore mostly generated by the component of the lift force in the streamwise direction induced by the spanwise vorticity (Pang et al., 2014), and this effect is reproduced by the LES.

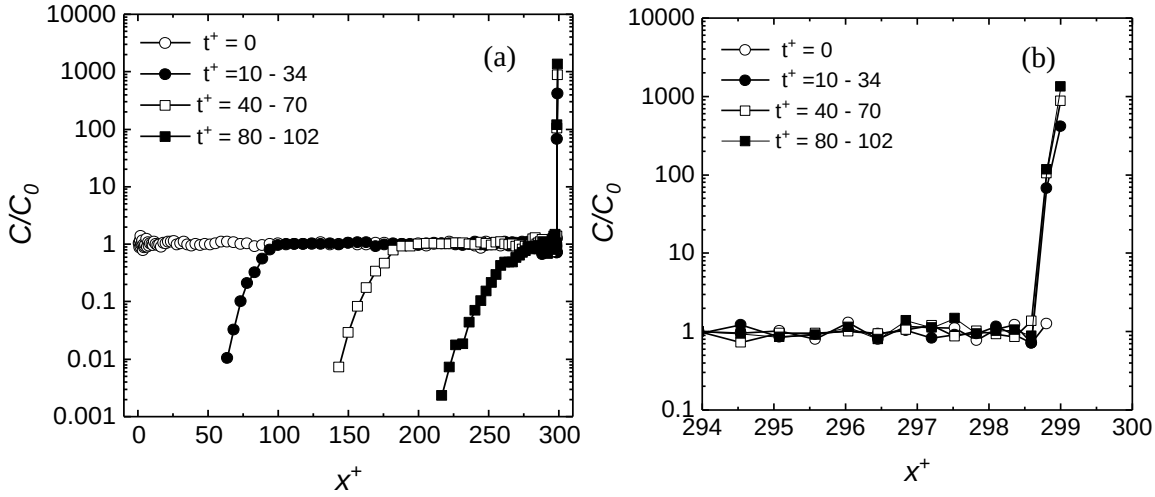

Figure 4.16 Time evolution of bubble concentration profiles in the two-way coupled simulations at $Re_\tau = 150$: (a) bubble concentration profiles across the horizontal channel; and (b) bubble concentration profiles close to the upper channel wall.

In the wall-normal direction, gravity-buoyancy is the dominant force, even if the lift force is expected to contribute by moving the bubbles towards the channel walls. The gravity-buoyancy force itself causes the lower density bubbles to mifgrate towards the upper wall of the channel, with the results given in Figure 4.16 showing the evolution of the microbubble concentration with time. Starting from an initially uniform bubble concentration, the bubbles gradually migrate from the lower channel wall to the upper wall and, by $t^+ = 102$, the majority of the bubbles have moved close to the latter wall.

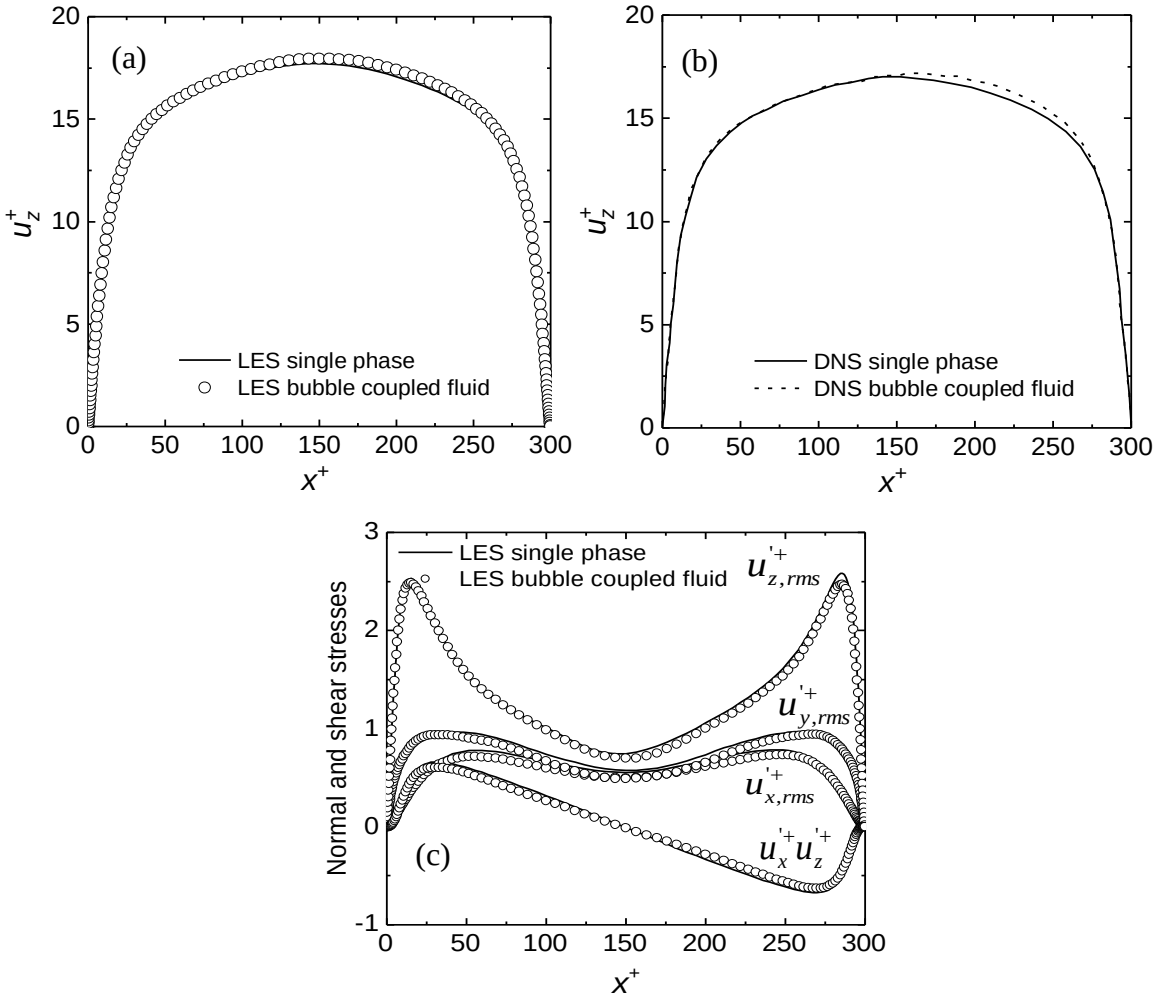

Figure 4.17 Comparison between two-way coupled and single-phase fluid statistics: (a) LES mean streamwise velocity; (b) DNS mean streamwise velocity (Pang et al., 2014); and (c) LES turbulent normal and shear stresses.

A comparison between the two-way coupled and the single-phase fluid mean streamwise velocities and turbulent stresses is given in Figure 4.17. The LES mean streamwise velocity is shown in Figure 4.17(a) and this can be compared with the DNS prediction as given in Figure 4.17(b). The LES turbulent normal and shear stresses are also shown in Figure 4.17(c). Relative to the single-phase, the mean velocity of the fluid phase exhibits a slight asymmetrical profile in the presence of microbubbles. More specifically, in the lower half of the channel ($0 < x^+ < 150$), the fluid velocity generally matches that of the single phase due to the negligible number of microbubbles in that region. In contrast, in the upper half of the channel ($151 < x^+ < 300$), the fluid phase mean velocity is slightly enhanced in the region away from the wall due to the presence of the microbubbles. As a consequence, the peak velocity is shifted slightly higher than the channel centre relative

to the single phase peak. Some small modifications are also visible in the turbulent stress profiles, in Figure 4.17(c) which, in agreement with Pang et al. (2014), are slightly reduced in the upper half of the channel, particularly in the streamwise direction.

4.3.1.2 Effect of flow Reynolds number

Additional simulations at $Re_\tau = 590$ were also carried out for the two-way coupled LES to study the effect of turbulence levels on microbubble dispersion and migration to the upper wall. Figure 4.18 shows the fluid velocity statistics, the bubble velocity statistics and bubble concentration profiles with time. For the fluid, the two-way coupled results are again compared with the single-phase profiles in Figure 4.18(a) and (b). The asymmetrical profiles which were observed at a shear Reynolds number $Re_\tau = 150$ are not apparent at the higher Reynolds number, with the mean velocity and turbulent stress profiles insignificantly different from the corresponding single-phase results.

This is as a result of the higher bulk flow velocity and turbulence levels that dominate the buoyancy effect on the bubbles and their movement towards the upper wall. This is confirmed by the results of Figure 4.18(c) and (d), where the mean velocity and turbulent stresses of the bubbles are almost identical to those of the continuous phase. Additonally, in Figure 4.19(e) and (f), it is seen that, although some effect of buoyancy is apparent with time near the lower channel wall, there is no significant accumulation of bubbles near the upper wall. As a consequence of the higher bubble dispersion by the turbulence, the concentration of bubbles, therefore, remains significant in the lower half of the channel, even at $t^+ = 1219$.

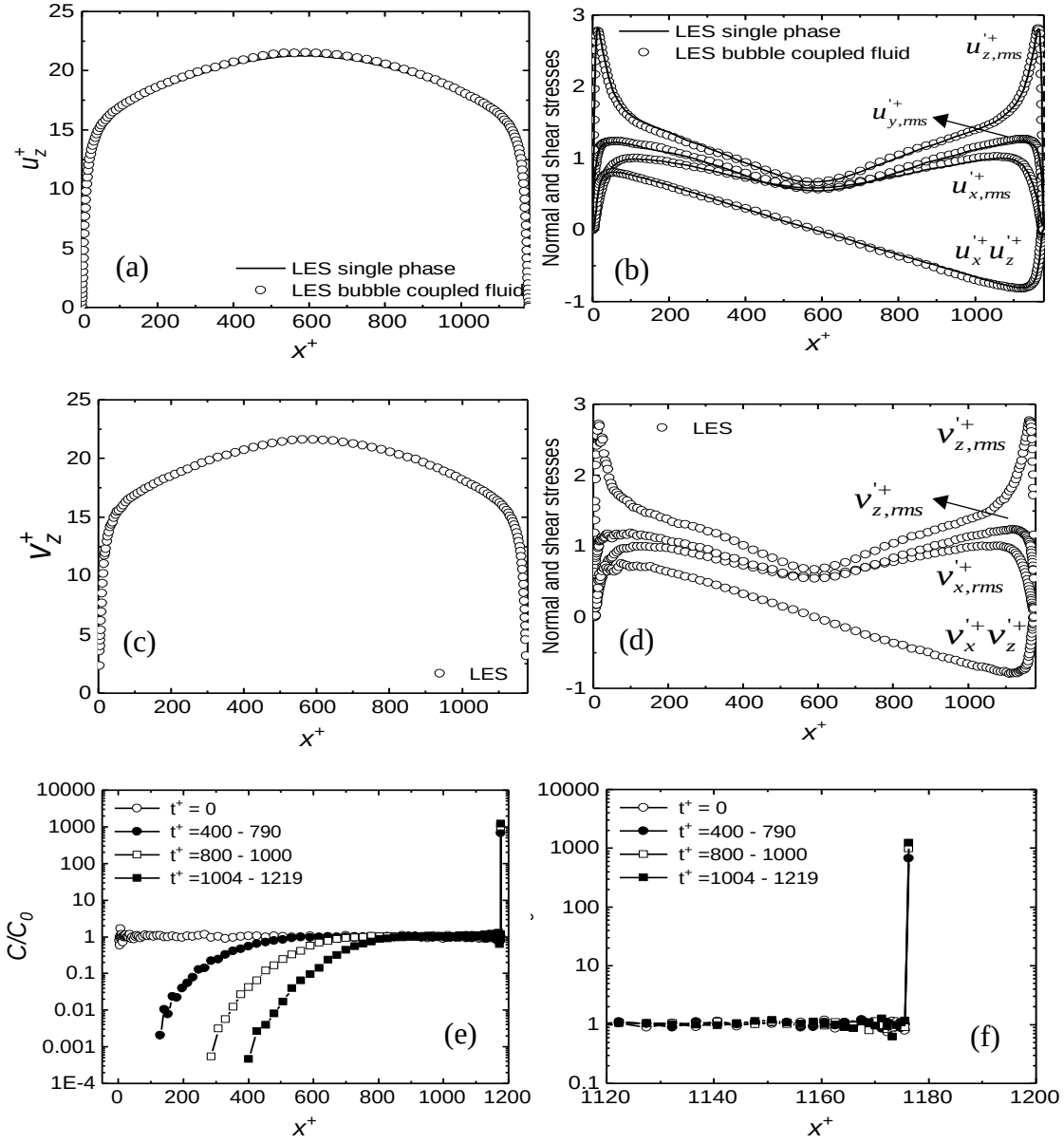

Figure 4.18 Fluid and bubble velocity statistics at $t^+ = 1219$, and time evolution of bubble concentration profiles, in two-way coupled simulations at $Re_\tau = 590$: (a) mean streamwise fluid velocity; (b) fluid turbulent normal and shear stresses; (c) mean streamwise bubble velocity; (d) bubble turbulent normal and shear stresses; (e) bubble concentration profiles across the horizontal channel; and (f) bubble concentration profiles close to the upper channel wall.

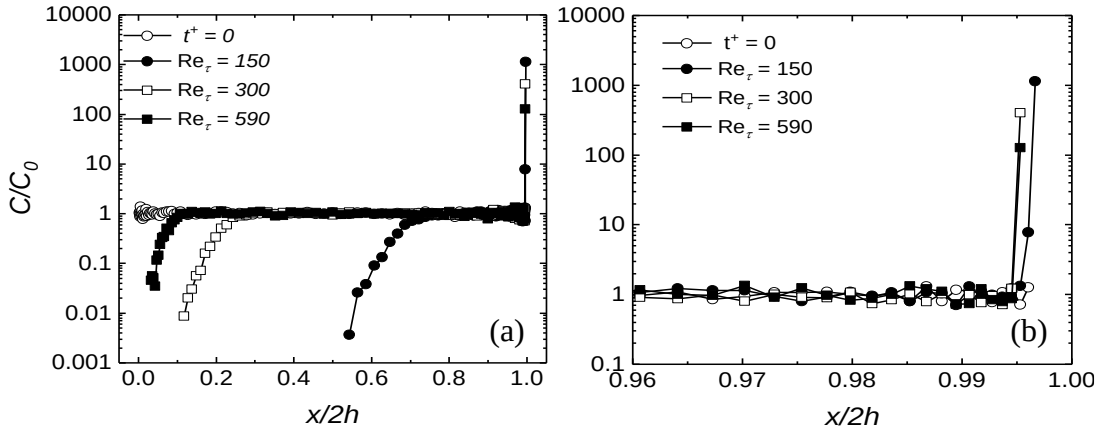

Figure 4.19 Time evolution of bubble concentration profiles at $t^+ = 70$ for different shear Reynolds numbers: (a) across the horizontal channel; and (b) close to the upper channel wall.

An additional simulation at the intermediate shear Reynolds number of $Re_\tau = 300$ was also performed, and results for the bubble concentration distribution in the channel at all three Reynolds numbers are shown in Figure 4.19. This allows further consideration of the time required for the microbubbles to move from the lower regions of the channel to the upper channel wall, with the predictions in Figure 4.19(a) plotted at a fixed time of $t^+ = 70$ and with distance given relative to the total channel height $2h^+$, expressed in wall units. At $Re_\tau = 150$, the microbubble concentration is negligible in the lower regions of the channel until $x/2\text{h} = 0.55$, such that more than half the channel is devoid of bubbles. In contrast, bubbles still occupy the majority of the channel height at $Re_\tau = 300$, and even more so at $Re_\tau = 590$, because their higher mean velocity and turbulence levels partially override the effects of buoyancy. Comparing the bubble concentration at $Re_\tau = 150$ and $Re_\tau = 590$ at the t^+ used in Figure 4.19(a), the migration rate of the microbubbles is 11 times faster at the lower shear Reynolds number. A correspondingly lower concentration of bubbles at the upper channel wall with increasing Re_τ is shown in Figure 4.19(b).

4.3.1.3 Effect of bubble size

The influence of bubble size was also studied using two additional bubble diameters ($d_b = 110$ μm and 330 μm), with simulations performed at shear Reynolds numbers of $Re_\tau = 150$ and $Re_\tau = 590$. The evolution of bubble concentration profiles at $Re_\tau = 150$ is

illustrated in Figure 4.20 and at $Re_\tau = 590$ in Figure 4.21. Both figures give results for all the three bubble sizes considered. In Figure 4.20, the segregation of the microbubbles and their movement towards the upper wall is increased with an increase in the bubble size. In Figure 4.20(a), some bubbles remain in the lower half of the channel at $t^+ \approx 200$, whilst in Figure 4.20(b), the lower half of the channel is practically emptied of bubbles by $t^+ \approx 100$, and by $t^+ \approx 38$ in Figure 4.20(c). Since the buoyancy force acting on the bubbles is proportional to their volume, and hence to the third power of the bubble diameter, it is increased eight times by doubling the bubble diameter. In contrast, larger bubbles tend to be less affected by turbulent dispersion. Therefore, the buoyancy force is clearly more influential than turbulent dispersion at the larger bubble diameters, with buoyancy promoting the greater segregation of the bubbles and their accumulation near the upper wall of the channel.

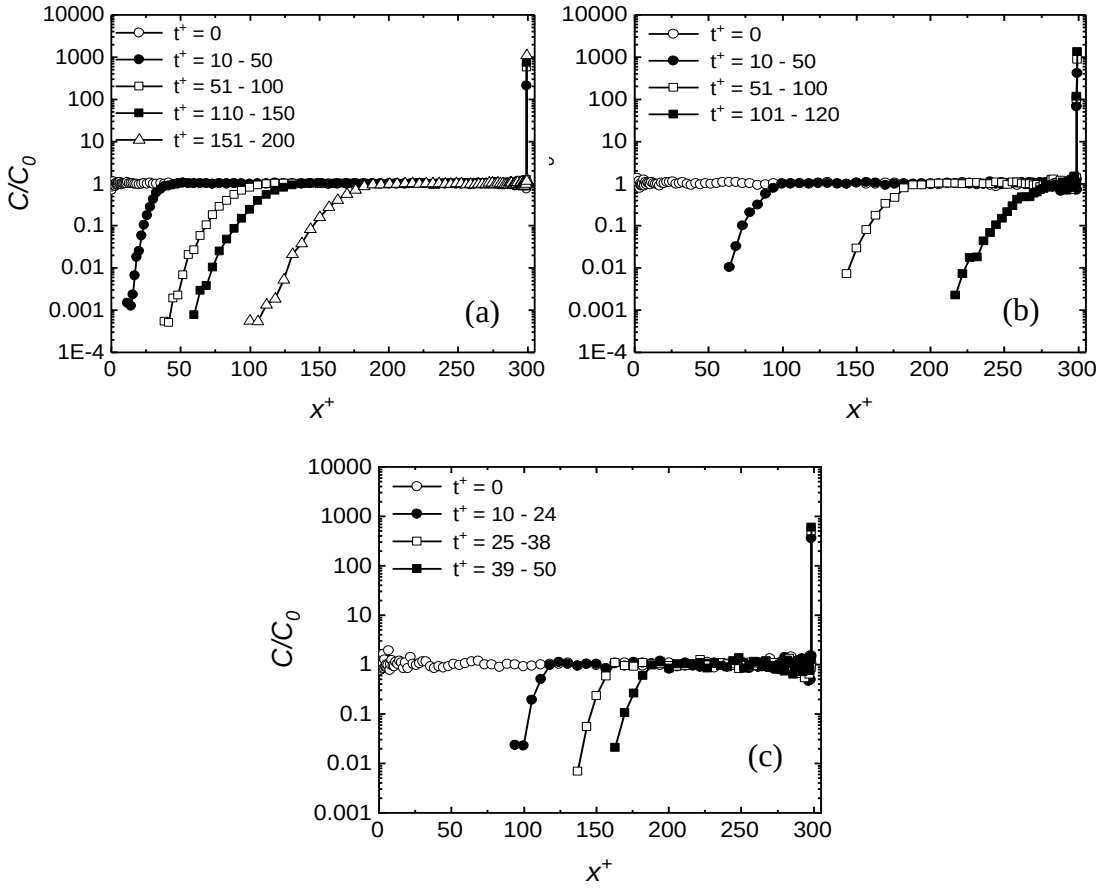

Figure 4.20. Bubble concentration profiles at $Re_\tau = 150$ for different bubble diameters: (a) 110 μm; (b) 220 μm; and (c) 330 μm.

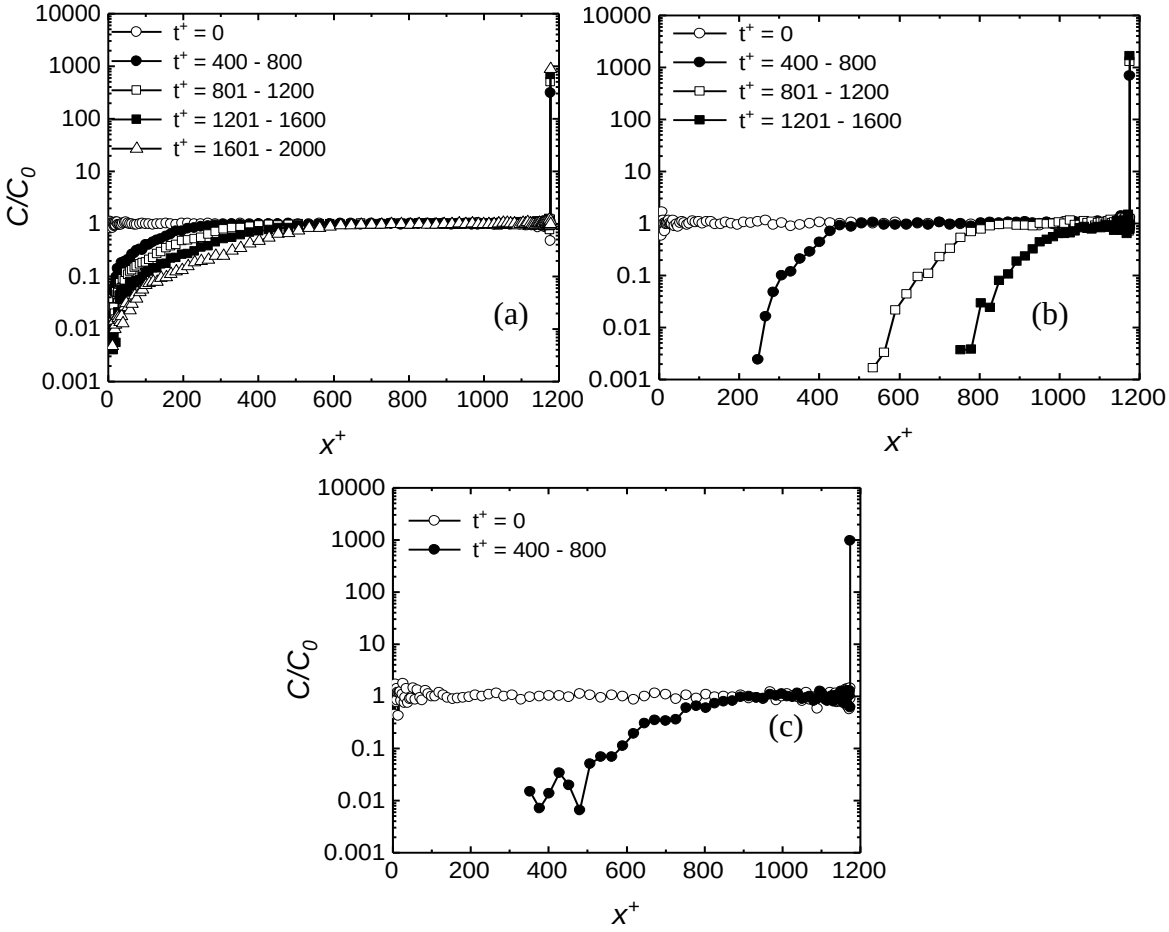

Figure 4.21 Bubble concentration profiles at Re_τ = 590 for different bubble diameters: (a) 110 μm; (b) 220 μm; and (c) 330 μm.

Results for microbubble preferential concentration at the higher shear Reynolds number are given in Figure 4.21. Similar to the results of Figure 4.20, the rate of microbubble migration upwards in the channel increases with bubble size, although this increase is slower when compared to the shear Reynolds number $Re_\tau = 150$ flow because of the higher bulk velocity and turbulence levels that increase the dispersion of the microbubbles.

Overall, results at the shear Reynolds number of 150 and bubble diameter of 220 μm show acceptable agreement with the DNS predictions of Pang et al. (2014) for single- and two-phase flows, and in terms of both the mean velocity and turbulent stresses. The results show the low density microbubbles migrating towards the upper channel wall with time under the influence of buoyancy, with the accumulation of microbubbles near

the upper wall modifying the liquid velocity field such that the mean velocity profile becomes asymmetric, in agreement with DNS predictions (Pang et al., 2014). Some slight modification of the turbulent stresses is also noted. Using the same computational conditions, the simulations were extended to a shear Reynolds number $Re_\tau = 590$. At the higher mean velocity and turbulence levels, the buoyancy effect is partially overridden by the turbulent dispersion of the microbubbles, with migration towards the upper channel wall significantly reduced as a consequence.

At both shear Reynolds numbers, the influence of microbubble diameter was also investigated, with simulations performed for 110 μm, 220 μm and 330 μm diameter bubbles. Buoyancy, being proportional to the bubble volume, increases bubble migration towards the upper channel wall and segregation of the bubbles in the upper half of the channel with increasing bubble diameter, with this effect reduced with increasing Reynolds number.

4.3.1.4 Force analysis in wall-normal direction

The individual forces acting on the microbubbles are analysed in more detail in this section. More specifically, the forces in the wall-normal direction are considered, in terms of the force per unit mass (Nkg^{-1}), since it is in this direction that the greatest change in bubble distribution occurs. Plots of all the individual forces acting on the microbubbles are presented for the Re_τ = 150 and Re_τ = 590 flows for a bubble diameter d_b = 220 μm and at t^+ = 200 in Figure 4.22. Similar results were found for simulations performed for all three bubble sizes considered and, therefore, only results for the 220 μm case are considered below.

Figure 4.22 shows the wall-normal profiles for all the forces acting on the microbubbles for both the shear Reynolds numbers considered. In both cases, the gravity-buoyancy force is, as expected, the dominant force with a constant value of 19.6 Nkg^{-1} in the direction of the upper wall. This force is balanced by drag, with other forces such as lift, added mass and pressure gradient being negligible. Because of their small magnitudes, Figure 4.22(b) and (d) use an expanded scale to better illustrate the variation in the latter forces. At the higher shear Reynolds number Re_τ = 590 in particular, although the gravity-buoyancy and drag forces are still dominant, the lift, added mass and pressure gradient

forces are seen to play a role, albeit small, in the near-wall region. Here, an increased positive lift contributes to pushing bubbles towards the wall, with a slightly counteracting effect from the added mass and pressure gradient forces also observed. Overall, however, the force analysis shows the dominant role of the gravity-buoyancy force and the balancing effect of the drag force that is generated as soon as the bubbles start to migrate towards the upper surface.

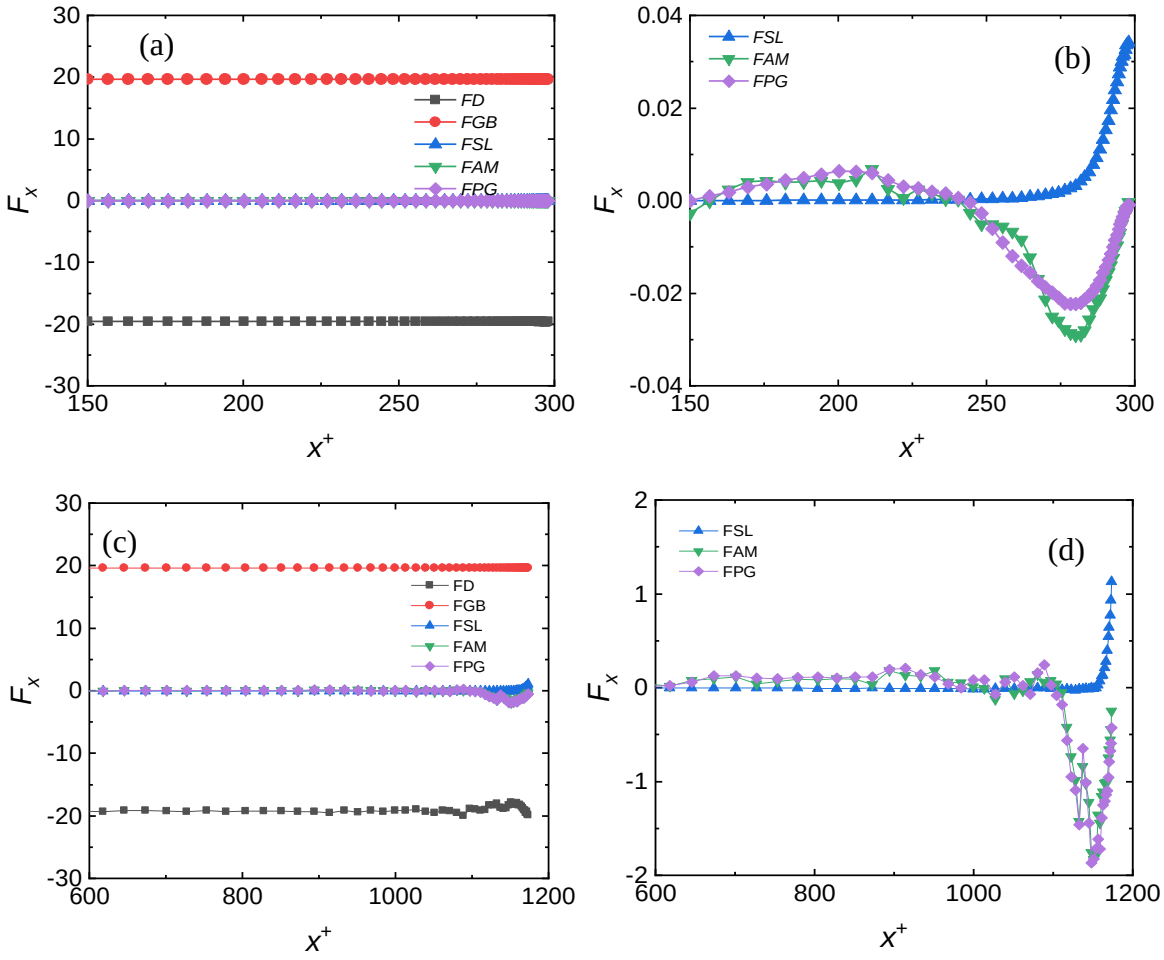

Figure 4.22 Forces acting in the wall normal direction for d_b = 220 μm bubbles and t^+ = 200: (a, b) Re_τ = 150; and (c, d) Re_τ = 590. Plots (b) and (d) show an expanded scale to highlight the magnitude of the smaller forces (FD = drag force, FGB = gravity-buoyancy force, FSL = shear lift force, FAM = added mass force and FPG = pressure gradient force).

4.3.2 Vertical Channel Flow

In this section, attention is shifted to the study of the flow of air microbubbles in a vertical (upflow and downflow) water channel. The DNS results of Molin et al. (2012) allow validation of the LES-based results at a shear Reynolds number $Re_\tau = 150$. Microbubbles with diameters $d_b = 110$ μm, 220 μm and 330 μm were considered to investigate the complex mutual interactions between turbulence and bubble size near the channel walls. A second set of simulations was carried out at the higher, and more industrially relevant, shear Reynolds number of $Re_\tau = 590$ to study the effect of turbulence on the bubble evolution towards or away from the wall regions promoted by lift and the modifications induced by the presence of bubbles in the continuous phase flow field. It is demonstrated that at this higher Reynolds number the coupling effect between the bubbles and the continuous flow rapidly diminishes, with preferential concentration or depletion of bubbles at the channel wall also reduced. This is due to the greater influence of turbulent dispersion in this flow, and the consequent impact on the forces acting on the bubbles.

4.3.2.1 Validation test case

Fully converged single-phase turbulent channel flows at shear Reynolds number $Re_\tau = 150$ and $Re_\tau = 590$ were considered. Water was used as the continuous phase with kinematic viscosity $v = 1.0 \text{ x } 10^{-7}$ m^{2}s^{-1} and density $\rho = 1000$ kgm^{-3}. The computational domain was a channel bounded by two infinite flat parallel walls as illustrated in Figure 4.10, with the *x*, *y*, and *z* axes pointing in the wall normal, spanwise and streamwise directions, respectively. The dimensions of the computational domain was set to $L_x \times L_y \times L_z = 2h \times 2\pi h \times 4\pi h$ and this was discretised using $N_x \times N_y \times N_z = 129 \times 128 \times 128$ grid points in the wall-normal, spanwise and streamwise directions, respectively. The computational grid was uniformly distributed along the *y* and *z* axes and non-uniform using a hyperbolic function (Gamet et al., 1999) in the wall-normal direction. The no-slip boundary condition was imposed at the channel wall (Tagawa et al., 2010) while periodic boundary conditions were imposed in the streamwise and spanwise directions, with the flow being driven by an imposed streamwise fixed pressure gradient.

Air bubbles with a density ρ_b = 1.3 kgm^{-3} were used as the dispersed phase and bubbles were uniformly introduced into the fully-converged single-phase flow solutions, with the initial velocity of the bubble equal to the fluid velocity at the bubble location, obtained by interpolation. Three bubble sizes, $d_b = 110, 220$ and 330 μm, were selected, and the bubble volume fraction was chosen as $\Phi = 1.0 \times 10^{-4}$, high enough to analyse the microbubbles effect on the continuous fluid field but, at the same time, low enough to ensure negligible bubble-bubble interaction. The corresponding total number of microbubbles for the respective bubble sizes are presented in Table 4.2 below. Two different flow configurations (upward and downward) were studied. The single-phase and two-way coupled values of the wall shear stress, the shear velocity and the shear Reynolds number for these cases are summarized in Molin et al. (2012) and presented in Table 4.3.

Table 4.2 Computational parameters for bubbles and liquid in the vertical channel simulations for the two flow Reynolds numbers.

Re_τ = 150		Re_b = 2272		$u_\tau (ms^{-1})$ = 7.5 × 10^{-3}		u_{bulk} = 0.114
$d_b(\mu m)$	d_b^+	$\tau_b(\mu s)$	τ_b^+	$\tilde{\tau}_b(s)$	$\tilde{\tau}_b^+$	n_b
110	0.83	0.87	4.89 × 10^{-5}	3.37 × 10^{-4}	0.02	181,272
220	1.65	3.50	1.97 × 10^{-4}	1.35 × 10^{-3}	0.07	22,660
330	2.48	7.87	4.42 × 10^{-4}	3.03 × 10^{-3}	0.17	6,714
Re_τ = 590		Re_b = 11033		u_τ = 2.95 x 10^{-2}		u_{bulk} = 0.552
d_b (μm)	d_b^+	$\tau_b(\mu s)$	τ_b^+	$\tilde{\tau}_b(s)$	$\tilde{\tau}_b^+$	n_b
110	3.25	0.87	7.61 × 10^{-4}	3.37 × 10^{-4}	0.29	45,318
220	6.49	3.50	3.04 × 10^{-3}	1.35 × 10^{-3}	1.17	5,664
330	9.74	7.87	6.84 × 10^{-3}	3.03 × 10^{-3}	2.64	1,678

Table 4.3. Non-dimensional wall shear stress, shear velocity and Reynolds number for the single-phase and the two-way coupled simulations at nominal shear Reynolds numbers $Re_\tau = 150$ and $Re_\tau = 590$.

Unladen flow	**Two-way coupled flow**	
	Upflow	**Downflow**
$Re_\tau = 150$	$Re_{\tau,2w\,uf} = 171$	$Re_{\tau,2w\,df} = 122$
$\tau_w^+ = 1$	$\tau_{w,2w\,uf}^+ = 1.31$	$\tau_{w,2w\,df}^+ = 0.66$
$u_\tau = 7.5 \times 10^{-3}\mathrm{ms}^{-1}$	$u_{\tau,2w\,uf} = 8.58 \times 10^{-3}\mathrm{ms}^{-1}$	$u_{\tau,2w\,df} = 6.11 \times 10^{-3}\mathrm{ms}^{-1}$
Unladen flow	**Upflow**	**Downflow**
$Re_\tau = 590$	$Re_{\tau,2w\,uf} = 612$	$Re_{\tau,2w\,df} = 562$
$u_\tau = 2.95 \times 10^{-2}\mathrm{ms}^{-1}$	$u_{\tau,2w\,uf} = 3.06 \times 10^{-2}\mathrm{ms}^{-1}$	$u_{\tau,2w\,df} = 2.81 \times 10^{-2}\mathrm{ms}^{-1}$
$\tau_w^+ = 1$	$\tau_{w,2w\,uf}^+ = 1.07$	$\tau_{w,2w\,df}^+ = 0.91$

The trajectories of individual microbubbles were obtained from integration of the Lagrangian tracking equation, Eq. (3.37), using a fourth-order Runge-Kutta scheme. Perfectly elastic collisions were assumed at the wall when the microbubble centre was at a distance from the wall less than the bubble radius. The time-step for the bubble tracker was chosen equal to that of the fluid solver time-step, and corresponding to roughly one-fourth of the bubble response time ($\tau_b = \rho_b d_b^2/18\mu$) for both Reynolds numbers (Table 4.2). The total simulation time in wall units, derived from $t^+ = tu_\tau^2/\upsilon$, was 1500 for upflow and 2000 for downflow at $Re_\tau = 150$, and 1200 for upflow and 1400 for downflow at $Re_\tau = 590$, with averaging carried out after 1000 t^+.

The simulation results are discussed below, and in particular the velocity fields for both the fluid and the microbubbles as well as the microbubble concentration profiles are considered. Validation of the single-phase flow results has already been considered in Figure 4.2 and Figure 4.4 at the beginning of this section. Here, bubbly flows in both upflow and downflow are first validated against the results of Molin et al. (2012) for bubble sizes $d_b = 110$ and $d_b = 220$. Results of extended simulations at $d_b = 330$ μm and $Re_\tau = 590$, for which no results are currently available in literature, are then addressed. Finally, the role and importance of the different forces acting on the bubbles

in the wall normal direction, and their effect on the bubble concentration profiles, are considered.

In Figure 4.23, the bubble enhanced fluid mean velocity profiles in the wall-normal direction are shown. More specifically, two-way coupled LES results are compared against the DNS results of Molin et al. (2012) at $Re_\tau = 150$, and for $d_b = 110$ μm and 220 μm bubbles, in both the upward and downward flow directions. In addition, LES results are also provided for the $d_b = 330$ μm case.

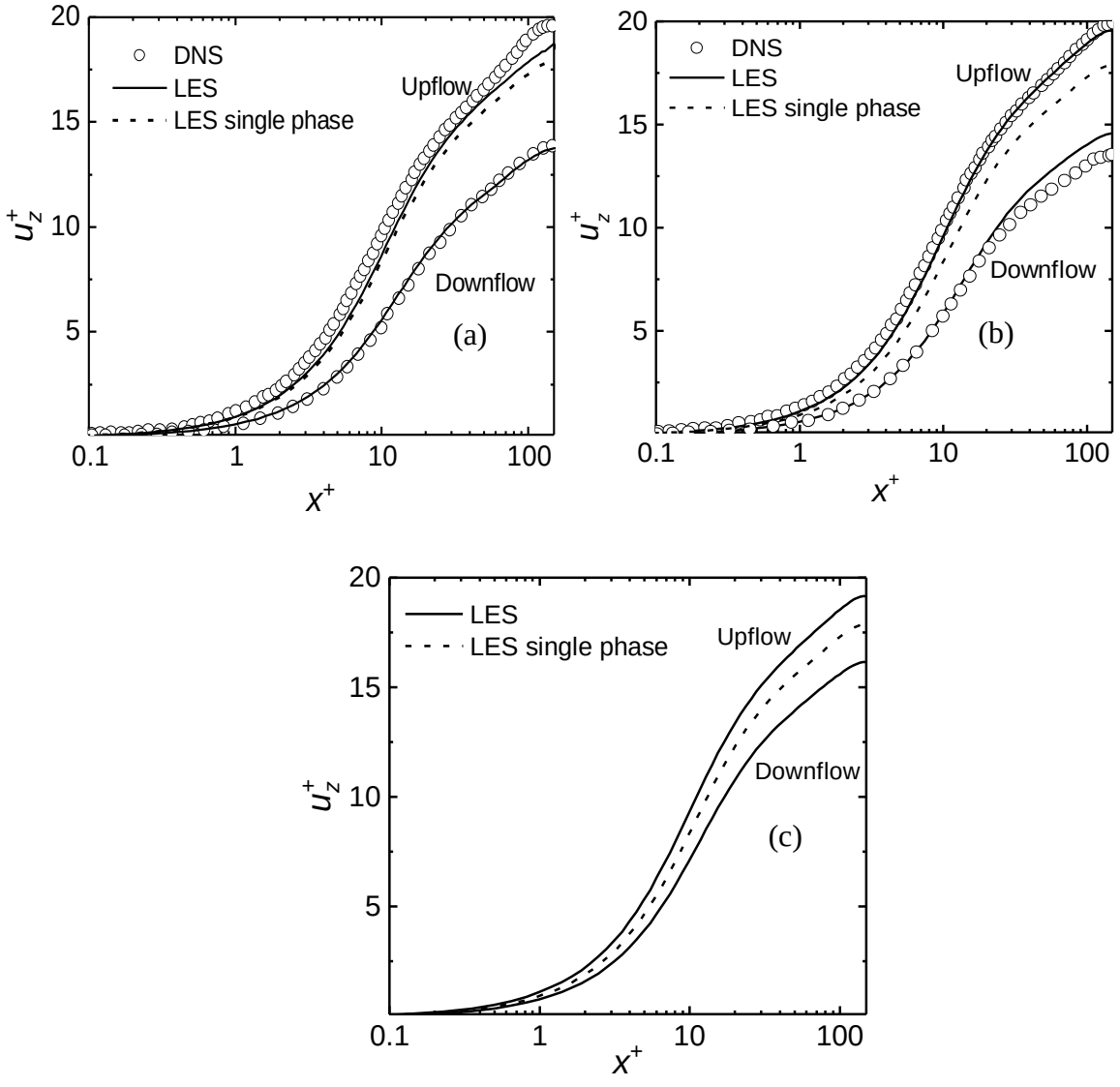

Figure 4.23 Bubble enhanced mean streamwise fluid velocity for the three bubble sizes: (a) $d_b = 110$ μm; (b) $d_b = 220$ μm; and (c) $d_b = 330$ μm.

In Figure 4.23(a), the LES mean streamwise bubble velocities peak at approximately 13 and 18.5 for downflow and upflow, respectively. This difference is reduced in Figure 4.23(b), where the velocity peaks at 14.8 in downflow and 19 in upflow, and further decreases in Figure 4.24(c) that shows peaks at 16 and 19. Equivalent bubble velocities are given in Figure 4.24. Overall, acceptably close agreement with the DNS predictions of Molin et al. (2012) is apparent for the two lower bubble diameters.

In Figure 4.25, the same mean streamwise fluid velocities for bubble sizes $d_b = 110$ μm and $d_b = 220$ μm are rescaled using the effective upflow, $u_{\tau,2w\,upf}$, and downflow, $u_{\tau,2w\,df}$, shear velocities after the introduction of the bubbles, with the present predictions compared against the rescaled DNS results. As already noted by Molin et al. (2012), the difference that is observed in Figure 4.23 is reduced when the upflow and downflow shear velocities are used to scale the velocity profiles for both bubble sizes.

More specifically, the LES profiles are almost superimposed and remain close to the single-phase profile in both flow configurations. As already noted, the total pressure drop was kept constant in these flows, but the gravitational loss in upflow and gain in downflow are modified by the introduction of the bubbles. Therefore, because of the reduced gravitational loss, the upflow is almost equal to a single-phase flow driven by an increased pressure gradient. In a similar way, the downflow is equivalent to a flow driven by a reduced pressure gradient because of the reduced gravitational gain.

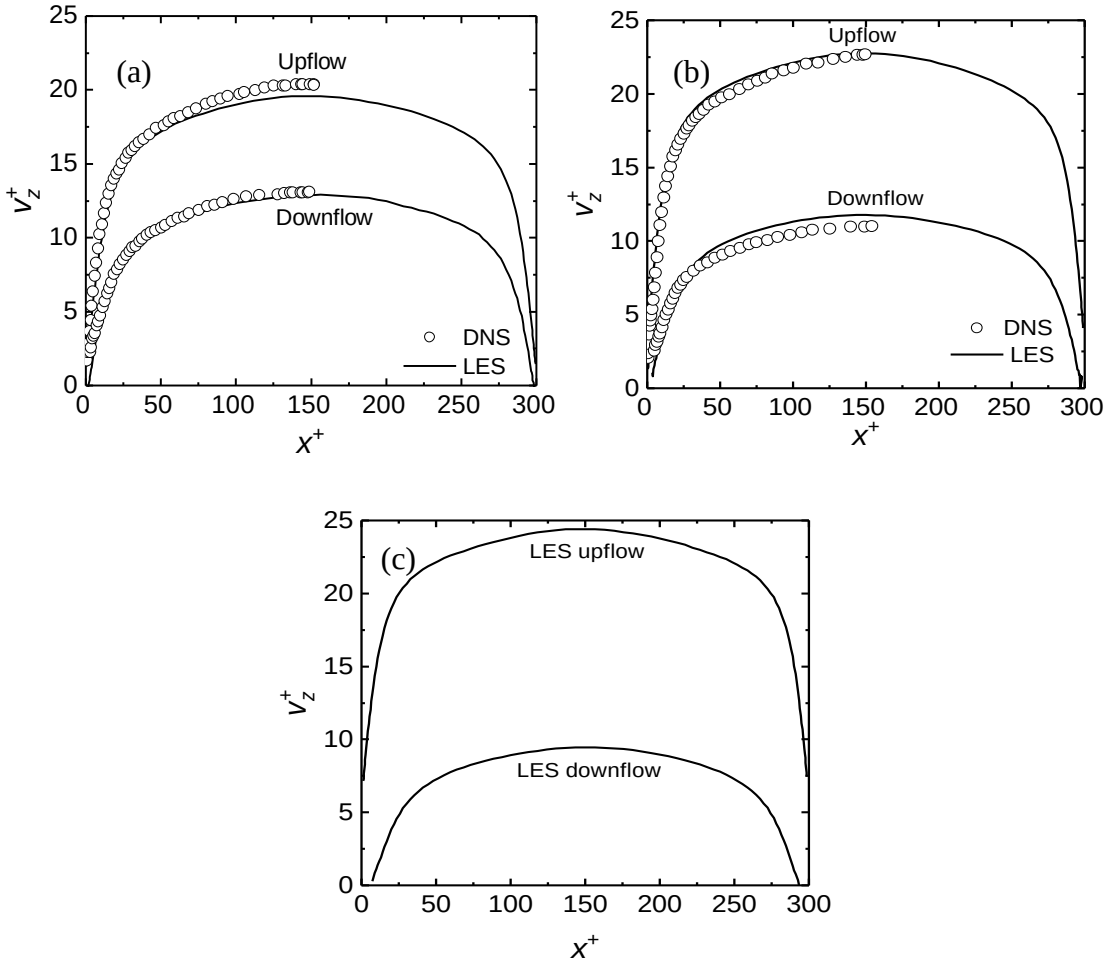

Figure 4.24 Mean streamwise bubble velocity for the three bubble sizes: (a) $d_b = 110\ \mu m$; (b) $d_b = 220\ \mu m$; and (c) $d_b = 330\ \mu m$.

The rms of the fluid velocity fluctuations scaled using the upflow and downflow shear velocities are shown in Figure 4.26 for bubble sizes $d_b = 110$ μm, $d_b = 220$ μm and $d_b = 330$ μm. For $d_b = 110\ \mu m$ and $d_b = 220\ \mu m$, LES-based results are compared with the DNS results of Molin et al. (2012).

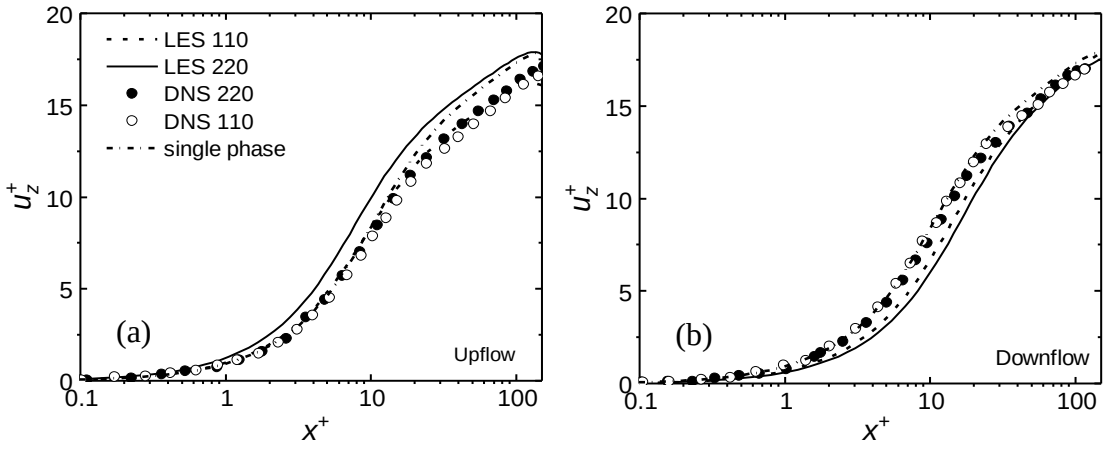

Figure 4.25 Mean streamwise fluid velocity rescaled with the effective shear velocities: (a) $u_{\tau,2w\,upf}$ for upflow; and (b) $u_{\tau,2w\,df}$ for downflow. ---- LES, $d_b = 110\ \mu m$; — LES, $d_b = 220\ \mu m$; ● DNS, $d_b = 110\ \mu m$; ○ DNS, $d_b = 220\ \mu m$; and -·- LES single phase.

As shown in Figure 4.26, and for both upflow and downflow, the bubbles alter not only the mean velocity but also the intensity of the turbulence in the fluid, and these effects are well reproduced in the LES simulations which show a good agreement with the DNS. When scaled using the actual shear velocities, rms values in Figure 4.26 look similar to those in a single-phase flow. Therefore, not only for the mean velocity, but also for the turbulence in the fluid, the upflow is equivalent to a single-phase flow with a slightly higher mass flow rate, and the downflow to a flow with a lower mass flow rate. Overall, the increase in flow rate results in a corresponding increase in the turbulence intensity. In upflow, the rms values are scaled using a higher shear velocity, whereas the equivalent reduction in downflow produces lower turbulence fluctuations. In addition, although of lower strength, there is also an effect of the bubble diameter on the fluid turbulence since, at $d_b = 330$ μm (Figure 4.26(e) and (f)), the largest deviations with respect to the single-phase profiles are observed.

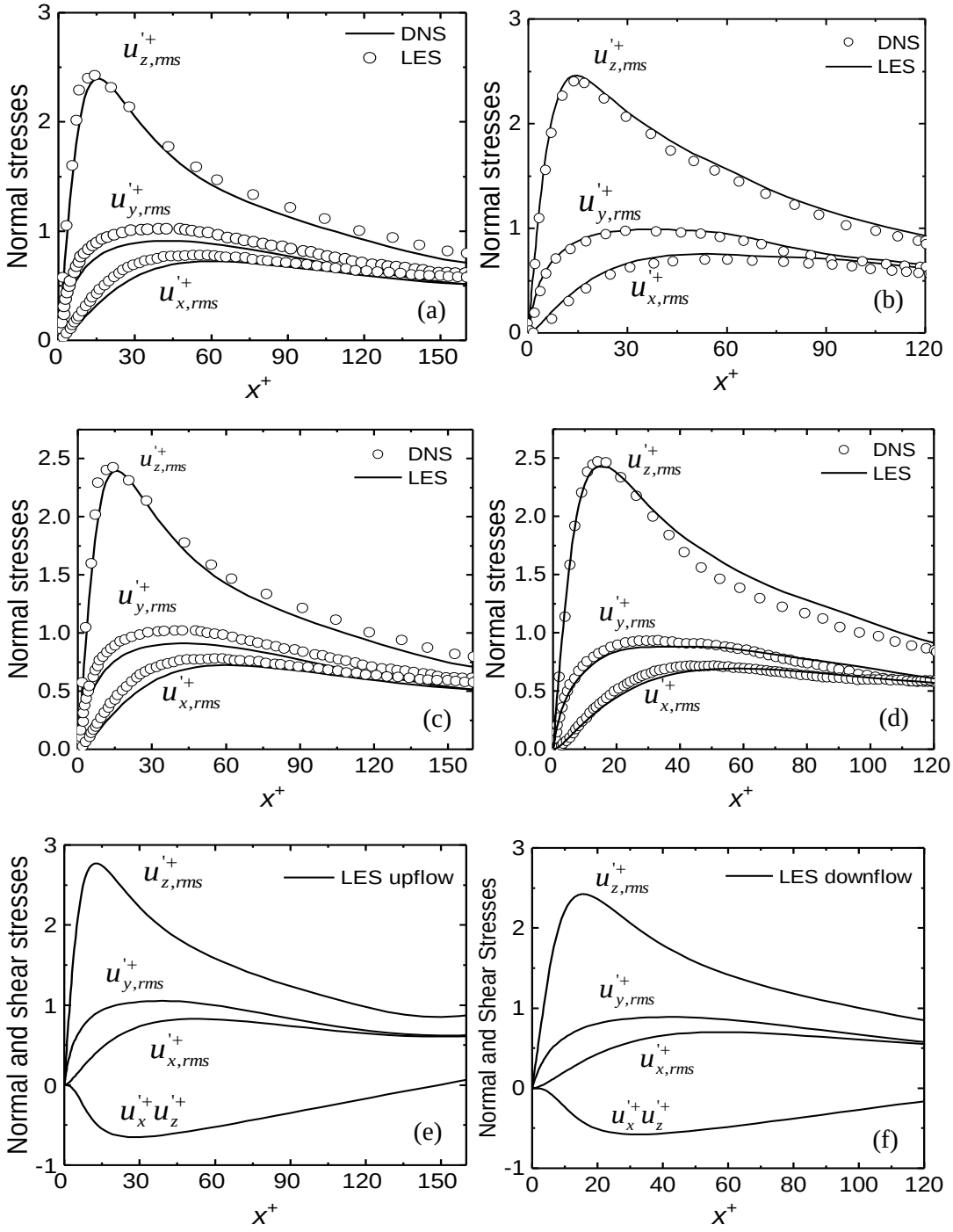

Figure 4.26 Rms of fluid velocity fluctuations and shear stress scaled with effective upflow and downflow shear velocity compared with DNS data: (a, b) $d_b = 110$ μm; (c, d) $d_b = 220$ μm; and (e, f) $d_b = 330$ μm.

The rms of the velocity fluctuations of the bubbles are given in Figure 4.27 for bubble sizes $d_b = 110\ \mu m$ and 220 μm, for which LES results are compared with those based on DNS and, for LES only, at $d_b = 330\ \mu m$, in both upflow and downflow configurations. Rms values are again scaled using the fluid-only, single-phase shear velocity. As is evident, in

upflow conditions the turbulent fluctuations are considerably higher than in the downflow case, and enhanced with respect to those of the continuous phase. In contrast, in downflow, the turbulence levels are decreased with respect to the single-phase flow.

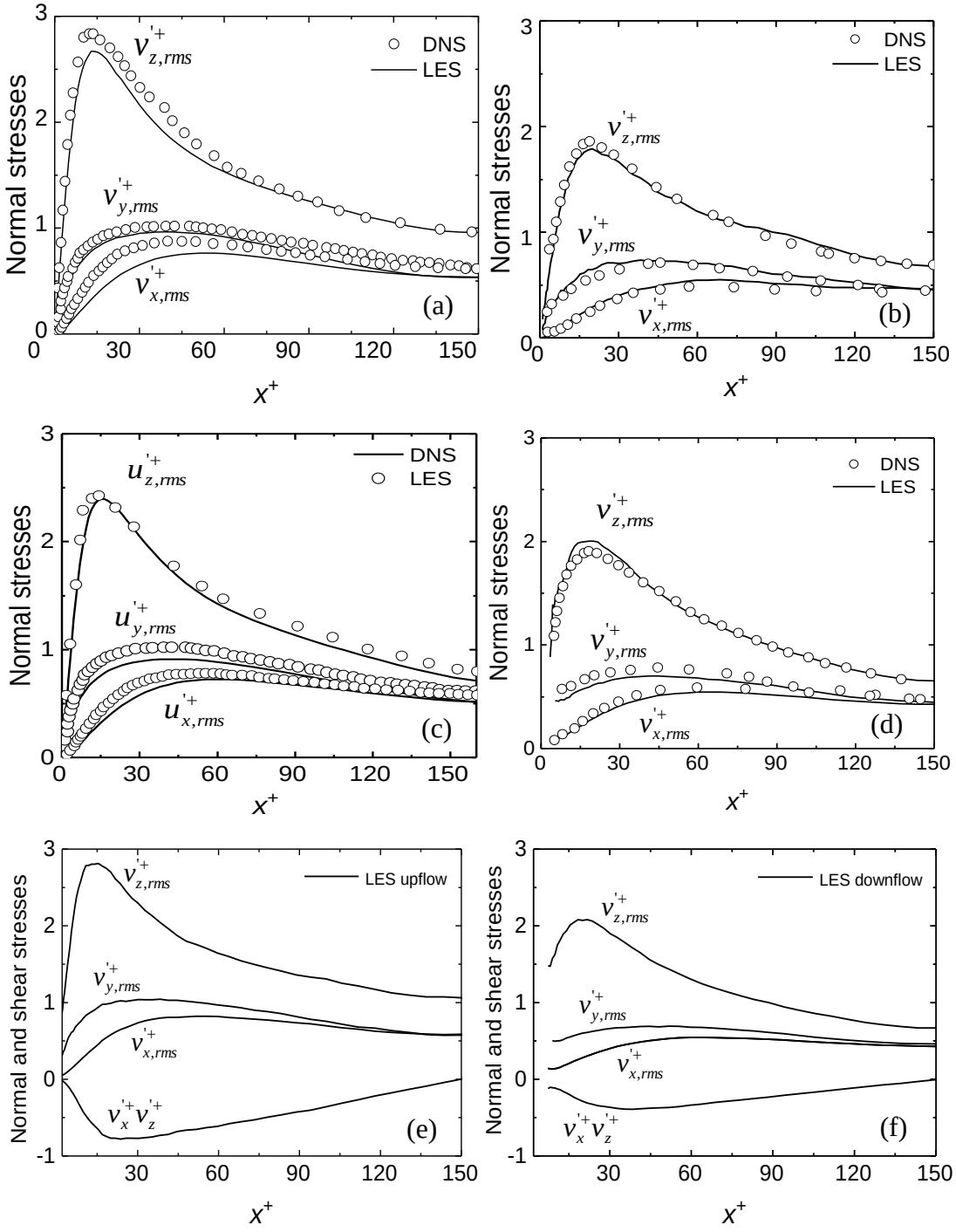

Figure 4.27 Rms of bubble velocity fluctuations and shear stresses scaled with effective upflow and downflow shear velocity compared with DNS data: (a, c, e) upflow; and (b, d, f) downflow. (a, b) $d_b = 110$ μm ; (c, d) $d_b = 220$ μm; and (e, f) $d_b = 330$ μm.

Overall, modifications in the turbulence level of the fluid, and the bubble phase turbulent statistics, are well-reproduced by the LES, with results in good agreement with the DNS-based solutions, and with similar trends found in the LES alone for a bubble diameter of $d_b = 330$ μm. It should be noted that, in downflow, and in particular for bubble diameters of $d_b = 220$ μm and 330 μm, the turbulence profiles are not defined in the very near-wall region. This is due, as will be discussed in more detail below, to the small number of bubbles in this region that arose due to bubble interaction with the fluid phase.

For microbubble flows, and for bubbly flows in general, of significant interest is how the distribution and concentration of the bubbles are affected by the fluid phase, and in particular by the levels of turbulence within the flow. As a consequence of their interaction with the continuous phase, bubbles may concentrate in specific regions of the flow and leave other areas depleted. In pipes and channels, it has been observed how small bubbles, that tend to remain spherical, concentrate near the wall in upflow and in the centre of the flow in downflow (Giusti et al., 2005; Wang and Maxey, 1993). This effect has been generally attributed to the action of the lift force, which pushes the bubbles perpendicularly to the direction of the main fluid motion, and in the direction of the negative, in upflow, and positive, in downflow, fluid velocity gradient.

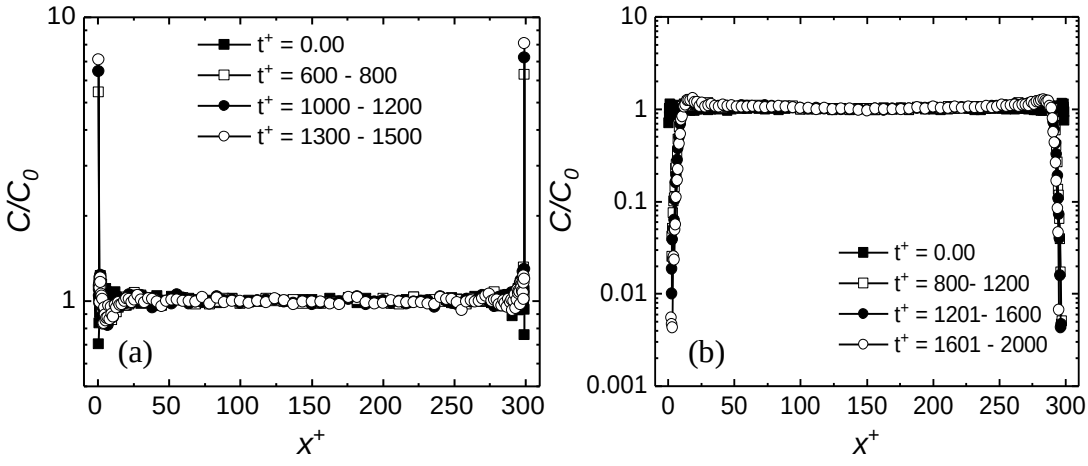

Figure 4.28 Time evolution of microbubble concentration in the wall normal direction for shear Reynolds number $Re_\tau = 150$ and $d_b = 110$ μm: (a) upflow; and (b) downflow.

The time evolution of bubble concentration in the wall-normal direction in both upflow and downflow is given in Figure 4.28, 4.29 and 4.30 for the three bubble sizes considered. In these figures, the full profile across the vertical channel domain, and details of the wall

region, are shown. To compute the bubble concentration, wall-normal direction space divisions were used. As previously, the average number of bubbles within each slab n_b was counted and divided by the volume of the slab, V, to obtain the local concentration $C = n_b/V$. The local concentration was then normalized by its initial value C_0. The ratio C/C_0 is therefore the normalized bubble number density and it is always greater than unity in flow regions were bubbles tend to segregate and smaller than unity in regions depleted of bubbles. The plots show concentration profiles averaged over consecutive time intervals to emphasize the evolution of the bubble concentration over time.

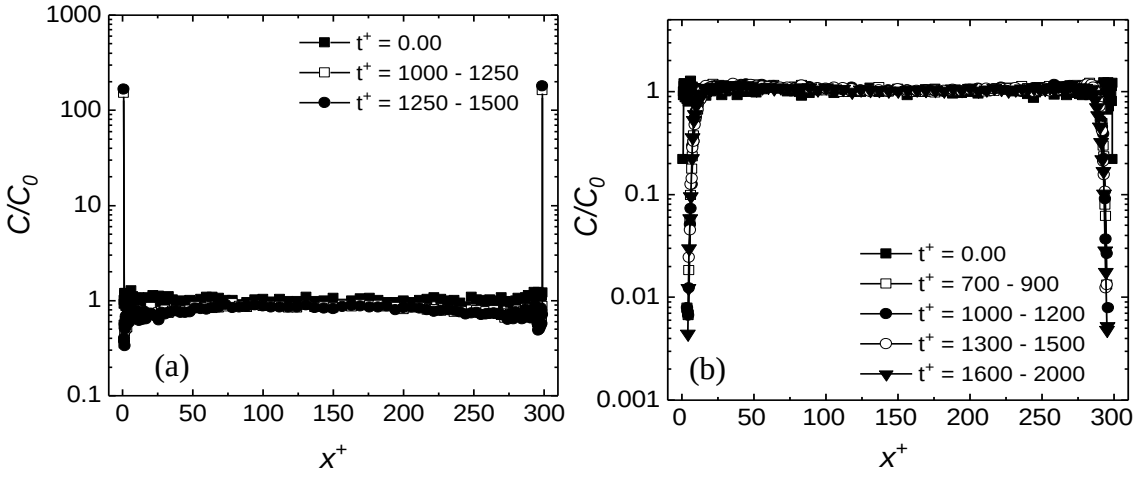

Figure 4.29 Time evolution of microbubble concentration in the wall normal direction for shear Reynolds number $Re_\tau = 150$ and $d_b = 220$ μm: (a) upflow; and (b) downflow.

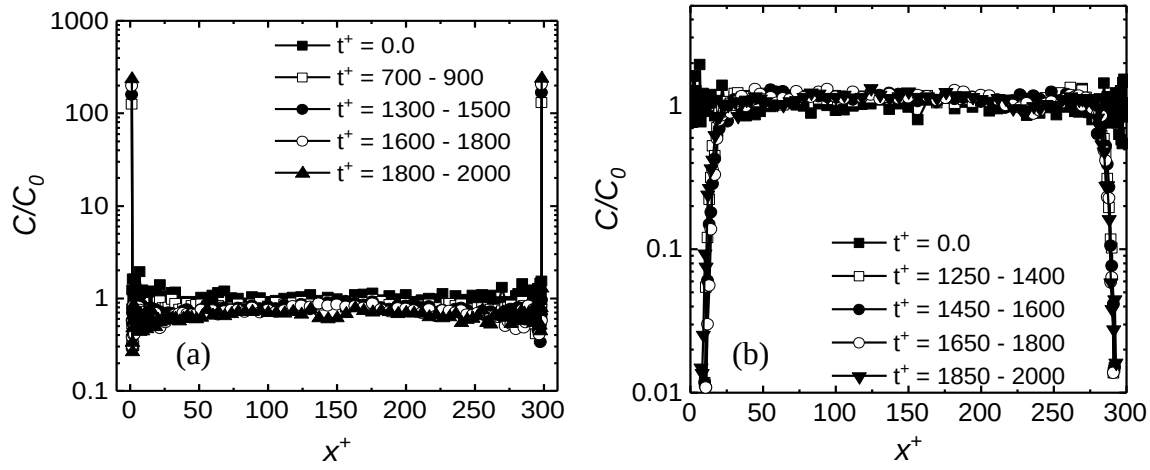

Figure 4.30 Time evolution of microbubble concentration in the wall normal direction for shear Reynolds number $Re_\tau = 150$ and $d_b = 330$ μm: (a) upflow; and (b) downflow.

The results show symmetric profiles of bubble concentration under all conditions. Starting from a uniform distribution at the beginning of a run, in upflow the bubbles tend to accumulate near the wall, generating a wall-peaked distribution. In contrast, in downflow the bubbles are moved from the near-wall region towards the channel centre, resulting, ultimately, in very low concentrations of bubbles close to the wall. These bubble-depleted regions near the walls are responsible for the problems noted above in relation to determining the turbulent bubble statistics due to the small bubble sample size when averaging. The concentration profiles obtained confirm findings from previous studies (Giusti et al., 2005; Shams et al., 2011; Serizawa et al., 1975; Hibiki et al., 2004). Examining the plots in more detail, it is observed that the increase or decrease of the concentration profiles near the wall, and the extent of the region affected, in particular for the downflow case, increases with bubble diameter (from Figure 4.28 to Figure 4.30). More specifically, the concentration in upflow increases from almost 10 for $d_b = 110\ \mu m$ in Figure 4.28, to more than 100 for $d_b = 330\ \mu m$ in Figure 4.30. In downflow, the depleted region ends to $x^+ \approx 10$ in Figure 4.28, and to $x^+ \approx 15$ in Figure 4.29, extending to values greater that $x^+ \approx 20$ in Figure 4.30. To investigate this phenomenon in more detail, and to further elucidate the mechanisms responsible for the qualitative shape of the concentration profiles obtained, the magnitude of each force acting on the bubbles in the wall normal direction is analysed in a later section.

4.3.2.2 Effect of flow Reynolds number

Since turbulence can significantly affect bubble behaviour, additional simulations at $Re_\tau = 590$, taking advantage of the less-demanding computational resources required by LES when compared to DNS, were also made to study the effect of the turbulence on the microbubble dispersion in vertical channels. For these simulations, the bubble diameter was chosen equal to 220 μm. Figure 4.31 shows fluid and bubble velocity and the turbulence statistics for both upflow and downflow, with bubble concentration profiles presented in Figure 4.32.

The distinctive differences between the results for upflow and downflow which were apparent at a shear Reynolds number $Re_\tau = 150$ are greatly reduced at $Re_\tau = 590$, with both profiles peaking at around 22.5 in the centre of the channel. For such flow, the effects

of the forces acting on the bubbles are partially over-ridden by the influence of turbulent dispersion. The normal and shear stresses for both flow configurations show no noticeable changes when compared to the single phase, as reflected in the results of Figure 4.31(b) and (Figure 4.31d). Mean bubble velocity profiles, which are provided in Figure 4.31(c), also show a reduced separation with respect to the same bubble diameter at shear Reynolds 150, with the upflow peaking at approximately 22.5 and the downflow at 20.5. As already noted, the relative velocity between the fluid and the bubbles is mostly a function of the bubble diameter, therefore it does not change significantly with an increase in the fluid velocity. Instead, the velocity magnitude of both the fluid and the bubbles, and the shear velocity, are greatly increased at the higher shear Reynolds number. Therefore, the importance of the relative velocity with respect to the velocity magnitude is significantly reduced and the magnitude of the separation between the upflow and downflow velocity profiles reduces.

Presented in Figure 4.32 is the microbubble concentration evolution in the wall-normal direction. The distribution profiles show a similar pattern to those obtained for the $Re_\tau = 150$ flow, with bubbles concentrating near the wall in upflow and moving towards the channel centre in downflow. However, the peak value of the bubble concentration in upflow, and the width and strength of the bubble depleted region in downflow, are both reduced because of the increased dispersion of the microbubbles due to the higher levels of turbulence. The predictions show symmetric profiles of bubble concentration under both conditions. Starting from a uniform distribution, therefore, in upflow the bubbles again tend to accumulate near the wall, generating a wall-peaked profile. In contrast, in downflow, the bubbles move away from the near-wall region. The magnitude of the Reynolds number is therefore seen to critically affect the impact of the flow on the microbubble concentration.

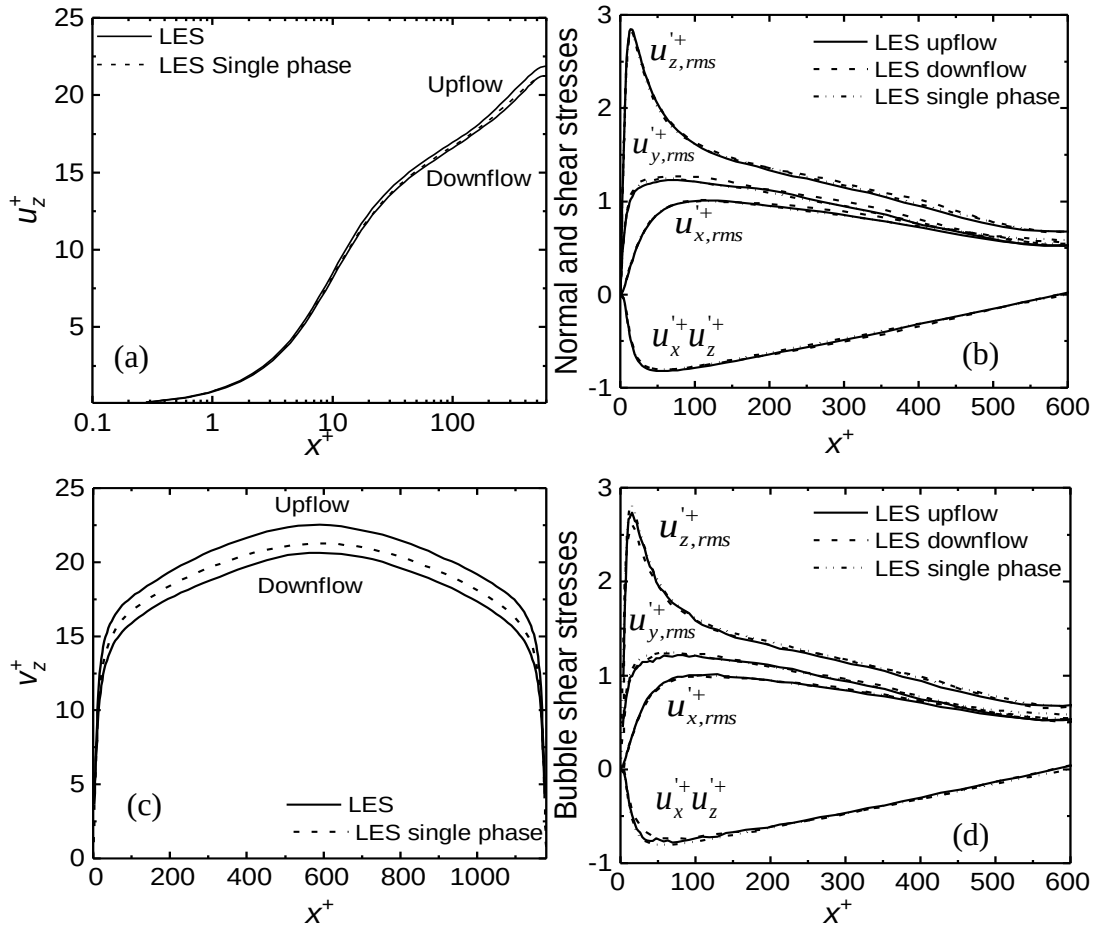

Figure 4.31 Fluid and bubble statistics for $Re_\tau = 590$ using bubble size $d_b = 220$ μm: (a) mean streamwise fluid velocity; (b) rms of fluid velocity fluctuations and shear stresses; (c) mean streamwise bubble velocity; and (d) rms of bubble velocity fluctuations and shear stresses.

To further establish the effects of Reynolds number, for bubble size $d_b = 220$ μm, concentration profiles at $t^+ = 1500$ at the two Reynolds numbers are compared for both upflow and downflow in Figure 4.33. In upflow, the peak near-wall concentration for the $Re_\tau = 150$ flow is greater than 100, while for the $Re_\tau = 590$ case the peak is reduced to approximately 10. The increase in the shear Reynolds number therefore reduces the value of the concentration peak at the wall in upflow, while the concentration near the wall remains fairly constant in downflow, although the extent of the depleted region reduces with increasing Reynolds number. These results confirm how higher levels of the turbulence enhance bubble mixing, generating more homogeneous concentration profiles and partially overriding the effect of the other forces acting on the bubbles.

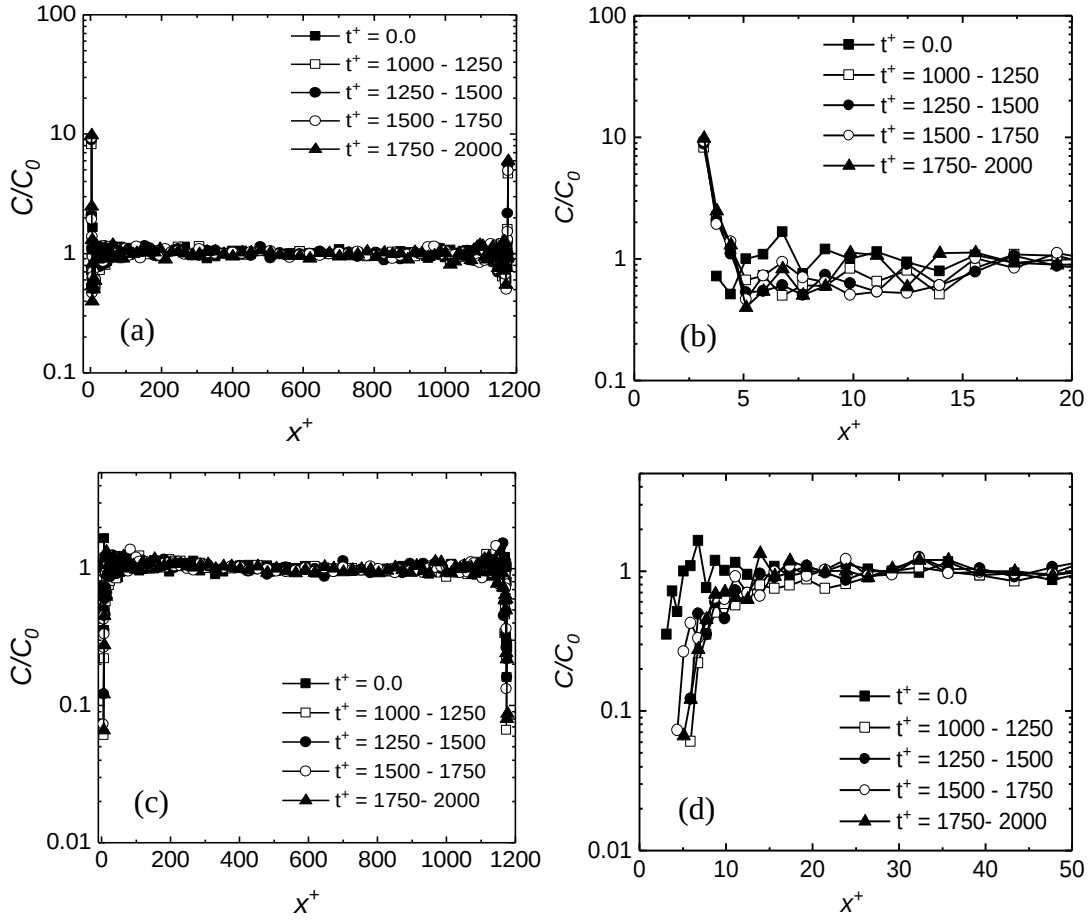

Figure 4.32 Time evolution of microbubble concentration for shear Reynolds number $Re_\tau = 590$ and $d_b = 220$ μm: (a, b) upflow; and (c, d) downflow.

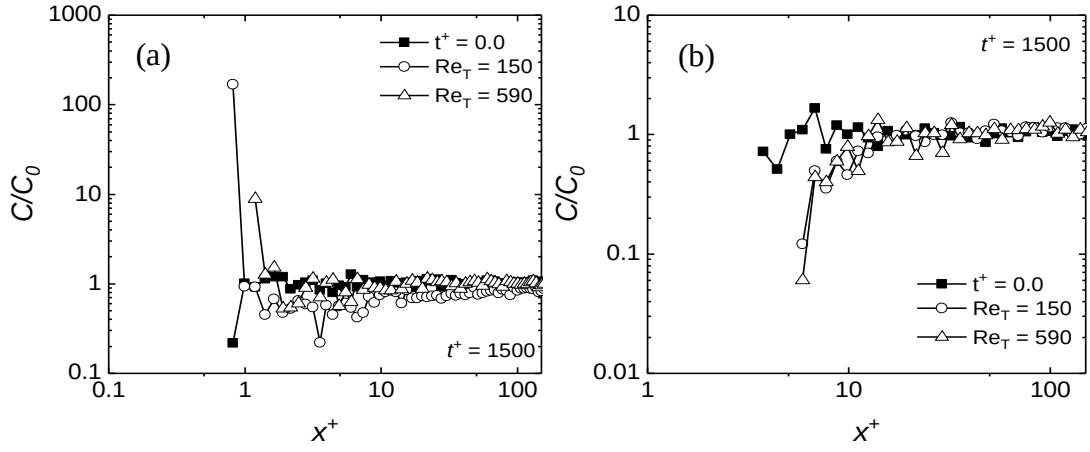

Figure 4.33 Instantaneous concentration profiles for the two reference Reynolds numbers at bubble size $d_b = 220$ μm: (a) upflow; and (b) downflow.

4.3.2.3 Force analysis in wall-normal direction

The forces acting on the bubbles (force per unit mass in N kg^{-1}) are shown for the $Re_\tau = 150$ vertical channel with upflow and downflow in Figure 4.34. Results are only provided for the d_b = 220 μm case as the other bubble sizes showed similar trends.

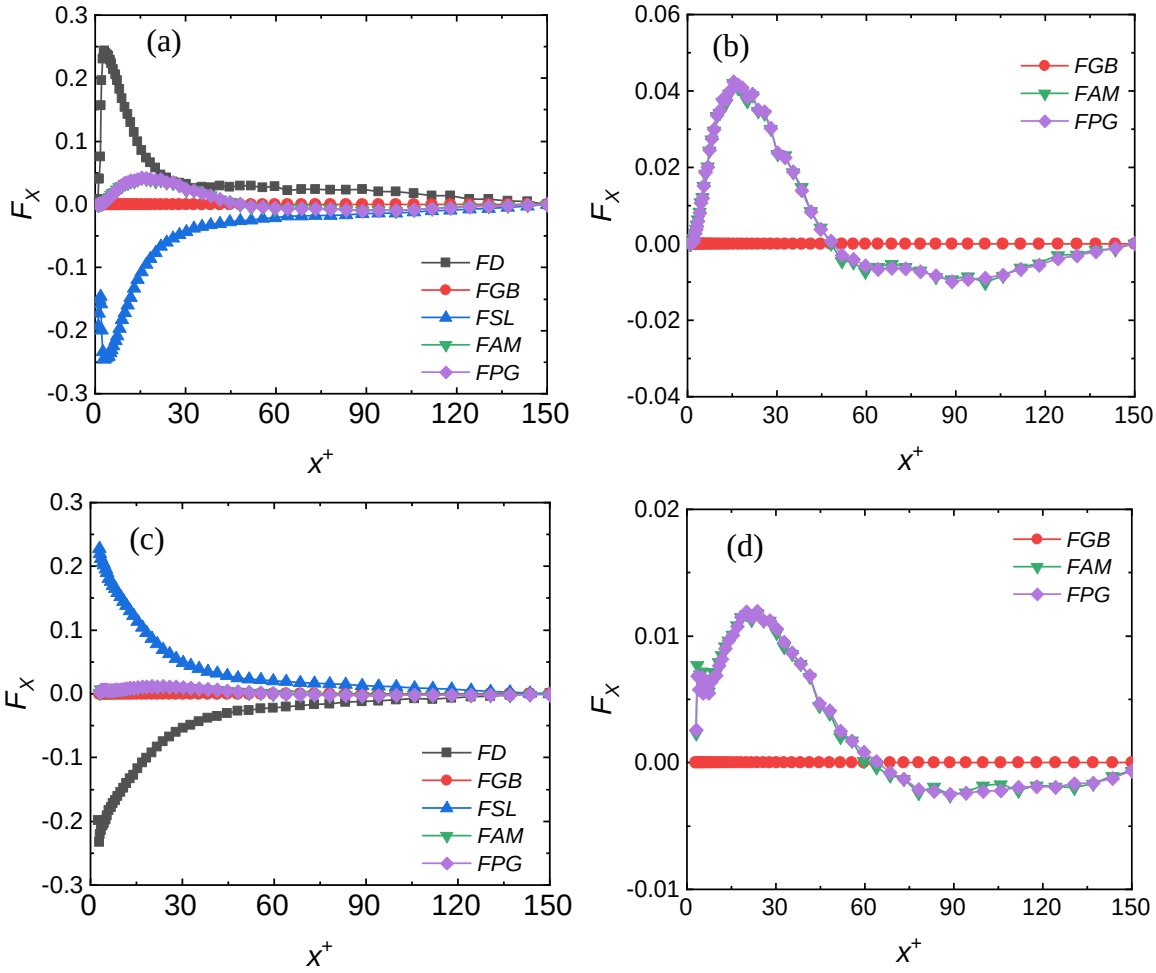

Figure 4.34 Forces acting in the wall normal direction for $d_b = 220$ μm bubbles at $Re_\tau = 150$: (a, b) upflow; and (c, d) downflow. (b) and (d) show an expanded scale to highlight the magnitude of the smaller forces (FD = drag force, FGB = gravity-buoyancy force, FSL = shear lift force, FAM = added mass force and FPG = pressure gradient force).

Overall, the drag and lift forces tend to be dominant, with the lift force pushing bubbles closer to the wall in upflow and towards the centre of the channel in downflow. This is confirmed by the change in sign in the lift force between the upflow to downflow cases. The lift force is also always opposed and balanced by the drag force. Clearly, both gravity and buoyancy do not play a significant role in the wall-normal direction, with their effect

acting in the vertical direction.There is also a not insignificant effect of the added mass and pressure gradient forces, although they are an order of magnitude less than the lift and drag forces. Both of these forces are directed towards the centre of the flow near the wall and, to a lesser extent, towards the wall in the centre of the channel. Therefore, in the near-wall region, they oppose the lift force in upflow and, in contrast, they support the lift force in downflow.

The role of the lift force is also addressed in Figure 4.35, where its magnitude for the three different bubble sizes is compared for the upflow and downflow cases. In both flow configurations, the magnitude of the lift force increases with bubble diameter, as expected. This is in agreement with earlier results (Figure 4.28, 4.29 and Figure 4.30) where, in the wall region, the concentration peak near the wall in upflow, and the extent of the bubble depleted region in downflow, were found to increase with the bubble diameter.

The forces are also plotted at $Re_\tau = 590$ in Figure 4.36. The lift force, which was dominant at $Re_\tau = 150$, is now significant only in the very near-wall region for both upflow and downflow. Instead, in the remainder of the channel, the pressure gradient and the added mass, which are more related to the fluid and bubble velocity magnitude, are now dominant. The effect of the high turbulence level is therefore to partially override the individual forces acting on the bubble, and the behaviour of the bubble is more related to the fluid turbulent flow. Due to the fact that increase in turbulence increase the vorticity of the flow, the added mass and pressure gradient forces, which are hydrodynamic forces, are observed to significantly increase in the regions where the vorticity is high.

An intermediate Reynolds number $Re_\tau = 300$ was again examined using the same bubble size and simulated under the same conditions as the other shear Reynolds number flows. The results are not shown here, but they demonstrated pressure gradient and added mass forces that were reduced in comparison to the $Re_\tau = 590$ case, but which were significantly greater than at $Re_\tau = 150$. The force analysis in Figure 4.36 agrees qualitatively with the findings of Spelt and Sangani (1997) who demonstrated that the bubble-phase pressure increases from zero to attain a maximum value, and then decreases, with distance away from the wall. To balance this, the drag force changes sign, which becomes the same as the lift in upflow and its opposite in downflow.

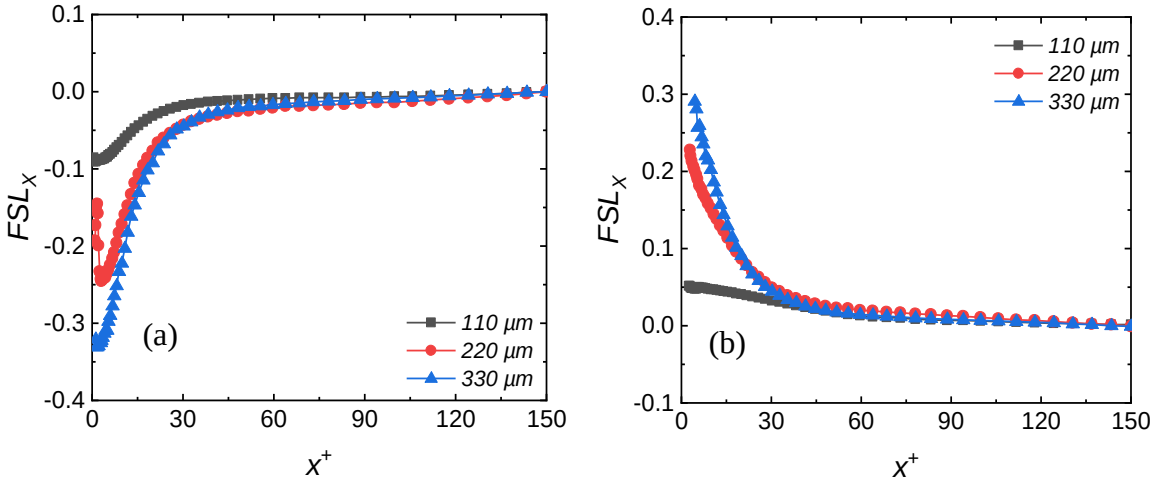

Figure 4.35 Lift force for the three microbubble sizes in the wall normal direction at $Re_\tau = 150$: (a) upflow; and (b) downflow.

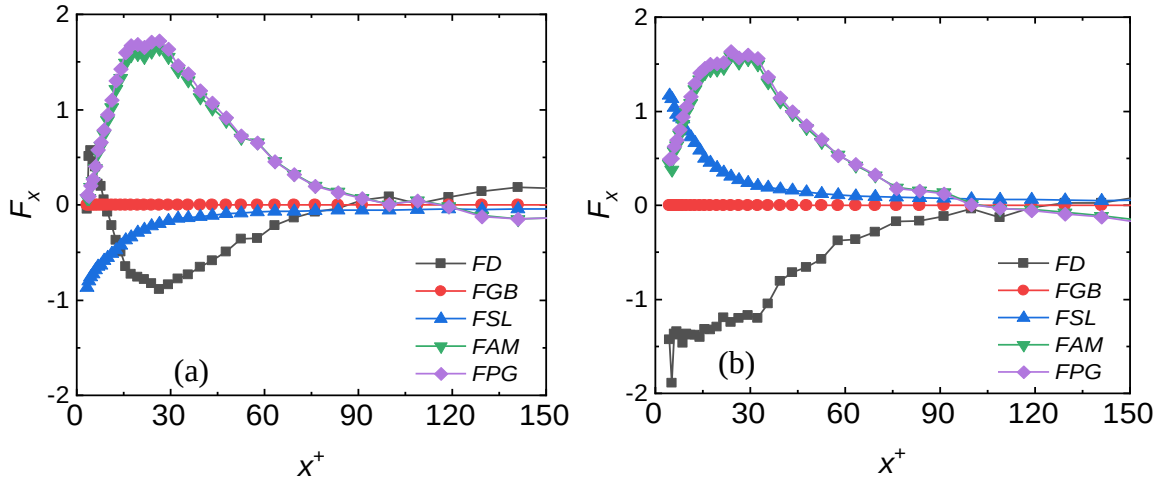

Figure 4.36 Forces acting on the bubbles in the wall normal direction at $Re_\tau = 590$ and for $d_b = 220$ μm: (a) upflow; and (b) downflow.

To recap, the behaviour of microbubbles in a vertical turbulent channel flow of water has been investigated using two-way coupled LES with a Lagrangian bubble tracker. Both upflow and downward flow configurations were simulated and the effect on the fluid of the presence of the bubbles was accounted. Two shear Reynolds number, $Re_\tau = 150$ and $Re_\tau = 590$, and three bubble sizes, $d_b = 110, 220, 330$ μm, were examined using a computational grid of 128 x 129 x 128 elements in the streamwise, wall normal and spanwise directions. LES results were first successfully compared with DNS data from

Molin et al. (2012) at $Re_\tau = 150$ and $d_b = 110$ and 220 μm, and LES simulations were later extend to a shear Reynolds $Re_\tau = 590$ and bubble diameter $d_b = 220$ μm.

The presence of the microbubbles strongly influences the fluid flow which becomes like a single-phase fluid flow at a higher mass flow rate in upflow and at a lower mass flow rate in downflow. Turbulence is enhanced in upflow and reduced in downflow, and velocity fluctuations for the bubbles are higher in upflow and lower in downflow with respect to the fluid phase. A different bubble distribution is found in the two flow configurations, with bubbles segregating at the wall in upflow and moving towards the centre of the channel in downflow. In the wall-normal direction, the lift force is the dominant force at a shear Reynolds $Re_\tau = 150$, and is responsible for the observed bubble distribution. The lift force is balanced by the drag force, and the pressure gradient and added mass forces are also significant.

LES results show good agreement when compared with available DNS-based predictions and, in view of its less demanding computational requirements, it was possible to extend the LES simulations to a higher shear Reynolds number flow, closer to those of industrial interest. At the same time, the accuracy obtained suggests that the level of detail reached with LES is sufficient to describe the fluid structures that affect the bubble behaviour. Overall, the LES and the Lagrangian bubble tracker can be used with confidence to predict these kinds of multiphase flows, with the potential to be applied to other flows of engineering interest.

4.4 Summary of One- and Two-way Coupled Results

LES coupled to a Lagrangian tracking approach was applied to investigate the dynamics of microbubbles in turbulent (horizontal, and vertical upflow and downflow) channel flows of water under one- and two-way coupling assumptions. First, the velocity statistics for single-phase and for solid particle-laden flows at Reynolds numbers Re_τ = 150, 300 and 590 were analysed and discussed. This work as perfomed by way of model validation. Bubbly flows under the one-way coupling assumption were then simluated in a vertical (upflow and downflow) channel at Re_τ = 150 and 590 with a bubble size of d_b = 220 μm. The motion of the bubbles was computed considering drag, gravity-buoyancy, pressure gradient and added mass forces, and both with and without the inclusion of the lift force

term to predict the effects of this force in the turbulent flows. Later, simulations were extended to the two-way coupling approach for horizontal and vertical channels (again in upflow and downflow), with bubbles of diameter 110, 220 and 330 μm and at Re_τ = 150 and 590.

The main findings of the work described in this chapter can be summarized as follows:

- Single-phase velocity and turbulence fields predicted with the LES at shear Reynolds numbers 150, 300 and 590 were in good agreement with the DNS predictions of Marchioli and Soldati (2007) and Marchioli et al. (2008). The same DNS databases for solid particle flows at the same Reynolds numbers were also successfully used to demonstrate the accuracy of the LPT in modelling dispersed multiphase turbulent flows.

- The coupled LES-LPT code was applied to the simulation of bubbly flows under the one-way coupling assumption in a vertical channel at Re_τ = 150. Substantial developments were introduced into the Lagrangian tracker to enable the model to predict the flow of gas bubbles in liquid flows. The DNS results of Giusti et al. (2005) for microbubbles of diameter d_b = 220 μm were then used to validate the LPT under these conditions, and good agreement was found.

- The impact of the lift force was found to be crucial in terms of the lateral migration and accumulation of bubbles. Bubbles evolve towards the channel walls in upflow and away from the walls in downflow. This was confirmed by comparison against zero-lift simulation results that did not show any lateral evolution.

- The lateral bubble evolution promoted by the lift force reduces with an increase in turbulence because of the competing effects of bubble motion and turbulent dispersion. Analysis which quantified these competing mechanisms is of benefit to the development of more accurate interfacial closures in computational approaches where they are entirely modelled, such as in the Eulerian-Eulerian two fluid model.

- The overall LES-LPT model was extended to two-way coupling to account for fluid-bubble intercations and feedback from the bubbles to the fluid phase. These additional capabilites allow the prediction of bubbly flows with increased bubble

volume fractions. Horizontal and vertical (upflow and downflow) channel flows at $Re_\tau = 150$ and 590, with bubbles of diameters $d_b = 110$, 220 and 330 μm, were predicted. The model was succesfully validated against DNS-based results at a Reynolds number of 150, and was then used to simulate flows at higher shear Reynolds numbers and bubble diameters, thereby extending the range of parameters studied beyond those already available in the literature.

- The presence of microbubbles in the flow field modulates the turbulence structure and the velocity field of the flow. In horizontal channel flow, an asymmetric flow profile develops due to bubble migration towards the upper channel wall. In the vertical channel flow, turbulence is increased in upflow and decreased in downflow after the injection of bubbles. Modulation of the turbulence increases with an increase in bubble size.

- Force analysis shows that the net gravity-buoyancy force dominates in the horizontal channel and it is counterbalanced by the drag force. In the vertical channel, the lift force was found to be the most dominant force, with its effect counterbalanced by drag. At shear Reynolds number 150, other forces were found insignificant. Consequently, bubbles migrate towards the upper channel wall in the horizontal chanel and, driven by the lift force, towards the walls in the vertical upflow and away from the walls in the vertical downflow.

- Turbulence only slightly affects bubble concentrations at a shear Reynolds number of 150. In contrast, at a shear Reynolds number $Re_\tau = 590$, the role of the turbulence is much more significant. In vertical channels, the lift force remains dominant only in the very near-wall region while, in the remainder of the channel, the pressure gradient and added mass forces become more influential and are balanced by the drag force. In the horizontal channel, the higher turbulence level partially supresses bubble accumulation near the upper wall.

- Insights into bubble behaviour available from these predictions, and the predicted impact of the bubbles on the fluid flow, improve our understanding of bubbly flows and provide necessary support to the development of improved Eulerian-Eulerian model closures, as already mentioned.

In this chapter, the overall model has been developed up to a two-way coupled capability. The model's accuracy has also been validated against DNS-based results available in the literature, and the model's capabilities demonstrated in a number of applications which extend the types of flow previously studied. In the following chapters, the present LES-LPT model is further developed to include a four-way coupled capability, accounting for bubble-bubble interactions, bubble coalescence and bubble breakup.

CHAPTER 5

FOUR-WAY COUPLED FLOWS WITH COALESCENCE

In this chapter, the model developed previously is extended to embody a four-way coupled approach by including the effects of bubble-bubble collisions and coalescence. Gas-liquid bubbly turbulent flows in horizontal channels, and downward and upward flows in vertical channels, are studied and the results compared with those obtained in the absence of gravity. Models and routines for bubble-bubble collision, based on a deterministic event-driven approach (Hoomans et al., 1996), and bubble coalescence, based on the film-drainage approach (Prince and Blanch, 1990; Tsouris and Tavlarides, 1994), are added to the overall LES-LPT model. In the flow, bubble-bubble collisions are first identified by the detection algorithm and, once a collision is detected, the likelihood of coalescence occurring is evaluated. A highly resolved LES with $129 \times 128 \times 128$ *computational nodes is used ensure the accuracy of the results. Two shear Reynolds numbers,* $Re_\tau = 150$ *and* 590*, and three bubble sizes,* $d_b = 110, 220$ *and* 330 μm*, are considered. Results are presented by comparing predictions obtained from the four-way coupled simulations with those obtained from the single-phase flow simulations, reported in a previous chapter. The key features of bubble coalescence in the flows examined, including the distribution of bubble collisions, coalescence efficiencies and the size of bubbles formed after coalescence, are presented. The effect of collisions and coalescences on the behaviour of the continuous phase flow, examined through profiles of the flow and turbulence fields, and the bubble wall-normal forces and their number density distribution, are also discussed.*

5.1 Bubble Coalescence in Horizontal Channel Flow

In this section, bubbly flow with coalescence is studied using large eddy simulation coupled to Lagrangian bubble tracking in a horizontal channel flow. The same conditions as applied in the previous section are employed, namely a water flow (density $\rho = 1000\ \mathrm{kgm^{-3}}$, kinematic viscosity $\nu = 10^{-6}\ \mathrm{m^2 s^{-1}}$ and surface tension $\sigma = 7.2 \times 10^{-2}\mathrm{Nm^{-1}}$) with air bubbles at shear Reynolds numbers 150 and 590. The overall properties of the flows are summarised in Table 5.1. Figure 5.1 shows a schematic of the channel configuration, in which periodic boundary conditions are applied in the

streamwise (z) and spanwise (y) directions, with the x-axis being in the wall-normal direction. The flow is driven using an imposed streawise fixed pressure gradient.

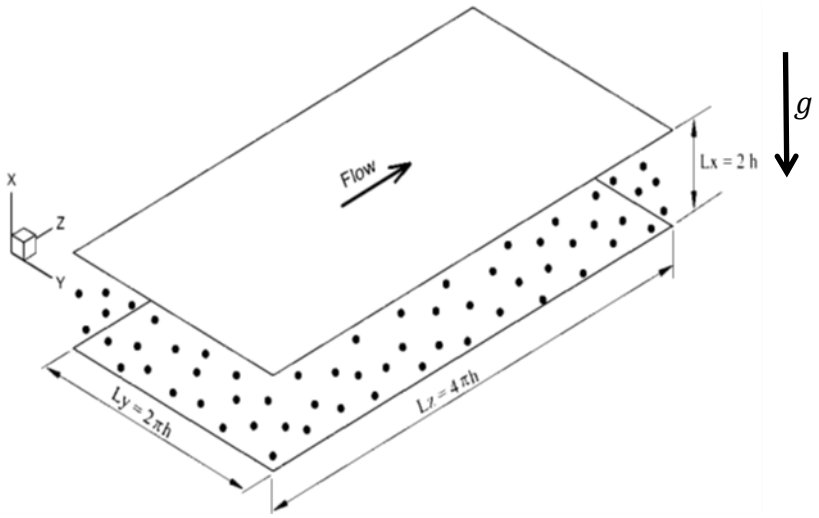

Figure 5.1 Horizontal channel configuration.

Bubbles were injected uniformly into the channel flow. In the flow, bubble-bubble collisions were identified by the detection algorithm and, once a collision was detected, the occurrence of coalescence was evaluated from the coalescence model based on the film-drainage theory, described in Section 3.5.2. This section of the study is chiefly aimed at investigating the effects of gravity on microbubble mixing, collision and subsequent events leading to coalescence, or collisions without coalescence.

Table 5.1 Computational parameters for the four-way coupled simulations.

Computational parameters		
Re_τ	150	590
Re_b	2272	11033
u_τ (ms^{-1})	7.5×10^{-3}	2.92×10^{-2}
u_b (ms^{-1})	0.1136	0.5517
n_b (-)	226550	56647
d_b (μm)	220	220

Presented in Figure 5.2 are the number of collision and coalescence events, and the number of bubbles of different sizes that are formed in the flow, as a function of time. Results for the four-way coupled simulations at a shear Reynolds number $Re_\tau = 150$ and bubble size $d_b = 220$ μm in a horizontal channel are compared with the same flow conditions without gravity. Figure 5.2(a, b) shows the number of bubble collisions, coalescences, and collisions without coalescence, while Figure 5.2(c, d) gives the number of bubbles of various sizes formed after coalescence. In Figure 5.2(a), all collisions result in coalescence until $t^+ = 40$, where the first collisions without coalescence are detected. At $t^+ = 100$, the number of collisions without coalescence recorded is around 12,000. In the no gravity test case, in contrast, at the same simulation time all collisions have resulted in coalescence. It was observed that the inclusion of the buoyancy-gravity force term in the bubble equation of motion introduced additional velocity fluctuations into the liquid turbulence which in turn enhanced bubble-bubble collisions, coalescences and collisions without coalescence. This is evident by comparing the results for flows with and without gravity in Figure 5.2 (a, b).

In Figure 5.2(c, d), the legends (1), (2), (3), (4), (5), etc., represent bubbles with a volume equal to one, two, three, four, five, etc., times that of the primary bubbles, for flows with and without gravity included. The total number of collisions continuously increases as the simulation progresses in both cases, with virtually all collision events resulting in coalescence in the zero-gravity case, as noted above. In the case with gravity, the number of collisions and coalescences is much higher, since the bubbles migrate towards the upper wall where turbulence levels are high (considered further below). In contrast, in the zero-gravity flow, the bubble distribution remains relatively uniform and a larger number of bubbles remain in regions of lower turbulence away from the walls.

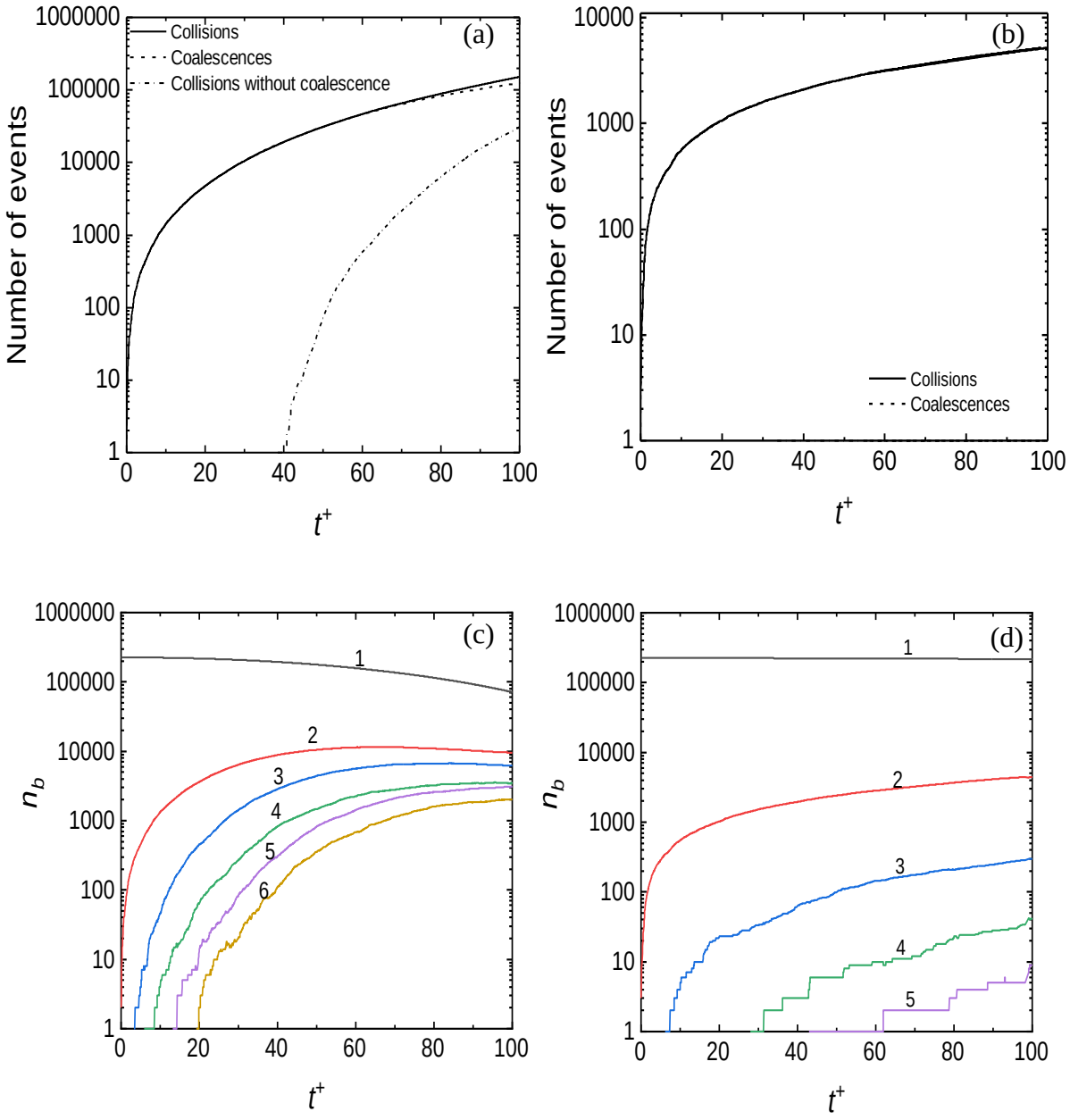

Figure 5.2 Collision and coalescence events (a, b) and number of bubbles of different sizes (c, d) in four-way coupled simulations at shear Reynolds number $Re_\tau = 150$ and bubble size 220 μm: (a, c) horizontal channel with gravity; and (b, d) channel with no gravity.

In Figure 5.3, the number density of bubble collisions and coalescences across the horizontal channel is presented. Calculation of the number density of the bubbles was performed by dividing the flow domain into 16 equally spaced bins in the wall-normal direction. In Figure 5.3(c) and (d), the instantaneous number of bubbles spatially averaged in each slab at $t^+ = 100$ for both test cases is presented. Figure 5.3(c) clearly shows how buoyancy pushes bubbles towards the upper channel wall, with no bubbles remaining in the bottom section of the channel. Instead, in Figure 5.3(d), the bubble distribution remains almost uniform due to the absence of gravity effects. In Figure 5.3(a) and (b), it is observed that the greatest number of bubble-bubble collisions is found near the channel walls. Approximately 100,000 collisions were recorded at the upper channel wall, and about 110 collisions near the lower wall, in the horizontal channel flow with gravity effects included. Where no gravity is considered (Figure 5.4(b)), the number of collisions recorded at both channel walls is quite similar at around 5000-5500, since fewer bubbles are present in the wall regions.

Not all collisions in the case with gravity result in coalescence, as is evident from the results of Figure 5.3(a). Since most bubbles are found near the upper wall (Figure 5.4(a)), this leads to an increase in turbulence levels in that region which, even if only small, increases the turbulence fluctuations in that region. This is turn reduces the contact time between bubbles during collisions which, therefore, leads to a reduction in the coalescence efficiency. Without gravity, there is a uniform bubble distribution (Figure 5.4(b)) which leads to a lower number of bubbles in the wall regions which do not induce the same enhancement in the turbulence field of the continuous phase, and hence all collisions lead to coalescence.

The coalescence efficiency is given in Figure 5.5. This efficiency is highest in the centre of the channel where turbulence levels are low, even for the channel flow with gravity effects included (Figure 5.5(a)), where the efficiency reaches almost 100%. Closer to the upper wall, this efficiency reduces, as previously discussed.

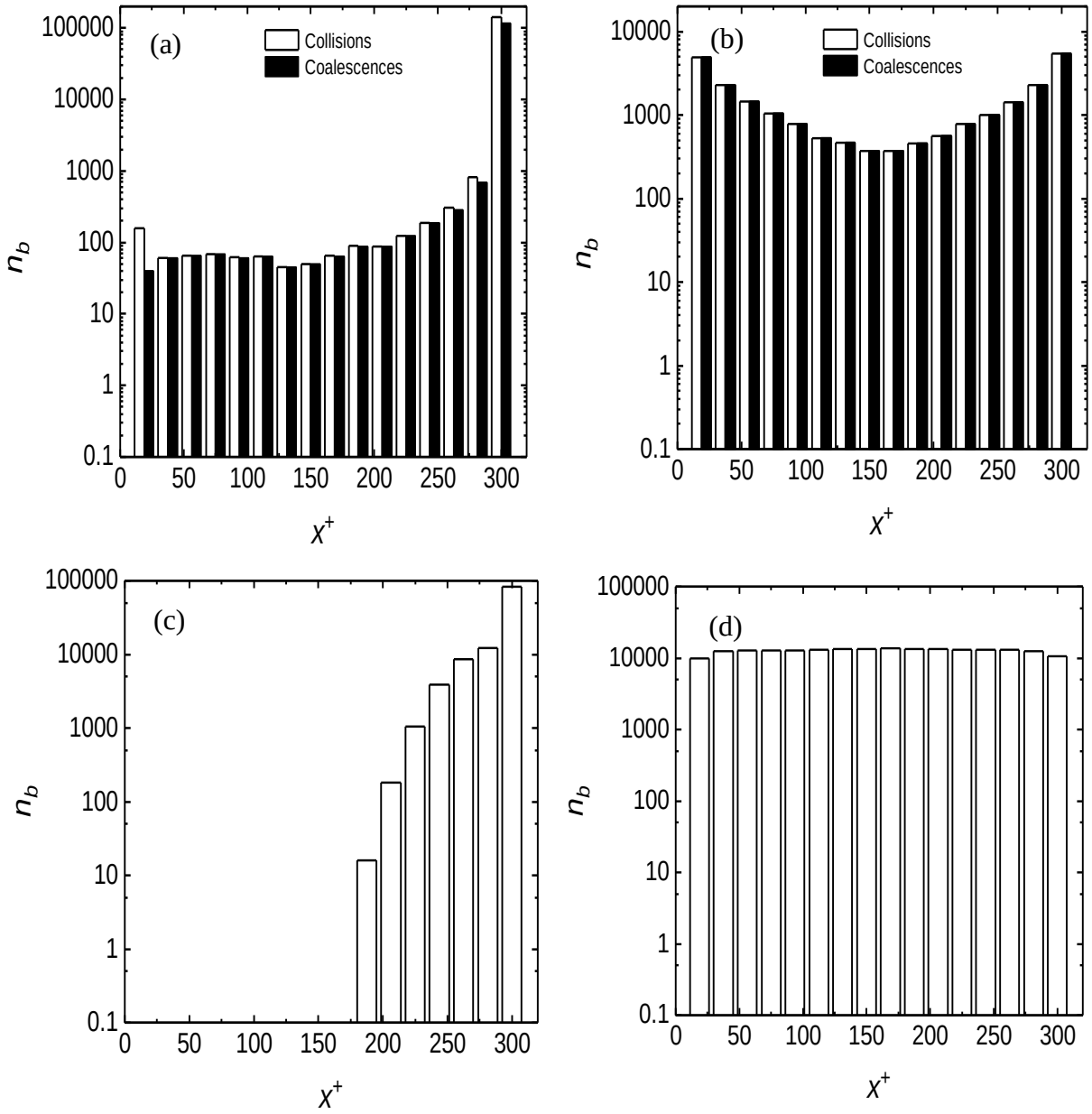

Figure 5.3 Distribution of bubbles across the channel at $t^+ = 100$ for both test cases: (a, b) number of bubble collisions and coalescences; and (c, d) number of bubbles (of any size) within the channel. (a, c) with gravity; and (b), (d) no gravity.

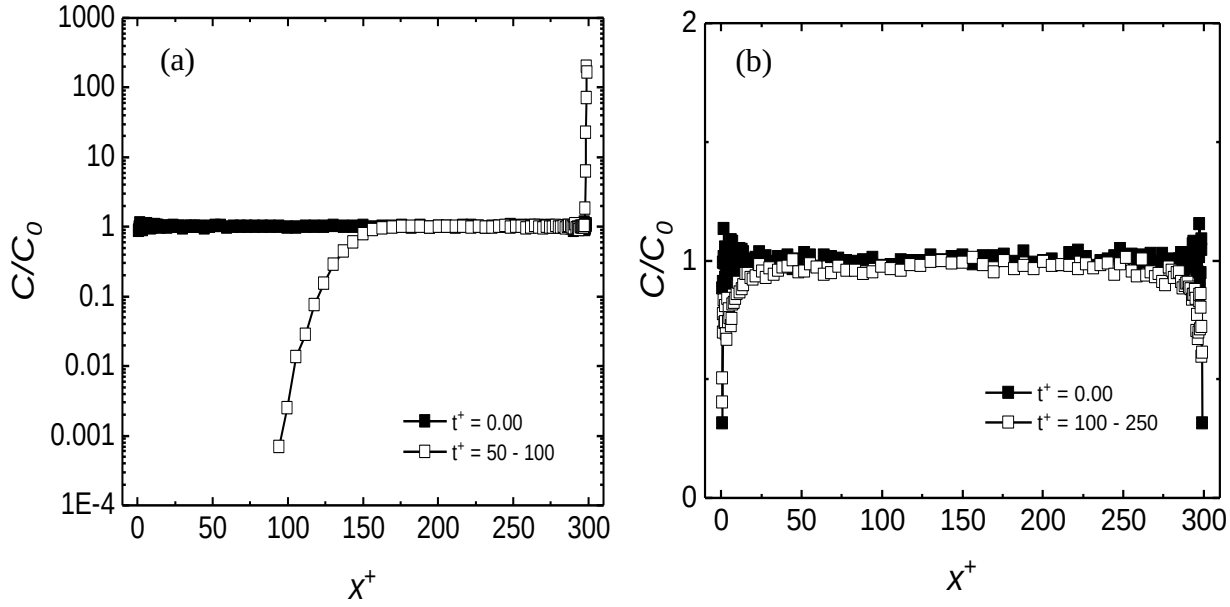

Figure 5.4 Microbubble wall-normal concentration profiles at shear Reynolds number $Re_\tau = 150$: (a) with gravity; and (b) no gravity. Upper wall is at $x^+ = 300$.

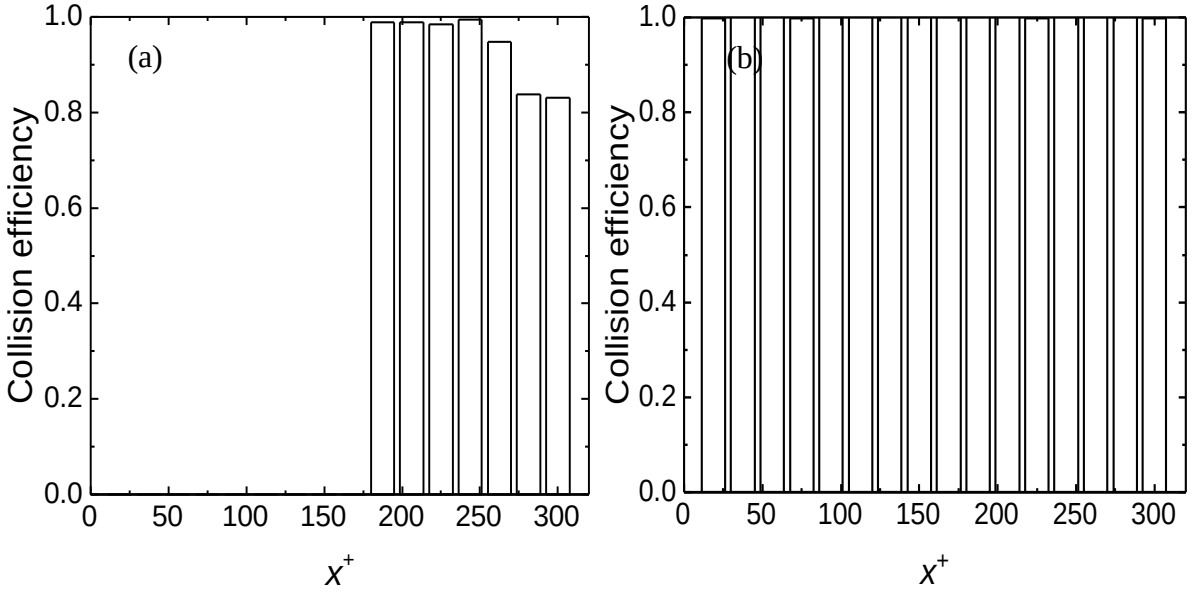

Figure 5.5 Collision efficiency at $t^+ = 100$: (a) with gravity; and (b) no gravity.

5.1.1 Reynolds Number Effect in Horizontal Channel Flow

Results for the same two test cases at the higher Reynolds number $Re_\tau = 590$ are presented in this section. At this higher turbulence level, a larger number of collisions without coalescence are found in the horizontal channel with gravity effects included (about 5000, Figure 5.6(a)), and some are also recorded in the no gravity flow case (about 40, Figure 5.6(b)). Similarly to what was observed at the lower Reynolds, the number of collisions and coalescences (11,000 and 10,000, Figure 5.6(a)) is higher with gravity than for the zero gravity flow (around 2,600 bubble collisions, Figure 5.6(b)). With regards to the different sizes of bubbles formed, more multi-sized bubbles are formed in the with gravity case when compared the flow with no gravity. Multi-sized bubbles of up to six primary bubbles are formed with gravity, as noted in Figure 5.6(c), whereas in the zero-gravity case (Figure 5.6(d)) the largest bubble size consists of five primary bubbles.

The bubble distribution across the horizontal channel shows the same qualititative trends as for the $Re_\tau = 150$ flow. Buoyancy pushes the bubbles towards the upper wall in the case with gravity (Figure 5.7(c) and Figure 5.8(a)), whilst an approximately symmetric profile is recorded in the zero gravity flow (Figure 5.7(d) and Figure 5.8(b)). However, in this case the higher levels of turbulence limit bubble migration and accumulation near the upper wall for the with gravity case. In Figure 5.4(a), therefore, at $t^+ = 50$ - 100, approximately 70% of the bubbles have already moved towards the upper channel wall. In contrast, in Figure 5.8(a), even at $t^+ = 500$ – 700 bubbles can still be found in the bottom half of the channel.

The collision efficiency is given in Figure 5.9, with the results showing again that the collision efficiency is higher in the centre of the channel than in the near wall regions. In the channel flow with gravity (Figure 5.9(a)), the collision efficiency is reduced near the upper wall with respect to that seen for the shear Reynolds number 150 case (Figure 5.5(a)). Also, an efficiency lower than 100% is found near the walls in the no gravity case due to the higher levels of turbulence in these regions. As for the lower turbulence case, the efficiency remains at approximately 100% in the centre of the channel in both test cases.

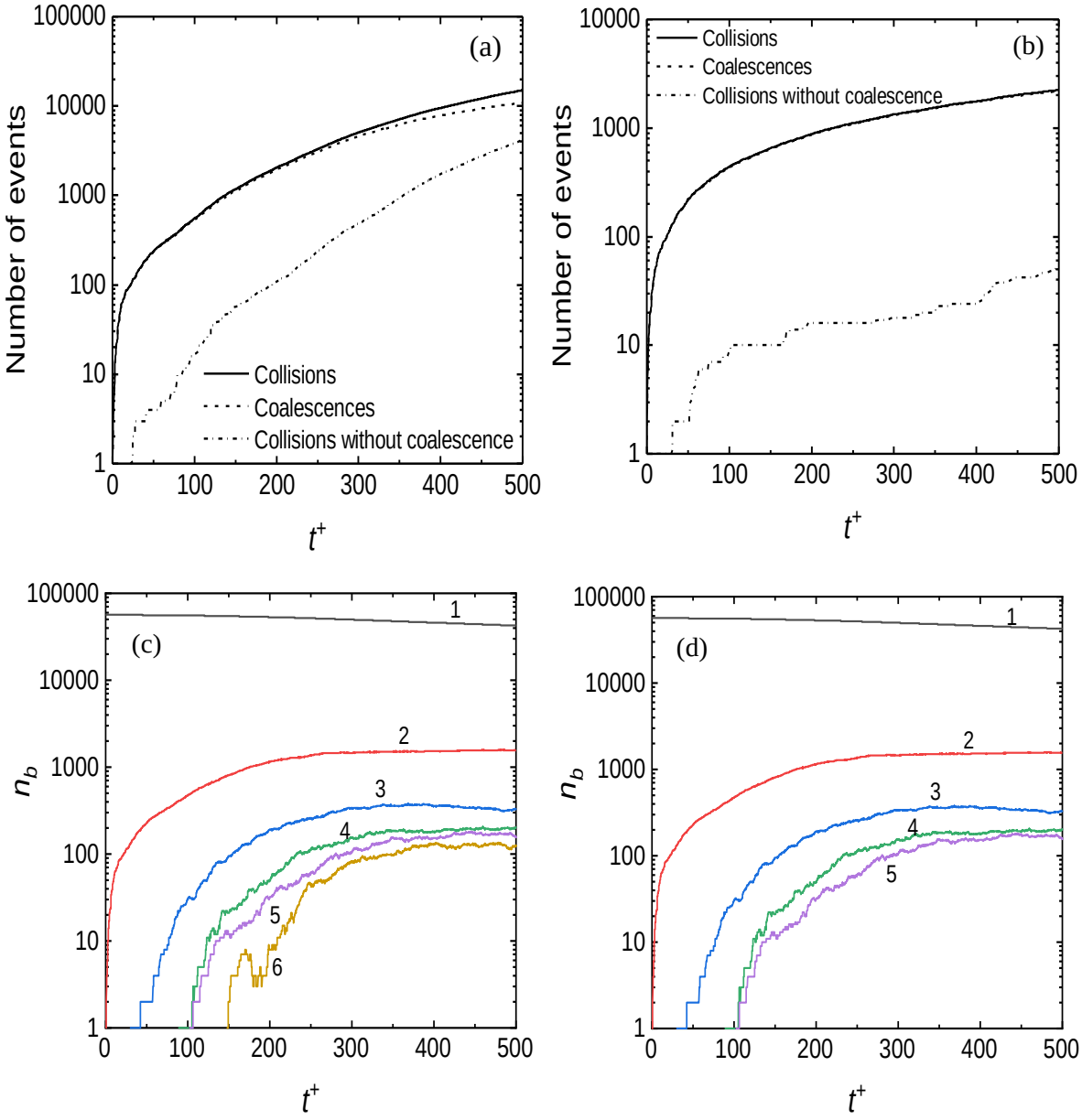

Figure 5.6 Collision and coalescence events (a, b) and number of bubbles of different sizes (c, d) in four-way coupled simulations at shear Reynolds number $Re_\tau = 590$ and bubble size 220 μm: (a, c) horizontal channel with gravity; and (b, d) channel with no gravity.

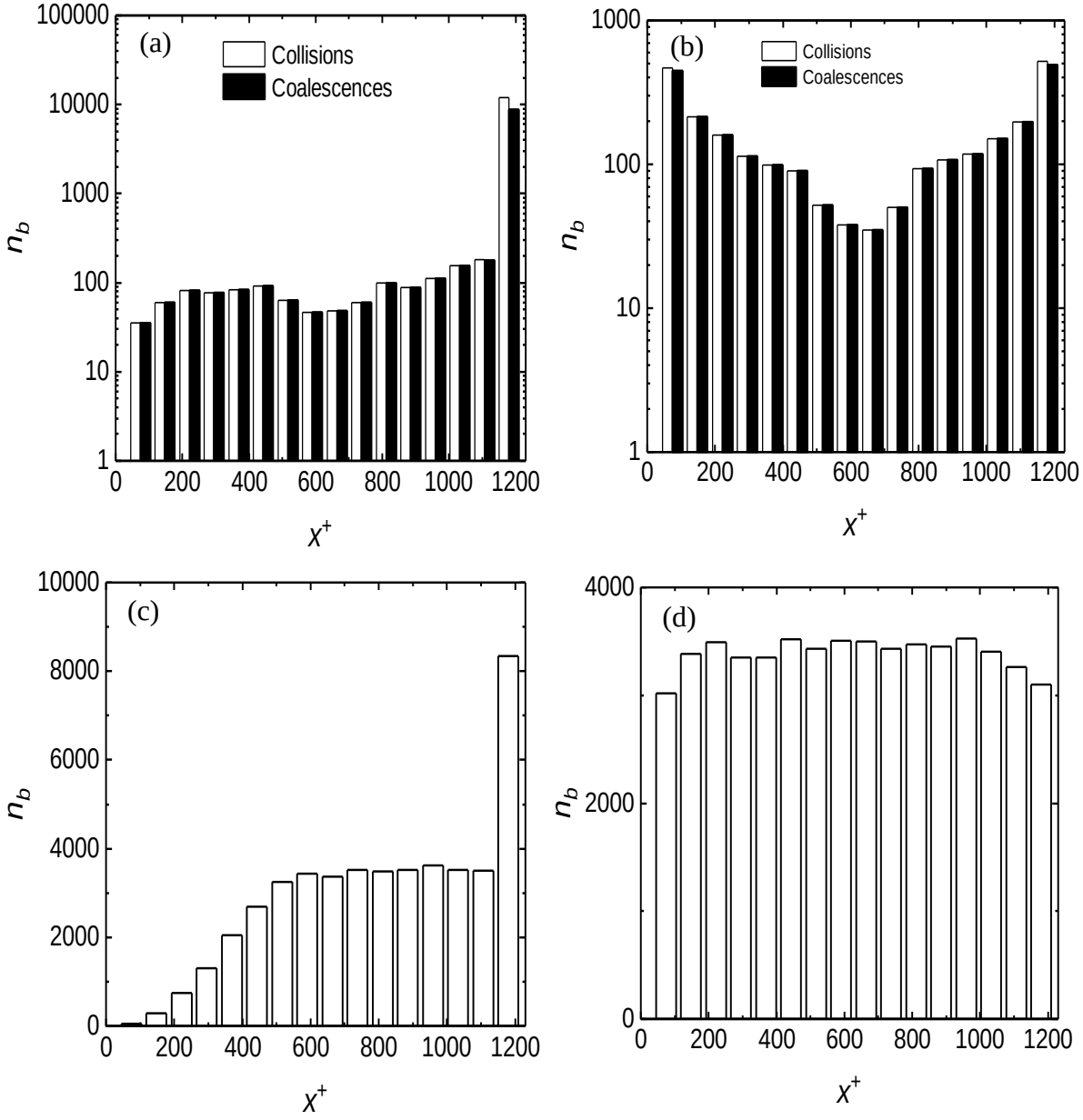

Figure 5.7 Distribution of bubbles across the channel at $t^+ = 500$ for both test cases: (a, b) number of bubble collisions and coalescences; and (c, d) number of bubbles (of any size) within the channel. (a, c) with gravity; and (b, d) no gravity.

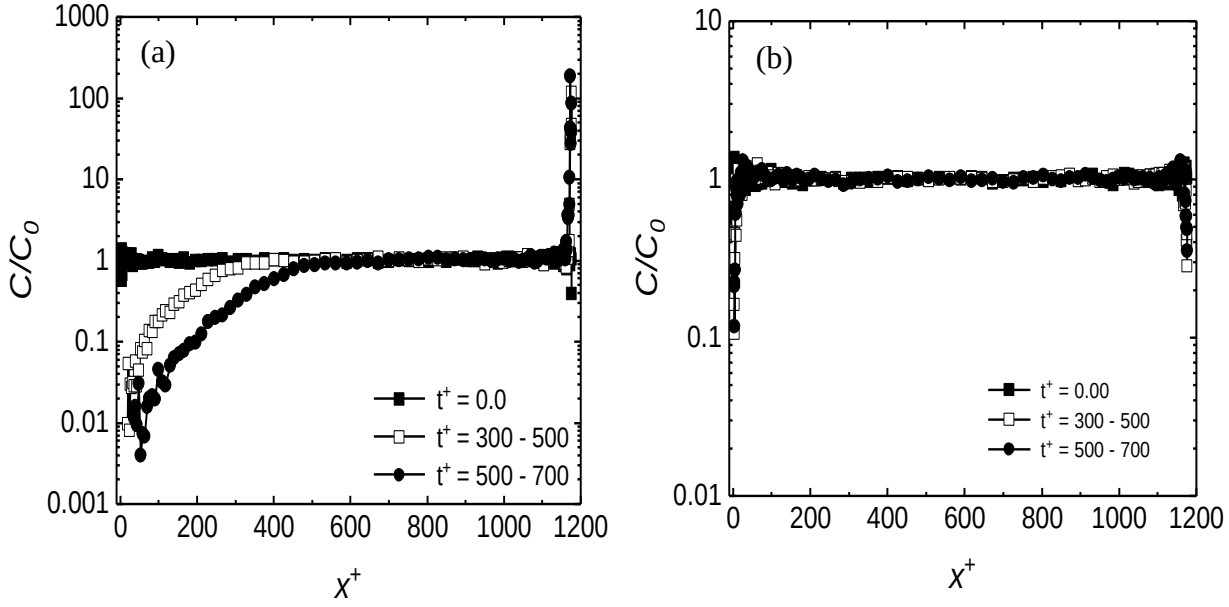

Figure 5.8 Microbubble wall-normal concentration profiles at shear Reynolds number $Re_\tau = 590$: (a) with gravity; and (b) no gravity. Upper wall is at $x^+ = 1200$.

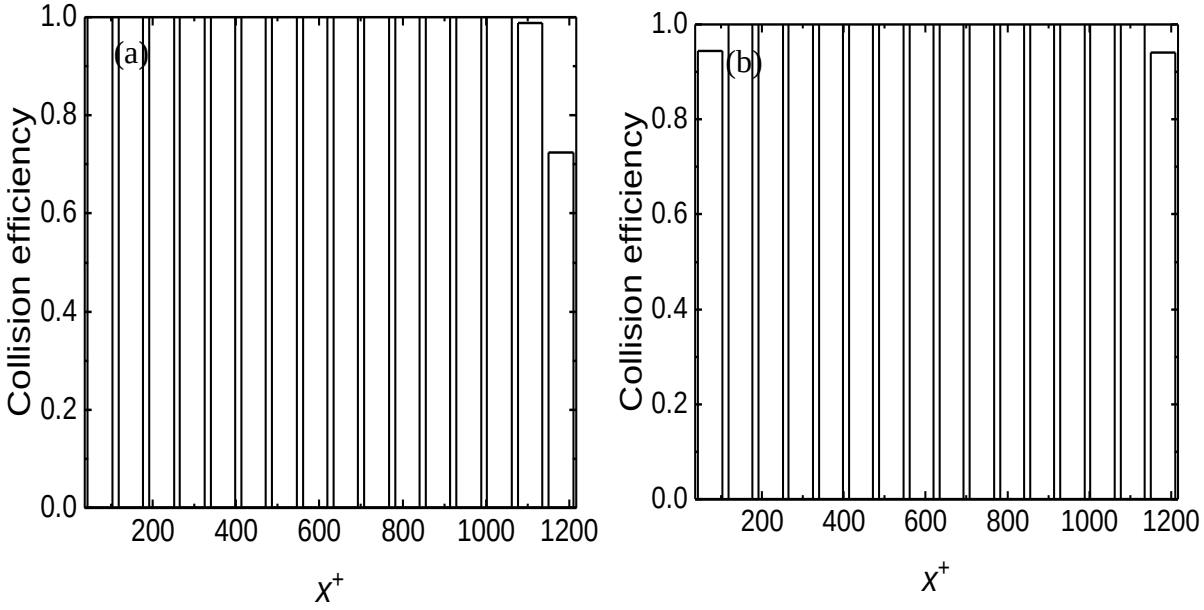

Figure 5.9 Collision efficiency at $t^+ = 500$: (a) with gravity; and (b) no gravity.

Comparing the results of Figure 5.2(a) with those of Figure 5.6(a), although the same volume concentration of bubbles and initial conditions were applied, the results are significantly different. In Figure 5.2, at the lower Reynolds number, the number of bubble coalescences is approximately ten times larger than for the higher turbulence case in Figure 5.6(a), despite the greater simulation time in the latter case. This demonstrates that at the lower Reynolds number, the levels of turbulence are sufficiently lower to allow increased bubble-bubble contact times during collisions, as compared to at the higher Reynolds number, which in turn increases the number of bubble coalescences, as the film drainage model of coalescence requires. The effect of buoyancy, which enhances bubble migration towards the upper wall, is relatively strong felt in the low Reynolds number case, whereas in the higher Reynolds number flow, the fluid turbulence to some extent overrides the buoyancy effect since, even at longer times, bubbles are still found in the centre of the channel. Lower Reynolds number flows are therefore best suited for drag reduction in marine vessel transportation (Pang et al., 2014), whilst higher Reynolds numbers are more effective in the transportation of crude and other petroleum products, as well as flow for assurance from production sites to storage sites (Hassan, 2014; Martínez-Palou et al., 2011).

5.2 Bubble Coalescence in Vertical Upward and Downward Channel Flows

The results of simulations using the LES-LPT code in vertical channels are presented in this section, starting with the shear Reynolds number Re_τ = 150 flow. First, the changes induced by the presence of microbubbles on the liquid–phase flow field are analysed. Presented in Figure 5.10 are the velocity statistics for the four-way coupled fluid flow for the three bubble sizes considered in comparison with the single-phase fluid flow for the upflow case. The fluid mean streamwise velocity profiles are shown in Figure 5.10 (a, c, e). It is clear that the four-way coupled fluid flow is enhanced by the presence of the bubbles, with the peak mean velocity increased above that of the single-phase flow. In Figure 5.10 (b, d, f), the rms of velocity fluctuations in the streamwise, spanwise and wall normal directions, in addition to the shear stress, are given. All the normal stresses and the shear stress are increased with respect to the single-phase flow in all cases, confirming the DNS results of Elghobashi (1994) who studies the modulation of the

continuous phase turbulence induced by solid particles of different Stokes numbers.

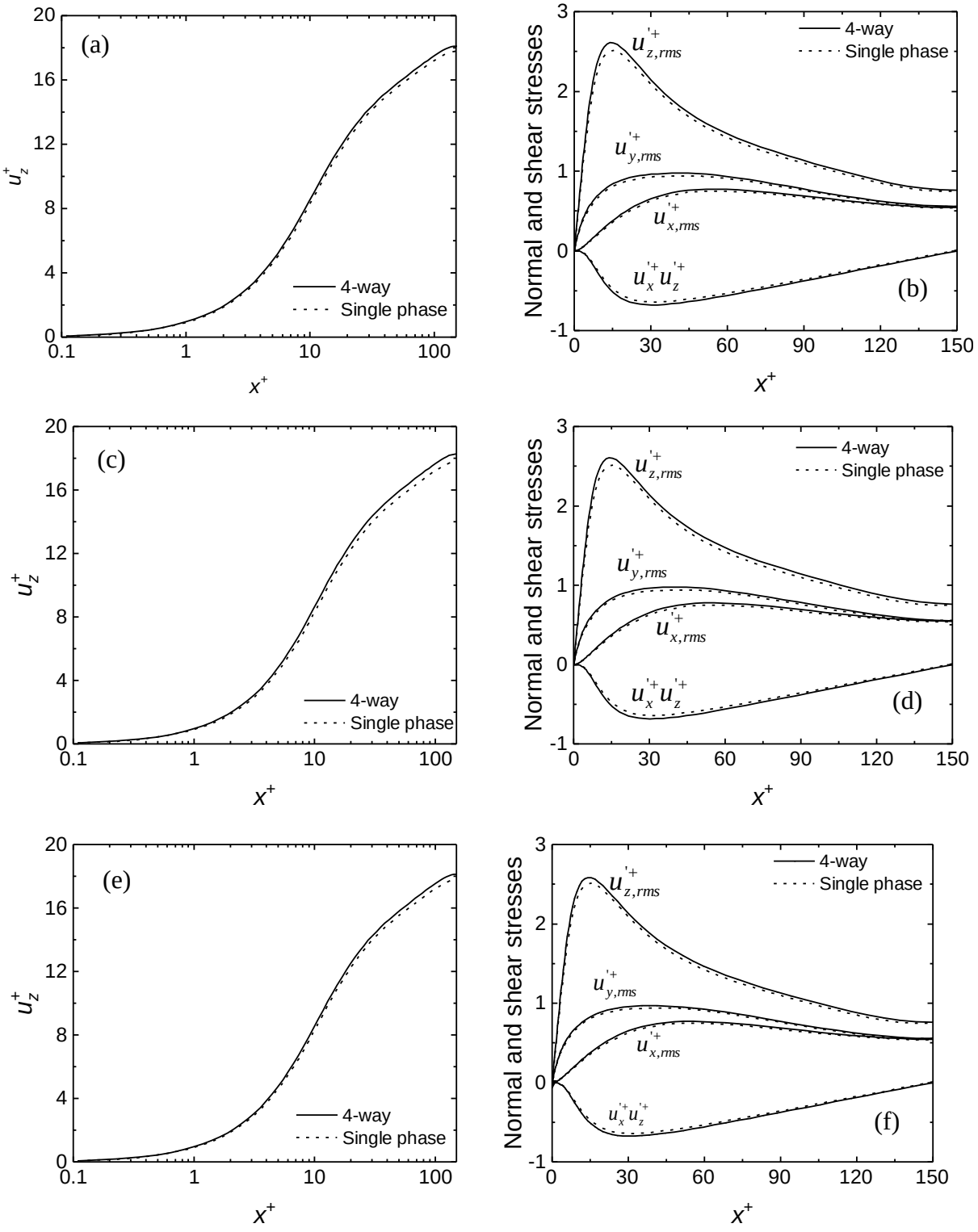

Figure 5.10 Fluid velocity statistics for four-way coupled simulation at shear Reynolds number $Re_\tau = 150$ for the three bubble sizes and vertical channel upflow: (a, c, e) mean fluid streamwise velocity; and (b, d, f) fluid normal and shear stresses. (a, b) $d_b = 110$ μm; (c, d) $d_b = 220$ μm; and (e, f) $d_b = 330$ μm.

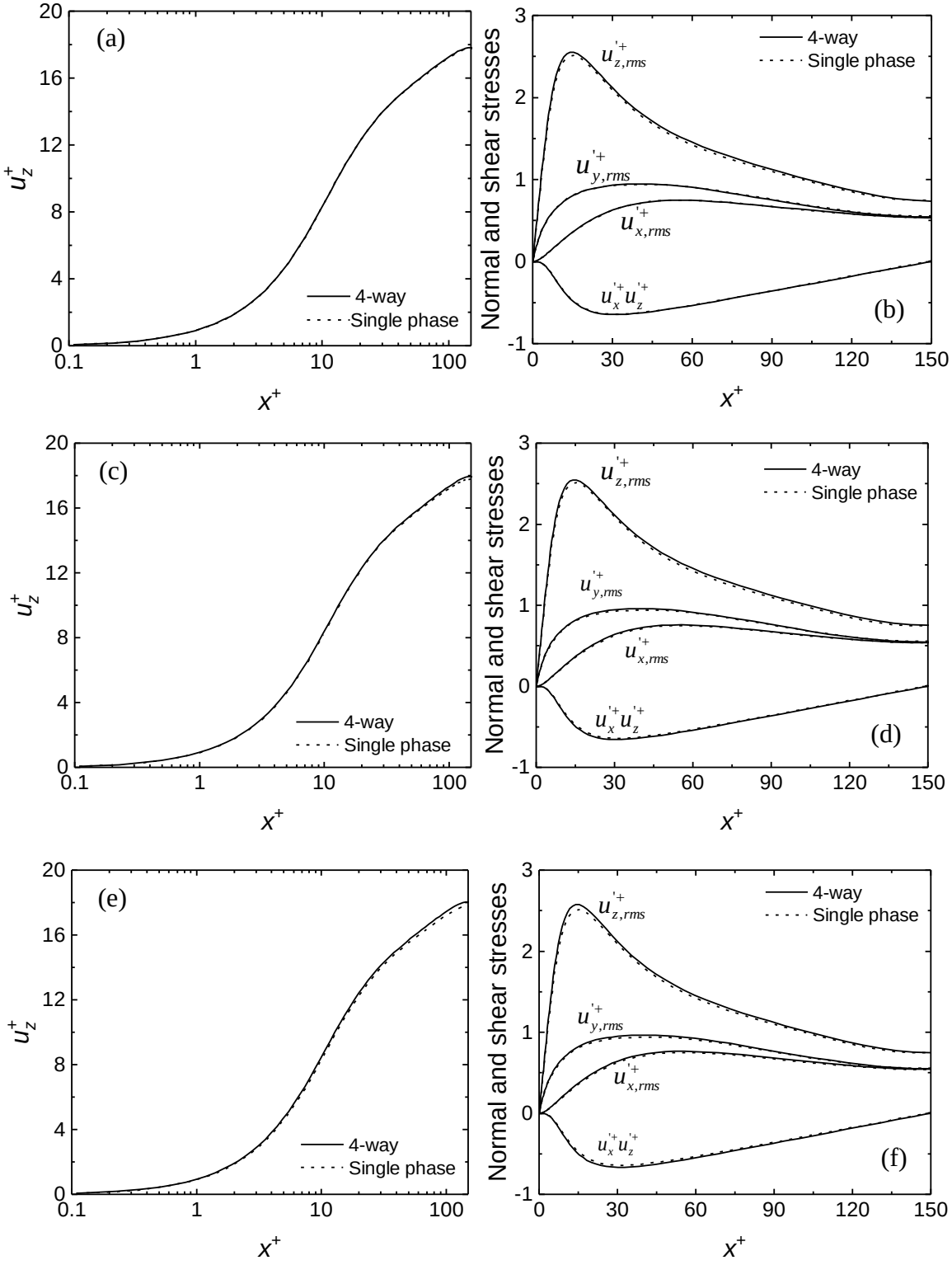

Figure 5.11 Fluid velocity statistics for four-way coupled simulation at shear Reynolds number $Re_\tau = 150$ for the three bubble sizes and vertical channel downflow: (a, c, e) mean fluid streamwise velocity; and (b, d, f) fluid normal and shear stresses. (a, b) $d_b = 110$ μm; (c, d) $d_b = 220$ μm; and (e, f) $d_b = 330$ μm.

Same quantities presented in Figure 5.10 for upflow are shown in Figure 5.11 for the vertical channel downward flow, where the four-way coupled results are again compared with the single-phase results for the three bubble sizes. The mean streamwise fluid velocity profiles do not show much difference form the single-phase flow, except for in Figure 5.11(c), which peaks at 17.5 due to the higher relative velocity induced by the increased bubble size. No significant changes are also found for the rms of the velocity fluctuations, and for the shear stress, except for the in streamwise direction that shows a slighlty increased turbulence level. Overall, the influence of the microbubbles is greater for the upflow case, whilst their effect is in general negligible in downflow. Similar results were obtained in the two-way coupled vertical channel flows considered in the previous chapter, and also in the DNS predictions of Molin et al. (2012).

Mean streamwise velocity profiles for the bubbles are shown in Figure 5.12 for the both the upflow and the downflow cases. Microbubbles flow faster than the fluid in upflow and slower than it in downflow due to the effects of buoyancy. The relative velocity between the microbubbles and the surrounding fluid flow leads to the occurrence of the interphase drag force. For upflow, the drag force accelerates the liquid phase. On the other hand, for downward flow, the drag force causes the surrounding fluid phase to decelerate. It is also worthy of note that the distinction between the upflow and downflow cases increases with increasing bubble size, as shown in Figure 5.12. For $d_b = 110$ μm bubbles, therefore, the upflow mean streamwise velocity peaks at 19.59, with $d_b = 220$ μm at 22.75 and with $d_b = 330$ μm at 23.42. For the downflow, the mean streamwise velocity for the three bubble sizes peaks at 15.50, 11.70 and 10.82, respectively.

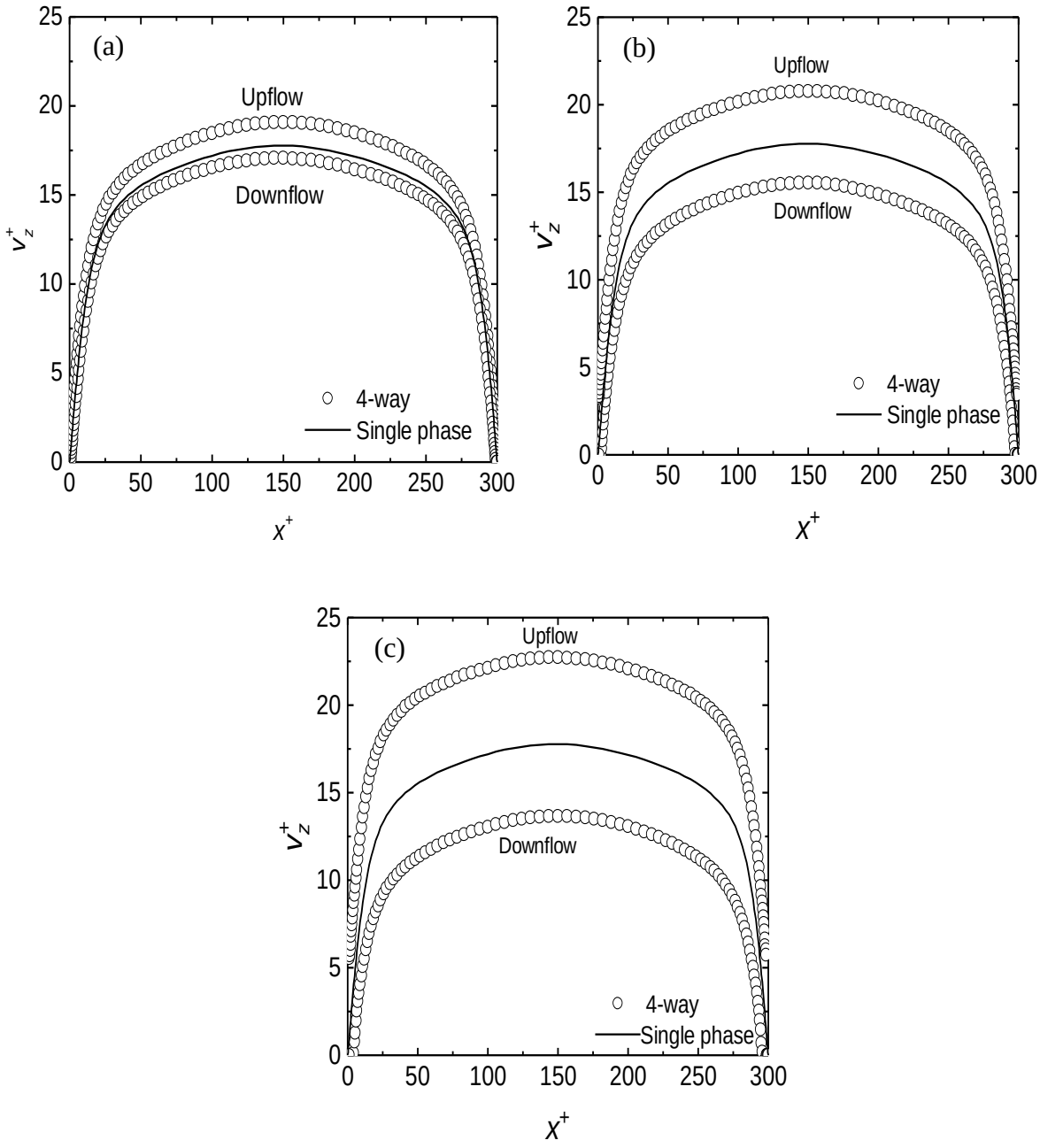

Figure 5.12 Bubble mean streamwise velocity profiles for the four-way coupled simulations at $Re_\tau = 150$: (a) $d_b = 110$ μm; (b) $d_b = 220$ μm; and (c) $d_b = 330$ μm.

The microbubble velocity fluctuations in the three directions, and the shear stress, for the three bubble sizes are plotted in Figure 5.13 for upflow (Figure 5.13 (a, c, e)) and downflow (Figure 5.13(b, d, f)). The plots show results over half the channel width due to symmetry within the flow. In the core of the channel and away from the near-wall region, bubble motion is, to a large extent, governed by the large-scale, energy-carrying turbulence structures, and the effect of the small-scale fluctuating velocity field is less significant. In the buffer layer and near-wall regions, however, the scale of the largest structures decreases, and the bubble motion becomes more sensitive to velocity fluctuations (i.e. bubble fluctuating velocities peak in the near-wall regions but are significantly lower at the core of the flow). In upflow, the streamwise velocity fluctuations, in particular, are enhanced for the three bubble sizes when compared to the single-phase profiles. This indicates the influence of the lift force in pushing bubbles towards the wall regions, and also the influence of four-way coupling which, as a result of the higher mass loading near the wall, increases the bubble velocity fluctuations. In contrast, in downflow the normal and shear stresses are not affected due to bubble migration away from the wall region, such that the stresses are generally in line with those observed for the single-phase flow for all three bubble sizes. From Figure 5.13, it is also noticeable that microbubble fluctuations in the streamwise direction in upflow are more significant than in the wall-normal and spanwise directions, when compared to the single-phase flow. Similar slight changes are also apparent in the bubble Reynolds shear stress, which decreases slightly in the region near the channel wall when compared to the single-phase results. Similar trends are observed for the downflow case, although to a lesser extent than in the upflow.

Presented in Figure 5.14 are the bubble wall-normal concentration plots for the vertical channel. Figure 5.14 (a, c, e) shows bubble concentrations in upflow, while Figure 5.14(b, d, f) gives equivalent results in downflow.

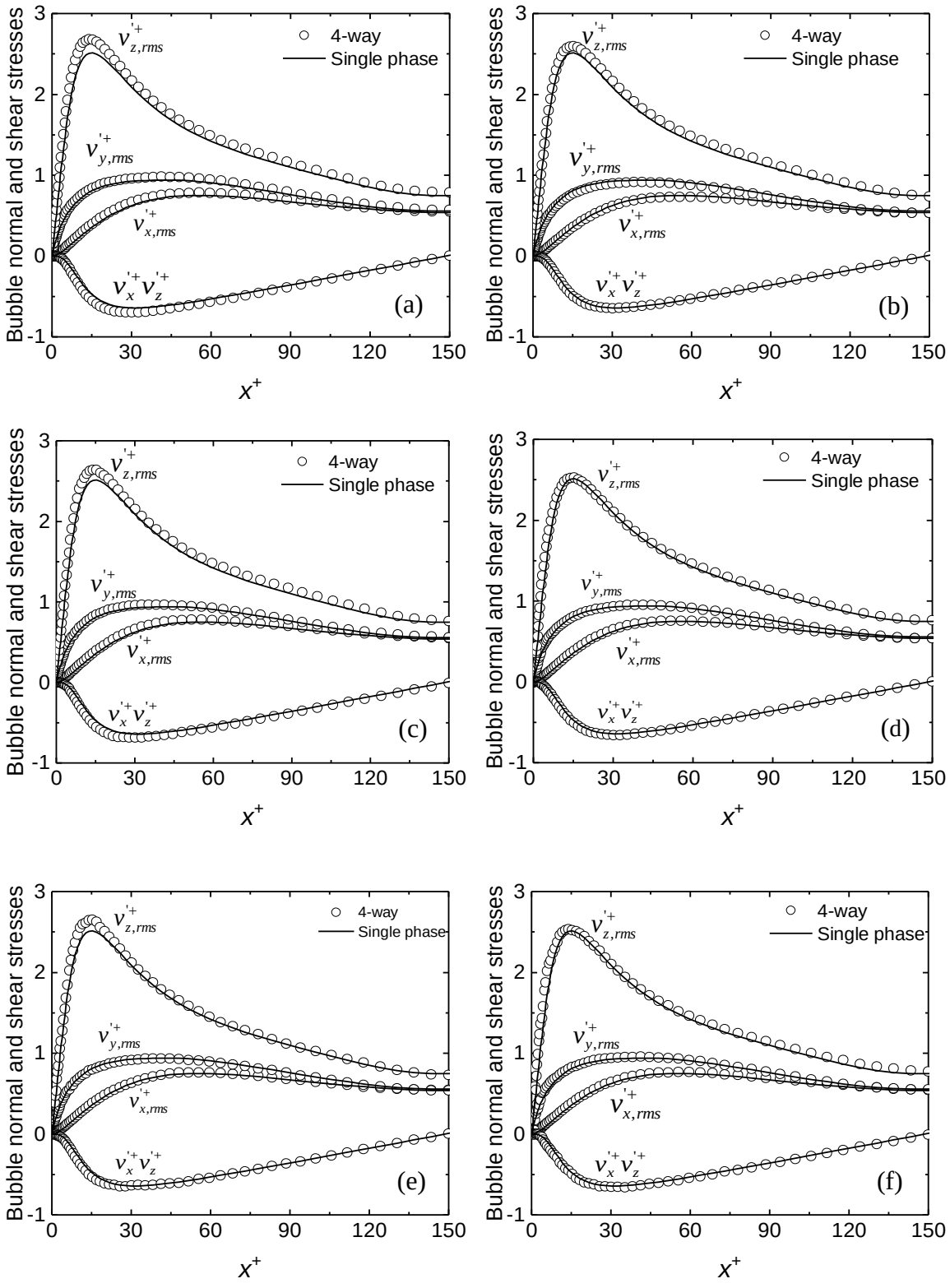

Figure 5.13 Bubble normal and shear stresses for upflow and downflow configurations at shear Reynolds number $Re_\tau = 150$ for the three bubble sizes in comparison with the single-phase flow: (a, b) $d_b = 110$ μm; (c, d) $d_b = 220$ μm; and (e, f) $d_b = 330$ μm. (a, c, e) upflow; and (b, d, f) downflow.

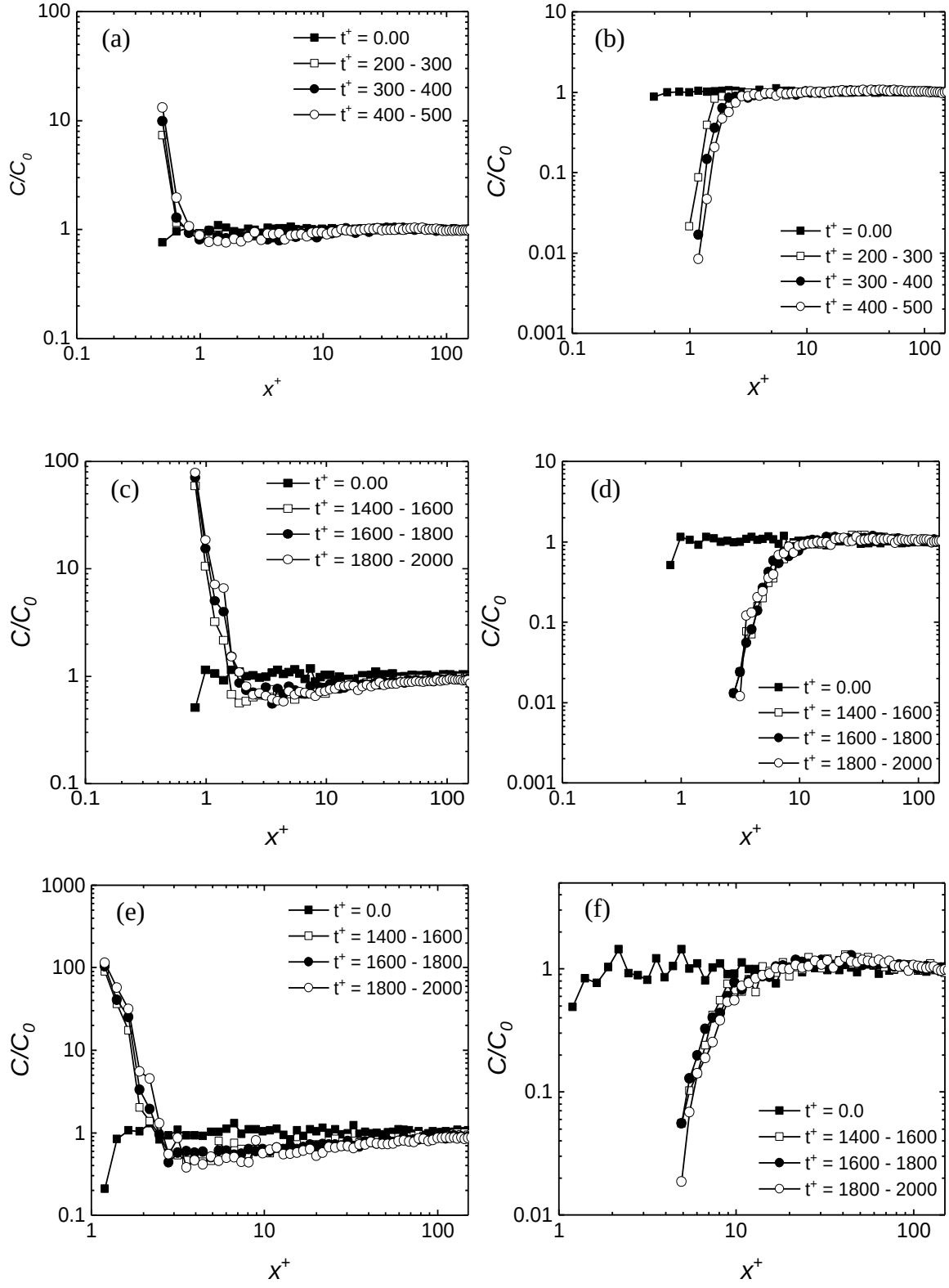

Figure 5.14 Microbubble wall-normal concentration profiles for vertical channel upflow and downflow: (a, c, e) upflow for $d_b = 110$ μm, $d_b = 220$ μm and $d_b = 330$ μm, respectively; and (b, d, f) downflow for $d_b = 110$ μm, $d_b = 220$ μm and $d_b = 330$ μm, respectively.

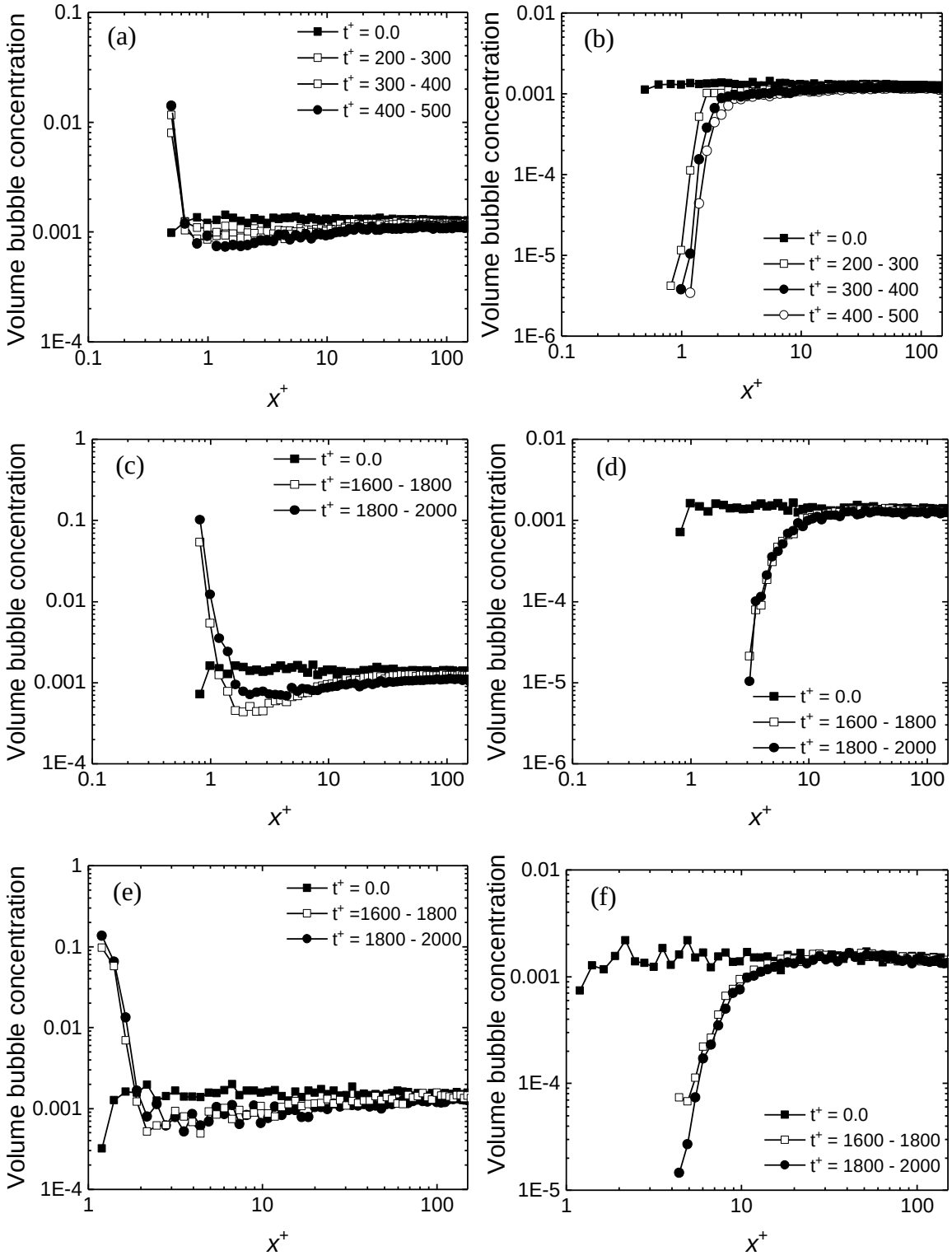

Figure 5.15. Microbubbles wall-normal volume concentration profiles for vertical channel upflow and downflow: (a, c, e) upflow for $d_b = 110$ μm, $d_b = 220$ μm and $d_b = 330$ μm, respectively; and (b, d, f) downflow for $d_b = 110$ μm, $d_b = 220$ μm and $d_b = 330$ μm, respectively.

Because of inter-bubble collisions, the bubble trajectories become random and therefore they are less influenced by coherent near-wall structures within the flow. As a result of the mechanism described by Marchioli et al. (2006), i.e. turbophoresis, which leads to bubble accumulation in the near-wall regions for one- and two-way coupled flows, bubble movement is inhibited and the concentration close to the wall is reduced in four-way coupled flows. It is worthwhile noting that, during coalescence, the number of bubbles reduces, and therefore the bubble concentration tends to slightly decrease with time. As a consequence, Figure 5.15 shows predictions of the relative volume of bubbles found in each cell in the computational domain with respect to time. The results given in this figure provide a clearer view of the bubble volume fraction evolution towards the channel walls in upflow, and away from the channel walls in downflow, with respect to increasing simulation time. Also shown in the figure is the initial volume fraction profile of 10^{-3}.

In upflow, the relative velocity between the bubbles and the fluid is positive. Therefore, the shear lift force always points to the channel wall and drives microbubbles towards the near-wall region. In contrast, in downflow, the relative velocity is negative, which changes the shear lift force direction. Thus, in this case, the shear lift force always points to the channel centre and pushes microbubbles away from the channel wall. In Figure 5.16, the wall-normal forces acting on the microbubbles are given. It is apparent that the drag and lift forces dominate in the near-wall region ($0 < \mathrm{x}^{+} < 30$). Other forces such as the pressure gradient, added mass and gravity-buoyancy are negligible compared to the drag and lift forces. The drag force acts as a counter balance to the lift force in both flow configurations. The lift force is always positive (i.e. towards the wall) for upflow, and as the bubble size increases, the lift force becomes more negative. For $d_b = 110$ μm the lift force is approximately -0.075 Nkg^{-1}, therefore, and -0.2 Nkg^{-1} for $d_b = 220$ μm and -0.3 Nkg^{-1} for $d_b = 330$ μm For downflow, the lift force is negative (i.e. away from the channel wall) and again increases with the bubble size.

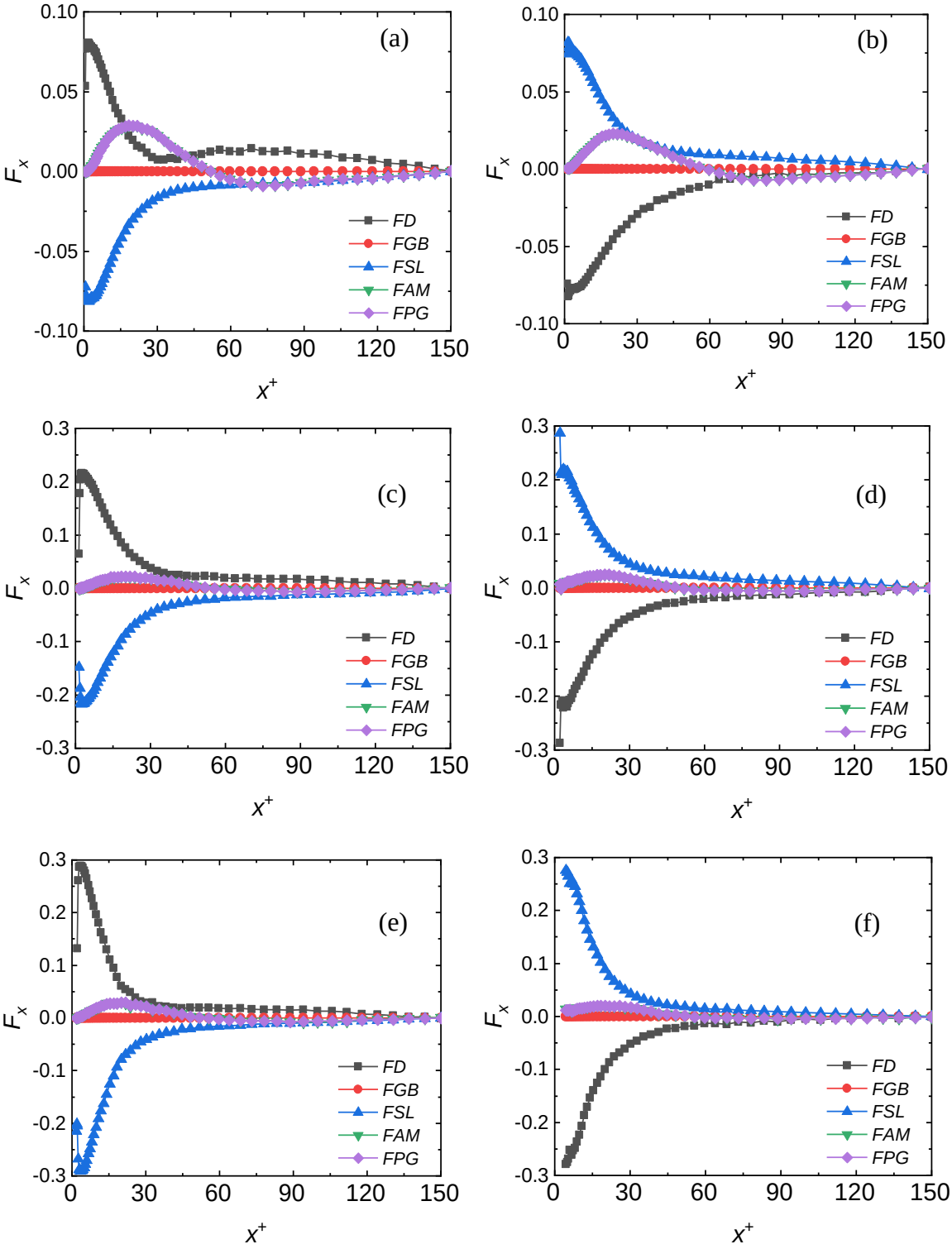

Figure 5.16. Wall-normal forces acting on the bubbles for shear Reynolds number $Re_\tau = 150$: (a, c, e) upflow for $d_b = 110$ µm, $d_b = 220$ µm and $d_b = 330$ µm, respectively; and (b, d, f) downflow for $d_b = 110$ µm, $d_b = 220$ µm and $d_b = 330$ µm, respectively (FD = drag force, FGB = gravity-buoyancy force, FSL = shear lift force, FAM = added mass force and FPG = pressure gradient force).

Figure 5.17 presents the number of bubble collisions, coalescences and collisions without coalescence for upfow and downflow at $Re_\tau = 150$, and for $d_b = 110$, 220 and 330 μm.

In upflow, and for $d_b = 110$ μm (Figure 5.17(a)), the number of bubble-bubble collisions continuously increases as the simulation progresses and almost all collision events result in coalescence, with the number of collisions without coalescence reaching a maximum value of approximately 1,000 at the end of the simulation. This almost 100% coalescence efficiency is due mainly to the low Reynolds number and the small bubble size. Specifically, the relatively low turbulence levels result in high bubble contact times that are sufficient for the liquid film trapped between the bubbles to drain off. For $d_b = 220$ μm (Figure 5.17(c)), the trend is similar to that at $d_b = 110$ μm. However, the number of bubbles separating without coalescing becomes significant from $t^+ = 200$, and the total number of collisions without coalescence recorded is approximately 20,000 at the end of the simulation. For d_b = 330 μm (Figure 5.17(e)) the number of bubbles colliding without coalescencing becomes significant at $t^+ = 420$, and at $t^+ = 2{,}000$ the total number of collisions without coalesce is around 20,000. From these results, the coalescence rate clearly reduces with increasing bubble size under the same flow conditions.

The number of bubble collisions, coalescences and collisions without coalescence for the downflow case are given in Figure 5.17(b, d, f). The number of bubbles collisions without coalescence for $d_b = 110$ μm becomes significant at $t^+ = 150$ and at $t^+ = 500$, the number of failed coalescences is similar to that for the upflow test case . For $d_b = 220$ μm, the number of collisions without coalescence begin to become significant at t^+ values around 170, and at $t^+ = 2{,}000$ a total of 1,100 failed coalescences have occurred. In Figure 5.17(f), collisions without coalescence are initially noted at $t^+ = 250$ and the total number of bubbles that collide but fail to coalesce is approximatley 500 at the end of the simulation. It is clear , therefore, that microbubble coalescence is favoured in upflow with respect to downflow. This is due to the fact that in upflow, the bubbles migrate towards the vertical channel walls promoting more collisions due to the higher levels of turbulence on those regions and, even if not all collisons result in coalescence, the overall increase in collisions still results in a higher number of coalescence events. As a consequence of the coalescence events, the number of bubbles reduces over time and progressively more larger bubbles are formed.

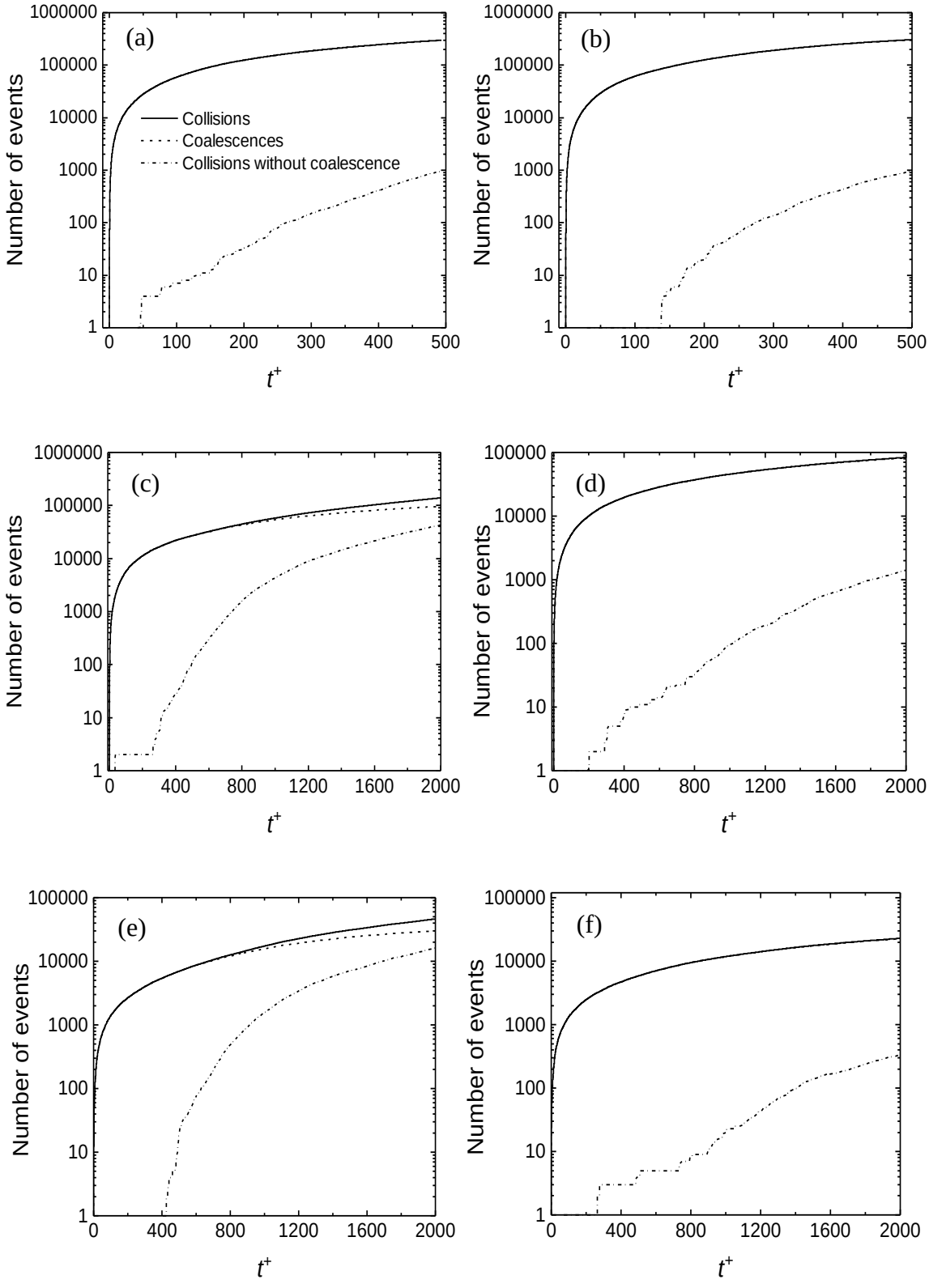

Figure 5.17 Number of bubble collisions, coalescences and collisions without coalescence at $Re_\tau = 150$: (a, c, e) upflow for $d_b = 110$ μm, $d_b = 220$ μm and $d_b = 330$ μm, respectively; and (b, d, f) downflow for $d_b = 110$ μm, $d_b = 220$ μm and $d_b = 330$ μm, respectively.

Figure 5.18 gives the number of bubbles with a volume equivalent of up to ten primary bubbles that are formed over the various times considered for the three primary bubbles sizes for both flow configurations. In Figure 5.18(a), for the upflow case, the number of primary bubbles of $d_b = 110$ μm injected into the flow was 1,812,720. At $t^+ = 500$, the number of single (primary) bubbles is reduced to approximately to one million, with the progressive formation of larger bubbles accounting for the reduction. In contrast, in Figure 5.18(b) for downflow, the number of single bubbles remaining in the flow is still greater that one million at the end of the simulation.

Figure 5.18(c) and (Figure 5.18d) give, respectively, results for the upflow and downflow cases for $d_b = 220$ μm up to $t^+ = 2000$. The initial number of bubbles injected was 227,000 in this case. There is no noticeable difference in the number of single bubbles and coalesced bubbles formed between the upflow and downflow cases. Rather, there is a sharp increase in the number of bubbles with a volume equal to 10 primary bubbles to around 1,100 in upflow compared to 800 in downflow. This trend is similar at $d_b =$ 330 μm, where the initial number of bubbles was 67,140. The number of bubbles with a volume equal to 10 primary bubbles in this case is about 110 in upflow compared with 90 for the downflow case. Overall, the rate of bubble coalescence increases with decreasing bubble size. These results are in line with those of He et al. (2015), where the authors' observed that small bubbles tends to coalesce more than larger bubbles, with the coalescence of small bubbles being a mechanism that is of improtance for drag reduction. Note that some bubble sizes have been omitted from the multi-sized bubble plots in Figure 5.18 for clarity, although the formation with time of increasingly larger bubbles is evident.

The spatial distribution of collisions and coalescences is presented in Figure 5.19. An almost 100% coalescence efficiency is confirmed in Figure 5.19(a) and (b), i.e. for upflow and downflow, for bubble size $d_b = 110$ μm. Overall, the largest number of coalescence events occurs near the channel wall, where the concentration of the bubbles and the turbulence levels are highest. The migration of bubbles towards the channel walls under the influence of the lift force for the upflow case increases the number of collisions and coalescences when compared with those for the downflow.

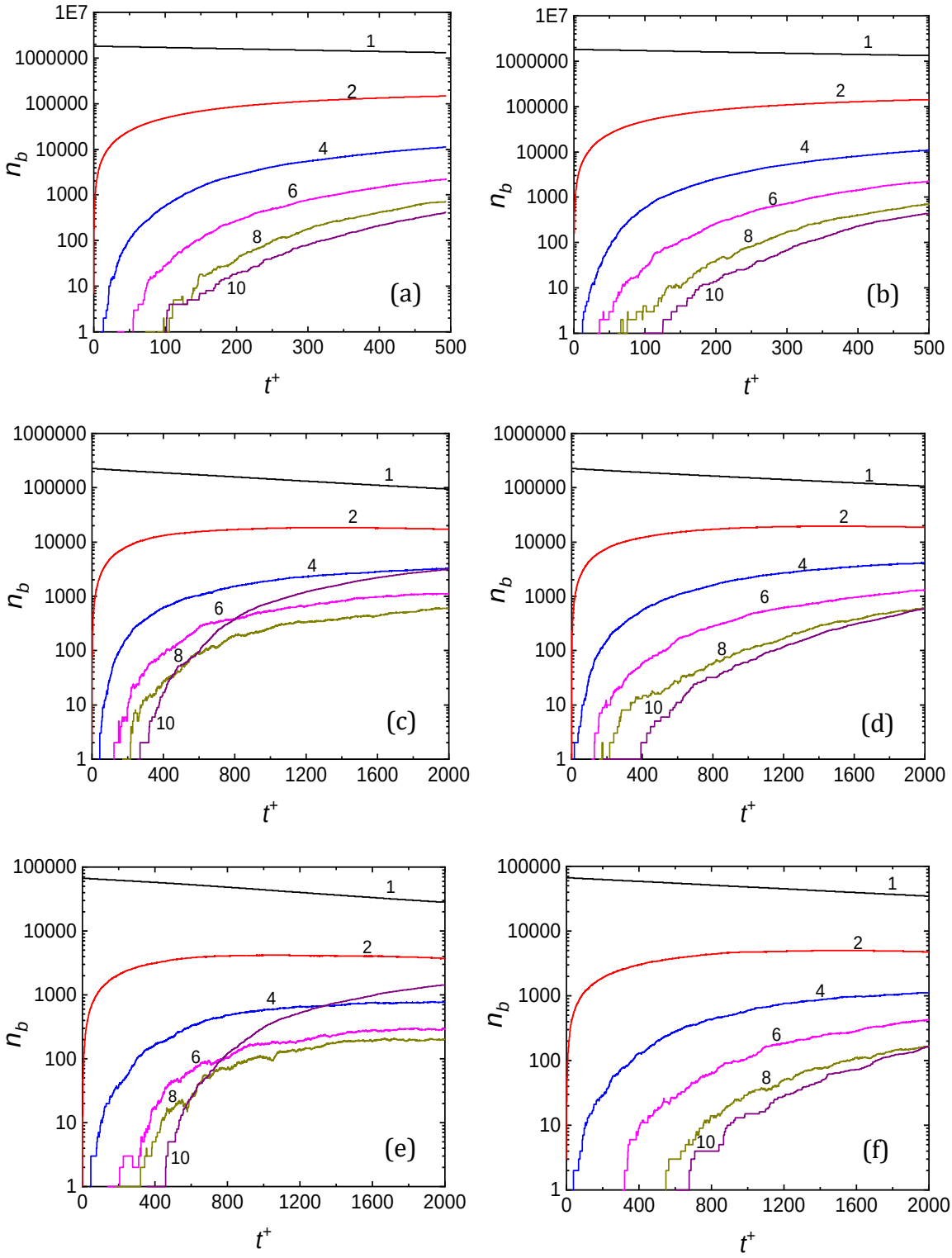

Figure 5.18. Number of bubbles of various sizes formed after coalescence in vertical channels at $Re_\tau = 150$: (a, c, e) upflow for $d_b = 110$ μm, $d_b = 220$ μm and $d_b = 330$ μm, respectively; and (b, d, f) downflow for $d_b = 110$ μm, $d_b = 220$ μm and $d_b = 330$ μm, respectively.

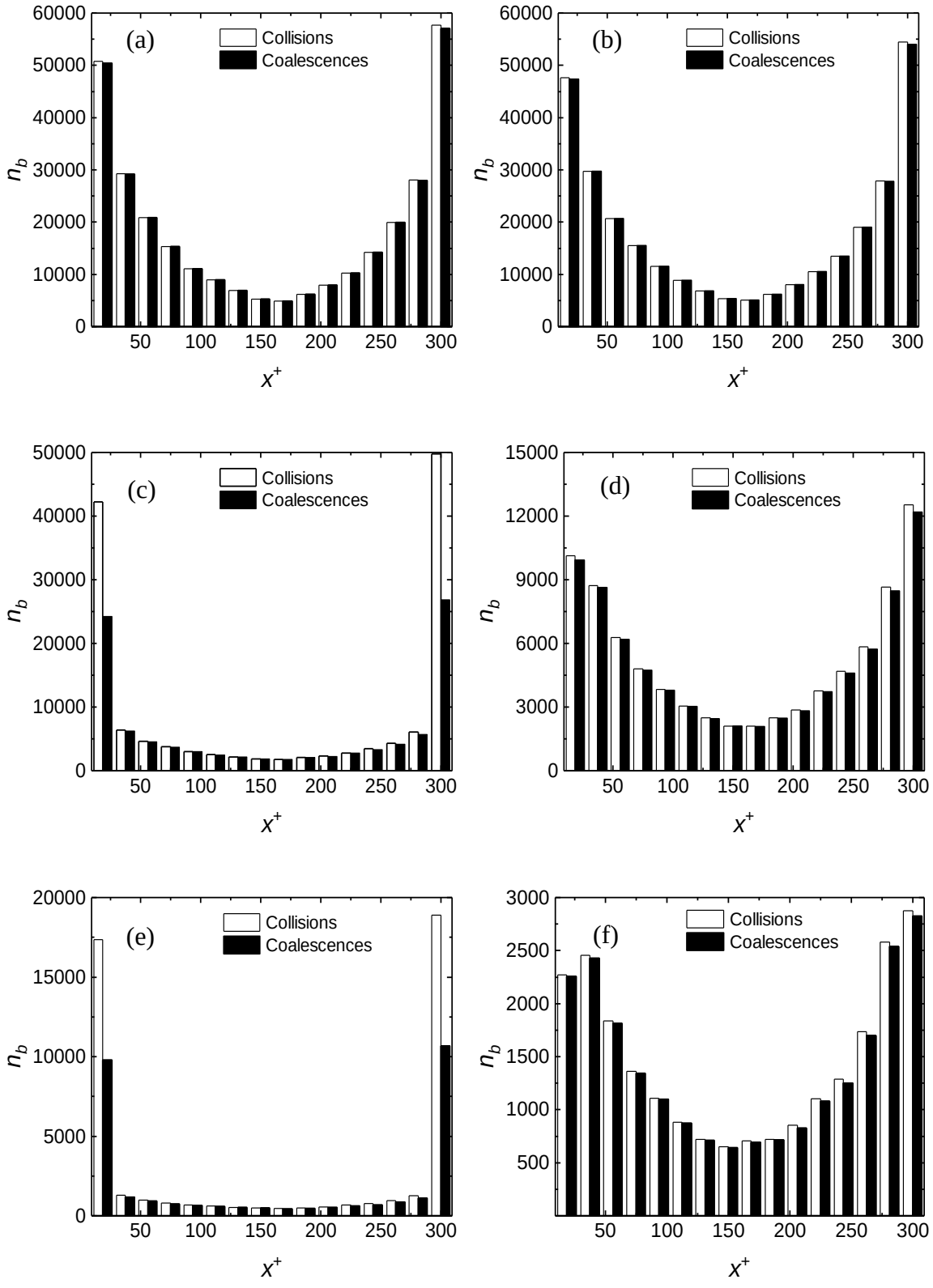

Figure 5.19. Number of bubble collisions and coalescences across the vertical channel at $Re_\tau = 150$: (a, c, e) upflow for $d_b = 110$ μm, $d_b = 220$ μm and $d_b = 330$ μm, respectively; and (b, d, f) downflow for $d_b = 110$ μm, $d_b = 220$ μm and $d_b = 330$ μm, respectively.

The spatial distribution of collisions and coalescences for bubble sizes $d_b = 220$ μm and $d_b = 330$ μm is also presented in Figure 5.19(c) and (d), and Figure 5.19(e) and (f), for upflow and downflow, respectively. The number of collisions increases towards the channel walls for all flow systems, while the collision efficiency reduces towards the walls as not all the collisions result in bubbles coalescence. It is also observed that there are a significantly greater number of collisions and coalescences recorded in the upflow configuration as compared to the downflow. This is again due to the lift force pushing bubbles to the walls in upflow, thereby increasing the bubble concentration in regions where the turbulence intensity is high, and enhancing the number of collisions. In contrast, in downflow, bubble movement away from the near-wall turbulent regions reduces the overall number of collisions and results in a more uniform distribution of these event across the channel.

5.2.1 Reynolds Number Effect in Vertical Upward and Downward Channel Flows

The increased shear in high Reynolds number flows increases the intensity of the turbulent regions, and therefore the bubble fluctuations and the number of bubble-bubble interactions. Further analysis is desirable to establish a quantitative and qualitative relationship between the bubble fluctuating velocity and its impact on bubble coalescence. Since turbulence can significantly affect bubble behaviour, additional simulations at $Re_\tau = 590$, taking advantage of the less-demanding computational resources required by LES as compared to DNS, were also made to study the effect of turbulence on microbubble dispersion in vertical channels. For these simulations, the bubble diameter chosen was 220 μm, as was done for the two-way coupled simulations reported in the previous chapter.

Presented in Figure 5.20 are the fluid mean streamwise velocity and the turbulence statistics for both upflow and downflow, compared with single-phase flow results. It is obvious that no remarkable differences are apparent. In Figure 5.21(a) and (b) the bubble velocity statistics are presented alongside the $Re_\tau = 150$ results with the same void fraction. The distinctive separation between upflow and downflow, which was visible at a shear Reynolds number $Re_\tau = 150$, is greatly reduced at $Re_\tau = 590$, with the upflow peaking at approximately 22.5 and the downflow at 20.5. In addition, the normal and

shear stress profiles shown in Figure 5.21(c) and (d), for upflow and downflow, respectively, are essentially in line with their corresponding single-phase flow profiles as a result of the higher turbulence levels tending to partially override other forces acting on the bubbles. The relative velocity between the fluid and the bubbles is mostly a function of the bubble diameter, therefore it does not change significantly with an increase in the fluid velocity. Instead, the velocity magnitude of both the fluid and the bubbles, and the shear velocity, are greatly increased at the higher shear Reynolds number. Therefore, the importance of the relative velocity with respect to the velocity magnitude is significantly reduced, as is the magnitude of the separation between upflow and downflow velocity profiles. This trend was also noted in the two-way coupled results.

Bubble concentration profiles and the forces acting on the bubbles in the wall-normal direction are presented in Figure 5.22 and 5.23, respectively. Evolution of the bubble concentration profiles is similar to that observed in the $Re_\tau = 150$ flow, with bubbles migrating towards the wall in upflow, and in the opposite direction in downflow. The peak value of the bubble concentration in upflow and downflow are reduced, however, due to the increased dispersion of the microbubbles caused by the higher levels of turbulence. This result confirms that, as expected, higher levels of turbulence enhance bubble mixing within the flow, generating more homogeneous concentration profiles and partially overridding the effect of other forces acting on the bubbles.

These forces are given in Figure 5.23, with the results showing similar trends to those observed in the $Re_\tau = 150$ predictions. In this case, however, the lift force, which was dominant at $Re_\tau = 150$, is now significant only in the near wall region in both upflow and downflow. Instead, in the remainder of the channel, the pressure gradient and the added mass force, which are more related to the fluid and bubble velocity magnitude, are now dominant. The drag force again counter balances the other forces and changes sign, being in the same direction as the lift force in upflow, except very close to the wall, and in the opposite direction in downflow.

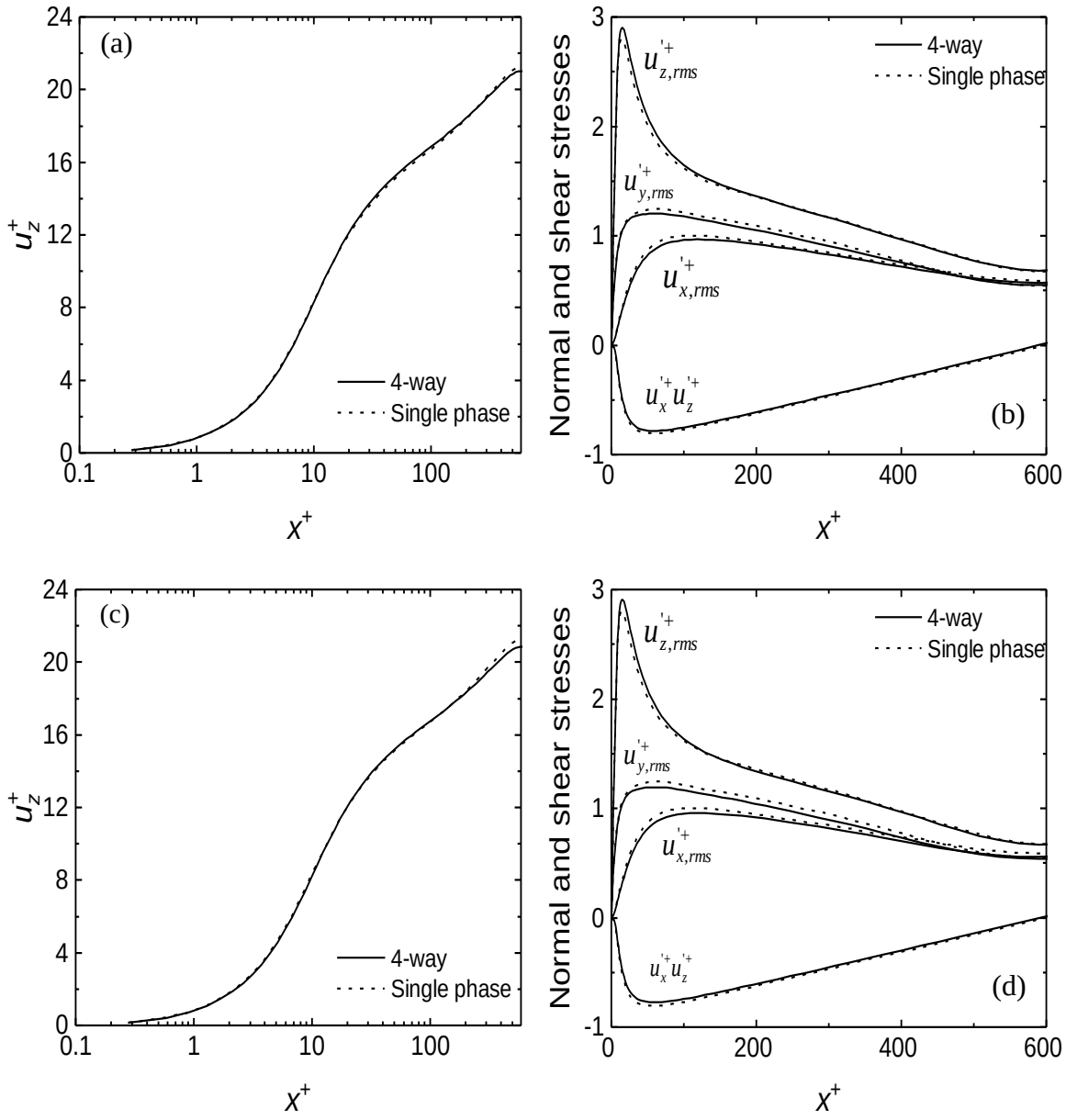

Figure 5.20. Fluid velocity statistics for four-way coupled simulation at shear Reynolds number $Re_\tau = 590$ and bubble size $d_b = 220$ μm in vertical channel flow: (a, b) mean fluid streamwise velocity; and (c, d) fluid normal and shear stresses. (a, c) upflow; and (b, d) downflow.

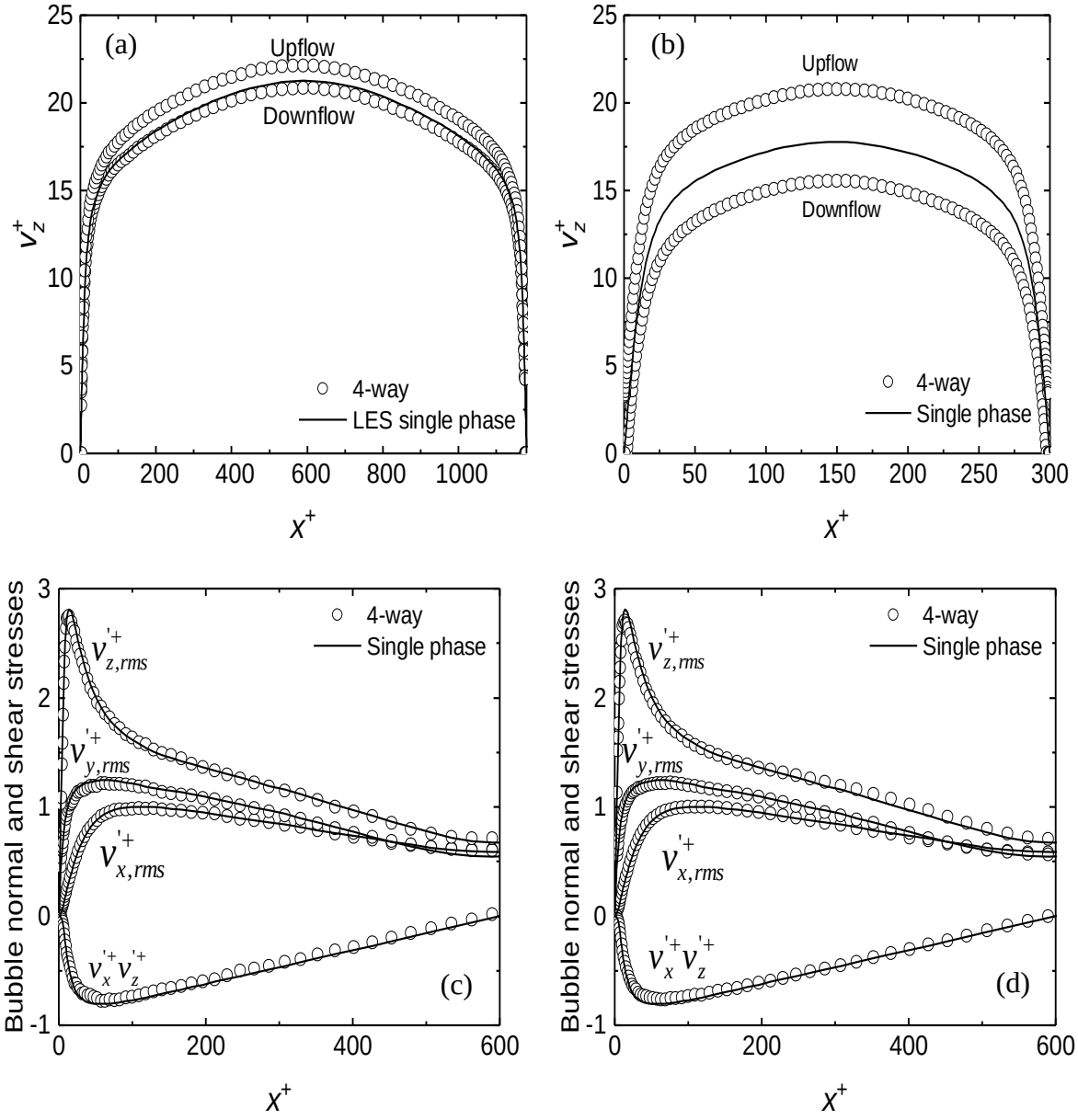

Figure 5.21. Bubble velocity statistics for four-way coupled simulation with $d_b = 220$ μm in vertical channel flows: (a, b) bubble mean streamwise velocity at $Re_\tau = 590$ and $Re_\tau = 150$, respectively; and (c, d) bubble normal and shear stresses for upflow and downflow at $Re_\tau = 590$, respectively.

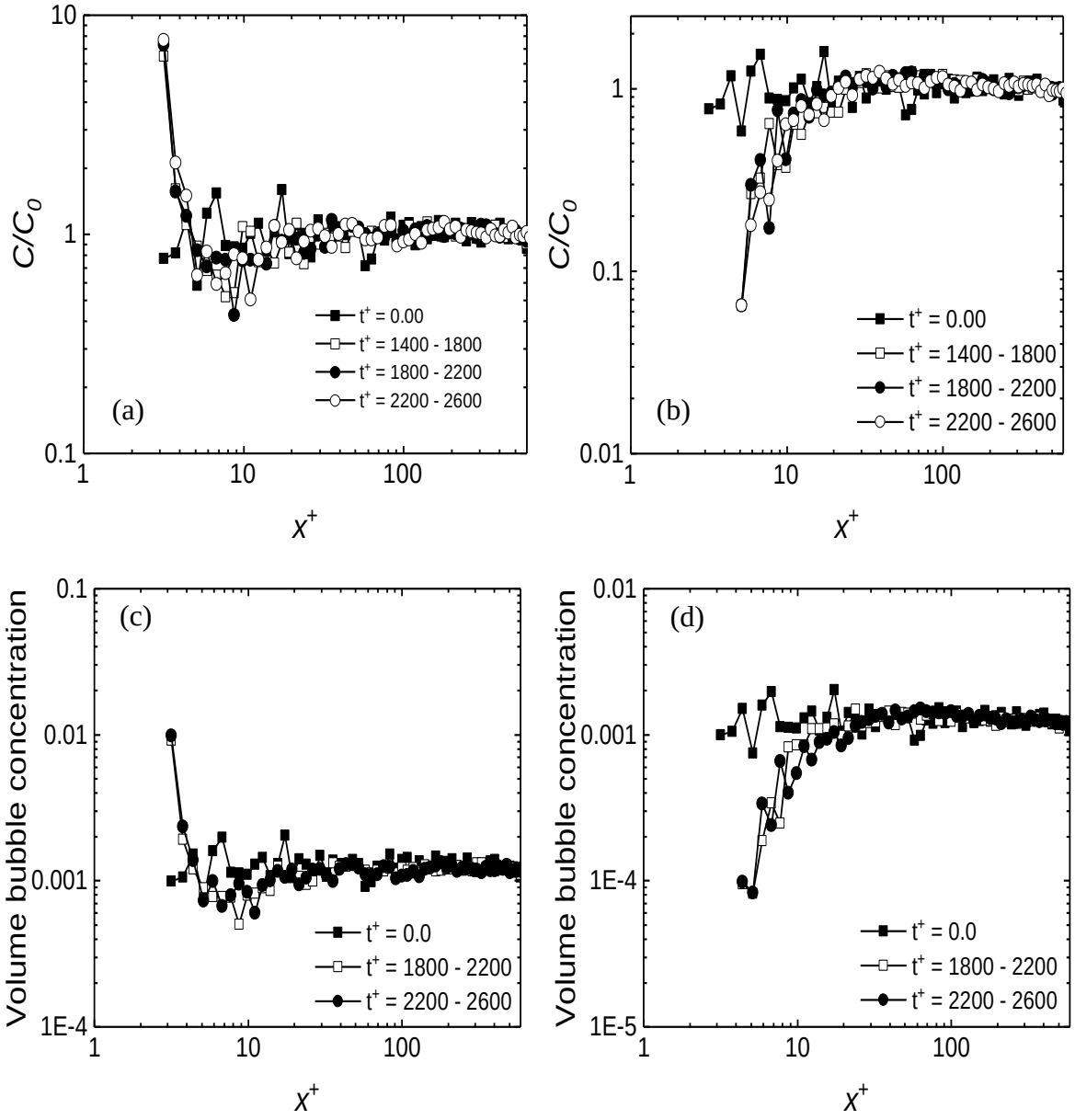

Figure 5.22. Bubble wall-normal concentration profiles at $Re_\tau = 590$ and $d_b = 220$ μm in vertical channel flows: (a, b) bubble concentration for upflow and downflow, respectively; and (c, d) bubble volume concentration for upflow and downflow, respectively.

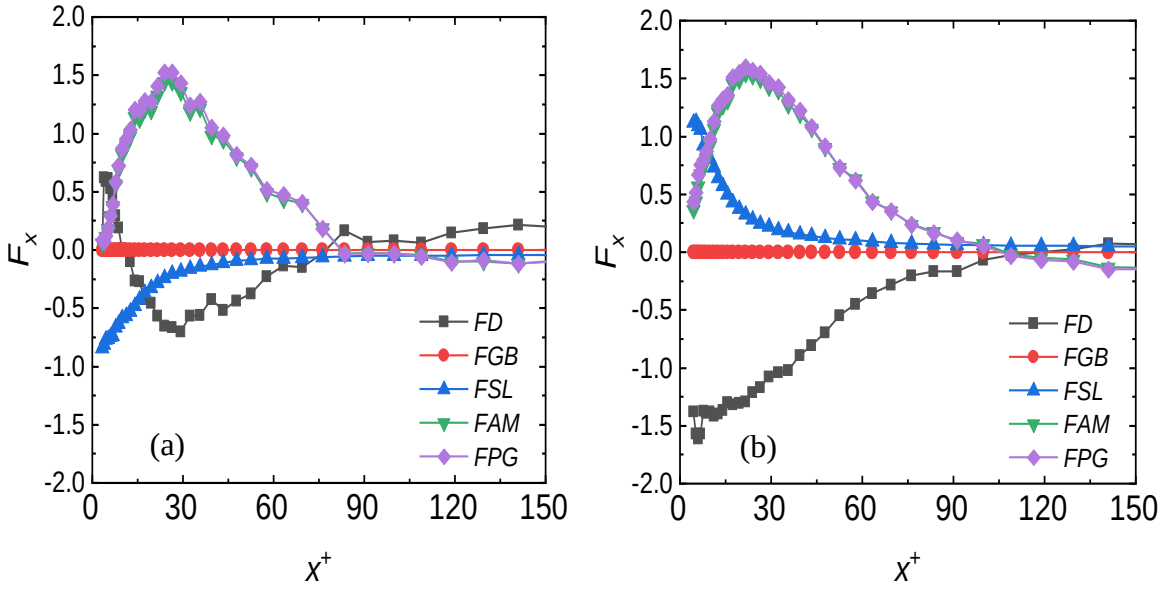

Figure 5.23. Wall-normal forces acting on the bubbles for shear Reynolds number $Re_\tau = 590$ and $d_b = 220$ μm in vertical channels: (a) upflow; and (b) downflow (FD = drag force, FGB = gravity-buoyancy force, FSL = shear lift force, FAM = added mass force and FPG = pressure gradient force).

Figure 5.24 below shows the number of bubble collisions, coalescences and collisions without coalescence for upflow and downflow. Figure 5.24(a) and (c) are for the upflow case, while Figure 5.24(b) and (d) are for downflow. In upflow, the number of collisions, coalescences and collisions without coalescence all increase with time, and not all collision events result in coalescence. The number collisions without coalescence is low however, with a value of 10 at $t^+ = 120$ and reaching a maximum value of about 356 at the end of the simulation. For downflow, an initial value of about 10 occurs at $t^+ = 40$ and this reaches a maximum value of approximately 132 for a simulation time of $t^+ = 2400$. More collisions without coalescence were recorded in upflow, as is to be expected, due to the net-buoyancy and relative velocity contributions resulting in higher levels of turbulence which leads to shorter bubble contact times that are insufficient for the liquid film trapped between the bubbles to drain off during bubble contact.

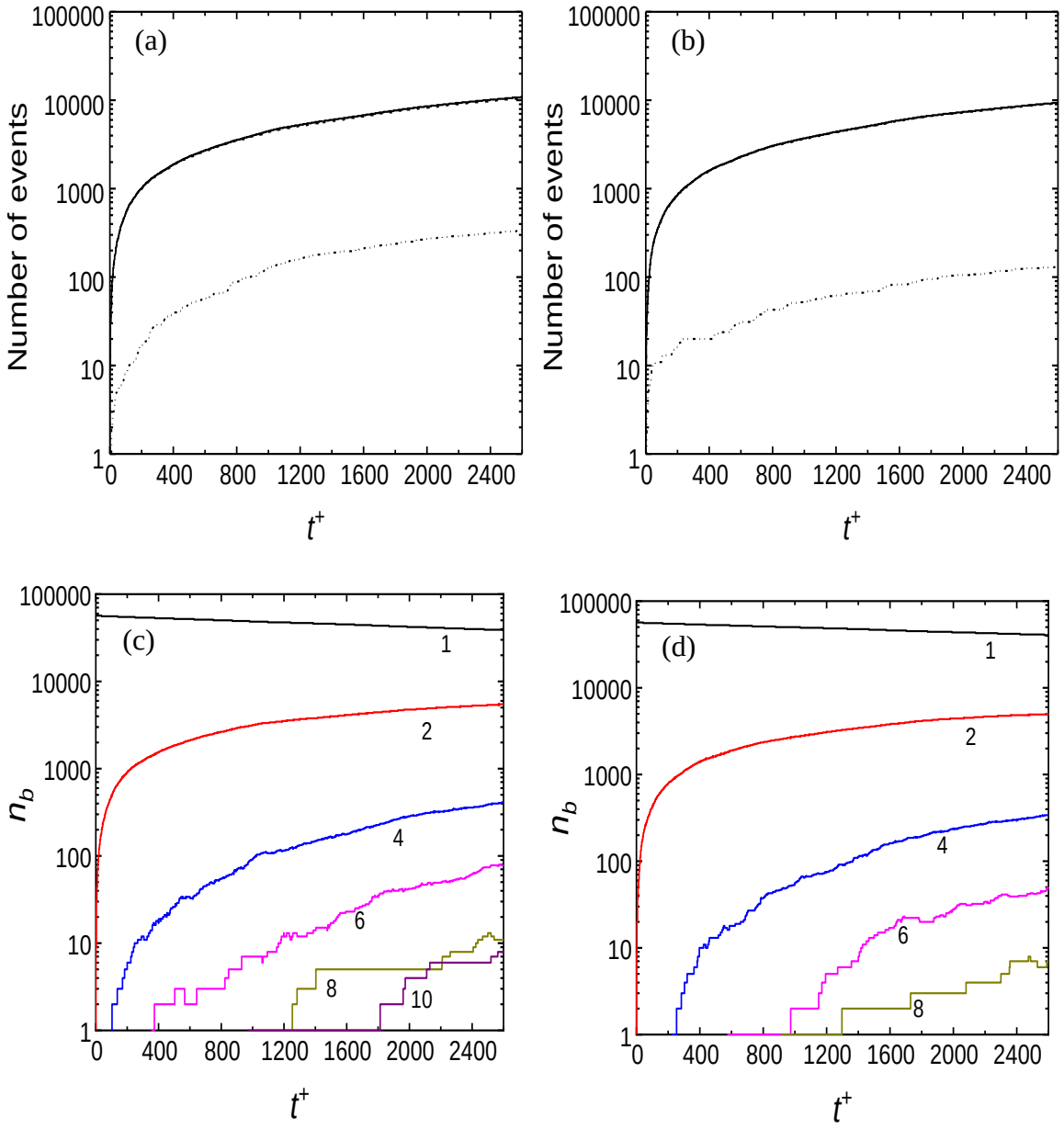

Figure 5.24. Number of bubble collisions, coalescences and collisions without coalescence, and the number of bubbles of various size formed, at $Re_\tau = 590$ an initial $d_b = 220$ μm: (a, b) number of bubble collisions, coalescences and collisions without coalescence; and (c, d) number of bubbles of various sizes formed after coalescence. The legends (1), (2), (4), (6), (8), etc., represent bubbles with a volume equal to one, two, four, six, eight, etc., times that of the primary bubbles. (a, c) upflow; and (b, d) downflow.

As noted earlier, the occurrence of coalescence events results in a reduced number of bubbles over time. In Figure 5.24(c) and (d), the multi-sized bubbles formed after coalescence is presented for upflow and downflow. The trends observed are similar to

those in the lower Reynolds number flow, although a longer simulation time was required at the higher Reynolds number because of the lower coalescence efficiency found in higher levels of turbulence. Comparing Figure 5.24(c) and (d), the rate of formation of multi-sized bubbles in upflow is faster than in downflow, as expected and in line with observations at the lower Reynolds number. Also, presented in Figure 5.25 is the spatial distribution of microbubble collisions and coalescences across the vertical channel width for upflow and downflow. In upflow, the number of coalescences recorded at both channel walls is about 14,000 and approximately 250 in the centre of the channel. In contrast, in downflow about 13,000 coalescences occur near the channel walls and approximately 300 in the centre of the channel. These results confirm the influence of buoyancy discussed previously, and are qualitatively in line with those observed at the lower Reynolds number.

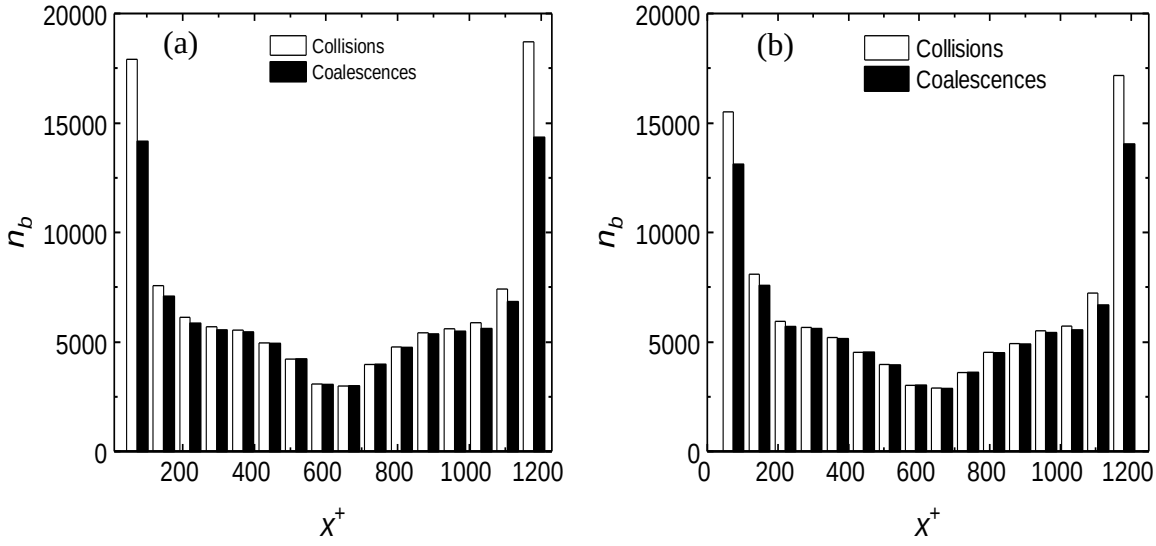

Figure 5.25. Number of bubble collisions and coalescences across the vertical channel at $Re_\tau = 590$ in vertical channels: (a) upflow; and (b) downflow.

It is clear that in upflow many bubbles, under the influence of the lift force, remain close to the vertical channel walls for most of the simulation time, whereas in downflow virtually no bubbles remain near the channel walls over the same time. Also, in the centre of the channel, the pattern of the bubbles' lateral movement with time is different between upflow and downflow. In upflow, the bubbles therefore move with significantly more interactions between them, whereas in downflow, bubble-bubble interactions are

less pronounced, particularly in the wall regions. This is as to be expected since, in upflow, the slip velocity of the bubbles in the vertical direction is in the same direction as the liquid velocity. For downflow, the slip velocity of bubbles in the vertical direction is in opposite direction of the liquid velocity. Therefore, the magnitude of the absolute vertical velocity of bubbles is much greater in upflow than in downflow. Hence the trajectories of bubbles in downflow are irregular whereas in upflow they are more in line with the fluid streamlines. These results show reasonable agreement with the findings of Biswas (2007).

5.3 Summary of Bubble Coalescence in Horizontal and Vertical Channel Flows

Four-way coupled simulations of bubbly flows in channels have been performed using the LES-LPT model. To do so, appropriate bubble collision and coalescence routines were added to the model developed and used in previous chapters. Firstly, a horizontal channel flow of water at shear Reynolds numbers 150 and 590 were simulated using 220 μm diameter, spherical air bubbles. The bubbles were found to move towards the upper channel wall with time, generating a large number of collisions and coalescences in that region, whilst the lower section of the channel becames depleted of bubbles. The results were compared with zero-gravity simulations, where the bubble velocity profile remains symmetric across the channel, with the number of collisions and coalescences at both channel walls also compared.

Subsequently, vertical upward and downward channels flows of water at shear Reynolds numbers of 150 and 590 were simulated, with air bubbles of 110, 220 and 330 μm in diameter. A greater number of collisions and coalescence events occurs at $Re_\tau = 590$ due to the enhanced bubble interaction promoted by the higher levels of turbulence. For the same reason, the associated lower bubble contact time results in a reduced coalescence efficiency than for the lower Reynolds number $Re_\tau = 150$ case. Larger numbers of bubble-bubble collisions and coalescences, but with a reduced efficiency of coalescence, occured in upflow when compared to downflow, partially because the bubbles increase turbulence levels in the fluids flow in upflow but reduce it in downflow. In addition, the lift force, by pushing bubbles towards the highest turbulence regions near the wall in

upflow, promotes bubble collision and coalescence with respect to downflow where the bubbles concentrate in lower turbulence regions in the centre of the channel.

Being able to predict changes in, and the evolution of, the bubble size distribution is crucial in bubbly flows, since the amount of interfacial area determines the rate of exchange of mass, momentum and energy between the phases. Specifically, in the absence of heat and mass transfer, the evolution of the size distribution is induced by the coalescence and breakup of bubbles. Coalescence of bubbles plays a major role in the bubble size evolution, promoting a wide bubble size distribution. Overall, the results presented in this chapter demonstrate the potential of the overall model for predicting microbubble coalescence in the types of flow considered. Previous studies of this kind have been mostly limited to bubble columns (Delnoij et al., 1997; van den Hengel et al., 2005; Lau et al., 2014) with bubbles millimeters in size. Also, DNS- and LES-based studies in closed ducts of various geometries have generally been limited to two-way coupled simulations. In contrast, the work described has been able to obtain detailed predictions of microbubble coalescence in channel flows using a range of bubble sizes (110, 220 and 330 μm), highlighting, amongst other parameters, the influence of bubble diameter on coalescence. Of particular interest with the approach adopted is the deterministic evaluation of collision, and coalescence, from the local resolved turbulence field. This approach is clearly superior to statistical models of coalescence based on averaged velocity and turbulence fields, which most macroscopic models that are applied to bubbly flows in the chemical and process engineering, pharmacology, water treatment and food industries (Rodríguez-Rodríguez et al., 2015) are based on. In the next chapter, this model will be used as a starting point and further develoepd to enable the full prediction of bubble size evolution with the introduction of a model for bubble breakup.

CHAPTER 6

FOUR-WAY COUPLED FLOW WITH COALESCENCE AND BREAKUP

In this chapter, the LES-LPT model is further extended with the addition of a model for bubble breakup to the four-way coupled model developed and applied in Chapter 5. The Martinez-Bazan et al. (1999) breakup model is adopted for inclusion in the Eulerian-Lagrangian technique. For a bubble breakup to occur, the turbulent flow structures surrounding the bubble must be sufficiently strong enough to deform its surface and overcome the surface restoring forces. Upward and downward vertical channel flows of water at shear Reynolds numbers of 150, 590 and 2000 are examined, with air bubbles of diameter $d_b = 110, 220$ *and* 2000 μm *dispersed within the flows. The ability of the model to predict both coalescence and breakup is evaluated, as well as the impact of the flow condition on the two phenomena. The tests start with a sensitivity analysis on the carrier phase turbulence energy dissipation rate that shows breakup cannot be achieved in the* Re_τ *= 150, 590 and 2000 water flows laden with air bubbles because of the high surface tension* $\sigma = 7.2 \times 10^{-2}$ Nm^{-1}*of such bubbles that restores the deformed surface. Additional simulations are performed for refrigerant R134a at a shear Reynolds number of 1154 dispersed with refrigerant bubbles of* $\sigma = 8.08 \times 10^{-3}$ Nm^{-1}*. Refrigerant bubbles break up more easily due to their lower surface tension. The breakup location is found to be near the channel walls, where the turbulence kinetic energy dissipation rate is highest. Coalescence and breakup are favoured in upflow conditions, with turbulence levels found to significantly impact the extent of bubble interaction. Coalescence is dominant at low turbulence levels, and breakup, which was only detected in the R134a flow, is favoured by high turbulence. The results demonstrate the capabilities of the overall model to predict bubble coalescence and breakup and its usefulness for predicting flows that are of industrial relevance, where interfacial area and bubble size distribution govern interfacial mass, momentum and heat transfer processes.*

6.1 Bubble Breakup Approach

The breakup model of Martinez-Bazan et al. (1999) was adopted since it is applicable within an Eulerian-Lagrangian framework, and was incorporated into the modified bubble tracker. The basic concept of the model is that for a bubble to break, its surface has to be deformed and further, the deformation energy required to do this must be provided by the surrounding fluid turbulent stresses. The minimum energy required to deform a bubble of size d_b is its surface energy, expressed in Eq. ((3.63) as $\tau_s(D) = 6\,\sigma/d_b$. When air bubbles are introduced into the turbulent carrier fluid phase, the velocity fluctuations of the turbulence field produce pressure deformation forces on the bubbles' surface. When these forces exceed the confinement forces due to surface tension, the bubble breaks up. Recalling Eq. ((3.65), the average deformation stress results from velocity fluctuations existing in the liquid between two points separated by a distance d_b: $\tau_t(d_b) = 0.5\left(\rho\beta\epsilon^{2/3}d_b^{2/3}\right)$. For a bubble to breakup, Eq. (3.69) must be greater than Eq. (3.67). The table below summarises the computational parameters used for the prediction of bubble breakup in water flows.

Table 6.1 Simulation parameters for bubble breakup.

Simulation parameters applied	
Reynolds number (Re_τ)	150, 590
Fluid density (ρ)	1000 kgm^{-3}
Bubble density (ρ_b)	1.3 kgm^{-3}
Reference bubble size (d_b)	220, 2000 μm
Batchelors constant (β)	8.2
Surface tension (σ)	7.2×10^{-2} Nm^{-1}

Based on the computational details given in Table 6.1, the plots presented in

Figure 6.1 show a balance of the turbulence kinetic energy dissipation rates at the reference Reynolds numbers of 150 and 590, using the bubble size $d_b = 220$ μm and an additional larger bubble size $d_b = 2000$ μm. Each figure gives the minimum, maximum and the average dissipation rate predicted in the carrier fluid across the channel. The larger bubbles were considered as they exhibit a lower surface restoring pressure and therefore tend to breakup more easily. In the plots, the threshold level of turbulence

kinetic energy dissipation rate required to breakup bubbles of the specified diameter are compared against the turbulence dissipation rates in the flow. Additionally, the vertical dotted line shows the location where the centre of bubbles of the specified size is located for a bubble in contact with the wall.

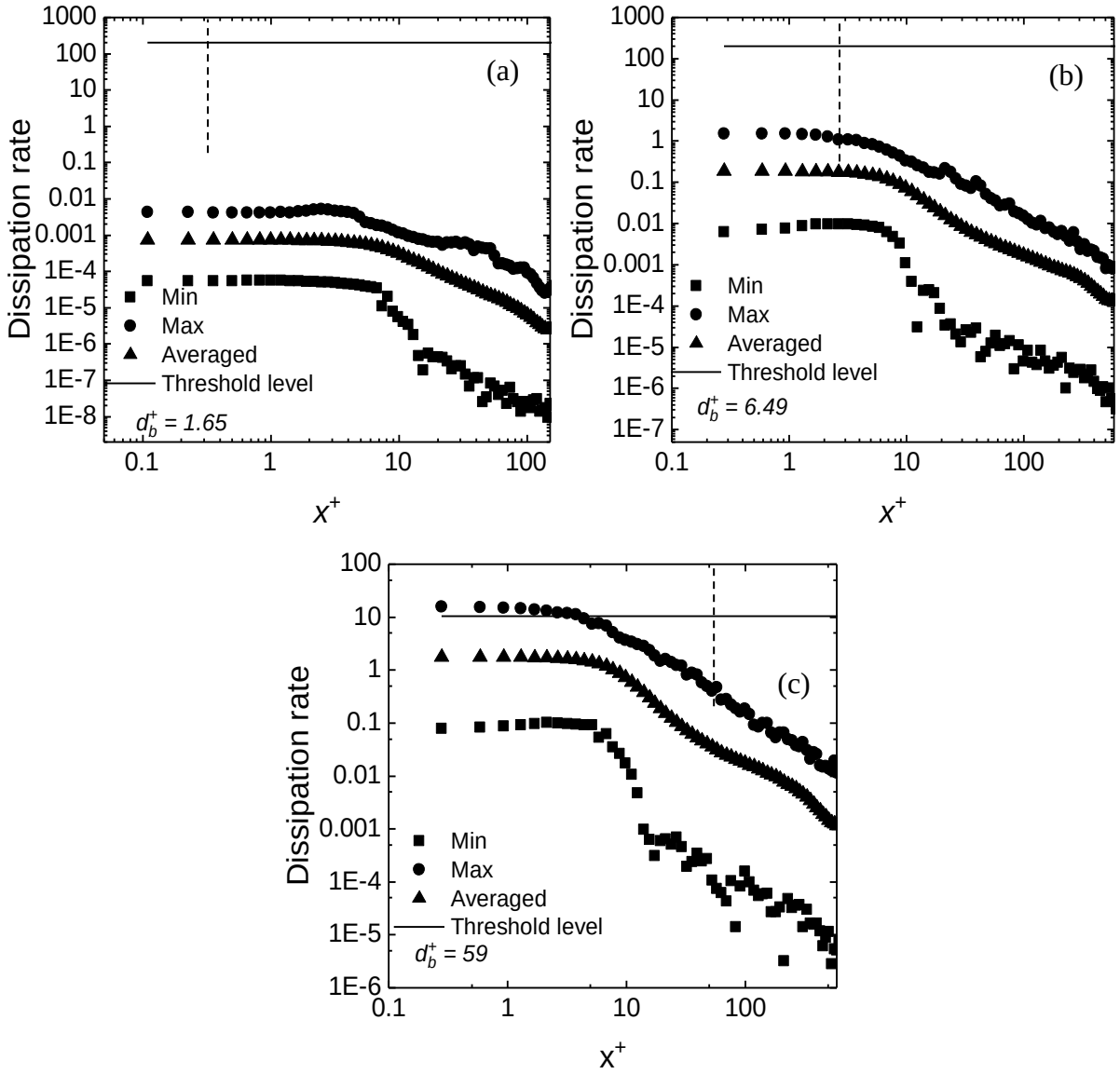

Figure 6.1 Turbulence kinetic energy dissipation rates across the channel in wall units: (a) $Re_\tau = 150$, d_b = 220 μm (1.65 wall units); (b) $Re_\tau = 590$, d_b = 220 μm (6.5 wall units); and (c) $Re_\tau = 590$, d_b = 2000 μm (59 wall units). Dashed line is the location of the centre of the bubble when it is closest to the channel wall.

In Figure 6.1(a), the flow of $Re_\tau = 150$ with a bubble of 220 μm is presented, while Figure 6.1(b) and (c) represent a flow of $Re_\tau = 590$ with bubble sizes 220 μm and 2000 μm, respectively. The threshold lines represent the dissipation rate required to break the bubble, with the centre of the bubble identified by the dashed line. Remember that since the Lagrangian bubble tracker makes a point particle assumption, it is the dissipation rate at the location of the bubble centre that must be considered in regards to bubble breakup. In Figure 6.1(a) and (b), the threshold level lies above the maximum turbulence kinetic energy dissipation rate in the fluid and hence no breakup is expected. In Figure 6.1(c) the maximum dissipation rate is slightly higher than the threshold level, but only very close to the wall and at locations where the bubble cannot interact with the flow turbulence since the position of the centre of the bubble lies at higher x^+ values. Therefore, no breakup is also expected for the flow considered in Figure 6.1(c).

Therefore, to observe and study bubble breakup, turbulent flows of refrigerant bubbles R134a, which have a much lower surface tension than air bubbles in water, were considered. Figure 6.2 represents turbulence kinetic energy dissipation rates and thresold levels for breakup for flows of refrigerant R134a at a shear Reynolds number $Re_\tau = 360$ with bubbles of different size.

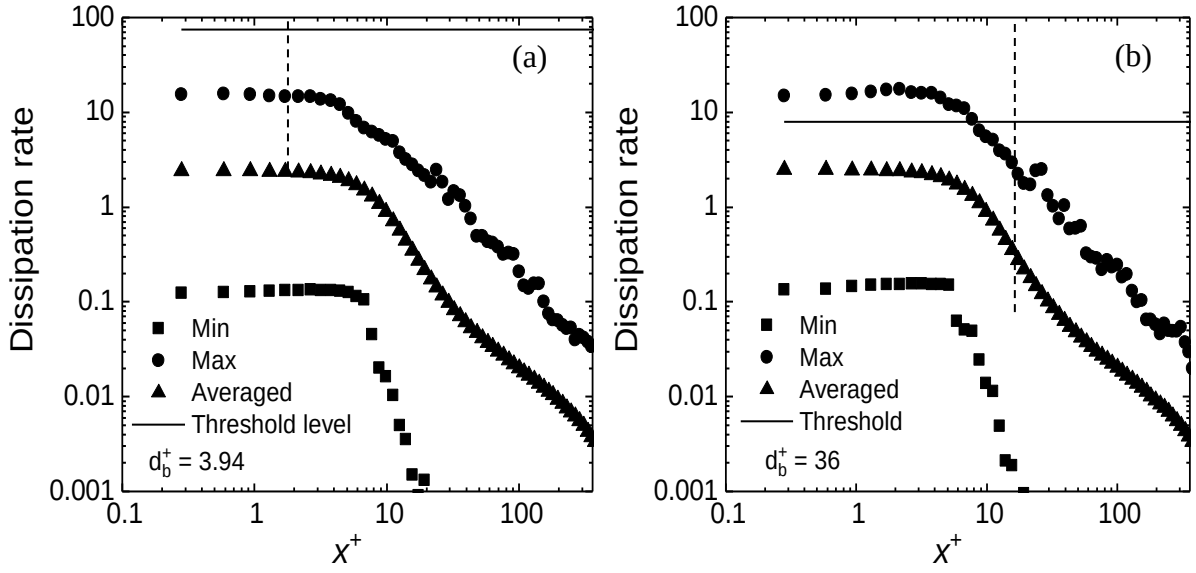

Figure 6.2 Turbulence kinetic energy dissipation rates across the channel in wall units for a flow of refrigerant at $Re_\tau = 360$: (a) d_b = 220 μm (3.94 wall units); and (b) d_b = 2000 μm (36 wall units).

Figure 6.2(a) represents bubbles of size $d_b = 220$ μm and Figure 6.2(b) of size $d_b = 2000$ μm. The threshold level again lies above the peak dissipation rate in Figure 6.2(a) and just below in Figure 6.2(b), but again, in Figure 6.2(b), the dissipation rate at the bubble centre is only just equal to the threshold and no breakup was observed during simulations.

6.2 Higher Reynolds Number Single-Phase Flow

Since turbulence levels in the flows investigated thus far where not sufficient to achieve bubble breakup, further work was carried out at a higher Reynolds number flow of water at $Re_\tau = 2000$, with a corresponding bulk Reynolds $Re_b = u_b h/\nu = 51{,}500$. The velocity statistics of the single phase flow were validated by comparing with the DNS results obtained by Bernardini et al. (2014). The LES results did not give perfect agreement with the DNS predictions, as shown in Figure 6.3, but the motivation behind moving to a higher Reynolds number flow was to allow testing of the ability of the overall model to predict bubble breakup, even under the known limitations of the LES with the computational grid employed. The DNS work used $8192 \times 1024 \times 4096$ nodes, which is far more than the number of nodes used in the present LES.

Table 6.2 Higher Reynolds number simulation parameters for bubble breakup.

Single phase flow parameters	
Reynolds number (Re_τ)	2000
Bulk Reynolds number (Re_b)	51500
Shear velocity (u_τ)	0.10 ms^{-1}
Bulk velocity (u_b)	2.18208 ms^{-1}
Fluid density (ρ)	1000 kgm^{-3}
Computational domain	$2h \times \pi h \times 2\pi h$

Table 6.2 present a summary of the single-phase flow properties. In Figure 6.3, the single-phase velocity statistics are presented and compared against the DNS results. The time-averaged mean streamwise velocity is plotted in Figure 6.3(a). The DNS peaks close to 25 whilst the LES peak is at 23.6, and close to the walls it is observed that the LES significantly over predicts the DNS. In Figure 6.3(b), the normal and shear stresses are

presented. The mean streamwise velocity fluctuations from the LES are high at 3.55 compared to an equivalent DNS prediction of approximately 3. The spanwise and wall-normal velocity fluctuations are under predicted when compared with the DNS reults, as is the shear stress considered. In Figure 6.3(c), a two-dimensional representation of the instantaneous velocity of the single phase flow is given. High velocities and turbulence levels are found in the flow, with turbulence dominating the majority of the channel, confining viscous effects and the viscous sublayer to very near-wall regions.

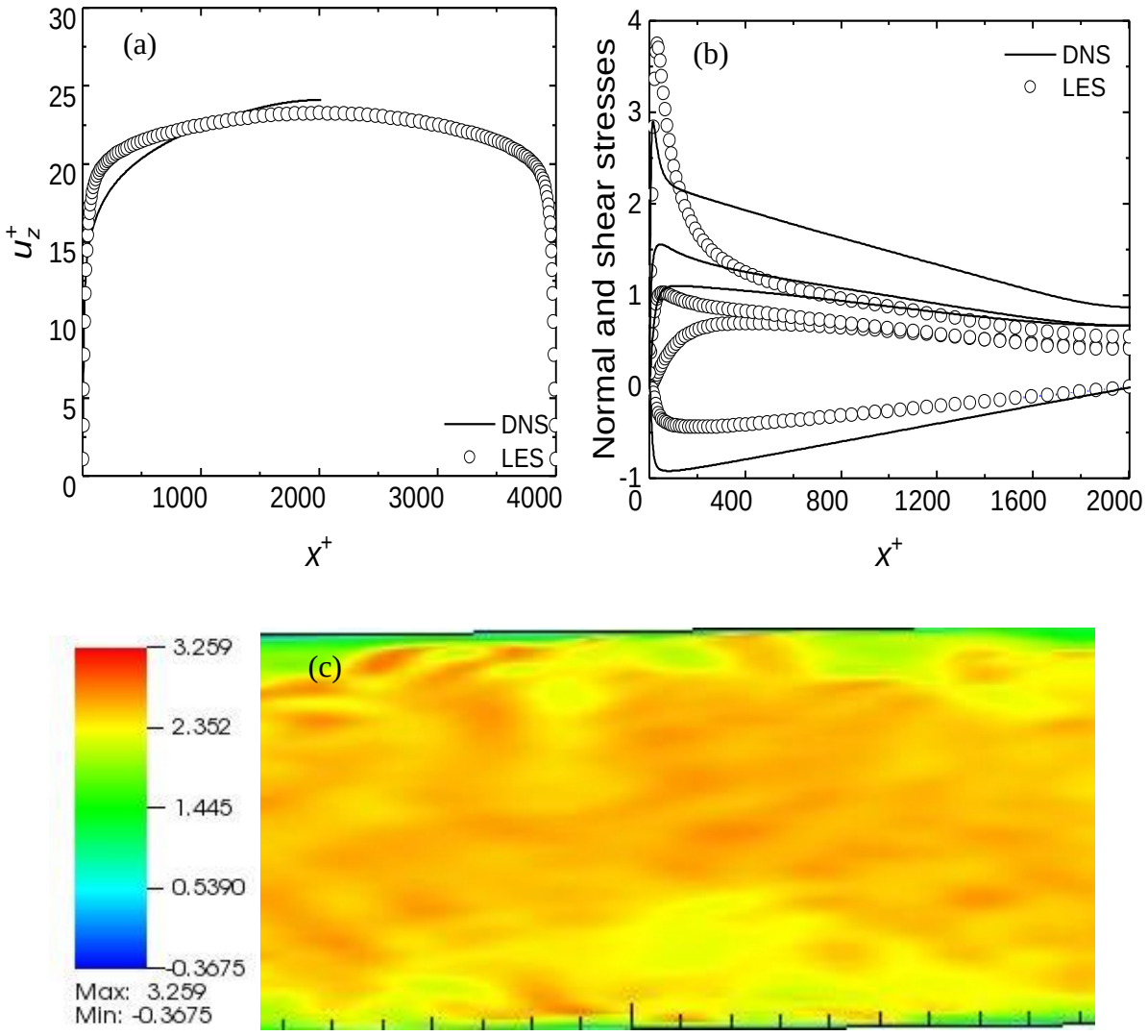

Figure 6.3 Single-phase predictions of Reynolds number $Re_\tau = 2000$ flow: (a) streamwise mean velocity in comparison with DNS (Bernardini et al., 2014) ; (b) normal and shear stresses in comparison with DNS; and (c) two-dimensional representation of LES instantaneous velocity.

Air bubbles of different sizes were injected into the flow to check whether the critical threshold level required to observe breakup was achieved, as shown in Figure 6.4. In Figure 6.4(a), no break is possible due to the small bubble size, with the critical level of turbulence kinetic energy dissipation rate required for bubble breakup still lying well above the dissipation rates in the flow. The same is true for $d_b = 220$ μm in Figure 6.4(b). However, in Figure 6.4(c), where the bubble size is $d_b = 2000$ μm, the turbulence dissipation rates at the bubble centre indicates that breakup may be possible.

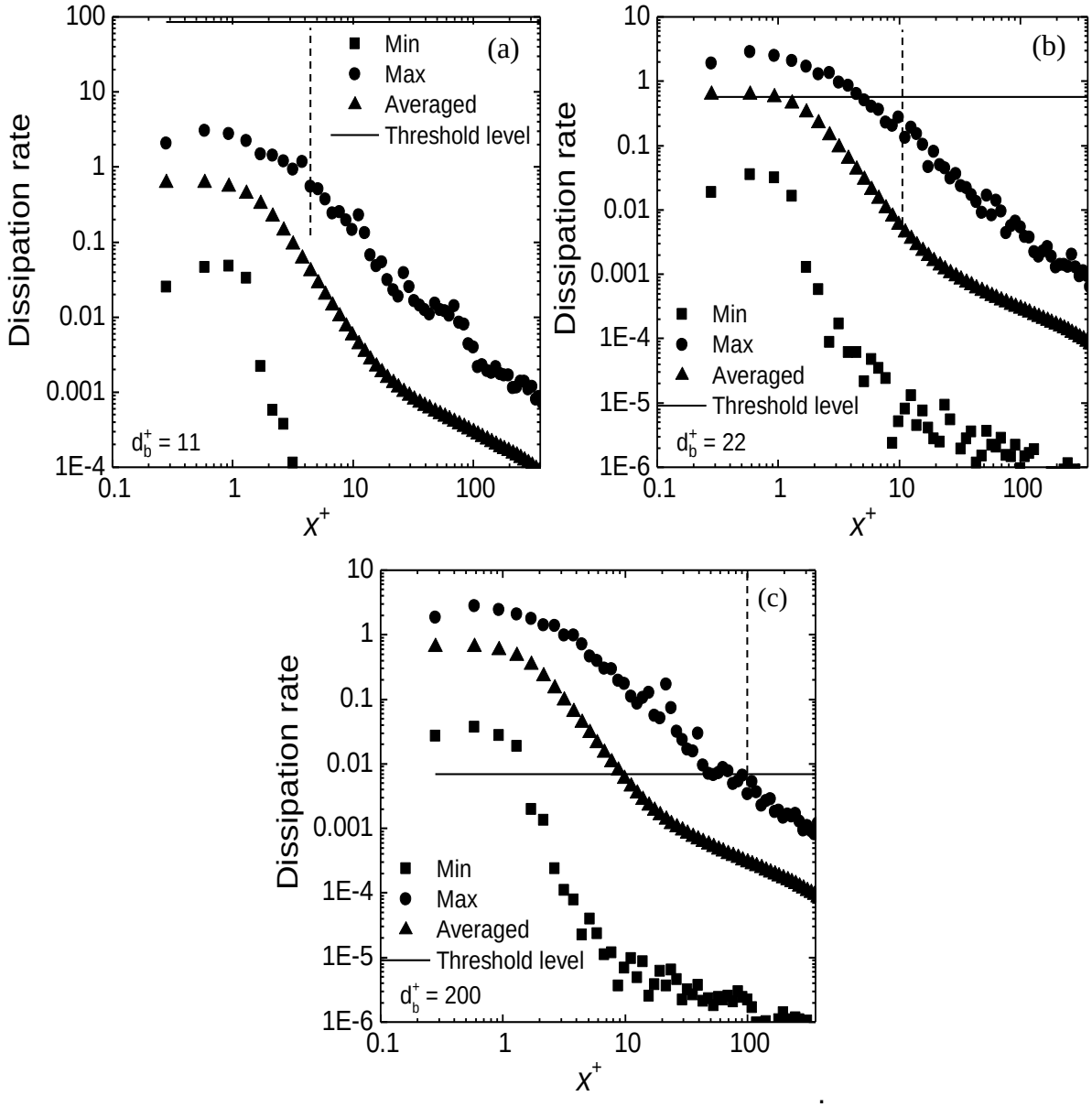

Figure 6.4 Turbulence kinetic energy dissipation rates across the channel in wall units at $Re_\tau = 2000$: (a) d_b = 110 μm (11 wall units); (b) d_b = 220 μm (22 wall units); and (c) d_b = 2000 μm (200 wall units).

Table 6.3 gives a summary of the number of bubble breakups recorded for the three bubble sizes noted in Figure 6.4 for a total simulation time of $t^+ = 900$. Only 11 bubble breakups were recorded for $d_b = 2000$ μm, with no breakups recorded for the other two bubble sizes, as anticipated. These results indicate that, even for the largest bubble size, the surface restoring pressure of the bubble is still sufficient to overcome the surface deformation induced by turbulent fluctuations.

Table 6.3 Breakup statistics for bubbles in water.

Bubble size	**Conditions**	**Number Breakups**	**Runtime**
$d_b = 110\ \mu m$	Breakup only	0	$t^+ = 900$
$d_b = 220\ \mu m$	Breakup only	0	$t^+ = 900$
$d_b = 2000\ \mu m$	Breakup only	11	$t^+ = 900$

In Figure 6.5, dissipation rate plots are shown at a shear Reynolds number of 1154 for a flow of refrigerant R134a. Note that this flow is equivalent to a $Re_\tau = 2000$ flow of water, taking into account the changes in physical properties of the carrier fluid. The same comparative analysis was carried out using refrigerant bubble sizes $d_b = 110$ μm, 220 μm and 2000 μm, with the aim of obtaining a more significant number of breakups. Figure 6.5(a) is for a bubble size $d_b = 110$ μm, Figure 6.5(b) for $d_b = 220$ μm while Figure 6.5(c) is for $d_b = 2000$ μm. From the results, it can be concluded that bubble breakup is likely to occur for all three bubble sizes. When the flows were run with bubbles present, very few breakup events were recorded at $d_b = 110$ μm, a reasonable number were found at $d_b = 220$ μm and at $d_b = 2000\ \mu m$ such events occurred sporadically. These observations are in line with the fact that bubbles will continue to breakup until the smallest size of bubble formed is one where the surface restoring pressure exceeds the turbulence kinetic energy dissipation rate generated by the flow. This is considered further below.

Having established that a $Re_\tau = 1154$ refrigerant R134a flow exhibited bubble breakup, further work for this case was undertaken, as described below.

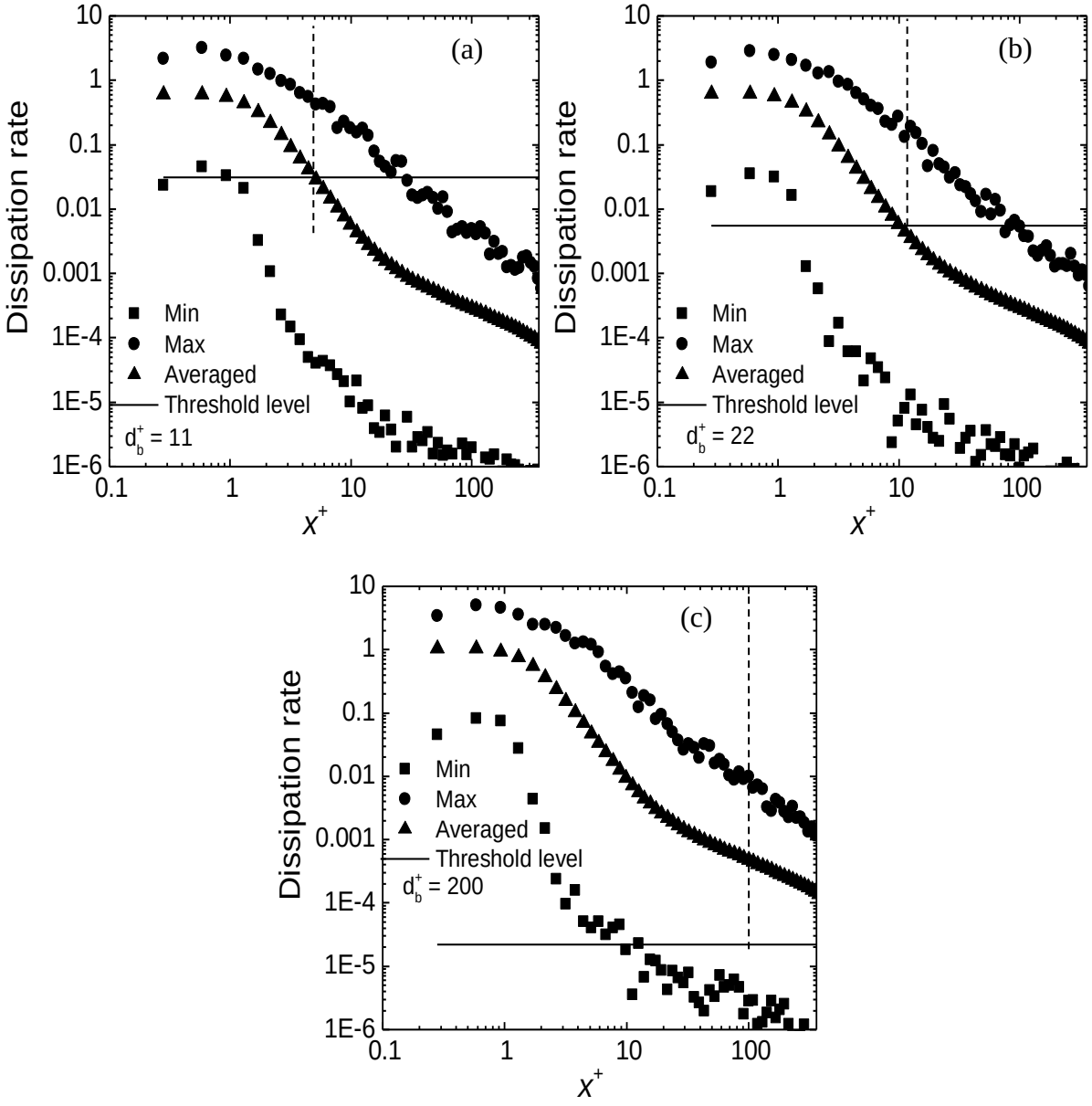

Figure 6.5 Turbulence kinetic energy dissipation rates across the channel in wall units for a flow of refrigerant R134a at $Re_\tau = 1154$: (a) d_b = 110 μm (11 wall units); (b) d_b = 220 μm (22 wall units); and (c) d_b = 2000 μm (200 wall units).

6.3 Breakup Results for Refrigerant Bubbles (R134a)

Following the very few number of breakups recorded in the air-water simulations, even at high Reynolds number, additional simulations at a high Reynolds number were also performed for a flow of refrigerant R134a, as noted above. Refrigerant bubbles of diameter $d_b = 110$ μm, 220 μm and 2000 μm were simulated in a flow at $Re_\tau = 1154$, in both upflow and downflow. The carrier and dispersed phase simulation parameters were

chosen at room temperature and are presented in Table 6.4. It is worthy of note that refrigerant R134a is the chemical compound 1, 1, 1, 2-tetra-fluoro-ethane, containing two atoms of carbon, four fluorine atoms and two atoms of hydrogen. Its chemical formula is CF_3CH_2F and its molecular weight 133.4. With respect to other refrigerants, such as hydrofluorocarbon (HFC) and R12, which have similar physical and thermodynamic properties, R134a depletes the ozone layer less and has very little greenhouse effect. The Motreal Protocol established in 1987 addressed the phase out of ozone depleting substances such as chlorofluorocarbons and hydrochlorofluorocarbons. In 2013, a collaboration between the Chinese government and the United States of America was successfully established to implement changes in HFC use with the objective of avoiding a rise of 0.5 ^{0}C in the global temperature that was forecast to occur by 2100 (Field and Hrnjak, 2007).

Table 6.4 Refrigerant bubbles (R134a) simulation properties.

Liquid-phase	**Gas-phase**
$\rho = 1206.5$ kgm^{-3}	$\rho_b = 28.4$ kgm^{-3}
$Re_\tau = 1154$	$\sigma = 8.08$ x 10^{-3} Nm^{-1}
$\nu = 9.697$ x 10^{-7} m^{2}s^{-1}	$d_b = 110$ μm, $n_b = 1812729$
	$d_b = 220$ μm, $n_b = 226591$
	$d_b = 2000$ μm, $n_b = 302$

The bubbles were initially injected uniformly within the computational domain and the initial velocity of each bubble was set equal to that of the fluid at the bubbles' location. The overall volume fraction of the dispersed bubbles was $\phi = 10^{-3}$. The initial concentration of the three bubble sizes was sampled at time $t^+ = 0.0$ to obtain the initial bubble distribution profiles presented in Figure 6.6. The total simulation period in wall units was $t^+ = 3000$, which was sufficient enough for a bubble with a speed equal to the average fluid velocity to move through the entire streamwise length of the channel more than twelve times. The time span utilised for averaging the statistics was $t^+ = 1500$ for all bubble sizes.

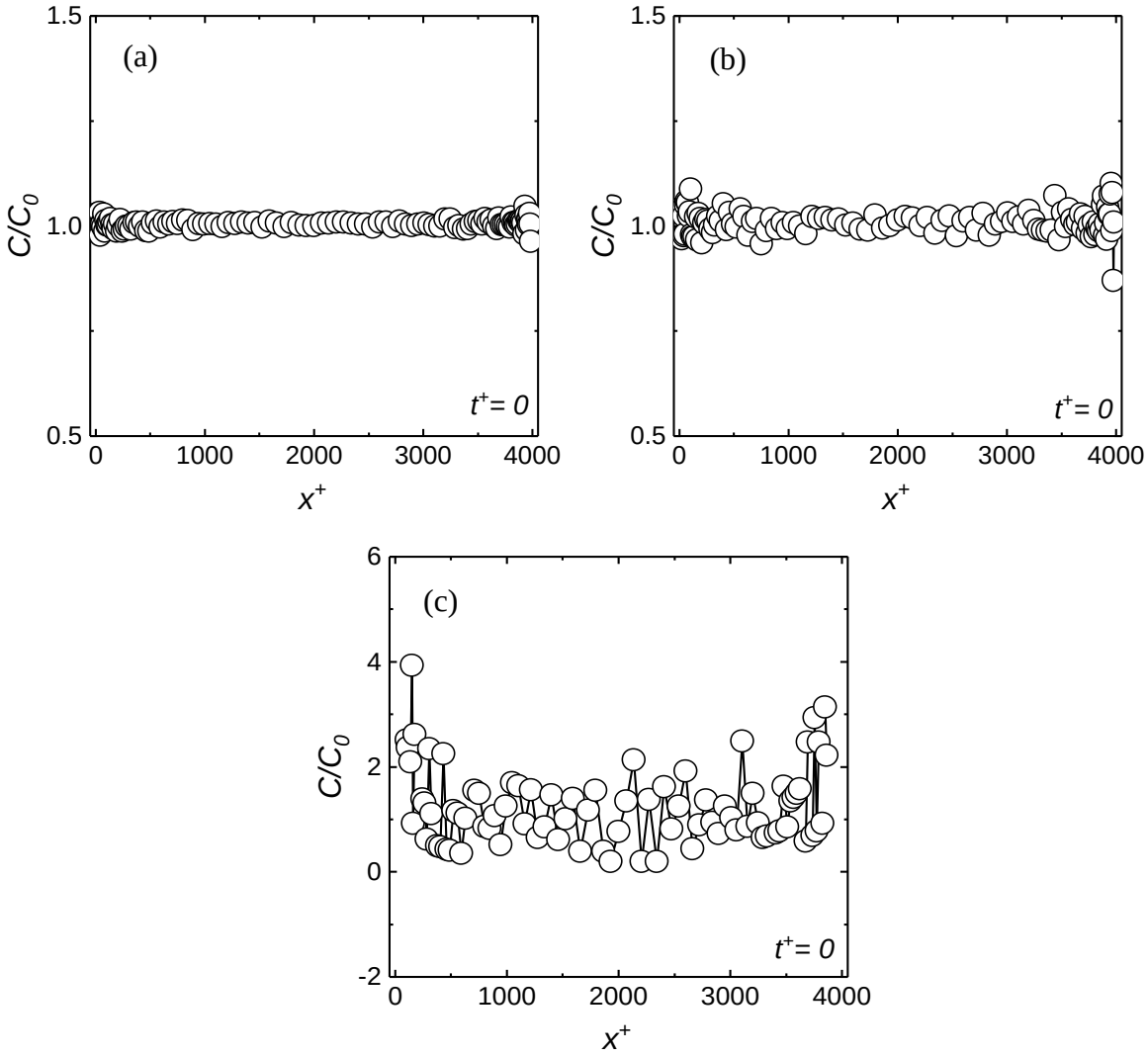

Figure 6.6 Initial bubble concentration profiles for the three bubble sizes at start-up of the simulations: (a) $d_b = 110$ μm; (b) $d_b = 220$ μm; and (c) $d_b = 2000$ μm.

The initial concentration plots in Figure 6.6 shown an approximately uniform distribution of bubbles across the channel for all bubble sizes. Figure 6.6(a) and (b) in particular are uniform, except close to the channel wall where some variation is inevitable. The profile in Figure 6.6(c) is significantly less uniform, however, although this was due to the larger bubble size. In this case, therefore, there were 129 computational nodes across the channel in the wall normal direction, and injecting 302 bubbles (Table 6.4) equally distributed resulted in some control volumes surrounding the nodes containing a reduced number of bubbles. The LES code was used in such a way that the mesh spacing close to the channel walls was smaller than elsewhere in the flow to ensure resolution of the flow behaviour close to solid surfaces. In such areas, the size of the

bubbles was larger than the mesh spacing, and some bubbles therefore occupied or overlapped into neighbouring cells, violating the point particle assumption. However, the simulation at the largest bubble size was nevertheless run to detect the occurrence of breakup and test the breakup model, also considering the fact that when breakup occurs progressively smaller bubbles are formed.

As noted, bubble breakup is determined by the level of the turbulence kinetic energy, and in particular its dissipation rate, within a flow, and in Figure 6.7 the number of bubble breakups with time is presented for bubble sizes $d_b = 110$ μm, 220 μm and 2000 μm. It can be seen that bubbles breakup in all three cases since the turbulent stresses on the bubble surface overcome the surface restoring effect of the surface tension (Martinez-Bazan et al., 1999; Sungkorn et al., 2012; Xue et al., 2017). In Figure 6.7(a) for $d_b = 110$ μm, the number of breakups in upflow is higher than in downflow, with a total number of 106 breakups recorded in upflow compared to 64 in downflow at the end of the simulation. It is noteworthy that despite the large number of bubbles injected (1,812,729), the number of breakups is still limited since the surface restoring pressure is high for a bubble of relatively small diameter, with high turbulence levels required to cause breakup. Bubble breakup is more significant in upflow because of the influence of the lift force in this case, which pushes bubbles towards the wall and into regions of high turbulence kinetic energy disspation rate, whilst in downflow the bubbles move towards the centre of the channel and away from such regions.

In Figure 6.7(b), the total number of breakups with time for $d_b = 220$ μm is presented. For the upflow, the number of breakups realised was 3,859, while the downflow gave 2,605 breakups, by the end of the simulation. The lower number in downflow is caused to some extent by the lower turbulence levels observed in the four-way coupled simulations in this case, as compared to in upflow, but mainly due to the accumulation of the bubbles driven by the lift force in the centre of the channel, where turbulence levels are low. It is clear that at times $0.0 \leq t^+ \leq 300$, there is a progressive increase in the number of bubble breakups, with more occurring in downflow than in upflow, with this trend observed for all bubble sizes. This is caused by bubble buoyancy effects conflicting with the downward flow direction and causing perturbations which result in additional breakup. The path of bubbles in downflow was therefore extremely irregular, as noted previously, whereas in upflow their paths were in line with the fluid streamlines and

relatively predictable. At later times, the number of breakups in upflow eventually exceeds that in downflow due to bubble migration towards the wall. Over $500 \leq t^+ \geq 2500$ in Figure 6.7(b), the breakup rate reduces and tends towards a steadily increasing rate, with the upflow experiencing a larger number of breakups. The plot for breakup of bubble size $d_b = 2000$ μm, with number of bubbles injected equal to only 302, is shown in Figure 6.7(c). The total number of breakups for upflow and downflow were 304 and 300, respectively, at the end of the simulation. The breakup rate here is faster than in the other two cases as larger bubbles have a low surface restoring capability, as in Eq. (3.67), and are highly buoyant. At $t^+ \geq 600$, all the primary bubbles had broken up into at least two equal sized bubbles in downflow, whereas in upflow further breakup continued to occur until $t^+ = 800$.

Figure 6.8 presents breakup locations across the vertical channel for the various bubble sizes. Figure 6.8(a) is for $d_b = 110$ μm at $t^+ = 800$, Figure 6.8(b) for $d_b = 220$ μm at $t^+ = 2600$, and Figure 6.8(c) is for $d_b = 2000$ μm at $t^+ = 800$. For the 110 μm and 220 μm bubble sizes, breakup occurs in the near-wall regions of the channel where the turbulence energy dissipation rate is high. The results in Figure 6.8(c) show a broader spatial distribution due to the fact that when these large bubbles break into two smaller bubbles, those daughter bubbles, which could now be tracked in the computational mesh, undergo further breakup if located in a region where the dissipation rate is sufficiently high.

Cumulative plots showing the number of bubble collisions, coalescences and breakups in upflow and downflow are presented in Figure 6.9(a) and (b) for bubble size $d_b = 110$ μm, Figure 6.9(c) and (d) for $d_b = 220$ μm, and Figure 6.9(e) and (f) for $d_b = 2000$ μm. As previously noted, all events occur at their highest levels in the near-wall regions. In these regions, due to the high turbulence levels, not all collisions result in coalescence because the contact time between bubbles is insufficient to allow for the liquid film trapped between the colliding bubbles to drain. In the centre of the channel, for the smaller bubble sizes at least, where the turbulence is lower and the contact time higher, almost all collisions result in coalescence. Hence, although coalescence events are much lower in number in the channel centre, their coalescence efficiency is high, in agreement with film-drainage theory. Breakup events for the smallest bubble size are relatively low in number since the surface restoring pressure is high for a bubble of relatively small diameter. For $d_b = 220$ μm, in regions where the turbulence is high enough for breakup to occur, the

number of breakup events almost matches the number of coalescences, although in these flows the high turbulence encourages slightly more coalescences than breakup events. Finally for the largest bubble size, the number of breakup events is greater than the number of collisions and coalescences in upflow and downflow. Again, this arises due to the large size of these bubbles and their low surface restoring capability. Overall, the results obtained show good qualitative agreement with previous experimental works for particle (Randolph, 1969) and bubble (Martinez-Bazan, 1998) breakup.

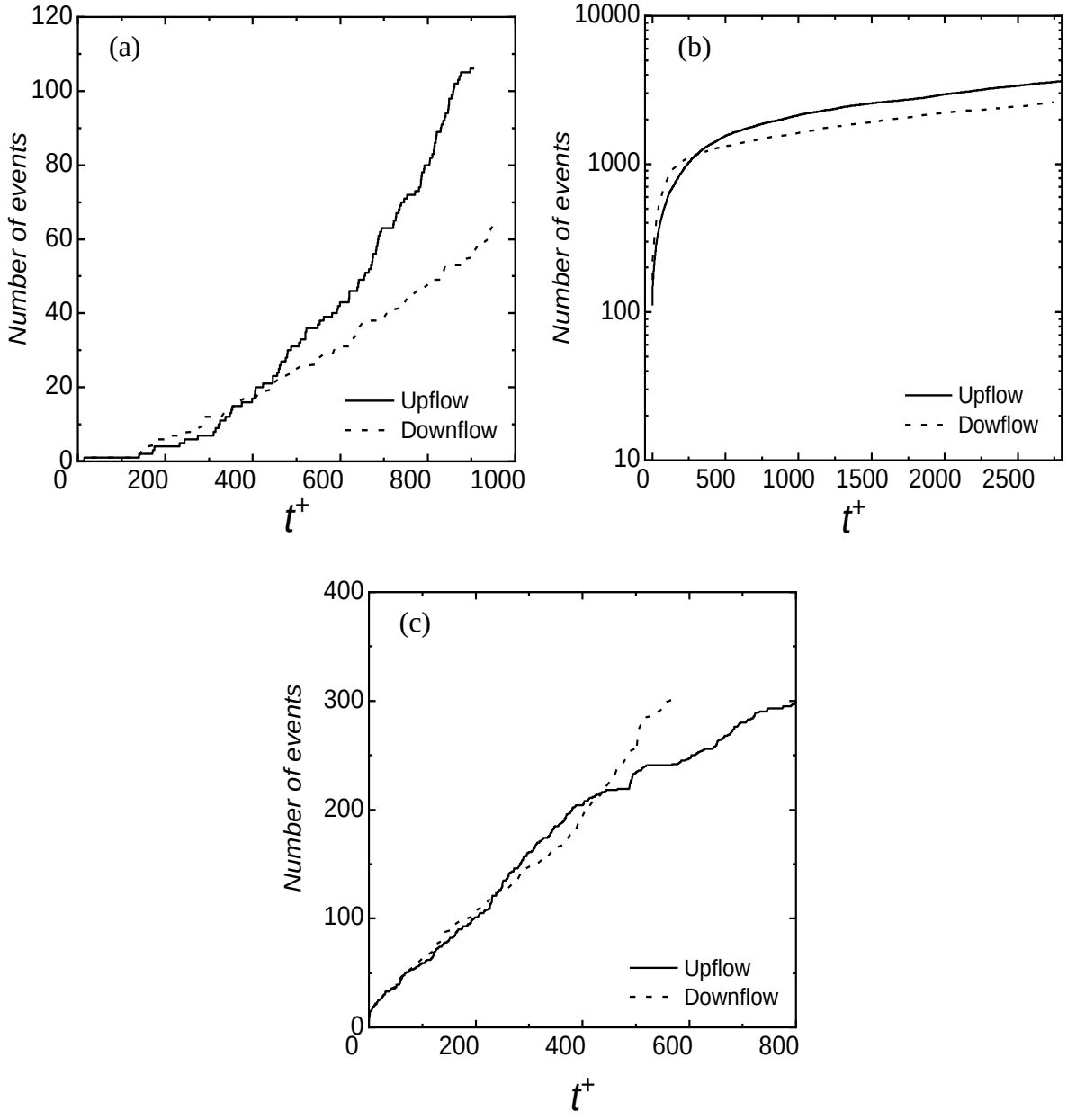

Figure 6.7 Number of bubble breakups with time for a flow of $Re_\tau = 1154$ with refrigerant R134a bubbles: (a) $d_b = 110$ μm; (b) $d_b = 220$ μm; and (c) $d_b = 2000$ μm.

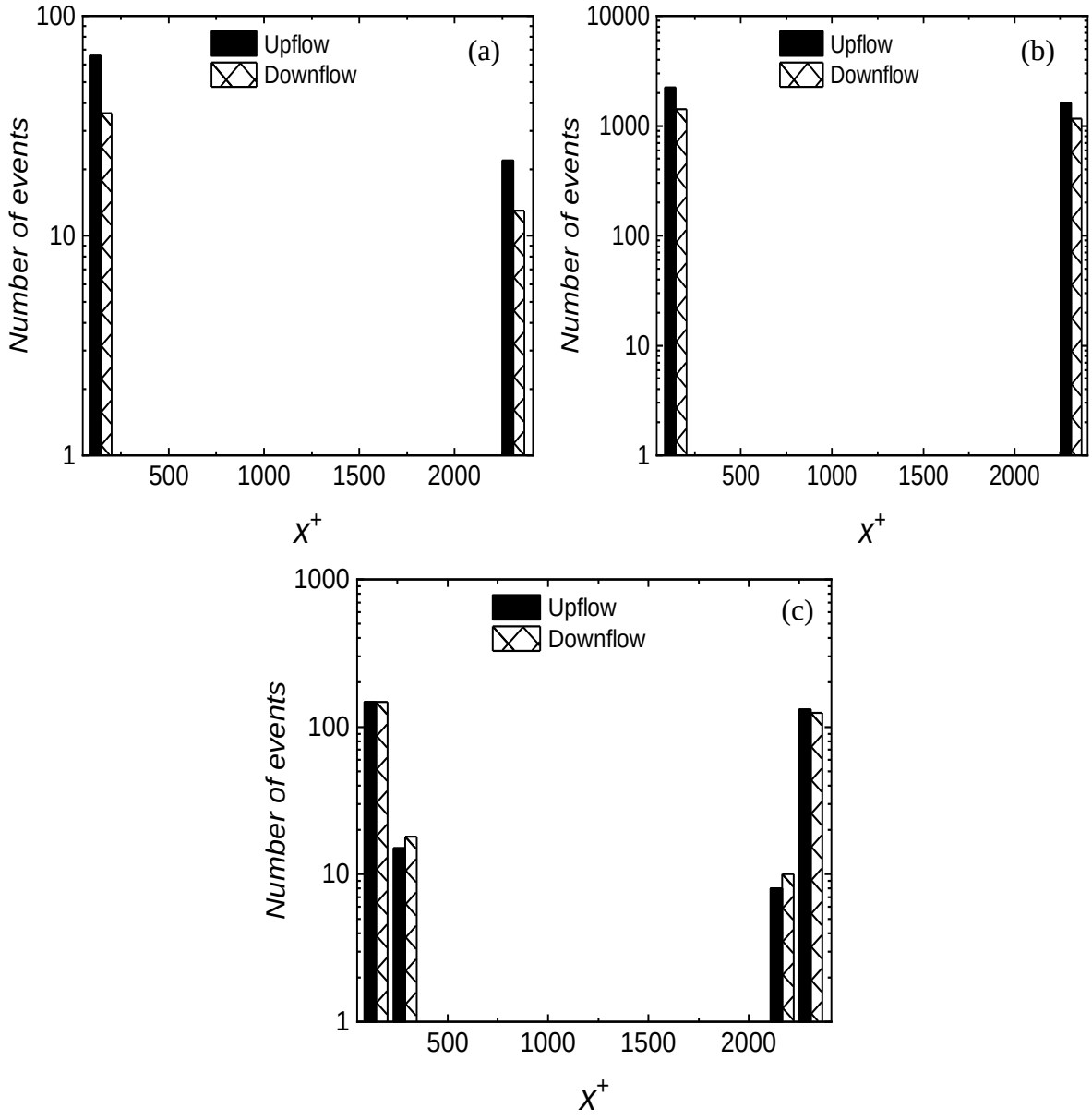

Figure 6.8 Breakup locations across the channel for a flow of $Re_\tau = 1154$ with refrigerant R134a bubbles: (a) $d_b = 110$ μm at $t^+ = 800$; (b) $d_b = 220$ μm at $t^+ = 2600$; and (c) $d_b = 2000$ μm at $t^+ = 600$.

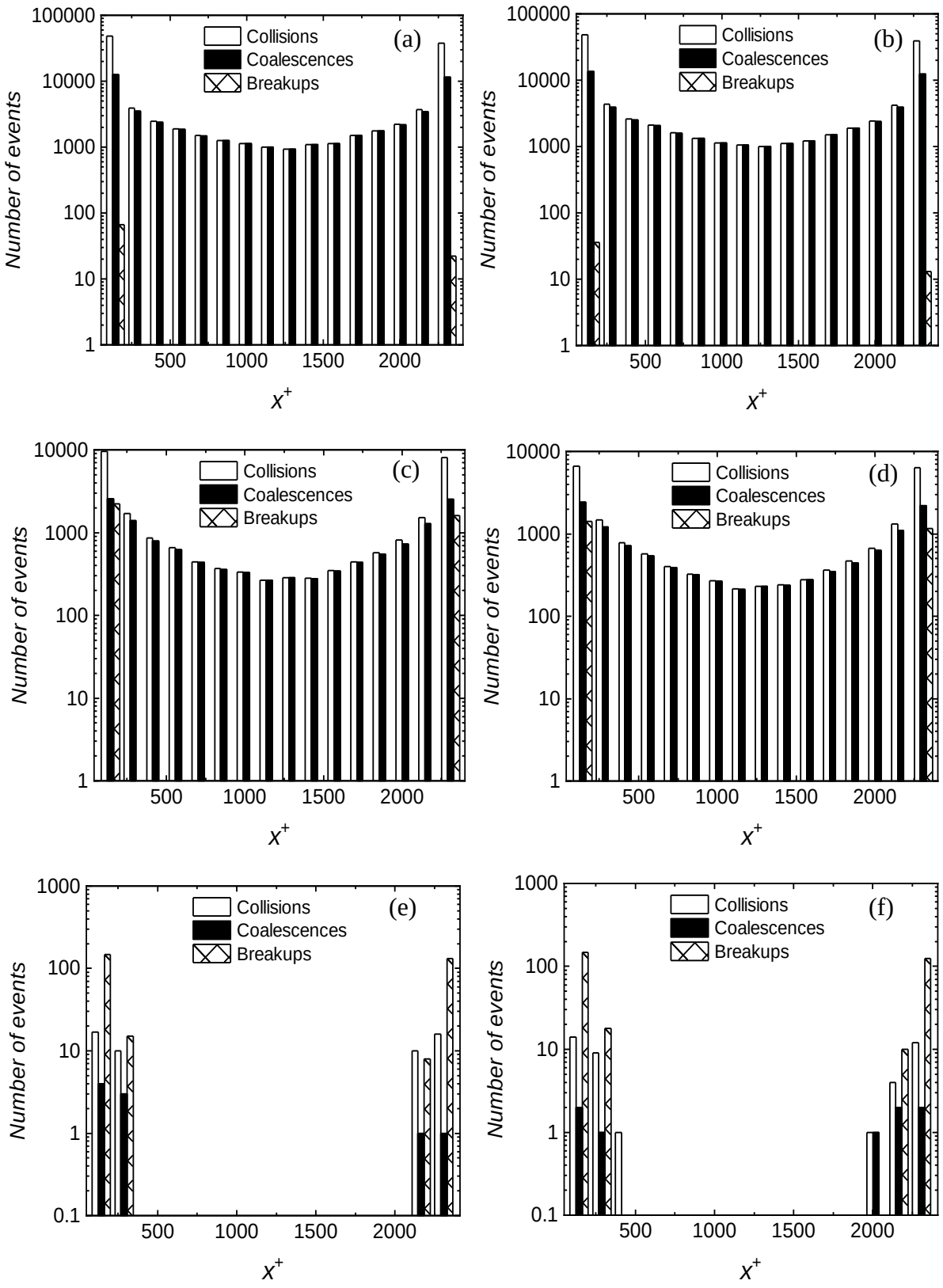

Figure 6.9 Number of bubble collisions, coalescences and breakups for a flow of $Re_\tau = 1154$ with refrigerant R134a bubbles: (a) $d_b = 110$ μm at $t^+ = 800$; (b) $d_b = 220$ μm at $t^+ = 2600$; and (c) $d_b = 2000$ μm at $t^+ = 600$. (a, c, e) upflow; and (b, d, f) downflow.

Lastly, from the results given in Figure 6.10 for the flow with $d_b = 220$ μm bubbles, it is seen that not all collisions result in coalescence as the flow turbulence structure does not allow sufficient contact time for the liquid film between the bubbles to drain and coalescence to occur, as noted above. In Figure 6.10(a), for upflow, a large number of bubble-bubble collisions occur, but with significantly fewer coalescences occurring at all times. The number of collisions without coalescence increases with time until at the end of the simulation the cumulative number of collisions without coalescence slightly exceeds those with. Similar trends are found for the downflow case, although here, at the end of the simulation, the number of collisons with and without coalescence are approximately equal. These trends occur due to the migration over time of bubbles towards the wall in upflow, where turbulence levels are high and film-drainage times are hence reduced, and in downflow due to the migration of bubbles towards the channel centre with lower turbulence levels, so that collisions without coalescence, relative to the upflow case, are fewer in number.

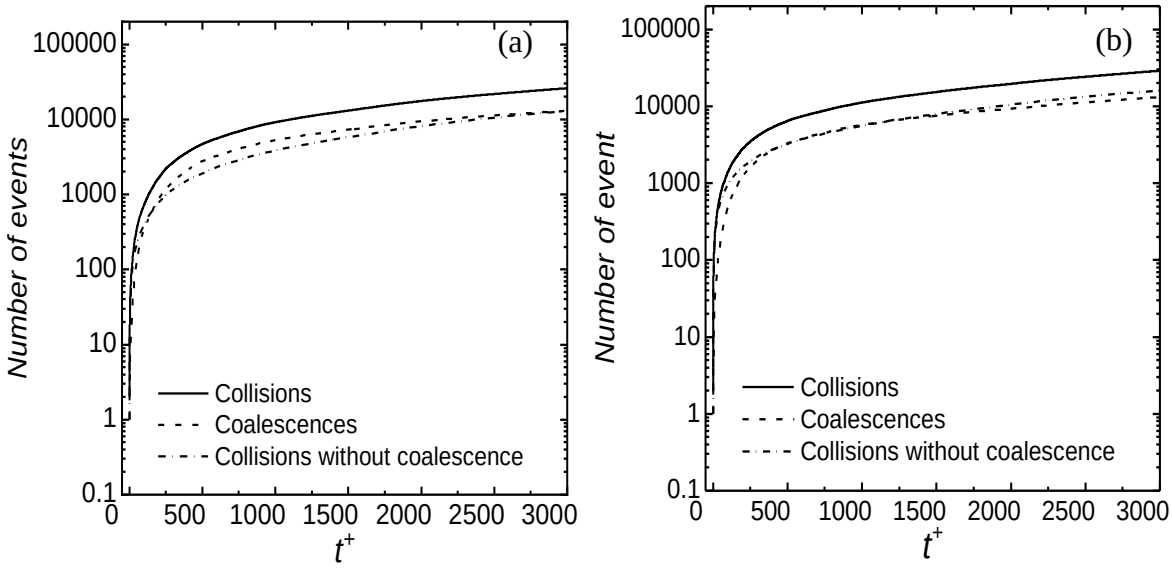

Figure 6.10 Number of bubble collisions, coalescences and collisions without coalescence for $Re_\tau = 1154$ with refrigerant R134a bubbles and $d_b = 220$ μm: (a) upflow; and (b) downflow.

6.4 Summary of Bubble Breakup Studies in Vertical Channel Flows

Four-way coupled simulations of bubbly flows in vertical channels have been performed using the enhanced LPT routine that handles both coalescence and breakup processes,

coupled to LES of the liquid phase. For bubble breakup to occur, the turbulent flow structures surrounding the bubble must be high enough to overcome the surface restoring force resulting from the surface tension. Two different water flow Reynolds numbers, Re_τ = 150 and 590, were simulated by injecting air bubbles of various sizes. No bubble breakup was recorded, and it has been demonstrated that this is as a result of the turbulence kinetic energy dissipation rate in the flow not being sufficiently large to deform and breakup the air bubbles dispersed in the flow. The flow turbulence level was consequently increased by performing runs at a shear Reynolds number $Re_\tau = 2000$, but only 11 bubble breakups were obtained for the large $d_b = 2000$ μm bubbles considered.

In order allow bubble breakup in reasonable quantities, additional simulations were performed for the case of refrigerant R134a at a shear Reynolds number of 1154, with refrigerant bubbles of $d_b = 110, 220$ and 2000 μm. This fluid was chosen due to its low surface tension which encourages bubble breakup. The ability of the overall model to predict coalescence and breakup in such flows has been evaluated, as well as the impact of the flow conditions on the two phenomena.

Results showed that breakup took place only in regions of the flow where the turbulence kinetic energy dissipation rate is sufficiently high to deform and break the three bubbles sizes injected, specifically in near-wall regions. Coalescence and breakup were favoured in upflow conditions under the influence of the lift force which promotes bubble migration towards the highly turbulent near-wall regions, with turbulence found to significantly impact the level of bubble interaction. Coalescence was dominant at low turbulence levels and breakup, which was only detected in the R134a flow, was favoured at high turbulence levels. The results also showed that coalescence is favoured at small bubble size but, as the bubble diameter is increased, the phenomena of breakup becomes comparable with and, at the highest bubble diameter considered, is favoured over coalescence. Overall, bubble breakup was found to be infrequent at low-medium turbulence levels or low-medium bubble sizes.

A review of previous work shows that bubble breakup studies have only been carried out in bubble columns and ducts, and for bubbles in the diameter range 2 mm $\leq d_b \leq$ 6 mm. No previous studies have achieved the prediction of microbubble breakup in any flow,

and hence the conclusions reached in relation to channel flows containing microbubbles are original.

The study of breakup is of importance industrially since interfacial transfer processes, linked to the bubble size distribtuion, impact on mixing as well as heat and mass transfer in bubbly flows. Overall, the results demonstrate the capabilities of the model derived to predict microbubble behaviour and changes in the bubble size distribution. Future developments should include application of the methodology to flows of industrial interest, and prediction of the full-evolution of the bubble size distribution in such flows through bubble coalescence and breakup.

CHAPTER 7

CONCLUSIONS AND RECOMMENDATIONS FOR FURTHER WORK

In this chapter detailed highlights of the conclusions drawn from this study are summarized. Further work is also proposed to improve and expand our understanding and ability to accurately predict bubble behaviour in multiphase flows, including their application to problems of industrial relevance.

7.1 Conclusions

The work described in this thesis was undertaken to gain insight into the complex nature of microbubbles in turbulent flows, starting using the simplest coupling technique between the phases and building to a more complex approach where bubble coalescence and breakup can be accommodated. The developments described have also led to improvments in our ability to accurately predict such flows. The results and conclusions reached are of relevance to processes employed in a wide range of applications, such as the transfer and processing of oil and gas, cooling in nuclear reactors and steam generators, bubble column reactors, and the evaporation and condensation of refrigerants in air conditioning equipment, to name but a few.

In particular, the influence of bubble interactions and fluid phase behaviour in turbulent flows on bubble dispersion have been investigated. The mathematical modelling technique used was based on the large eddy simulation (LES) methodology embodied in the BOFFIN LES code, with complete flow solutions provided by coupling the LES to a Langrangian bubble tracking technique which was used for the prediction of bubble motion and interaction.

The BOFFIN LES flow solver and the Lagrangian approach have been used previously for studying solid particulate flows. These were modified and extended in this work to cover bubbly flows. In addition to the main models for the LES and the bubble tracker, the sub-grid scale model within the LES and the way in which momentum feedback from the

bubbles to the fluid are handled were described. Bubble force models, the bubble collision model and models for the coalescence and breakup of bubbles implemented in the overall model were also presented, and were included to allow a systematic study of bubbles in turbulent flows with a view to provide methods for their accurate prediction and to allow insight into the physics of bubbly flows. The modified Lagrangian tracker accounts for gravity-buoyancy, drag, lift, pressure gradient and added mass forces acting on the bubbles. The complete model has been applied to turbulent horizontal, and vertical upward and downward, channel flows to investigate the dynamics of bubbles in one-way, two-way and four-way coupled flow regimes.

The introduction of coupling effects between the phases was preceded by simulating single-phase channel flows at four Reynolds numbers in order to validate the LES predictions. The results generated by the LES were validated against direct numerical simulations (DNS) of channel flows with shear Reynolds numbers, $Re_\tau = 150$, 300, 590 and 2000 (Marchioli et al., 2008; Marchioli and Soldati, 2007; Moser et al., 1999; Bernardini et al., 2014). It is worthy of note that in any CFD modelling, it is critical to compare and validate any predictions against experimental data, where available, or the predictions of well-proven and high accuracy first principles models such as DNS. In circumstances where experimental data is scarce, as in the present case, DNS is the most accurate approach for predicting single-phase (and two-phase bubbly) flows given its fundamental nature and lack of simplifying assumptions. The predictions of DNS are currently used in this way by both the fluid dynamics and combustion research communities to provide benchmark solutions for the validation of less accurate modelling approaches. Overall, the LES showed good qualitative and quantitative agreement with the mean streamwise velocities, and normal and shear stresses, predicted using DNS.

Following implementation of the bubble tracker, the impact of the lift force in one-way coupled flows was found to be crucial in terms of the migration and accumulation of bubbles. Bubbles migrate towards the channel walls in vertical upflows, and away from the walls in downflow, though the action of the lift force. Confirmation of this was found by comparison against zero-lift simulation results that did not show any lateral bubble migration. The results obtained show good agreement with the numerical studies of

Giusti et al. (2005) and Molin et al. (2012), and the experimental works of Tomiyama et al. (2002) and Ogasawara et al. (2004).

The presence of microbubbles in the flow modulates the velocity field and turbulence structure of the continuous phase in two-way coupled flows. In the horizontal channel flow, an asymmetric velocity flow profile develops due to the bubbles' migration towards the upper channel wall. In the vertical channel flow, turbulence is increased in upflow and decreased in downflow after the injection of bubbles. Modulation of the turbulence was also found to increase with an increase in bubble size.

Forces analyses in the wall-normal direction show bubbles migrating towards the upper wall under the influence of the gravity-buoyancy force which is dominant in the horizontal channel, with it being counterbalanced by the drag force. In the vertical channel, it was shown that for both upflow and downflow the drag and lift forces tend to be dominant, with the lift force pushing bubbles closer to the wall in upflow and towards the centre of the channel in downflow. This is confirmed by the change in sign in the lift force between the upflow to downflow cases. The lift force is also always opposed and balanced by the drag force. Clearly, both gravity and buoyancy do not play a significant role in the wall-normal direction, with their effect acting in the vertical direction.

To account for bubble coalescence, the bubble tracker was modified to include a deterministic hard-sphere model for bubble-bubble collisions and a film-drainage model for bubble coalescence. In the flow, bubble-bubble collisions are identified by a detection algorithm and, once a collision is detected, the likelihood of coalescence is evaluated using the film-drainage theory. The updated tracker was subsequently applied to study the influence of gravity on bubble mixing, bubble migration, inter-bubble collisions and bubble coalescence. This was first carried out by running four sets of simulations in a horizontal channel, with and without the gravity-buoyancy force term applied, using flows of Re_τ = 150 and 590 laden with 220 μm diameter spherical bubbles, with the results demonstrating the significant influence of gravity on bubble migration, collision and coalescence when compared with predictions for zero gravity flows.

Upward and downward vertical channel flows of water at shear Reynolds numbers of 150 and 590 with air bubbles of diameter d_b = 110, 220 and 330 μm dispersed within the

flows were also investigated using the same model, with the influence of the lift force, bubble size, flow configuration and turbulence on microbubble coalescence considered. In the vertical channel, and as noted, bubbles migrate towards the wall in upflow and towards the channel centre in downflow, with the lift force dominant in the wall-normal direction and largely responsible for the lateral bubble dispersion. Features of the bubble distribution in such flows were well captured by the model, as was the impact of flow Reynolds number, with higher Reynolds numbers overridding the effects of lift and leading to less bubble accumulation in the centre of the channel or at the walls. Microbubble preferential concentration was found to increase with increasing bubble size. A greater number of bubble-bubble collisions and coalescences, but at a reduced efficiency of coalescence, were also observed close to the walls in vertical channel upflows, when compared to the downflow configuration, due partially to bubbles increasing the turbulence level in upflow but reducing it in downflow, but mainly due to the migration of bubbles to near-wall regions where bubble concentrations and turbulence levels are high. A greater number of collision and coalescence events also occurred at $Re_\tau = 590$ due to enhanced bubble mixing and interaction promoted by high levels of turbulence.

Coalescence of bubbles plays a major role in bubbly flows, promoting a wide bubble size distribution. Overall, the results obtained for the above four-way coupled flows demonstrate the potential of the overall model for predicting microbubble coalescence. Previous studies of this kind have been mostly limited to bubble columns (Delnoij et al., 1997; van den Hengel et al., 2005; Lau et al., 2014) with bubbles of millimeters in size. In addition, DNS- and LES-based studies in closed ducts of various geometries have also been performed, but these are mainly limited to two-way coupled simulations. In this work, detailed studies of microbubble coalescence in channel flows for a range of bubble sizes have been performed, highlighting, amongst other parameters, the influence of bubble diameter on coalescence. Of particular interest with the approach adopted is the deterministic evaluation of collision, and coalescence, based on the locally resolved turbulent flow field. This approach has clear advantages, in terms of detail and accuracy, over the macroscopic statistical models of coalescence based on averaged velocity and turbulence fields which are generally applied in the prediction of bubbly flows in the

chemical and process engineering, pharmacology, water treatment and food industries (Rodríguez-Rodríguez et al., 2015).

A criteria for bubble breakup was also introduced into the bubble tracker, based on the approach of Martinez-Bazan et al. (1999) which best suited the Eulerian-Langrangian technique adopted in this work. For a bubble to break, the flow surrounding the bubble must be sufficiently turbulent to deform the bubble and overcome its surface restoring force. Upward and downward vertical channel flows of water at shear Reynolds numbers of 150, 590 and 2000 were examined, with air bubbles of diameter d_b= 110, 220 and 2000 μm dispersed within the flows. The ability of the model to predict breakup was evaluated, as well as the impact of the flow condition. However, studies revealed that the carrier phase turbulence kinetic energy dissipation rate, used to quantify bubble breakup in the model of Martinez-Bazan et al. (1999), was not sufficient within the flows investigated to cause bubble breakup. This was largely due to the high surface tension of air-in-water bubbles that restores any bubble surface deformation. Additional simulations in a vertical channel were therefore performed for the case of a refrigerant R134a flow at a shear Reynolds number of 1154 with dispersed refrigerant bubbles with a significantly lower surface tension.

It was concluded that bubbles with low surface tension breakup more easily, as would be anticipated. Predictions of the bubble size distribution resulting from breakup events, which assume that when a primary bubble breaks two daughter bubbles with uniformly distributed volumes are formed, showed good qualitative agreement with previous experimental work (Randolph, 1969; Martinez-Bazan, 1998). The location of breakup events was found to be in the near channel wall regions where the turbulence kinetic energy dissipation rate is highest. It was found that more bubble breakups occurred for the $d_b = 220\ \mu m$ bubble size than for the 110 μm and 2000 μm bubbles also considered. This is because 110 μm bubbles possess a high surface restoring force, whereas in the 2000 μm case this was due to the small number of bubbles within the flow (used to maintain a constant bubble volume fraction across the three sizes of bubble considered). Simulations including coalescence and breakup also demonstrated that both phenomena are favoured in upflow conditions, with the higher turbulence level found close to solid surfaces significantly impacting the extent of bubble interaction. Coalescence is dominant

at low turbulence levels and increases with decreases in bubble size, whereas breakup, which was only detected in the R134a flow, is favoured at high turbulence levels.

The results given in previous chapters demonstrate the ability of the overall model to predict bubble coalescence and breakup and, ultimately, its usefulness for predicting flows that are of industrial relevance where interfacial area and bubble size distribution govern interfacial mass, momentum and heat transfer processes.

7.2 Recommendations for Further Work

Based on the conclusions of this study, there remains a number of areas that are worthy of further investigation. Recommendations for future work are presented below.

LES is an attractive tool for complex flow modelling, and represents the next generation of CFD tool for use by industry, but in its application inaccuracies inevitably occur since it does not resolve all turbulence length and timescales. Although models are available that can predict sub-grid scale velocity fluctuations, these embody significant simplifying assumptions. Therefore, by using direct numerical simulation as the basis of bubbly flow predictions, with simple one-way through to complex four-way coupling with bubble coalescence and breakup, more realistic and accurate predictions will be obtained that reveal more insight into the physics of bubbly flows. DNS by definition solves the Navier–Stokes equations numerically without any turbulence modelling, with the whole range of spatial and temporal scales of turbulence resolved. Results are of the highest accuracy, but computationally expensive, although the increasing availability of high performance computers makes their use feasible.

The Lagrangian bubble tracking approach is less attractive when the volume fraction of bubbles is high. This approach was used in the present work to allow the tracking of individual bubbles within the flow, and to allow insight into bubble behaviour. However, in many practical applications the volume fraction of bubbles is significantly higher than considered in this work. Coupling LES with an Eulerian based method for predicting bubble behaviour should therefore also be pursued. Generally, the effects of interest in bubbly flows are best described in a Lagrangian framework, although at high volume fractions the computational effort required becomes significant. In pursuing Eulerian

approaches, however, the results of Lagrangian-based simulations, as described in this thesis, are of value, together with experimental data, in allowing their formulation and validation, for example in providing physical details of bubble dynamics and carrier fluid-bubble interactions.

Improvement of the Lagrangian bubble tracker described to account for multiple collisions, as opposed to the binary collisions assumed in the present work, is also required, although this will be very challenging to implement and will inevitably lead to increases in computational cost.

Bubble breakup was difficult to obtain based on the model used in this work, and this may have been due, to some extent, to inaccuracies within the model. Additional studies are therefore required to precisely quantify the turbulence properties that are responsible for bubble deformation and ultimately bubble breakup, with such studies being of value in the reformulation of overall models of breakup. Likewise, the model employed in this work for bubble coalescence would benefit from further investigation, with detailed studies of coalescence again of benefit to improvements in model accuracy. The type of work necessary to provide such understanding is covered in the following point.

During the breakup studies, it was found that breakup was only recorded in the highest turbulence kinetic energy dissipation regions within a flow (close to the channel walls). The LES predictions were made using a numerical mesh structured in such a way that the grid was finer in the wall regions to ensure resolution of flow behaviour close to solid surfaces. However, this meant that larger bubbles of $d_b = 2000\ \mu m$ tended to overlap control volumes thereby violating the point-wise particle assumption implicit in Lagrangian approaches of the type employed. Therefore, it would be useful to pursue studies of bubbly flows using interface tracking techniques, either with LES or DNS. Such techniques would allow the accurate prediction of the dynamics of bubbles of any size, and indeed shape. However, the limitation is that such approaches are computationally intensive and hence limited to orders of magnitude fewer bubbles than considered in this work. Nevertheless, their use would allow improvements in both Lagrangian and Eulerian approaches to modelling bubbly flows.

By introducing additional models for heat transfer and boiling within the overall flow solver it could be applied more broadly to the prediction of boiling flows, as encountered in many engineering processes and nuclear reactor thermal hydraulics.

By changing the flow geometry from a channel flow to a pipe, as applied most frequently in industry, the overall model could be used to provide useful information about the physical mechanisms governing bubble-laden turbulent flows in such geometries. Indeed, applying the model more broadly to a wider range of flow types of practical relevance would be beneficial.

Lastly, and perhaps most importantly, there is a paucity of detailed and reliable experimental data on bubbly flows, with very few studies concerning bubble coalescence and breakup. Detailed experimental studies in simple flow geometries on microbubble coalescence and breakup would be very useful, as would detailed measurements of both the continuous and dispersed phases, and would allow validation of predictions of models of the type developed in this work. Detailed experiments on single bubbles, pairs of bubbles and high volume fractions of bubbles would all be useful, not only in allowing validation of overall models, but also in justifying many of the sub-models embodied within them.

References

Afkhami, M., Hassanpour, A., Fairweather, M. and Njobuenwu, D.O. 2015. Fully coupled LES-DEM of particle interaction and agglomeration in a turbulent channel flow. *Computers & Chemical Engineering.* **78**, pp.24-38.

Antal, S.P., Lahey, J.R.T. and Flaherty, J.E. 1991. Analysis of phase distribution in fully developed laminar bubbly two-phase flow. *International Journal of Multiphase Flow.* **17**, pp.635-652.

Apte, S.V., Mahesh, K. and Lundgren, T. 2003. An Eulerian-Lagrangian model to simulate two-phase/particulate flows in complex geometries. *Center for Turbulence Research, Annual Research Briefs.* **161**, pp.161-171.

Ashgriz, N. and Poo, J.Y. 1990. Coalescence and separation in binary collisions of liquid drops. *Fluid Mechanics.* **221**, pp.183-204.

Auton, T.R., Hunt, J.C.R. and Prud'homme, M. 1988. The force exerted on a body in inviscid unsteady nonuniform rotational flow. *Journal of Fluid Mechanics.* **197**, pp.241-265.

Badreddine, H., Sato, Y., Berger, M. and Nieno, B. 2017. A three-dimensional, immersed boundary, finite volume method for the simulation of incompressible heat transfer flows around complex geometries. *International Journal of Chemical Engineering.* **2017**, pp.14-28.

Balachandar, S. and Eaton, J.K. 2010. Turbulent dispersed multiphase flow. *Annual Review of Fluid Mechanics.* **42**, pp.111-133.

Baldwin, B. and Barth, T. 1991. A one-equation turbulence transport model for high Reynolds number wall-bounded flows. *29th Aerospace Sciences Meeting, American Institute of Aeronautics and Astronautics.*

Baldyga, J. and Bourne, J.R. 1995. Interpretation of turbulent mixing using fractals and multifractals. *Chemical Engineering Sciences.* **50**, pp.381-400.

Bataille, J. and Lance, M. 1991. Turbulence in the Liquid-phase of a uniform bubbly air water-flow. *Journal of Fluid Mechanics.* **222**(95).

Becker, S., Sokolichin, A. and Eigenberger, G. 1994. Gas-liquid flow in bubble columns and loop reactors: Part II. Comparison of detailed experiments and flow simulations. *Chemical Engineering Science.* **49**, pp.5747-5762.

Bensow, R.E. 2011. Simulation of the unsteady cavitation on the Delft Twist22 foil using RANS, DES and LES. In: *2nd International Symposium on Marine Propulsors*, *Hamburg, Germany*.

Berger, M. and Aftosmis, M. 1998. Aspects (and aspect ratios) of cartesian mesh methods. In: Bruneau, C.-H. ed. *Sixteenth International Conference on Numerical Methods in Fluid*

Dynamics: Proceedings of the Conference Held in Arcachon, France, 6-10 July 1998. Berlin, Heidelberg: Springer Berlin Heidelberg, pp.1-12.

Bernardini, M., Pirozzoli, S. and Orlandi, P. 2014. Velocity statistics in turbulent channel flow up to Re_T = 4000. *Journal of Fluid Mechanics.* **742**, pp.171-191.

Bhaga, D. and Weber, M.E. 1980. In-line interaction of a pair of bubbles in a viscous liquid. *Chemical Engineering Science.* **35**, pp.2467-2474.

Bini, M. and Jones, W. 2007. Particle acceleration in turbulent flows: A class of nonlinear stochastic models for intermittency. *Physics of Fluids.* **19**, p035104.

Bini, M. and Jones, W.P. 2008. Large-eddy simulation of particle-laden turbulent flows. *Journal of Fluid Mechanics.* **614**, pp.207–252.

Bishop, R.F. 1975. Thermo-fluid dynamic theory of two-phase flow. *Physics Bulletin.* **26**, pp.544-556.

Biswas, S. 2007. *Direct numerical simulation and two-fluid modelling of multi-phase bubbly flows*. PhD Thesis thesis, Worcester Polytechnic Institute.

Bogdevich, V.G., Evseev, A.R., Malyuga, A.G. and Migirenko, G.S. 1977. Gas saturation effect on near-wall turbulence characteristics. In: BHRA, ed. *Second International Conference on Drag Reduction*, *Cambridge, England*. pp.25–37.

Boisson, N. and Malin, M.R. 1996. Numerical prediction of two-phase flow in bubble columns. *International Journal for Numerical Methods in Fluids* **23**, pp.1289-1310.

Bokkers, G.A., Laverman, J.A., Annaland, M.V.S. and Kuipers, J.A.M. 2006. Modelling of large-scale dense gas-solid bubbling fluidised beds using a novel discrete bubble model. *Chemical Engineering Science.* **61**, pp.5290-5302.

Bolotnov, I.A., Lahey Jr, R.T., Drew, D.A., Jansen, K.E. and Oberai, A.A. 2010. Spectral analysis of turbulence based on the DNS of a channel flow. *Computers and Fluids.* **39**, pp.640-655.

Brabcová, Z., Karapantsios, T., Kostoglou, M., Basařová, P. and Matis, K. 2015. Bubble-particle collision interaction in flotation systems. *Colloids and Surfaces: Physicochemical and Engineering Aspects.* **473**, pp.95-103.

Bratland, O. 2010. *Pipe flow 2: Multi-phase flow assurance.*

Brennen, E.C. 1995. *Cavitation and bubble dynamics.* London: Oxford University Press.

Breuer, M. and Alletto, M. 2012. Efficient simulation of particle-laden turbulent flows with high mass loadings using LES. *International Journal of Heat and Fluid Flow.* **35**, pp.2-12.

Breuer, M. and Almohammed, N. 2015. Modelling and simulation of particle agglomeration in turbulent flows using a hard-sphere model with deterministic collision

detection and enhanced structure models. *International Journal of Multiphase Flow.* **73**, pp.171-206.

Brooks, C.S. and Hibiki, T. 2016. Modelling and validation of interfacial area transport equation in subcooled boiling flow. *Journal of Nuclear Science and Technology.* **53**, pp.1192-1204.

Bunner, B.M. 2000. *Numerical simulation of gas-liquid bubbly flows*. PhD thesis, University of Michigan.

Calderbank, P.H., Moo-Young, M.B. and Bibby, R. 1964. Third European symposium chemical reaction engineering. In: *North Holland, Amsterdam* p.91.

Ceccio, S.L. 2010. Friction drag reduction of external flows with bubble and gas injection. *Annual Review of Fluid Mechanics.* pp.183-203.

Chahed, J., Roig, V. and Masbernat, L. 2003. Eulerian-Eulerian two-fluid model for turbulent gas-liquid bubbly flows. *International Journal of Multiphase Flow.* **29**, pp.23-49.

Chapman, S. and Cowling, T.G. 1961. The mathematical theory of non-uniform gases. *Cambridge University Press, Cambridge.*

Chen, P., Sanyal, J. and Duduković, M.P. 2005. Numerical simulation of bubble columns flows: effect of different breakup and coalescence closures. *Chemical Engineering Science.* **60**, pp.1085-1101.

Chen, S. and Doolen, G.D. 1998. Lattice Boltzmann method for fluid flows. In: *Annual Review of Fluid Mechanics*. pp.329-364.

Chesters, A.K. 1991. The modelling of coalescence processes in fluid-liquid dispersions: a review of current understanding *Chemical Engineering Research and Design.* **69**, pp.259-270.

Cheung, C., Duan, X., Yeoh, G., Tu, J., Krepper, E. and Lucas, D. 2010. An assessment of average bubble number density model for bubbly flows. In: *17th Australasian Fluid Mechanics Conference 2010*, *Auckland, New Zealand*. University of Auckland, pp.535 -538.

Cheung, S.C.P., Yeoh, G.H. and Tu, J.Y. 2007. On the modelling of population balance in isothermal vertical bubbly flows :Average bubble number density approach. *Chemical Engineering and Processing.* **46**, pp.742-756.

Choi, H. and Moin, P. 1994. Effects of the computational time-step on numerical simulations of turbulent flow. *Computational Physics* **113**, pp.1-4.

Christopher, E.B. 2005. *Fundamentals of Multiphase Flows.* Cambridge University Press 2005.

Cinosi, N., Walker, S.P., Bluck, M.J. and Issa, R. 2014. CFD simulation of turbulent flow in a rod bundle with spacer grids (MATIS-H) using STAR-CCM+. *Nuclear Engineering and Design.* **279**, pp.37-49.

Clarke, D., Salas, M. and Hassan, H. 1986. Euler calculations for multi-element airfoils using Cartesian grids. *American Institute of Aeronautics and Astronautics.* **24**, pp.1128-1135.

Cliff, R., Grace, J.R. and Weber, M.E. 1978. *Bubbles, drops and particles.* New York.

Colin, C., Fabre, J. and Kamp, A.M. 2012. Turbulent bubbly flow in pipe under gravity and microgravity conditions. *Journal of Fluid Mechanics.* **711**, pp.469-515.

Colombo, M. and Fairweather, M. 2015. Multiphase turbulence in bubbly flows: RANS simulations. *International Journal of Multiphase Flow.* **77**, pp.222-243.

Colombo, M. and Fairweather, M. 2016. RANS simulation of bubble coalescence and break-up in bubbly two-phase flows. *Chemical Engineering Science.* **146**, pp.207-225.

Coulaloglou, C.A. and Tavlarides, L.L. 1977. Description of interaction processes in agitated liquid-liquid dispersions. *Chemical Engineering Science.* **32**, pp.1289–1297.

Coulson, J.M., Richardson, J.F., Backhurst, J.R. and Harker, J.H. 1978. *Chemical engineering. Vol.2, Unit operations.*

Crabtree, J.R. and Bridgwater, J. 1971. Bubble coalescence in viscous liquids. *Chemical Engineering Science.* **26**, pp.839-851.

Dabiri, S. and Tryggvason, G. 2015. Heat transfer in turbulent bubbly flow in vertical channels. *Chemical Engineering Science.* **122**, pp.106-113.

Darmana, D., Deen, N.G. and Kuipers, J.A.M. 2006. Parallelization of an Euler-Lagrange model using mixed domain decomposition and a mirror domain technique: Application to dispersed gas-liquid two-phase flow. *Journal of Computational Physics.* **220**, pp.216-248.

Davidson, L. 2017. *An Introduction to turbulence models*. PhD thesis, Chalmers university of technology.

De Matos, A., Rosa, E.S. and Franca, F.A. 2004. The phase distribution of upward co-current bubbly flows in a vertical square channel. *Journal of the Brazilian Society of Mechanical Sciences and Engineering.* **26**, pp.308-316.

Deardorff, J.W. 1970. A numerical study of three-dimensional turbulent channel flow at large Reynolds numbers. *Journal of Fluid Mechanics.* **41**, pp.453-480.

Deen, G.N. 2001. Multiphase particle image velocimetry measurements in a bubble column. *Chemical Engineering Science.* **8**, pp.6700-6003.

Deen, N.G., Solberg, T. and Hjertager, B.H. 2001. Large eddy simulation of the Gas–Liquid flow in a square cross-sectioned bubble column. *Chemical Engineering Science.* **56**(21-22), pp.6341-6349.

Deen, N.G., van Sint Annaland, M. and Kuipers, J.A.M. 2004. Multi-scale modeling of dispersed gas–liquid two-phase flow. *Chemical Engineering Science.* **59**, pp.1853-1861.

Deju, L., Cheung, S.C.P., Yeoh, G.H. and Tu, J.Y. 2013. Capturing coalescence and break-up processes in vertical gas-liquid flows: Assessment of population balance methods. *Applied Mathematical Modelling* **37**, pp.8557-8577.

Delnoij, E. 2001. *Fluid dynamics of gas-liquid bubble columns: a theoretical and experimental study*. PhD thesis, Twente University.

Delnoij, E., Kuipers, J.A.M. and van Swaaij, W.P.M. 1997. Computational fluid dynamics applied to gas-liquid contactors. *Chemical Engineering Science.* **52**, pp.3623-3638.

Delnoij, E., Westerweel, J., Deen, N.G., Kuipers, J.A.M. and van Swaaij, W.P.M. 1999. Ensemble correlation PIV applied to bubble plumes rising in a bubble column. *Chemical Engineering Science.* **54**, pp.5159-5171.

Descamps, M.N., Oliemans, R.V.A., Ooms, G. and Mudde, R.F. 2008. Air-water flow in a vertical pipe: experimental study of air bubbles in the vicinity of the wall. *Experiments in Fluids.* **45**, pp.357-370.

Di Mare, L. and Jones, W.P. 2003. LES of turbulent flow past a swept fence. *International Journal of Heat and Fluid Flow.* **24**, pp.606-615.

Dhotre, M.T., Deen, N.G., Niceno, B. and Khan, Z. 2012. Large eddy simulation for dispersed bubbly flows: a review. *International Journal of Chemical Engineering.* **2013**, pp.1-22.

Dhotre, M.T., Deen, N.G., Niceno, B., Khan, Z. and Joshi, J.B. 2013. Large eddy simulation for dispersed bubbly flows: A review. *International Journal of Chemical Engineering.* **2013**, pp.1-22.

Durbin, P.A. and Reif, B.A.P. 2010. Reynolds Averaged Navier–Stokes Equations. *Statistical Theory and Modeling for Turbulent Flows.* John Wiley & Sons, Ltd, pp.45-56.

Elghobashi, S. and Truesdell, G.C. 1992. Direct simulation of particle dispersion in a decaying isotropic turbulence. *Fluid Mechanics.* **242**, pp.655-700.

Elghobashi, S. 1994. On predicting particle-laden turbulent flows. *Applied Scientific Research.* **52**, pp.309-329.

Enwald, H., Peirano, E. and Almstedt, A.E. 1996. Eulerian two-phase flow theory applied to fluidization. *International Journal of Multiphase Flow.* **22**, pp.21-66.

Esmaelli, A. and Tryggvason, G. 1999. Direct numerical simulations of bubbly flows Part 2. Moderate Reynolds number arrays. *Journal of Fluid Mechanics.* **385**, pp.325-358.

Estrade, J.P., Carentz, H., Lavergne, G. and Biscos, Y. 1999. Experimental investigation of dynamic binary collision of ethanol droplets-a model for droplet coalescence and bouncing. *International Journal of Heat and Fluid Flow.* **20**, pp.486 – 491.

Faires, J.D. and Burden, R.L. 1994. *Numerische Methoden-Näherungsverfahren und ihre praktische Anwendung.*

Fan, R., Marchisio, D.L. and Fox, R.O. 2004. Application of the direct quadrature method of moments to polydisperse gas-solid fluidized beds. *Powder Technology.* **139**, pp.7-20.

Ferante, A. and Elghobashi, S. 2004. On the physical mechanisms of drag reduction in a spatially developing turbulent boundary layer laden with microbubbles. *Journal of Fluid Mechanics.* **503**, pp.345-355.

Field, B.S. and Hrnjak, P.S. 2007. *Two-Phase pressure drop and flow regime of refrigerants and Refrigerant-Oil mixtures in small channels* [Manuscript]. At*:* University of Illinois, Air Conditioning and Refrigeration Center. 217.

Fischer, G. 1965. A survey of finite-difference approximations to the primitive equations. *Monthly Weather Review.* **93**, pp.1-10.

Fox, D.G. and Lilly, D.K. 1972. Numerical simulation of turbulent flows. *Reviews of Geophysics.* **10**, pp.51-72.

Fox, R.O., Laurent, F. and Massot, M. 2008. Numerical simulation of spray coalescence in an Eulerian framework: Direct quadrature method of moments and multi-fluid method. *Journal of Computational Physics* **227**, pp.3058-3088.

Fraga, B., Stoesser, T., Lai, C.C.K. and Socolofsky, S.A. 2016. A LES-based Eulerian–Lagrangian approach to predict the dynamics of bubble plumes. *Ocean Modelling.* **97**, pp.27-36.

Fromm, J.E. and Harlow, F.H. 1963. Numerical solution of the problem of vortex street development. *Physics of Fluids.* **6**, p975.

Fukagata, K., Zahrai, S., Kondo, S. and Bark, F.H. 2001. Anomalous velocity fluctuations in particulate turbulent channel flow. *International Journal of Multiphase Flow.* **27**, pp.901-917.

Fulgosi, M., Lakehal, D., Banerjee, S. and Yadigaroglu, G. 2001. Direct numerical simulation of turbulence and interfacial dynamics in counter-current air-water flows. In: Geurts, B.J., et al. eds. *Direct and Large-Eddy Simulation IV.* Dordrecht: Springer Netherlands, pp.443-452.

Gamet, L., Ducros, F., Nicoud, F. and Poinsot, T. 1999. Compact finite difference schemes on non-uniform meshes. Application to direct numerical simulations of compressible flows. *International Journal for Numerical Methods in Fluids.* **29**, pp.159-191.

Gentry, R.A., Martin, R.E. and Daly, B.J. 1966. An Eulerian differencing method for unsteady compressible flow problems. *Journal of Computational Physics.* **1**, pp.87-118.

Germano, M., Piomelli, U., Moin, P. and Cabot, W. 1991. A dynamic subgrid scale eddy viscosity model. *Physics of Fluids* **A 3**, p1760.

Germano, M., Piomelli, U., Moin, P. and Cabot, W. 1991. Turbulence: The filtering approach. *Journal of Fluid Mechanics.* **238**, pp.325-336.

Ghosal, S., Ghosh, J.K. and Samanta, T. 1995. On convergence of posterior distributions. pp.2145-2152.

Ghosal, S. and Moin, P. 1995. The basic equations for the large eddy simulation of turbulent flows in complex geometry. *Journal of Computational Physics.* **118**, pp.24-37.

Giusti, A., Lucci, F. and Soldati, A. 2005. Influence of the lift force in direct numerical simulation of upward/downward turbulent channel flow laden with surfactant contaminated microbubbles. *Chemical Engineering Science.* **60**, pp.6176-6187.

Gore, R.A. and Crowe, C.T. 1989. Effect of particle size on modulating turbulent intensity. *International Journal of Multiphase Flow.* **15**, pp.279-285.

Göz, M.F., Bunner, B., Sommerfeld, M. and Tryggvason, G. 2002. Direct Numerical Simulation of Bubble Swarms with a Parallel Front-Tracking Method. In: Breuer, M., et al. eds. *High Performance Scientific and Engineering Computing.* Berlin Heidelberg: Springer, pp.97-106.

Göz, M.F., Sommerfeld, M. and Laín, S. 2006. Instabilities in Lagrangian tracking of bubbles and particles in two-phase flow. *American Institute of Chemical Engineers.* **52**, pp.469-477.

Grube, M.C. 2015. *Hydrodynamics, mass transfer and chemical reactions in bubble columns*. PhD thesis, Graz University of Technology.

Gruber, M.C., Radl, S. and Khinast, J.G. 2013. Coalescence and Break-Up in Bubble Columns: Euler-Lagrange Simulations Using a Stochastic Approach. *Chemie Ingenieur Technik.* **85**, pp.1118-1130.

Gutiérrez-Torres, C.C., Hassan, Y.A. and Jimenez-Bernal, J.A. 2008. Turbulence structure modification and drag reduction by microbubble injections in a boundary layer channel flow. *Journal of Fluids Engineering.* **130**, pp.111304-111304.

Hammami, A. and Ratulowski, J. 2007. Precipitation and deposition of asphaltenes in production systems: A flow assurance overview. In: Mullins, O.C., et al. eds. *Asphaltenes, Heavy Oils, and Petroleomics.* New York, NY: Springer New York, pp.617-660.

Harlow, F.H. and Welch, J.E. 1965. Numerical calculation of time-dependent viscous incompressible flow of fluid with a free surface. *Physics of Fluids.* **8**, pp.2182–2189.

Hassan, Y.A., Blanchat, T.K., Seeley Jr, C.H. and Canaan, R.E. 1992. Simultaneous velocity measurements of both components of a two-phase flow using particle image velocimetry. *International Journal of Multiphase Flow.* **18**, pp.371-395.

Hassan, A. 2014. Bubbly Two-Phase Flow: Part II- Characteristics and Parameters. *American Journal of Fluid Dynamics.* **4**, pp.115-180.

He, C., Bi, X.T. and Grace, J.R. 2015. Monitoring electrostatics and hydrodynamics in gas–solid bubbling fluidized beds using novel electrostatic probes. *Industrial and Engineering Chemistry Research.* **54**, pp.8333-8343.

Hedlund, A. 2014. *Evaluation of RANS turbulence models for the simulation of channel flow*. Master thesis, Uppsala University.

Hewitt, G.F. 2011. *Gas-liquid flow Thermopedia. [Accessed 09 July 2018] Available from: http://www.thermopedia.com/content/2/.* [Online].

Hibiki, T., Mi, Y., Situ, R. and Ishii, M. 2003. Interfacial area transport of vertical upward bubbly two-phase flow in an annulus. *International Journal of Heat and Mass Transfer.* **46**, pp.4949-4962.

Hibiki, T., Goda, H., Kim, S., Ishii, M. and Uhle, J. 2004. Structure of vertical downward bubbly flow. *International Journal of Heat and Mass Transfer.* **47**, pp.1847-1862.

Hinze, J.O. 1955 Fundamentals of the hydrodynamic mechanism of splitting in dispersion processes. *American Institute of Chemical Engineers.* **1**, pp.289–295.

Hinze, J.O. 1975. *Turbulence.* New York, USA: MacGraw-Hill,.

Hirt, C.W. and Nichols, B.D. 1981. Volume of fluid (VOF) method for the dynamics of free boundaries. *Journal of Computational Physics* **39**, pp.201-225.

Hoomans, B.P.B., Kuipers, J.A.M., Briels, W.J. and van Swaaij, W.P.M. 1996. Discrete particle simulation of bubble and slug formation in a two-dimensional gas-fluidised bed: a hard-sphere approach. *Chemical Engineering Science* **51** pp.99–118.

Hosokawa, S. and Tomiyama, A. 2004. Turbulence modification in gas–liquid and solid-liquid dispersed two-phase pipe flows. *International Journal of Heat and Fluid Flow.* **25**, pp.489-498.

Hosokawa, S., Sou, A. and Tomiyama, A. 2007. Multi-fluid simulation of turbulent bubbly pipe flows. In: *Proceedings of the 6th International Conference on Multiphase Flow, Leipzig, Germany*.

Hosokawa, S., Suzuki, T. and Tomiyama, A. 2010. Effects of bubbles on turbulence properties in a duct flow. **22**, pp.211-232.

Howarth, W.J. 1964. Coalescence of drops in a turbulent flow field. *Chemical Engineering Science.* **19**, pp.33-38.

Irfan, M. and Muradoglu, M. 2017. A front tracking method for direct numerical simulation of evaporation process in a multiphase system. *Journal of Computational Physics.* **337**, pp.132-153.

Ishii, M. and Kim, S. 2004. Development of one-group and two-group interfacial area transport equation *Nuclear Science and Engineering* **146**, pp.257-273.

Israelachvili, J.N. 2011. Strong Intermolecular Forces: Covalent and Coulomb Interactions. *Intermolecular and Surface Forces (Third Edition).* San Diego: Academic Press, pp.53-70.

Jones, C. and Zuber, N. 1979. Slug-annular Transition with Particular Reference to Narrow Rectangular Ducts. In: *In Two-phase Momentum, Heat and Mass Transfer in Chemical, Process and Energy Engineering Systems*. pp.345-355.

Jones, W.P., Di Mare, L. and Marquis, A.J. 2002. *LES-BOFFIN: User's Guide.* London.

Jones, W.P., Marquis, A.J. and Vogiatzaki, K. 2014. Large-eddy simulation of spray combustion in a gas turbine combustor. *Combustion and Flame.* **161**, pp.222-239.

Kanai, A. and Miyata, H. 2001. Direct numerical simulation of wall turbulent flows with microbubbles. *International Journal for Numerical Methods in Fluids.* **35**, pp.593-615.

Kang, I.S. and Leal, L.G. 1987. Numerical solution of axisymmetric, unsteady free-boundary problems at finite Reynolds number.I: Finite-difference scheme and its application to the deformation of a bubble in a uniaxial straining flow. *Physics of Fluids.* 30, pp.1929–1940.

Kataoka, I., Ishii, M. and Serizawa, A. 1986. Local formulation and measurements of interfacial area concentration in two-phase flow. *International Journal of Multiphase Flow.* **12**, pp.505-529.

Kataoka, I. and Serizawa, A. 1989. Basic equations of turbulence in gas-liquid two-phase flow. *International Journal of Multiphase Flow.* **15**, pp.843-855.

Kleissl, J., Meneveau, C. and Parlange, M.B. 2002. *Effects of stability and filter size on model coefficients and intermittency of sub-filter fluxes in the atmospheric boundary layer.*

Kolmogorov, A.N. 1949. *On the disintegration of drops in a turbulent flow* Dokl. Akad. Nauk SSSR 66. pp.825–828.

Krishna, R., van Baten, J.M. and Urseanu, M.I. 2000. Three-phase Eulerian simulations of bubble column reactors operating in the churn-turbulent regime: a scale up strategy *Chemical Engineering Science* **55**, pp.3275-3286.

Kuerten, J.G.M., Geurts, B.J., Vreman, A.W. and Germano, M. 1999. Dynamics inverse modeling and its testing in large-eddy simulation of the mixing layer. *Physics of Fluids.* **11**, pp.3778-3785.

Kurose, R. and Komori, S. 1999. Drag and lift forces on a rotating sphere in a linear shear flow. *Journal of Fluid Mechanics.* **384**, pp.183-206.

Kuschel, M. and Sommerfeld, M. 2010. Experimental investigation of droplet collisions with higher viscosity. In: *23rd Annual Conference on Liquid Atomization and Spray Systems, Brno, Czech Republic*.

Laborde-Boutet, C., Larachi, F., Dromard, N., Delsart, O. and Schweich, D. 2009. CFD simulation of bubble column flows: Investigations on turbulence models in RANS approach. *Chemical Engineering Science.* **64**, pp.4399-4413.

Laccarino, G. and Verzicco, R. 2003. Immersed boundary technique for turbulent flow simulations. In: *Center for Turbulence Research, Stanford University*. American Society of Mechanical Engineers.

Lain, S., Bröder, D. and Sommerfeld, M. 1999. Experimental and numerical studies of the hydrodynamics in a bubble column. *Chemical Engineering Science.* **54**, pp.4913-4920.

Lahey Jr, R.T., Cheng, L.Y., Drew, D.A. and Flaherty, J.E. 1980. The effect of virtual mass on the numerical stability of accelerating two-phase flows. *International Journal of Multiphase Flow.* **6**, pp.281-294.

Lain, S., Bröder, D., Sommerfeld, M. and Göz, M.F. 2002. Modelling hydrodynamics and turbulence in a bubble column using the Euler-Lagrange procedure. *International Journal of Multiphase Flow.* **28**, pp.1381-1407.

Lakehal, D., Meier, M. and Fulgosi, M. 2002. Interface tracking towards the direct simulation of heat and mass transfer in multiphase flows. *International Journal of Heat and Fluid Flow.* **23**, pp.242-257.

Lance, M. and Bataille, J. 1991. Turbulence in the liquid phase of a uniform bubbly air–water flow. *Journal of Fluid Mechanics.* **222**, pp.95-118.

Lance, M., MariÉ, J.L., Moursali, E., Bataille, J., Suzanne, C., Roig, V., Bel Fdhila, R. and Masbernat, L. 1996. Experimental study of turbulent bubbly shear flows. *Chemical Engineering Communications.* **141-142**, pp.51-70.

Lasheras, J.C., Eastwooda, C., Martínez-Bazánb, C. and Montañésc, J.L. 2002. A review of statistical models for the breakup of an immiscible fluid immersed into a fully developed turbulent flow. *International Journal of Multiphase Flow.* **28**, pp.247-278.

Lau, Y.M. 2013. *Coalescence and break-up in dense bubbly flows*. PhD thesis, Technische Universiteit Eindhoven.

Lau, Y.M., Bai, W., Deen, N.G. and Kuipers, J.A.M. 2014. Numerical study of bubble breakup in bubbly flows using a deterministic Euler-Lagrange framework. *Chemical Engineering Science.* **108**, pp.9-22.

Lee, C.H., Erickson, L.E. and Glasgow, L.A. 1987. Bubble breakup and coalescence in turbulent Gas-Liquid dispersions. *Chemical Engineering Science.* **59**.

Lee, B.J., Toorman, E. and Fettweis, M. 2014. Multimodal particle size distributions of fine-grained sediments: mathematical modeling and field investigation. *Ocean Dynamics.* **64**, pp.429-441.

Lee, H. and Balachandar, S. 2017. Effects of wall roughness on drag and lift forces of a particle at finite Reynolds number. *International Journal of Multiphase Flow.* **88**, pp.116-132.

Legendre, D. and Magnaudet, J. 1998. The lift force on a spherical bubble in a viscous linear shear flow. *Journal of Fluid Mechanics.* **368**, pp.81-126.

Lehr, F., Millies, M. and Mewes, D. 2002. Bubble-Size distributions and flow fields in bubble columns. *American Institute of Chemical Engineers.* **48**, pp.2426-2443.

Leonard, A. 1974. Energy cascade in large eddy simulations of turbulent fluid flows. *Advance Geophysics.* **18**, pp.237-248.

Levich, V.G. 1962. Physicochemical Hydrodynamics. Engelwood Cliffs, N.J.: Prentice Hall.

Liao, Y. and Lucas, D. 2009. A literature review of theoretical models for drop and bubble breakup in turbulent dispersions. *Chemical Engineering Science.* **64**, pp.3389-3406.

Liao, Y. and Lucas, D. 2010. A literature review on mechanisms and models for the coalescence process of fluid particles. *Chemical Engineering Science.* **65**, pp.2851-2864.

Liffman, K. 1992. A direct simulation Monte-Carlo method for cluster coagulation. *Computational Physics* **100**, pp.116-127.

Lilly, D.K. 1967. The representation of small scale turbulence in numerical simulation experiments. In: *Proceedings of the IBM Scientific Computing Symposium on Environmental Sciences, Yorktown Heights*. H. H. Goldstine IBM, pp.195–210.

Liu, T.J. 1997. Investigation of the wall shear stress in vertical bubbly flow under different bubble size conditions. *International Journal of Multiphase Flow* **23**, pp.1085–1109.

Liu, T.J. and Bankoff, S.G. 1993. Structure of air-water bubbly flow in a vertical pipe-I. liquid mean velocity and turbulence measurements. *International Journal of Heat and Mass Transfer.* **36**, pp.1049-1060.

Liu, Z., Qi, F., Li, B. and Jiang, M. 2015. Multiple Size Group Modeling of Polydispersed Bubbly Flow in the Mold: An Analysis of Turbulence and Interfacial Force Models. *Metallurgical and Materials Transactions* **46**, pp.933-952.

Lopez de Bertodano, M., Lahey Jr, R.T. and Jones, O.C. 1994. Phase distribution in bubbly two-phase flow in vertical ducts. *International Journal of Multiphase Flow.* **20**, pp.805-818.

Lu, A., Fernandez, J. and Tryggvason, G. 2005. The effect of bubbles on the wall drag in a turbulent channel flow. *Physics of Fluids.* **17**((095102)).

Lu, J. and Tryggvason, G. 2008. Effect of bubble deformability in turbulent bubbly upflow in a vertical channel. *Physics of Fluids.* **20**, p040701.

Lucas, D., Krepper, E. and Prasser, H.M. 2005. Development of co-current air–water flow in a vertical pipe. *International Journal of Multiphase Flow.* **31**, pp.1304-1328.

Luo, H. and Svendsen, H.F. 1996. Theoretical Model for Drop and Bubble Breakup in Turbulent Dispersions *American Institute of Chemical Engineers.* **42** pp.1225-1233.

Maisels, A., Einar Kruis, F. and F, H. 2004. Direct simulation Monte Carlo for simultaneous nucleation, coagulation, and surface growth in dispersed systems. *Chemical Engineering Science* **59**, pp.2231-2239.

Mallouppas, G. and van Wachem, B. 2013. Large Eddy Simulations of turbulent particle-laden channel flow. *International Journal of Multiphase Flow.* **54**(Supplement C), pp.65-75.

Marchioli, C., Picciotto, M. and Soldati, A. 2006. Particle dispersion and wall-dependent turbulent flow scales: implications for local equilibrium models. *Journal of Turbulence.* **7**, pp.1–12.

Marchioli, C. and Soldati, A. 2007. Reynolds number scaling of particle preferential concentration in turbulent channel flow. In: *Proceedings of the 11th EUROMECH European Turbulance Conference, Porto, Portugal*. pp.298-300.

Marchioli, C., Soldati, A., Kuerten, J.G.M., Arcen, B., Tanière, A., Goldensoph, G., Squires, K.D., Cargnelutti, M.F. and Portela, L.M. 2008. Statistics of particle dispersion in direct numerical simulations of wall-bounded turbulence: Results of an international collaborative benchmark test. *International Journal of Multiphase Flow.* **34**, pp.879-893.

Martinez-Bazan, C. 1998. *Splitting and dispersion of bubbles by turbulence*. PhD thesis, University of California, San Diego.

Martinez-Bazan, C., Montanes, J.L. and Lasheras, J.C. 1999. On the breakup of an air bubble injected into a fully developed turbulent flow. Part 1. Breakup frequency. *Journal of Fluid Mechanics.* **401**, pp.157-182.

Martínez-Palou, R., Mosqueira, M.d.L., Zapata-Rendón, B., Mar-Juárez, E., Bernal-Huicochea, C., de la Cruz Clavel-López, J. and Aburto, J. 2011. Transportation of heavy and

extra-heavy crude oil by pipeline: A review. *Journal of Petroleum Science and Engineering.* **75**, pp.274-282.

Mashayek, F. and Pandya, R.V.R. 2003. Analytical description of particle/droplet-laden turbulent flows. *Progress in Energy and Combustion Science.* **29**, pp.329-378.

Mattson, M.D. 2011. *Euler-Lagrangian Simulations of Turbulent Bubbly Flow*. PhD thesis, University of Minnesota.

Mattson, M.D. and Mahesh, K. 2012. A one-way coupled, Euler–Lagrangian simulation of bubble coalescence in a turbulent pipe flow. *International Journal of Multiphase Flow.* **40**, pp.68-82.

Maxey, M.R. 1990. On the Advection of Spherical and Non-Spherical Particles in a Non-Uniform Flow. *Philosophical Transactions: Physical Sciences and Engineering.* **333**, pp.289-307.

Maxey, M.R. and Riley, J.J. 1983. Equation of motion for a small grid sphere in a nonuniform flow. *Physics of Fluids.* **26** pp.883-889.

Mazzitelli, I.M., Lohse, D. and Toschi, F. 2003. The effect of microbubbles on developed turbulence. *Physics of Fluids.* **15**, pp. L5-L8.

McCabe, W.L., Smith, J.C. and Harriott, P. 1993. *Unit operations of chemical engineering.* McGraw-Hill New York.

McLaughlin, J.B. 1991. Inertial migration of a small sphere in linear shear flows. *Journal of Fluid Mechanics.* **224**, pp.261-274.

Merkle, C.L. and Deutsch, S. 1989. Microbubble Drag Reduction. In: Gad-el-Hak, M. ed. *Frontiers in Experimental Fluid Mechanics.* Springer Berlin Heidelberg, pp.291-335.

Molin, D., Marchioli, C. and Soldati, A. 2012. Turbulence modulation and microbubble dynamics in vertical channel flow. *International Journal of Multiphase Flow.* **42**, pp.80-95.

Moser, R.D., Kim, J. and Mansour, N.N. 1999. Direct numerical simulation of turbulent channel flow up to Reτ=590. *Physics of Fluids.* **11**, pp.943-945.

Mudde, R.F., Groen, J.S. and Van den Akker, H.E.A. 1997. Liquid velocity field in a bubble column: LDA experiments. . *Chemical Engineering Science.* **52**, pp.4217-4224.

Mudde, R.F. 2005. Gravity-driven bubbly flows. *Annual Review of Fluid Mechanics.* **37**, pp.393-423.

Mukherjee, A., Kandlikar, S.G. and Edel, Z.J. 2011. Numerical study of bubble growth and wall heat transfer during flow boiling in a microchannel. *International Journal of Heat and Mass Transfer.* **54**, pp.3702-3718.

Müller, E. 1994. Fundamentals of gas-dynamical simulations. In: Contopoulos, G., et al. eds. *Galactic Dynamics and N-Body Simulations.* Berlin, Heidelberg: Springer Berlin Heidelberg, pp.313-363.

Narsimhan, G., Gupta, J.P. and Ramkrishna, D. 1979. A model for transitional breakage probability of droplets in agitated lean liquid-liquid dispersions. *Chemical Engineering Science.* **34**, pp.257-265.

Njobuenwu, D.O. 2010. *Modelling and simulation of particulate flows in curved ducts*. thesis, University of Leeds.

Njobuenwu, D.O. and Fairweather, M. 2014. Effect of shape on inertial particle dynamics in a channel flow. *Flow, Turbulence and Combustion.* **92**, pp.83-101.

Njobuenwu, D.O. and Fairweather, M. 2015. Dynamics of single, non-spherical ellipsoidal particles in a turbulent channel flow. *Chemical Engineering Science.* **123**, pp.265-282.

Njobuenwu, D.O. and Fairweather, M. 2017. Simulation of deterministic energy-balance particle agglomeration in turbulent liquid-solid flows. *Physics of Fluids.* **29**, p083301.

Ogasawara, T., Tagawa, Y., Fujiwara, A., Takagi, S. and Matsumoto, Y. 2004. The clustering phenomena near the wall in a turbulent bubbly channel flow. In: *3rd International Symposium on Two-Phase Flow Modelling and Experiments Pisa*. pp.22-24.

Olmos, E., Gentric, C., Vial, C., Wild, G. and Midoux, N. 2001. Numerical simulation of multiphase flow in bubble column reactors. Influence of bubble coalescence and breakup. *Chemical Engineering Science.* **56**, pp.6359-6365.

Onslow, R.T.J., Thomas, N.H. and Whitehouse, R.J.S. 1993 Vorticity and sandwaves: the dynamics of ripples and dunes. In: *Turbulence: Perspectives on flow and sediment Transport*: John Wiley and Sons, London, pp.279-293.

Otake, T., Tone, S., Nakao, K. and Mitsuhashi, Y. 1977. Coalescence and breakup of bubbles in liquids. *Chemical Engineering Science.* **32**, pp.377-383.

Pang, M. and Wei, J. 2016. Investigation on effect of flow direction on hydrodynamics for vertical channel bubbly flow. *International Journal of Multiphysics.* **10**, pp.379-395.

Pang, M., Wei, J. and Yu, B. 2010. Numerical study of bubbly upflows in a vertical channel using the Euler-Lagrange two-way model. *Chemical Engineering Science.* **65**, pp.6215-6228.

Pang, M., Wei, J. and Yu, B. 2016. Investigation on influences of bubble location and momentum transfer direction on liquid turbulence modification for the dilute bubbly flow. *International Journal of Fluid Mechanics Research.* **43**, pp.161-181.

Pang, M., Wei, J. and Yu, B. 2013. Turbulence Modulation by Small Bubbles in the Vertical Upward Channel Flow. *Advances in Mechanical Engineering.* **5**, p379839.

Pang, M.J., Wei, J.J. and Yu, B. 2014. Numerical study on modulation of microbubbles on turbulence frictional drag in a horizontal channel. *Ocean Engineering.* **81**, pp.58-68.

Perry, H.R. and Green, D.W. 2008. *Perry's chemical engineers' handbook.* Eighth ed. New York: McGraw-Hill.

Peskin, C.S. 1972. *Flow patterns around heart valves: a digital computer method for solving the equations of motion.* . PhD thesis, Albert Einstein College of Medicine, Univ Microfilms.

Pfleger, D. and Becker, S. 2001. Modelling and simulation of the dynamic flow behaviour in a bubble column *Chemical Engineering Science.* **56**, pp.1737-1745.

Pfleger, D., Gomes, S., Gilbert, N. and Wagner, H.G. 1999. Hydrodynamic simulations of laboratory scale bubble columns fundamental studies of the Eulerian-Eulerian modelling approach. *Chemical Engineering Science* **54**, pp.5091-5099.

Piomelli, U. and Liu, J. 1995. Large-eddy-simulation of rotating channel flow using a localized dynamic model. *Physics of Fluids.* **7**, pp.839-848.

Pitsch, H. 2006. Large-eddy simulation of turbulent combustion. *Annual Review of Fluid Mechanics.* **38**, pp.453-482.

Porté-Agel, F., Meneveau, C. and Parlange, M.B. 2000. A scale-dependent dynamic model for large-eddy simulation: application to a neutral atmospheric boundary layer. *Journal of Fluid Mechanics.* **415**, pp.261-284.

Prince, M.J. and Blanch, H.W. 1990. Bubble coalescence and breakup in air-sparged bubble columns. *American Institute of Chemical Engineers.* **36**, pp.1485-1499.

Prosperetti, A. and Tryggvason, G. 2009. *Computational methods for multiphase flow.* Cambridge university press.

Randolph, A.D. 1969. Effect of crystal breakage on crystal size distribution in a mixed suspension crystallizer. *Industrial and Engineering Chemistry Fundamentals* **8**, pp.58-63.

Ren, Q., Zhou, W., Pan, L., Liu, H., Yu, B., Ye, T. and Li, S. 2017. Experimental Study of the Sub-Channel Flow Regimes in 5×5 Rod Bundles With Simplified Grid Spacer. (57878), pV009T015A021.

Rhie, C.M. and Chow, W.L. 1983. Numerical study of the turbulent flow past an airfoil with trailing edge separation. *American Institute of Aeronautics and Astronautics.* **21**, pp.1525-1532.

Rivero, M., Magnaudet, J. and Fabre, J. 1991. New results on the forces exerted on a spherical body by an accelerated flow. *Cambridge Royal Academy Science* Paris, pp.1499-1506.

Rodríguez-Rodríguez, J., Sevilla, A., Martínez-Bazán, C. and Gordillo, J.M. 2015. Generation of Microbubbles with Applications to Industry and Medicine. *Annual Review of Fluid Mechanics.* **47**, pp.405-429.

Sagaut, P., Garnier, E. and Deville, M. 2002. Large Eddy simulation of shock/homogeneous turbulence interaction. *Computers and Fluids.* **31**, pp.245-268.

Schiller, L. and Naumann, Z. 1935. A drag coefficient correlation. *Ver. Deutsch. Ing.*, pp.77-318.

Schutte, K.C.J., Portela, L.M., Twerda, A. and Henkes, R.A.W.M. 2015. Hydrodynamic perspective on asphaltene agglomeration and deposition *Energy and Fuels. .* **29**, pp.2754-2767.

Schwarzkopf, J.D., Sommerfeld, M., Crowe, C.T. and Tsuji, Y. 2011. *Multiphase flows with droplets and particles.* CRC press.

Sene, K.J., Hunt, J.C.R. and Thomas, N.H. 1994. The role coherent structures in bubble transport by turbulent shear flows. *Journal of Fluid Mechanics.* **259**, pp.219-240.

Serizawa, A., Kataoka, I. and Michiyoshi, I. 1975. Turbulence structure of air-water bubbly flow II. local properties. *International Journal of Multiphase Flow.* **2**, pp.235-246.

Shams, E., Finn, J. and Apte, S.V. 2011. A numerical scheme for Euler-Lagrange simulation of bubbly flows in complex systems. *International Journal for Numerical Methods in Fluids.* **67**, pp.1865-1898.

Shu, T., Toshiyuki, O., Masato, F. and Yoichiro, M. 2009. Surfactant effect on the bubble motions and bubbly flow structures in a vertical channel. *Fluid Dynamics Research.* **41**, p065003.

Sommerfeld, M. 2001. Validation of a stochastic Lagrangian modelling approach for inter-particle collisions in homogeneous isotropic turbulence. *International Journal of Multiphase Flow.* **27**, pp.1829-1858.

Sommerfeld, M., Bourloutski, E. and Broder, D. 2003. Euler/Lagrange calculations of bubbly flows with consideration of bubble coalescence. *Canadian Journal of Chemical Engineering.* **81**, pp.508-518.

Spelt, P.D.M. and Sangani, A.S. 1997. Properties and Averaged Equations for Flows of Bubbly Liquids. *Applied Scientific Research.* **58**, pp.337-386.

Sridhar, G. and Katz, J. 1995. Drag and lift forces on microscopic bubbles entrained by a vortex. *Physics of Fluids* **7**, pp.389-399.

Subramaniam, S. 2013. Lagrangian–Eulerian methods for multiphase flows. *Progress in Energy and Combustion Science.* **39**, pp.215-245.

Sungkorn, R. 2011. *Euler-Lagrange modeling of dispersed gas-liquid reactors*. PhD thesis, Graz University of Technology.

Sungkorn, R., Derksen, J.J. and Khinast, J.G. 2012. Euler-Lagrange modeling of a gas–liquid stirred reactor with consideration of bubble breakage and coalescence. *American Institute of Chemical Engineers.* **58**, pp.1356-1370.

Tagawa, Y., Ogasawara, T., Takagi, S. and Matsumoto, Y. 2010. Surfactant effects on single bubble motion and bubbly flow structure. *America Institute of Physics Conference Proceedings.* **1207**, pp.43-48.

Taitel, Y., Bornea, D. and Dukler, A.E. 1980. Modelling flow pattern transitions for steady upward gas-liquid flow in vertical tubes. *American Institute of Chemical Engineers.* **26**, pp.345-354.

Tanaka, T. and Tsuji, Y. 1991. Numerical simulation of gas-solid two-phase flow in a vertical pipe: On the effect of inter-particle collision. In: *Gas-solid flows*, pp.123-128.

Thomas, N.H., Auton, T.R., Sene, K. and Hunt, J.C.R. 1983 Entrainment and transport of bubbles by transient large eddies in multiphase turbulent shear flows. In: *International Conference on Physical Modelling of Multiphase Flows, Coventry, UK.* BHRA.

Thorpe, S.A. 1982. On the clouds of bubbles formed by breaking wind-waves in deep water, and their role in air-sea gas transfer. *Philosophical Transactions of the Royal Society of London.* **A304**(1483), pp.155-210.

Tomiyama, A., Tamai, H., Zun, I. and Hosokawa, S. 2002. Transverse migration of single bubbles in simple shear flows. *Chemical Engineering Science.* **57**, pp.1849-1858.

Tryggvason, G., Bunner, B., Esmaeeli, A., Juric, D., Al-Rawahi, N., Tauber, W., Hun, J. and Jan, Y.J. 2001. A front-tracking method for the computations of multiphase flow. *Computational Physics.* **169**, pp.708 -759.

Tsouris, C. and Tavlarides, L.L. 1994. Breakage and coalescence models for drops in turbulent dispersions. *American Institute of Chemical Engineers.* **40**, pp.395-406.

Udaykumar, H.S., Shyy, W. and Rao, M.M. 1996. A mixed Eulerian-Lagrangian method for fluid flows with complex and moving boundaries *Numerical Methods of Fluids* **22**, pp.691-705.

Unverdi, S.O. and Tryggvason, G. 1992. A front-tracking method for viscous, incompressible, multi-fluid flows. *Computational Physics* **100**, pp.25–37.

van den Hengel, E.I.V., Deen, N.G. and Kuipers, J.A.M. 2005. Application of coalescence and breakup models in a discrete bubble model for bubble columns. *Industrial and Engineering Chemistry Research* **44**, pp.5233-5245.

van den Berg, T.H., van Gils, D.P.M., Lathrop, D.P. and Lohse, D. 2007. Bubbly turbulent drag reduction is a boundary layer effect. *Physical Review Letters.* **98**, p084501.

Vreman, B., Geurts, B.J., Deen, N.G., Kuipers, J.A.M. and Kuerten, J.G.M. 2009. Two- and Four-Way Coupled Euler–Lagrangian Large-Eddy Simulation of Turbulent Particle-Laden Channel Flow. *Flow, Turbulence and Combustion.* **82**, pp.47-71.

Wang, L. and Maxey, M. 1993. The motion of microbubbles in a forced isotropic and homogeneous turbulence. *Applied Scientific Research* **51**, pp.291-296.

Wang, S.K., Lee, S.J., Jones Jr., O.C. and Lahey Jr., R.T. 1987. 3-D turbulence structure and phase distribution in bubbly two-phase flows. *International Journal of Multiphase Flow.* **13**, pp.327-343.

Wilcox, D.C. 2006. *Turbulence modeling for CFD.* California DCW industries La Canada.

Wilkinson, P.M., Van Schayk, A., Spronken, J.P.M. and Van Dierendonck, L. 1993. The influence of gas density and liquid properties on bubble breakup. *Chemical Engineering Science.* **48**, pp.1213-1226.

Xu, J., Zhang, J., Liu, H. and Wu, Y. 2012. Oil-gas–water three-phase upward flow through a vertical pipe: Influence of gas injection on the pressure gradient. *International Journal of Multiphase Flow.* **46**, pp.1-8.

Xu, J., Dong, S., Maxey, M.R. and Karniadakis, G.E. 2007. Turbulent drag reduction by constant near-wall forcing. *Journal of Fluid Mechanics.* **582**, pp.79-101.

Xu, J., Maxey, M.R. and Karniadakis, G.E. 2002. Numerical simulation of turbulent drag reduction using micro-bubbles. *Journal of Fluid Mechanics* **468**, pp.271–281.

Xue, J., Chen, F., Yang, N. and Ge, W. 2016. Eulerian-Lagrangian Simulation of Bubble Coalescence in Bubbly Flow using the Spring-dashpot Model. *Chinese Journal of Chemical Engineering.*

Xue, J., Chen, F., Yang, N. and Ge, W. 2017. Eulerian-Lagrangian simulation of bubble coalescence in bubbly flow using the spring-dashpot model. *Chinese Journal of Chemical Engineering.* **25**, pp.249-256.

Yamamoto, Y., Potthoff, M., Tanaka, T., Kajishima, T. and Tsuji, Y. 2001. Large-eddy simulation of turbulent gas–particle flow in a vertical channel: effect of considering inter-particle collisions. *Journal of Fluid Mechanics.* **442**, pp.303-334.

Yang, K., Zhao, L. and Andersson, H.I. 2017. Preferential particle concentration in wall-bounded turbulence with zero skin friction. *Physics of Fluids.* **29**, p113302.

Yang, X. and Thomas, N.H. 1994 Simulation of particle and bubble dispersion in turbulent free shear flows. . *Numerical Methods for Multiphase Flow.* **85**(ASME FED), pp.259-268.

Ye, T., Mitta, l.R., Udaykumar, H.S. and Shyy, W. 1999. An accurate Cartesian grid method for viscous incompressible flows with complex immersed boundaries. . *Computational Physics* **156**, pp.209-240.

Yeo, K., Dong, S., Climent, E. and Maxey, M.R. 2010. Modulation of homogeneous turbulence seeded with finite size bubbles or particles. *International Journal of Multiphase Flow.* **36**, pp.221-233.

Yuan, Y., Li, X. and Tu, J. 2016. Numerical modelling of air–nanofluid bubbly flows in a vertical tube using the MUltiple-SIze-Group (MUSIG) model. *International Journal of Heat and Mass Transfer.* **102**, pp.856-866.

Zeeuw, D. and Powell, K. 1991. An adaptively refined Cartesian mesh solver for the Euler equations. *AIAA Journal Paper.* **1991**, p1542.

Zeitling, M.A. and Tavlarides, L.L. 1972. Fluid-fluid interactions and hydrodynamics. . *Canadian Journal of Chemical Engineering.* **50**, pp.207-215.

Zhang, H., Yokomine, T. and Kunugi, T. 2015. Turbulence modulation of the upward turbulent bubbly flow in vertical ducts. *Nuclear Engineering and Technology.* **47**, pp.513-522.

Zhou, L. 2015. Two-phase turbulence models in Eulerian-Eulerian simulation of gas-particle flows and coal combustion. *Procedia Engineering.* **102**, pp.1677-1696.

Zhou, L. 2018. Chapter 1 Some Fundamentals of Dispersed Multiphase Flows. In: Zhou, L. ed. *Theory and Modeling of Dispersed Multiphase Turbulent Reacting Flows.* Butterworth-Heinemann, pp.1-8.

Zhou, L.X. 2010. Advances in studies on two-phase turbulence in dispersed multiphase flows. *International Journal of Multiphase Flow.* **36**, pp.100-108.

Zhou, Y. and Bai, H. 2011. Recent advances in active control of turbulent boundary layers. *Science China Physics, Mechanics and Astronomy.* **54**, pp.1289-1295.

Ziegenhein, T., Garcon, M. and Lucas, D. 2016. Particle tracking using micro bubbles in bubbly flows. *Chemical Engineering Science.* **153**, pp.155-164